Universidade do Minho
Escola de Ciências

Ricardo Jorge Estrada Morais Gonçalves de Sousa

Polymer based materials for printed batteries

maio de 2017

Ricardo Jorge Estrada Morais Gonçalves de Sousa **Polymer based materials for printed batteries**

UMinho | 2017

Universidade do Minho
Escola de Ciências

Ricardo Jorge Estrada Morais Gonçalves de Sousa

Polymer based materials for printed batteries

Tese de Doutoramento em Ciências
Área de Especialização em Física

Trabalho efetuado sob a orientação do
Professor Doutor Senentxu Lanceros-Mendez
e da
Professora Doutora Maria Manuela Silva Pires Silva

maio de 2017

DECLARAÇÃO

Nome: Ricardo Jorge Estrada Morais Gonçalves de Sousa

Endereço electrónico: id4447@alunos.uminho.pt

Título tese: Polymer based materials for printed batteries

Orientadores: Professor Doutor Senentxu Lanceros-Mendez

Professora Doutora Maria Manuela Silva Pires Silva

Ano de conclusão: 2017

Designação do Doutoramento: Doutoramento em Ciências – Área de Especialização em Física

Universidade do Minho, 26/05/2017

Assinatura: Ricardo Estrada Sousa

STATEMENT OF INTEGRITY

I hereby declare having conducted my thesis with integrity. I confirm that I have not used plagiarism or any form of falsification of results in the process of the thesis elaboration.

I further declare that I have fully acknowledged the Code of Ethical Conduct of the University of Minho.

University of Minho, 26 de Maio de 2017

Full name: Ricardo Jorge Estada Morais Gonçalves de Sousa

Signature: Ricardo Estada Sousa

Acknowledgments

I would like to express my sincere gratitude to my supervisors, Professor Senentxu Lanceros-Mendez and Professora Maria Manuela Silva for the opportunity, the continuous assistance, motivation and dedicated involvement in every step throughout my PhD study, and also for the incentives widen my research from various perspectives.

I am also very grateful to Doctor Carlos Costa for his friendship and for always being so supportive of my research work. His encouragement, guidance and constant feedback were also indispensable to reach the objectives of the research. The impact of his work on my own study is obvious throughout this dissertation.

This thesis is also the result of many experiences I have encountered at Electroactive Smart Materials group (ESMG) from remarkable individuals who I also wish to acknowledge. To them, I would like to thank all the great team spirit, encouragement and friendship. To the Energy sub-group I would like to transmit special thanks for the stimulating discussions, research work, and the familiar environment. All of you have been there to assist me when I needed.

A special thanks to my family for the unconditional love. Thanks for being so close to me during this long period and available to share your time supporting and encouraging me to pursuit my dreams. Words cannot express how grateful I am.

Polymer based materials for printed batteries

Abstract

There is an increasing interest in thin and flexible energy storage devices to meet modern society needs in applications such as radio frequency sensing, interactive packaging and other consumer products. Printed batteries satisfy these requirements and can also be an excellent alternative to conventional batteries for many applications. The interest in printed batteries is related to the fact of being thin, flexible and with simple integration into devices, associated to low production costs. The manufacturing of printed batteries is not simple and requires the ink formulation to be optimized for each printing technique. The ink formulation of the different materials needed for developing printed batteries has been little explored for the development of energy storage systems. Several works have been focusing on the development of inks for cathodes and anodes, the separator being still one of the larger challenges requiring strong research efforts.

The objective of this work is to produce battery separators based on poly(vinylidene fluoride-co-hexafluoropropene), P(VdF-HFP), and poly(vinylidene fluoride-co-chloro-trifluoroethylene), P(VdF-CTFE), due to its low crystallinity and high melting temperature, that can be formulated as suitable inks. For the battery separator, it is intended to establish a correlation between processing conditions, morphology, physico-chemical properties and battery performance. In relation to the inks for the cathodes, the objective was to produce new inks based on $LiFePO_4$ for screen-printing of batteries. Finally, inks for the anode were also formulated based on graphite.

Thus, the microstructure of P(VdF-HFP) and P(VdF-CTFE) membranes obtained from solution was evaluated as a function of polymer concentration and solvent evaporation temperature. The formation of a porous membrane is attributed to a liquid-liquid phase separation process. For P(VdF-HFP) and P(VdF-CTFE) membranes, the β-phase content, thermal, mechanical, dielectric and piezoelectric properties were evaluated and strongly depend on the initial polymer concentration and solvent evaporation temperature.

Cycling tests performed on Li/Sn-C and Li/$LiFePO_4$ half-cells based on P(VdF-HFP) polymer electrolyte membranes evidenced nominal capacities ranging from 70% to 90% of the theoretical value with very good capacity retention and charge/discharge efficiency close to 100%, even at high current rates, and 100% of deep of discharge (DoD). In relation to P(VdF-

CTFE) membranes, the best ionic conductivity value at room temperature is 1.5 $mS.cm^{-1}$ for the membranes prepared with 20 wt.% initial copolymer concentration and solvent evaporation temperature at 25 ℃, leading to a degree of porosity of 60% and an electrolyte uptake value of 292%. The prepared P(VdF-CTFE) separator membranes show good cyclability and rate capability. At C/10 and 2C discharge values of 168 and 102 $mA.h.g^{-1}$, respectively, are obtained. The ink for C-$LiFePO_4$ based cathodes presents a delivered capacity value of 81 $mA.h.g^{-1}$ after 50 cycles at 2C (charge and/or discharge process in half an hour) and with coloumbic efficiency of 100%. With respect to the anode, the discharge capacity values at C/6 and 2C are 152 and 32 $mA.h.g^{-1}$, showing their suitability for printed anodes.

Thus, the developed materials for battery separators, cathodes and anodes show suitable characteristics for the development of screen printable lithium-ion batteries.

Materiais poliméricos para baterias impressas

Resumo

Existe um interesse crescente em dispositivos de energia de armazenamento finos e flexíveis, por forma a ir de encontro às necessidades da sociedade moderna em aplicações tais como sensores de radiofrequência, embalagens interativas e outros produtos de consumo. Baterias impressas satisfazem estes requisitos e podem ser também uma excelente alternativa às baterias convencionais em diversas aplicações. O interesse nas baterias impressas está relacionado com o facto de serem finas, flexíveis e de integração simples em dispositivos, associado a baixos custos de produção. A fabricação de baterias impressas não é simples e requer a formulação de tintas a ser otimizada para cada técnica de impressão. A formulação das tintas dos diversos materiais necessários para o desenvolvimento de baterias impressas tem sido pouco explorada no desenvolvimento de sistemas de armazenamento de energia. Vários trabalhos desenvolvidos têm-se concentrado no desenvolvimento de tintas para cátodos e ânodos, continuando o separador a ser um dos maiores desafios, requerendo fortes esforços de investigação.

O objetivo deste trabalho é produzir separadores de baterias baseados em poli(fluoreto de vinilideno-co-hexafluoropropileno), P(VdF-HFP), e poli(fluoreto de vinilideno-co-cloro-trifluoroetileno), P(VdF-CTFE), devido à sua baixa cristalinidade e alta temperatura de fusão, em que estes podem ser formuladas como tintas. Para o separador da bateria, pretende-se estabelecer uma correlação entre condições de processamento, morfologia, propriedades físico-químicas e desempenho das baterias. Em relação à tinta para os cátodos, o objetivo era produzir uma nova tinta com base em $LiFePO_4$, para screen-printing de baterias. As tintas para os ânodos foram baseadas em ânodo.

Assim, a microestrutura de membranas de P(VdF-HFP) e P(VdF-CTFE) obtidas a partir de uma solução foi avaliada em função da concentração de polímero e da temperatura de evaporação do solvente. A formação de uma membrana porosa é atribuída ao processo de separação de fases líquido-líquido. Para membranas de P(VdF-HFP) e P(VdF-CTFE), a fase β e as propriedades térmicas, mecânicas, dielétricas e piezoelétricas foram avaliadas e dependem, fortemente, da concentração inicial de polímero e da temperatura de evaporação do solvente.

Testes de ciclo carga-descarga realizados em “half-cell” de Li/Sn-C e Li/$LiFePO_4$ com membranas P(VdF-HFP), evidenciaram capacidades nominais que variam de 70% a 90% do

valor teórico, com boa capacidade de retenção e uma eficiência de carga/descarga perto dos 100%, mesmo em altas taxas de corrente e 100% de profundidade de descarga (DoD). Em relação a membranas de P(VdF-CTFE), o melhor valor de condutividade iónica à temperatura ambiente é de 1,5 $mS.cm^{-1}$ para a membrana preparada com uma concentração de polímero 20 wt.% e temperatura de evaporação do solvente a 25 ℃, conduzindo a um grau de porosidade de 60% e um valor de absorção do eletrólito de 292%. As membranas de P(VdF-CTFE) preparadas mostram bons ciclos carga/descarga e capacidade de taxa. Para C/10 e 2C são obtidos valores de descarga de 168 e 102 $mA.h.g^{-1}$, respetivamente. A tinta para o cátodo, baseada em C-$LiFePO_4$, apresenta, após 50 ciclos a 2C (é a taxa mais rápida) um valor de capacidade de 81 $mA.h.g^{-1}$ (processo de carga e/ou descarga em meia hora) e com eficiência colombiana de 100%. Referente ao ânodo, os valores da capacidade de descarga a C/6 e 2C são 152 e 32 $mA.h.g^{-1}$, o que indica ser uma boa abordagem para ânodos impressos.

Assim, os materiais desenvolvidos para os separadores de bateria, cátodos e ânodos, mostram características adequadas ao desenvolvimento de baterias de iões de lítio impressas por screen-printing.

Table of contents

List of abbreviations

BMIM+TF	1-butyl-3-methylimidazolium trifluoromethanesulfonate
CNF	Carbon Nanofibres
CNT	Carbon Nanotubes
CTFE	Chlorotrifluoroethylene
DEC	Diethyl carbonate
DEM	1,2-dimethoxyethane
DMC	Dimethyl carbonate
DMF	N, N-dimethylformamide
DoD	Deep of discharge
DOD	Drop on demand
DOL	1,3-dioxolane
EC	Ethylene carbonate
EMC	Ethyl Methyl Carbonate
ETPTA	Ethoxylated trimethylolpropane triacrylate
HFP	Hexafluoropropene
GPE	Gel polymer electrolyte
NMP	N-methyl-2-pyrrolidone
PVdF	Polyvinylidene fluoride
P(VdF-CTFE)	Poly(vinylidene fluoride-co-chloro-trifluoroethylene)
P(VdF-HFP)	Poly(vinylidene fluoride-co-hexafluoropropene)
PVdF-TrFE	Poly(vinylidene fluoride-co-hexafluoropropene)
PAA	Poly(acrylic acid)
PC	Propylene carbonate
PDMS	Poly(dimethylsiloxane)
PE	Poly(ethylene)
PEG	Poly(ethylene glycol)
PEI	Polyethyleneimine
PEO	Poly(ethylene oxide)
PMMA	Poly(methyl methacrylate)
PP	Poly(propylene)
PS	Polystyrene
Zn+Tf	Zinc trifluoromethanesulfonate

List of figures

List of tables

1. Introduction

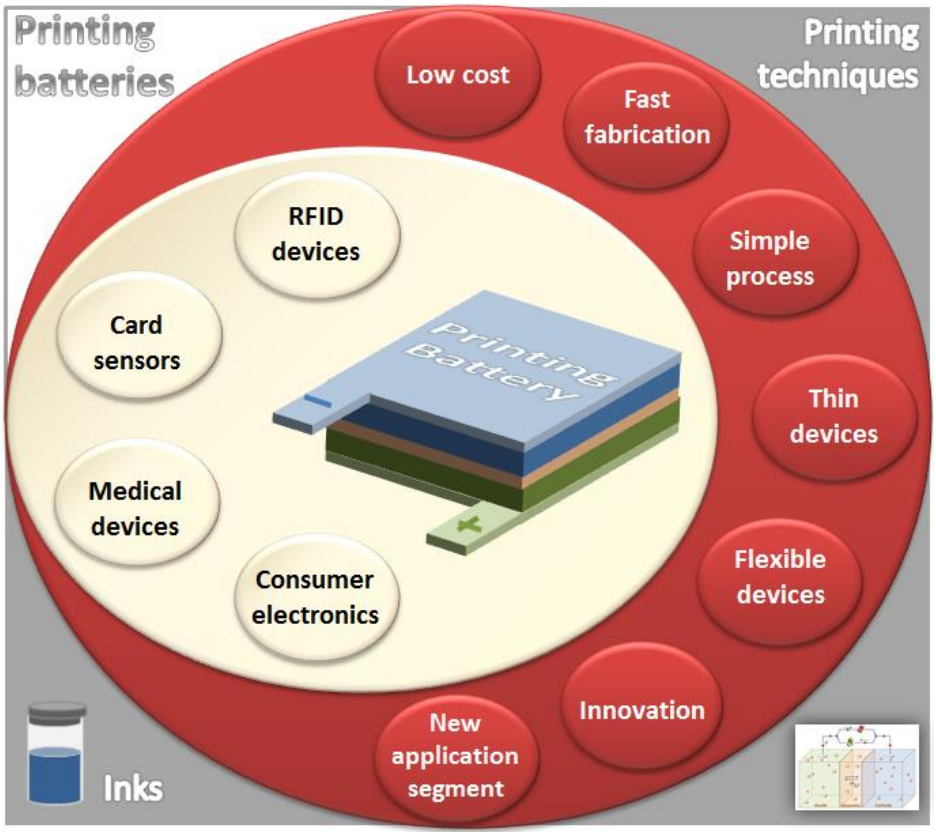

This chapter describes the most important developments in printed batteries: the advantages and disadvantages of printed batteries are highlighted with respect to conventional batteries and the main printing techniques and applications are presented. The chapter is organized in two sections devoted to research and industrial developments, respectively. The main challenges and future research and development needs in this field are also discussed. Finally, the objectives of the present work and the structure of the document are presented.

This chapter is based on the following publication: “Advances and Future Challenges in Printed Batteries”, R. E. Sousa, C. M. Costa and S. Lanceros-Méndez, ChemSusChem, 8 (21), 2015, 3539 – 3555.

1.1. Printed batteries

Printing electronics is a technology that involves the printing of electronic circuits and components such as sensors, transparent electrodes and light emitting devices [1] in different substrates such as paper, plastic and textile, using standard or specific printing processes and equipments [2]. It requires the development of materials' inks, i.e., dielectric, semiconductive or conductive inks based on polymers, metal nanoparticles or composites that are used to print active devices [3]. In this sense, recent advances in conductive inks through their stabilization in dispersions and novel formulations as well as in flexible substrates promise to deliver new applications and open new markets [4]. The most important advantages of printing electronics are low cost, flexibility and simplicity of production. Fabrication of electronics is particularly interesting for large area devices which do not require high density patterning, such as radio frequency identification (RFID) tags, light-emitting diodes (LEDs), health monitoring tags, memories, flexible displays, smart labels, batteries, active clothing and photovoltaics [5 – 6].

Batteries have an increasingly strong technological impact in our society and have become an essential part of our daily lives [5]. By moving away from batteries that contain heavy metal towards eco-friendly ones, it is observed the beginning of a new paradigm of power devices [7]. For a long time, conventional batteries were bulky and heavy. Nowadays, it is possible to obtain printed batteries thinner than a millimeter and lighter than a gram, which can be produced cost-effectively through a printing process and in large scale [8].

All batteries fabricated by printing technologies are denominated printed batteries [9]. In its true sense, flexible batteries [10] and/or micro-batteries [11] can also be included in this scope, whenever obtained by printing.

Printed batteries are based on solid polymer or composite gels electrolytes with ionic conductivities close to high performance liquid electrolytes, in addition to having anode and cathode materials [8]. The combination of materials based on conductive inks with high-throughput printing techniques in battery systems has enabled the fabrication of functional systems that are customizable, with large area, thinner, low-cost and mechanically flexible [6, 12]. The result of this combination is expressed in small, high-power, flexible and light-weight rechargeable lithium-based batteries [12]. Furthermore, when combined with a roll-to-roll production method, it enables batteries to be fabricated at high speed on roll-to-roll machinery that join the various layers of the battery in a continuous run process, reducing the productions steps and costs [12].

An overview on printed battery components, technologies, applications and advantages is shown in Figure 1.1.

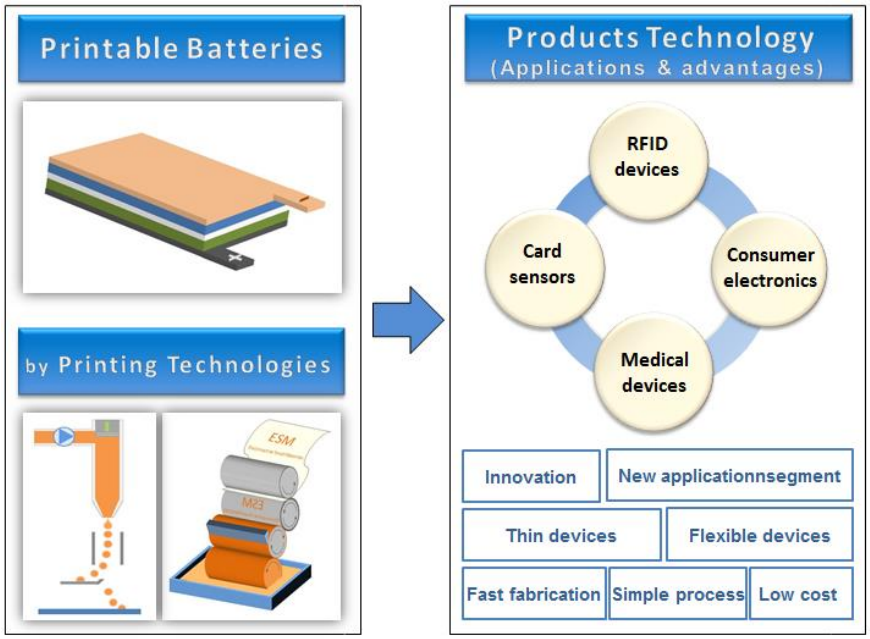

Figure 1.1. Overview on the main issues regarding printable batteries.

There is a strong recent interest in ultrathin, flexible, safe energy storage devices to meet the various design and power needs of modern gadgets. To build such fully flexible and robust electrochemical devices, multiple components with specific electrochemical and interfacial properties need to be integrated into single units [13]. The performance characteristics of energy devices are essentially determined by the structural and electrochemical properties of the electrode materials. Other important component is the electrolyte that limits high-power capability and packaging designs [13]. The characteristics of the printed batteries differ significantly from those of conventional batteries and the key differentiating factor is its integration, beyond of other properties such as capacity, weight, dimensions and safety [8], and tends to be thinner and eco-friendly. Currently, strong research efforts are being devoted to improve performance of batteries and developing new fabrication processes. There are already several companies on the market (as seen in Chapter 2), producing printable batteries suitable for costumer products with specific designs and characteristics.

From smart cards to radio-frequency identification (RFID) security and information devices, to thin film medical products, printed batteries can provide the required power. New products and applications that require on-board battery power are increasingly emerging [14]. Further, transparent devices have recently attracted substantial attention, but as battery electrode materials are not transparent and have to be thick enough to store energy, the development of transparent printed batteries is still a challenge [15].

Taking account the new applications (e-labels, e-packaging, e-posters, medical disposable) that resulted from the combination of the printing electronics and battery technologies, the global market value expected in 2015 is $0.15 billions of dollars [16].

While it is demonstrated that printed batteries market is strongly increasing, the manufacturers of these new types of batteries face important challenges [17].

1.2. Main advantages and disadvantages of printed batteries

1.2.1. Advantages

Printing electronics offers a potential for high-volume manufacture, driving down production cost, and allowing larger area, flexible, compact and portable devices [5]. Further, it facilitates production and integration [5] and it is suitable for large area devices which do not require high density patterning such as batteries [5 – 6].

The reasons for using a printed battery would generally be either to lower the cost or to enable specific design features that only printing can provide [17]. Printed batteries basically combine the advantages associated with thin-film technologies – lightweight, flexible, integration, etc. – with the low manufacturing cost typically associated with printing [17]. It is possible to obtain printed batteries thinner than a millimeter [6, 8, 12], lighter than a gram [8], mechanically flexible and customizable [6, 12], which can be produced cost-effectively in large scale [6, 8, 12].

Many printing technologies are capable of producing electrical components with functional polymers and materials on flexible media, patterning them in a variety of ways [18]. On the other hand, by the use of specifically formulated conductive inks in screen-printing, flexography or inkjet, a variety of products are now able to be produced [18], the emergence of novel ink formulations and flexible substrates promising to deliver new markets and applications [4].

It is only a matter of time before these technologies and applications advance to a level where they can be mass-produced in more complex forms, such as car batteries and portable electronics [18].

1.2.2. Disadvantages

Printable batteries have still the drawbacks of a developing technology, still optimizing materials and processes to maximize performance. However, the most serious problem for these batteries is its cost [17]. The main factor retarding the market entrance for the printed batteries at the present time is their higher cost with respect to conventional batteries. However, there have really been some ways to address this problem. Conventional batteries are very inexpensive and it is currently impossible for printable batteries to compete with them [17, 19]. It will change as production volume increases and technology improves [19]. Efforts in this sense must include new manufacturing approaches [17, 19], including the simplification of the manufacturing methods which is translated into a reduction of costs [19].

The addressable market for these types of new battery technologies is small (the powered smartcard is a good example of printable battery applications) [17]. In this context, manufacturers have also the need to develop products in which the batteries are integrated, such as cosmetic patches [17]. In this context, printed battery industries have often worked with original equipment manufacturers (OEMs) to build an integrated application system [19 – 20]. However, it seems difficult, at the present stage, to be able to compete on price alone with the conventional battery market [19].

Recent commercial attempts to develop "battery inks" show high manufacturing costs and produce small nominal voltages [18]. Improvements in the refinements in areas of printability and material quality and performance are thus essential [18].

The main advantages and disadvantages of printed batteries are resumed on Table 1.1.

Table 1.1. Main advantages and disadvantages of printed batteries.

Advantages	Disadvantages
Flexibility Compact and portable Easy production and integration Fabrication of large area devices Customizable	Currently higher cost Non-optimized manufacturing process New inks materials needed

1.3. Printed batteries vs. conventional batteries

Printed batteries hardly will be able to compete with conventional batteries in applications that do not show constraints with respect to size, shape or accessibility [20]. Printing battery technology is thus meant to fill the gap of conventional batteries in which size and high density power are main requirements of some highly advanced electronic devices [20].

Printed batteries are suited for a variety of specific applications, as it will be described in the next chapter [19], manufactured through printing technologies [21], attractive due to tailorable size, flexibility and the possibility of low-cost manufacturing in large areas, turning them economically attractive [19].

The main features of printed batteries are presented in Figure 1.2.

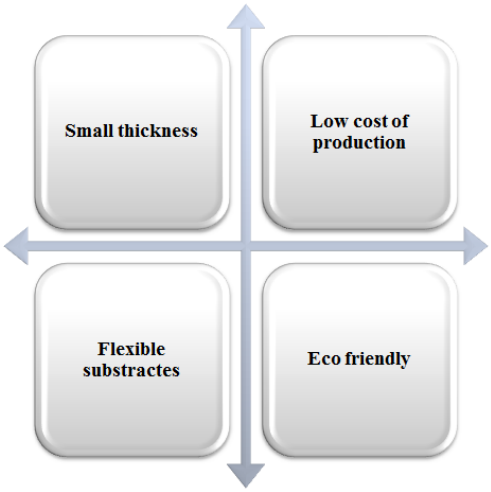

Figure 1.2. Main features of the printed batteries.

The key factors and features of printed batteries are:

Small thickness: Conventional batteries are not adequate for several electronic applications, including antennas [22], biosensors [23] and RFID devices [24], among others. Printed batteries with small thickness and optimizable forms printed directly onto various substrates are the ideal for high performance printed electronics.

Low-cost of production: One of the advantages of printed batteries is the prospect of low-cost devices. After optimization of the experimental procedure, mask costs are eliminated, enabling cost effective manufacturing, even in low volume production. Further, it can also be integrated in the same production line that the application device [25].

Flexible substrates: Typically, polymer substrates show high resistance to chemicals, are light weight and flexible. This flexibility facilitates the manufacturing process [26] and allows novel applications areas.

Eco-friendly: Printing batteries show safety and eco-friendly advantages. Eco-friendly means free of toxins, heavy metals and rare earth elements. Further, they require low energy, either during the manufacturing process or during operation. The reduction of the solid material waste during manufacturing is a key feature of printing batteries [27].

Currently, the only component in a printed battery that is not solid is the electrolyte. Normally, this component can be composite gel where the separator layer being typically soaked with an organic liquid electrolyte (salt dissolved into a polar or ionic liquid to produce an ion-conducting solution and then, an inert polymeric material [28], the process being determined by a time depending swelling process. With the development of solid-state electrolyte inks, these batteries could become entirely printed, which is still more advantageous [21] than the manufacturing current processes.

Other fundamental step in printed battery manufacturing is encapsulation [29], used for protection and, mostly important, to reduce humidity and maintain the electrolyte solution inside the battery [30].

Other storage energy device that can be fabricated based on printing techniques is supercapacitor. The supercapacitor in comparison with batteries have high specific power (W/kg), excellent rapid charging/discharging rate, long cycle life (>100 000 cycles), simple principles, fast dynamics of charge propagation and low maintenance cost [31].

1.4. Relevant applications

Printed batteries are suitable for a wide range of applications. The most highlighted applications of printed batteries are radio frequency identification (RFID) devices, sensors, powered cards, smart toys and medical devices, which also show the highest potential market demand. The common requirements for printed batteries for their use in these applications are being thin, flexible and disposable. Printed batteries can also be applied in products that require on-board battery power and that are continuously emerging [9]. RFID devices (Figure 1.3) use radio waves to communicate to a host device, the main application being automatically identifying and tracking tags attached to objects [32].

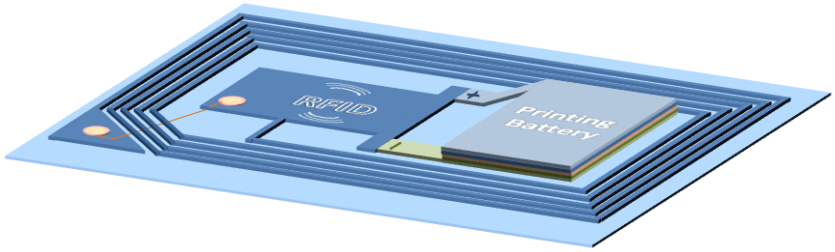

Figure 1.3. Graphical representation of an RFID device.

There are two types of RFID devices: active and passive. The difference among them is that active RFID uses an internal power source (battery) within the tag to continuously power it and its radio frequency (RF) communication circuit, whereas passive RFID relies on RF energy transfer from the reader to the tag to power it [33]. The limitation of active RFID tag performance is directly related with its battery [34]. The combination of printed batteries with RFID devices opens possibilities to extend the RFID performance in distance and will allow a rapid expansion to its market, evaluated in $9.2 billion dollars [35].

Powered cards are also applications where printed batteries can be increasingly used. Figure 1.4 shows an example of powered cards with an incorporated battery.

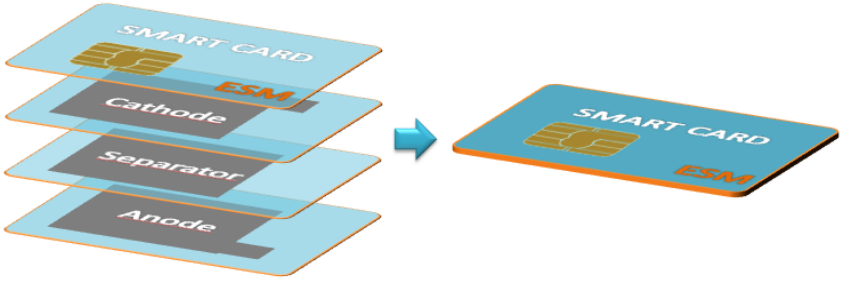

Figure 1.4. Representation of a powered card.

These cards contain memory chips or microprocessors which require embedded battery, enabling applications such as one time password (OTP) cards, secure access, financial cards and gift cards, among others [36].

The miniaturization of electronics allowed strong advances in the area of medicine, with the development of novel medical devices in which printed batteries can be considered advantageous taking into account their size and flexibility. One example of medical devices using printed batteries is transdermal drug delivery (TDD) systems where batteries power the integrated circuit that ensures proper dosage control until [37]. Figure 1.5 shows an example of these medical devices.

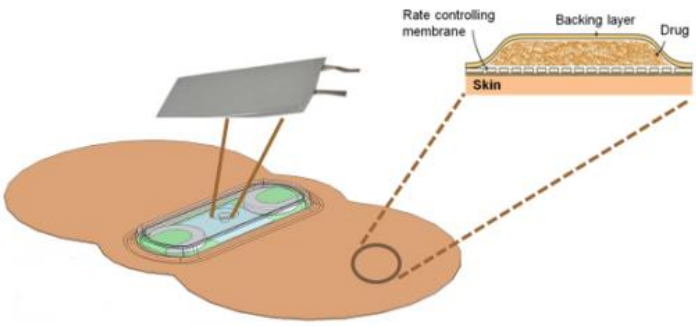

Figure 1.5. Example of the transdermal drug delivery system.

Printed batteries can also be used in other health monitoring systems, in wound care and cosmetic uses, wireless patches for patient monitoring such as electrocardiogram, vital signs monitoring and patient wristbands [38].

Other potential applications for printed batteries include sensors and smart toys. Depending on the application of the sensor, a printed battery coupled to the sensor provides long-term remote monitoring and data acquisition [39].

Finally, other important applications of printed batteries are small power electronic devices that need energy harvesting since that source of energy is rarely available. This energy is harvested from ambient light, thermal gradients, vibration/motion, electromagnetic radiation, etc. [16].

In relation to parameters performance of printed batteries which include power and energy values, lifetime and discharge rate, they depend on the application. For example, RFID tag requires only 5.14 μW during the active state with a current consumption of 700 nA at 1.5 V, which represents five year operation with a 50 mA.h capacity battery [40].

The active and sleep power of smart card component are 15.1 mW and 4.9 μW, respectively, and using a battery with 25 mA, the autonomy of the smart cart with adiabatic circuit is almost 18 months [41].

For TDD systems, the typical pumping capacity value is 57 $\mu A.cm^{-2}$, and using a printed battery with a capacity of 247 mW.h, the pump continuously works for 12 days [42].

1.5. Printing techniques for printed batteries

Printing technology is a reproducible process in which an ink is applied to a substrate with the objective to transfer a specific pattern [4a, 43]. The object printed can be an image, text, graphics or a device [44].

In the past few decades, printing technologies have evolved from being just a tool to print information into a generator of functionalities, leading to their widespread utilization in printing electronics [43].

Generally, printing technologies are classified in two classes: conventional and digital printing. The difference among these two classes is that conventional printing requires the use of mask [4, 27].

Figure 1.6 shows the most important printing techniques that can be used for printing batteries, divided into the two main printing classes.

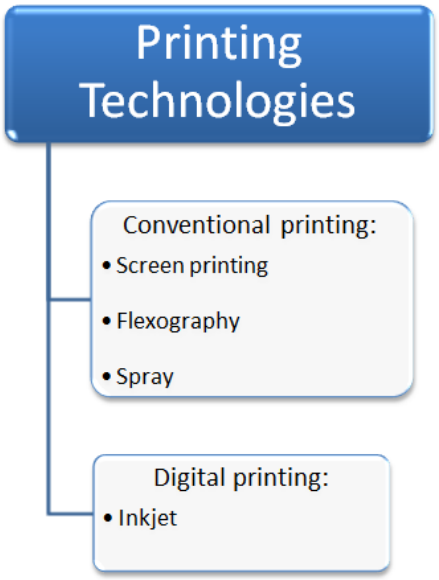

Figure 1.6. Techniques for battery printing divided into the two main printing classes. Figure adapted from [4].

The main techniques used in conventional printing are spray, flexography and screen. Typically, these techniques require the use of a printing plate (the mask) to be reproduced and can be used for rapid and large-scale production [43]. In contrast with conventional printing, digital printing does not require the use of printing plate and the printed object relies on the application of individual droplets that are ejected from a nozzle [45].

Independently of the printing technique, the common characteristic in all techniques is the use of inks. The ink is then the main component of the printing techniques. The fine control of important characteristics of inks, such as viscosity and surface tension, is essential for suitable printing. Ink characteristics which also affect print quality are flow, wetting and solubility [46]. Typically, the inks for printed batteries are composed by solvent, binder and a solid component. This solid component is constituted by one or more components depending on the application [47].

The curing process is essential, independently of the type of ink. For solution-based inks, the quality of the printed object depends on the volatility of the solvent used and the viscosity of

the ink [48]. A suspension-based ink is also being increasingly used for printed batteries and involves the use of colloidal suspensions and nanoparticles. The most used ones are conductive inks composed by conductive fillers [47].

Table 1.2 shows the most relevant parameter values related to the different printing techniques and including both ink and printing pattern characteristics. In particular, the ink viscosity is critical in defining printing technique and pattern quality [49] and presents a range of values for each printing technique.

Table 1.2. Characteristic values of the viscosity and surface tension of the ink, layer thickness, resolution and throughput for the different printing methods [4, 44, 51].

Printing technique	**Viscosity / Pa.s**	**Surface Tension / $mN.m^{-1}$**	**Layer thickness / µm**	**Resolution / µm**	**Throughput / m^2s^{-1}**
Flexographic	0.05-0.5	13.9-23	0.04-2.5	30-80	3-30
Spray	< 0.15	----	25-20000	Areal coating	3-45
Screen	0.5-50	38-47	0.015-100	20-100	2-3
Inkjet /Piezo	0.005-0.02	15-25	< 0.05-20	15-100	0.01-0.5

The most common types of inkjet printers are based on piezoelectric heads, from which a droplet is ejected directly on the substrate by the action of the piezoelectric actuators [50].

In relation to the other parameters shown in Table 1.2, it is particularly relevant to stress the higher resolution of inkjet printing and the larger throughput representing the velocity of printing of spray technique.

In this way, Table 1.3 shows the most important advantages and disadvantages of the different printing techniques.

Considering both the advantages and disadvantages of each printing technique, the choice of the printing technique for batteries must take into account the size of the battery and the ink viscosity for each component of the battery. All the aforementioned printing techniques show versatility and are able to integrate the existing manufacturing lines of industries [4a].

Screen printing and inkjet printing are the most used printing techniques for printed batteries, related to the range of materials that can be formulated as inks, and the possibility to apply them in various production scales, ranging from prototypes to large-scale production.

Table 1.3. Main advantages and disadvantages of the different printing techniques.

Printing technique	Main features	
	Advantages	**Disadvantages**
Flexographic	- Low plate pattern - High throughput - Thin layers	- Plate degradation due to solvents
Spray	- High throughput - High thickness variation	- Low resolution - Excessive overspray - Poor painting efficiency
Screen	- Robust - Simple - Thick layers	- Resolution - High ink viscosity - High throughput
Inkjet /Piezo	- Non-contact - Small ink quantities - Low viscosity inks	- High throughput - Nozzle reliability

1.5.1. Flexography

Flexographic printing is a relief printing technique where the image is printed from protruding elements on a plate cylinder. The image is transferred to any type of substrate including plastic, metallic films and paper, among others [52]. A uniformly cylinder, called anilox cylinder, is used to adjust the amount of ink transferred onto the substrate as shown in Figure 1.7.

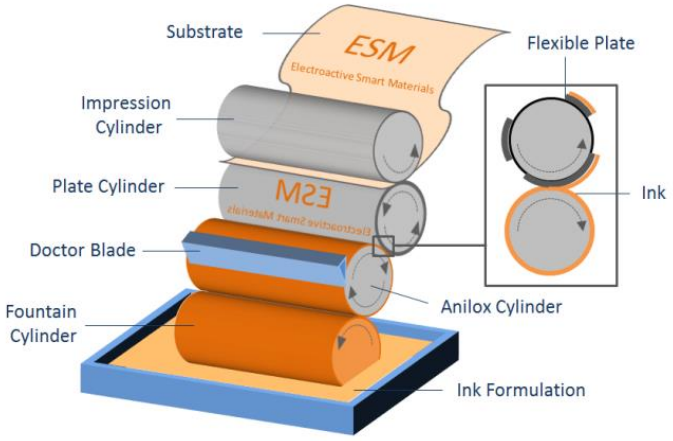

Figure 1.7. Schematic illustration of flexographic printing.

The uniform thickness of the ink is controlled by the number of engraved cells (mostly inverted pyramids) (Figure 1.7), ensuring an evenly and rapid transfer of a controlled amount of ink to the printing plate [52]. The anilox roll is the most sensitive part of the flexographic process. It is typically fabricated in chrome-coated ceramics or stainless steel, and the excess of ink is removed from it by a doctor blade process. The ink is transferred onto the raised image elements of the flexible printing plate and further onto the substrate. The reliefs on the printing cylinder pick out ink from the anilox roll, and printing occurs by pressing the substrate against the impression cylinder [27].

The main advantage of using flexography for printing electronics and batteries is the speed and potential to produce integrated smart packages [18].

1.5.2. Spray

Spray printing is characterized by a collection of moving droplets in the direction of the substrate, resulting from an atomization process as shown in Figure 1.8.

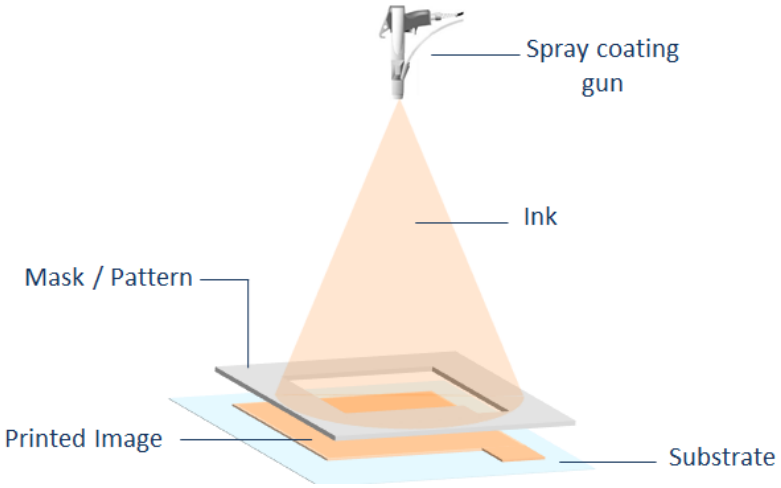

Figure 1.8. Schematic illustration of spray printing.

There are different conventional spray printing techniques based on air and electric field (electrostatic) [53]. In the electrostatic spray technique, the droplets are injected in the direction of the substrate by a high voltage applied to the nozzle. Air spray technique, on the other hand, is based on air-pressure, being more used than the previous one. Finally, there are also hybrid spray techniques based on both electrostatic and air pressure spray techniques.

Spray printing allows to print a relatively wide variety of ink viscosities and thicknesses, which mainly determine the droplet size [54]. Typically, the printer layers are dried after every printing unit. For the mass production of printed electronics, several parameters such as substrate

characteristics, humidity and temperature, among others, must be taken into account. The use of spray printing for battery printing has a strong potential due to its easy operation and flexibility in industrial scale systems [4, 27].

1.5.3. Screen printing

In printed electronics, screen printing is the most popular technology as it is faster and more versatile than other printing technologies. It further adds simplicity, speed and adaptability to the fabrication process [55].

In screen printing, ink is pressed with a squeegee through a screen onto the substrate as shown in Figure 1.9.

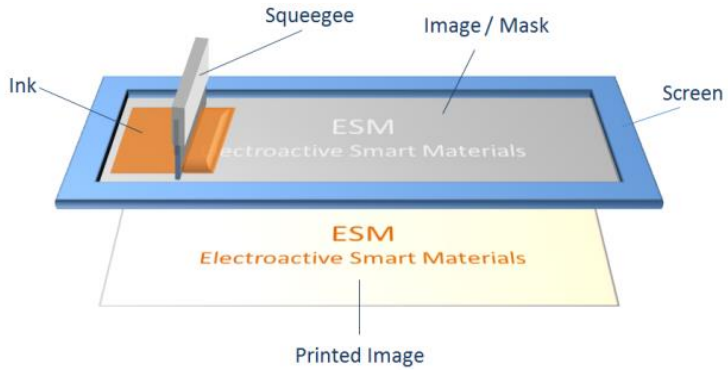

Figure 1.9. Schematic illustration of flatbed type screen printing technique.

The screen is made of a porous mesh. Due to the simplicity of the process, a wide variety of substrates and inks can be used, allowing a thinner layer which is typical for screen printing.

There are two main types of screen printing techniques: flatbed and rotary.

The flatbed process type is illustrated in Figure 1.9 and, as previously indicated, the ink is pressed with a squeegee through a flat screen onto the substrate. In rotary screen printing, ink is pushed through a perforated metal or polyester screen cylinder onto the substrate with a squeegee in movement [56]. Thus, rotary screen printing has the highest throughput, edge definition/resolution and achievable wet thickness.

Independently of the type, screen printing is an inexpensive, large-area printing technique with good control over the deposition area. The quality of screen-printed films highly depends on the number of fibers in the screen mesh, the tension of the mask, the distance from the mask to the substrate, the characteristics (hardness, edge) and process parameters (speed, pressure, angle) of the squeegee, the temperature, the humidity and the air flow around the printing area [27]. Also, the ink viscosity is linked to all mentioned parameters, and has to be critically adjusted to match the mesh used in the screen mask.

Finally, stencil printing is very similar to screen printing and both processes generally use the same equipment. The difference between these printing techniques is that in stencil printing, the image is a set of open patterns in a solid foil [44].

1.5.4. Inkjet printing

Inkjet printing is currently the most studied technique for producing low-cost printed electronics [45]. Inkjet printing relies on the formation of individual droplets that are ejected from a nozzle directly onto the substrate. As shown in Figure 1.10 the inkjet technique can be based on continuous flow or drop-on-demand (DOD) where a droplet is ejected on the substrate only when needed [57].

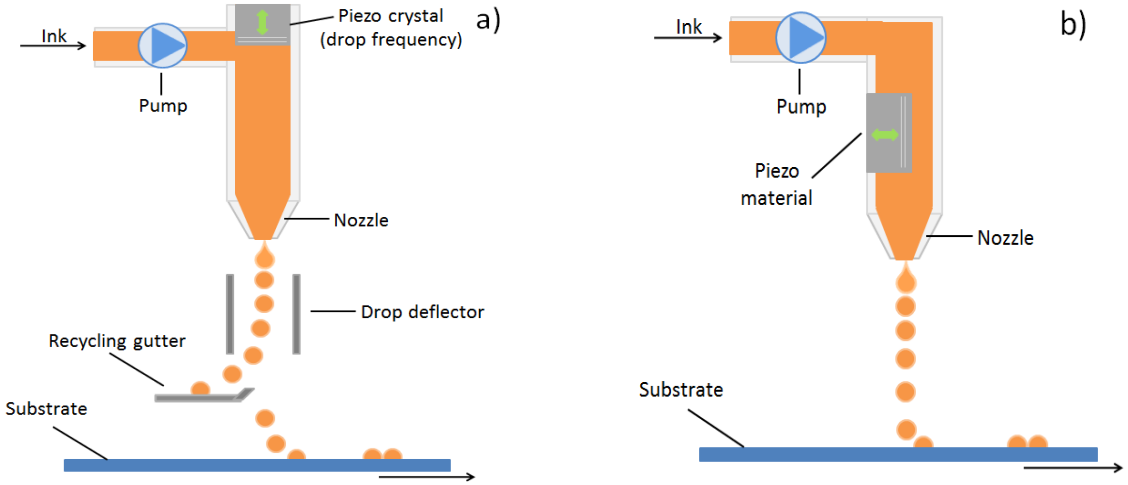

Figure 1.10. Schematic illustration of inkjet printing: a) continuous flow and b) drop-on-demand (piezoelectric).

With respect to the last one, there are two types of drop-on-demand inkjet printers: thermal and piezoelectric. Thermal inkjet printers deposit ink from the nozzle by heating the ink until a bubble is formed, thus forcing a small drop of ink out from the nozzle. Piezoelectric inkjet printers use piezoelectric actuation to force the ink out of the nozzle [55a, 57]. This one has the largest potential in printed electronics since the ink viscosity remains constant during the jetting, thus leading to a more reliable and accurate droplet formation and jetting, leading to increasing print quality and speed, as well as a wider range of suitable materials [27, 51a].

Inkjet printing is a relatively new technology on an industrial scale and presents some limitations with respect to processing speeds and ink formulation (viscosity) (Table 1.2) [45, 55a]. The precision of this technique is the highest among printing techniques, being able to obtain structures in the range of nanometers by increasing the electric field value along with the distance between nozzle and substrate [52].

In summary, the printing techniques affect the properties of printed batteries through the size and thickness of the different printed layer. The large size of printed battery increases the capacity value of the batteries and the most important techniques for obtaining large batteries are screen and spray printing. For applications that require low capacity (μA.h), i.e., small size and low thickness, the best printing technique is inkjet printing, taking account its advantages.

Generally, for different applications, the ideal of printed batteries are larger areas and thicker layers of the different components.

Tailoring of printed batteries is necessary to optimize its performance taking in account the application requirements and the best printing technique for these requirements.

1.6. Printing batteries

Batteries, invented by Alessandro Volta in 1800, are nowadays the essential electrochemical power source for the consumer electronics market and are one of the keys for the revolution of the road transportation concept (electric and hybrid vehicles) [58].

Typically, batteries are classified into primary (single-use) and secondary and the difference between them is that secondary batteries can be recharged and used several times [59]. Independently of the chemical material that composes the electrodes and the size of batteries, the main components in a battery are positive electrode (cathode), negative electrode (anode) and separator as it is shown in Figure 1.11.

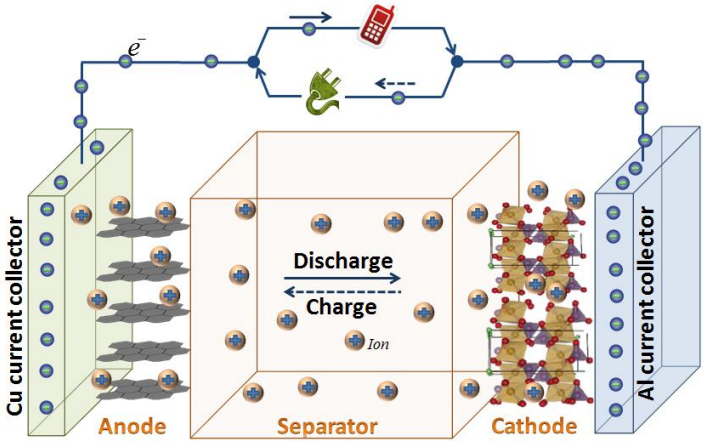

Figure 1.11. Schematic representation of the main components and the charge and discharge process of a battery.

During the charging process, the ions move from the cathode to the anode and during the discharge process, the movement is made on the opposite direction [60]. In printed batteries, the most used battery types are lithium and zinc, and just the electrodes are printed. Normally, the

separator component is not printed and is composed by porous membrane with electrolyte solution (salts are dissolved into a polar solvent). The electrolyte solution into porous membrane is produced through the uptake (soaked) or injection process [28a].

Lithium-ion (Li-ion) batteries have advantages with respect to other types of batteries (zinc, nickel-metal hydride (NiMH)), such as being compact, lightweight, high average discharge rate (~3.7 V) and showing the highest energy density (100-265 $Wh.kg^{-1}$) [61]. Materials based on carbon (i.e., graphite, carbon nanotubes (CNTs) and carbon nanofibers (CNF)) are used as anode active materials [62]. For example, for the anodes based on graphite, the electrochemical reaction of a Li-ion battery system is:

$$C_n + xLi^+ + xe^- \underset{d}{\overset{c}{\rightleftharpoons}} C_nLi_x$$

where c represents the charge process and d represents the discharge process. For cathode materials, many active materials have been used, i.e., lithium cobalt oxide ($LiCoO_2$), lithium manganese dioxide ($LiMnO_2$) and lithium iron phosphate ($LiFePO_4$), that are transition metal oxides. For example, for cathodes based on $LiFePO_4$, the electrochemical reaction of a Li-ion battery system is:

$$\boldsymbol{LiFePO_4 \underset{d}{\overset{c}{\rightleftharpoons}} Li_{1-x}FePO_4 + xLi^+ + xe^-}$$

where c represents the charge process and d represents the discharge process.

In relation to zinc-manganese dioxide batteries (Zn/MnO_2), they show certain advantages such as high energy content, lower internal resistance, large shelf life and low cost, and thus, could replace lithium batteries in many applications [63].

Printed batteries based on manganese dioxide or zinc have lower cost materials in comparison with materials for Li-ion batteries. One fundamental process in printed batteries is its sealing that has as main objective to keep constant the atmosphere inside the battery and affect its life time. The sealing process consists in sealing layer based on polymer glue that can be activated by heat or pressure application [64]. Further, these materials can be formulated into inks to be printed by screen printing process onto a variety of substrates in line with other manufacturing steps.

There are several other battery types that result from the combination of the different elements that are being developed to power small electronics devices, as we will show in the next subsection.

1.6.1. Printed battery developments

This subsection is structured in three parts, devoted to the developments in Li-ion batteries, zinc/manganese dioxide batteries and other battery types, respectively. For each part, the materials and electrolyte solutions will be presented, as well as the main characteristics of the battery, such as capacity and related properties and the used printing technique. This information is chronologically ordered, to evaluate the evolution of the area, and further discussed.

1.6.1.1. Lithium-ion batteries

The main characteristics of the developed printed batteries based on Li-ion are summarized in Table 1.4.

Table 1.4. Development for printed batteries based on Li-ion batteries and their main properties and components.

Battery Type	Anode	Cathode	Separator / Electrolyte	Printing technique	Capacity / voltage	Ref
Li-ion	$Li_4Ti_5O_{12}$	$LiMn_2O_4$	40% PEG, 25% PEO, 20% lithium salt and 15% γ-LiAlO	Screen printing	150 mAh/g	[65]
Li-ion	Li-metal or Fe/Si multilayer	Zr-$LiCoO_2$	1M $LiPF_6$ in EC:DEC (1:1)	Screen printing	250 μAh/cm^2 / 2V	[71]
Li-ion /HPE/MoOxSy-on-Si	Li	MoS_2	$LiAsF_6$ EC:DEC	Multiple processes	-------	[69]
Li-ion	SnO_2	Li	1M $LiPF_6$ in EC:DMC (1:1)	Inkjet printing	812.7 mAh/g at 33 μA/cm^2	[70]
Li-ion	Li	$LiCoO_2$	polypropylene separator soaked with 1M $LiPF_6$ in EC:DEC (1:1)	Screen printing	179 μAh/cm^2	[72]
Li-ion	Li	$LiCoO_2$	LiPON	Screen printing	125 μAh/cm^2	[66]
Li-ion	Graphite: MCMB6-28	$LiCoO_2$	-----	----	100 mAh	[73]
Li-ion	Li	$LiCoO_2$	1M $LiPF_6$ in EC:DMC (1:1)	Inkjet printing	120 mAh/g	[74]
Li-ion	$Li_4Ti_5O_{12}$	$LiCoO_2$	Xerox paper with $LiPF_6$ in EC/DEC	doctor-blade-coated	120 mAh/g	[75]
Li-ion	Li	$LiCoO_2$	LLZONb or Li_3BO_3	screen-printing	85 mAh/g / 3V to 4.1V	[67]
Li-ion	Li	graphene-ink with 0.1 M TiO_2 nanoparticles	1 M $LiClO_4$	---------	241 mAh/g	[76]
Li-ion	Li	$Li_4Ti_5O_{12}$	1M $LiPF_6$ in EC:EMC (1:1)	Micro printing	~146 mAh/g	[77]

Li-ion	Li	$LiCoO_2$	UV (ultraviolet)-cured ethoxylated trimethylolpropane triacrylate (ETPTA) polymer matrix, high-boiling point liquid electrolyte (1M $LiPF_6$ in ethylene carbonate (EC)/propylene carbonate (PC): 1/1 (v/v)), and alumina (Al_2O_3) nanoparticles	mechanically imprinted with a maze-patterned PDMS stamp	130 mAh/g	[78]
Li-ion	$Li_4Ti_5O_{12}$	$LiCoO_2$	PMMA with SiO_2 + 1 M $LiPF_6$ solution in 1:1 (v/v) mixture of EC:DMC	spray-painting technique	3.91 V and 100 mAh/g for LCO and 1.5 V and 125 mAh/g for LTO	[79]
Li-ion	$Li_4Ti_5O_{12}$	$LiFePO_4$	1M $LiClO_4$ in EC:DMC	3D-printing	1.6 mAh/cm^2	[80]
Li-ion	Graphite	$LiCoO_2$	P(VDF-HFP)+silica+ 1 M $LiPF_6$ dissolved in EC/PC EMC (1.5:1.0:1.5 w/w/w),	Screen-printing	2.5 mAh/cm^2	[68]
Li-ion	Graphite	-----	1M $LiClO_4$ in EC:DEC (1:1) soaked on standard whatman separator	Spray deposition	350 mAh/g	[81]
Li-ion	Lithium metallic	$LiMn_2O_4$	1M $LiPF_6$ in EC:DMC (1:1) soaked on standard whatman separator	Laser-printing	-----	[82]
Li-ion	Lithium metallic	$Li_4Ti_5O_{12}$	1M $LiPF_6$ in EC:EMC (1:1)	3D-printing	-----	[83]
Li-ion	$Li_4Ti_5O_{12}$	$LiFePO_4$	silica based ionogels confining ionic liquid	Inkjet printing	300 µAh/cm^2	[84]
Li-ion	Graphene/ Sulphur	$LiMn_2O_4$	microporous tri-layer membrane (PP/PE/PP) Celgard 2320 soaked in 1.0 M $LiN(CF_3SO_2)_2$ and 0.2M $LiNO_3$ in DME and DOL	Spray printing	1500 mAh/g	[85]

Screen printing technique is used for the preparation of electrodes based on $Li_4Ti_5O_{12}$ and $LiMn_2O_4$ materials in Li-ion batteries with high capacity (~150 mA.h.g^{-1}) [65] and thick-film electrodes (~6 µm), with a mixture of a carbon-coated $LiCoO_2$ powder and an epoxy resin, which shows high adhesion strength between the printed cathode and the current collector [66].

Li_3BO_3 and LLZONb solid electrolytes are also fabricated by screen printing [67]. Lithium metal as the active anode material was deposited on the opposite side of the LLZONb pellet using a vacuum deposition process. The printed battery fabricated by screen printing shows high coulombic efficiency and the electrochemical performance of the battery is comparable to that for a lithium-ion battery fabricated by physical vapor deposition.

Sequential screen printing (wet) processes have been applied in the fabrication of a pouch-type flexible thin-film Li-ion battery, printing consecutive layers for the current collector, positive and negative electrodes and gel polymer electrolyte [68]. It was shown that optimum conditions of each process are determined by adjusting the paste or slurry compositions to achieve lower surface resistance of each layer (current collector and electrodes) and higher ionic conductivity for the gel polymer electrolyte [68].

Three-dimensionally (3D) micro-batteries are being fabricated in order to increase battery capacity [69]. Three-dimensional perforated Si substrates with high aspect ratio vertical channels have been prepared using inductively coupled plasma (ICP) etching in that a hybrid-polymer electrolyte is coated [69]. Inkjet printing was used for the preparation of SnO_2 electrodes, with the thickness of the monolayer being ~ 770 – 780 nm [70]. This work demonstrated that inkjet printing is suitable for the preparation of thin film electrodes for lithium-ion batteries [70]. 3D patterned $Li_4Ti_5O_{12}$ electrode materials have been fabricated by a micro printing technology [77], and the cell shows much better charge and discharge capacities than a conventional cell with a flat $Li_4Ti_5O_{12}$ electrode at high rates [77]. Highly ion-conductive, bendable polymer electrolytes were fabricated, being also conformable to 3D micropatterned architectures of electrodes over large areas [78]. This work is particularly relevant as it shows that polymer electrolytes are directly writable or printable onto complex and flexible substrates taking into account their rheological characteristics as shown in Figure 1.12.

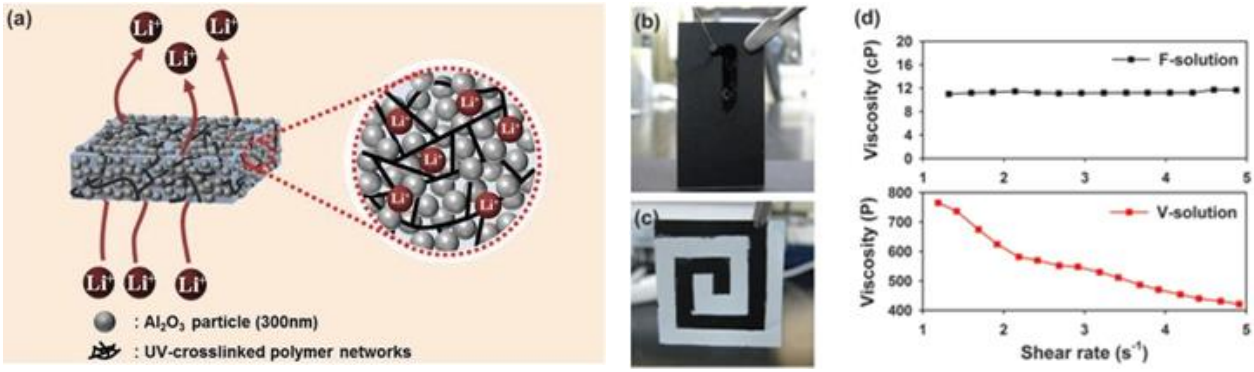

Figure 1.12. a) Conceptual illustration of a printable, flexible, shape-conformable c-GPE. b) Dripping characteristic of a liquid electrolyte that does not incorporate Al_2O_3 nanoparticles (designated as F-solution). c) Non-dripping behaviour of UV-curable electrolyte mixture before UV-crosslinking reaction (designated as V-solution). d) Comparison of viscosity (as a function of shear rate) between the F- and V-solution [78].

It is shown that the challenge in the development of 3D-structured and/or printed flexible batteries is the maintenance of proper contact in order to facilitate electrochemical reaction at the interface between polymer electrolytes and electrodes [78]. Through painting technique, Li-ion

batteries were fabricated by sequentially spraying the component paints on desired surface using an airbrush operating at 40 psi of compressed air [79]. The paints can be sprayed through a set of masks fabricated according to the desired device geometry. The temperature of the substrate was controlled from 90 – 120 ℃ using a heat gun or hot plate.

The separator shows low ionic resistance, with an ionic conductivity of 1.24×10^{-3} $S.cm^{-1}$. In Li-ion polymer batteries, well-controlled micro-porosity of polymer separators is essential for optimal electrolyte uptake and for the formation of a microporous gel electrolyte (MGE) with high ionic conductivity and retention upon cycling [79]. Before assembling the Li-ion cell, spray printed LCO/polymer and LTO/polymer stacks were tested in half cell configuration, showing the expected plateau potentials (3.91 V for LCO and 1.5 V for LTO), good initial capacities (100 $mA.h.g^{-1}$ for LCO, 125 $mA.h.g^{-1}$ for LTO) and suitable capacity retention upon cycling [79].

It was also demonstrated [81] that spray printing of aqueous slurries can be successfully implemented on a pilot paper machine for rapid and reliable large-scale production of self-standing Li-ion battery electrodes, using natural micro-fibrillated cellulose as a binder. The feasibility of the proposed process in producing well-functioning electrodes has been demonstrated by evaluating the long-term electrochemical behaviour at room temperature.

In the work of L. Hu et al. [75], all components of a Li-ion battery were integrated into a single sheet of paper by a simple lamination process. Free-standing, lightweight CNT thin films (~0.2 $mg.cm^{-2}$) were used as current collectors for both anode and cathode and were integrated with the battery electrode materials through a simple coating and peeling process. LTO/CNT and LCO/CNT coin cells have been fabricated for half-cell tests in which lithium metal foil and xerox paper were used as the counter electrode and separator, respectively.

3D printing has been used for the fabrication of Li-ion batteries based on $Li_4Ti_5O_{12}$ (LTO, mean diameter of 50 nm) and $LiFePO_4$ (LFP, mean diameter of 180 nm), as shown in Figure 1.13.

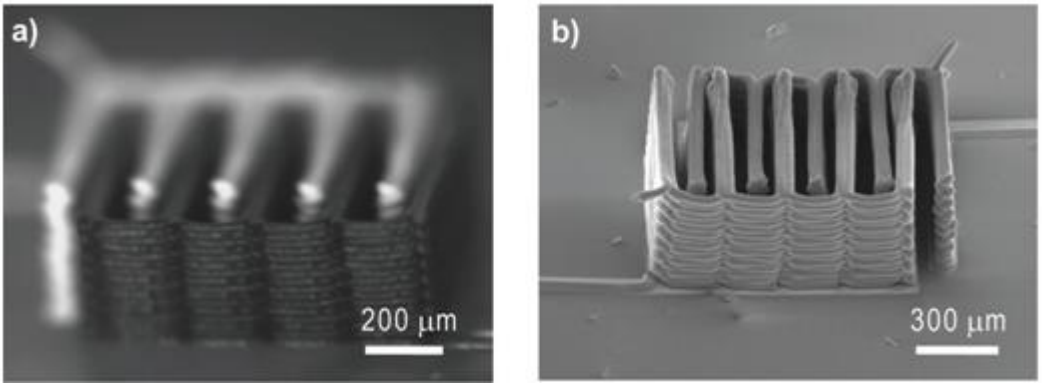

Figure 1.13. a) Optical and b) SEM images of printed and annealed 16-layer interdigitated LTO-LFP electrode architectures [80].

This 3D-battery shows high areal energy density of 9.7 $J.cm^{-2}$ at a power density of 2.7 $mW.cm^{-2}$ [80]. $LiMn_2O_4$ composite material was laser-printed onto flexible Al substrates for the development of porous thick-film cathodes with thickness of 60 μm. The laser-printed cathode films were calendered and/or laser structured in order to manufacture 3D microstructures with improved electrical contact to the Al substrate and to improve the electrolyte wetting behaviour [82]. The 3D-patterned electrode is characterized by lined patterns with a high aspect ratio [83]. The cell using 3D-patterned electrode showed much better rate capability than that using a conventional flat electrode.

Delannoy et al. [84] showed that technology of all-solid state ink-jet printed micro-batteries is safe and with competitive performances in comparison to the standard all solid state micro-batteries. High ionic conductivity and compatibility with porous composite electrodes allow good electrochemical cycling performance: thus, a full Li-ion cell with $LiFePO_4$ and $Li_4Ti_5O_{12}$ porous composite electrodes shows a surface capacity of 300 μAh cm^{-2} for more than 100 cycles.

High capacity (~1500 $mA.hg^{-1}$) was found in Li-ion batteries with anode based on graphene and sulphur materials through the spray printing method [85].

1.6.1.2. Zn/MnO_2 batteries

Table 1.5 summarizes the main characteristics of printed batteries based on Zn/MnO_2.

Table 1.5. Development of printed batteries based on Zn/MnO_2 and their main properties and components.

Battery Type	Anode	Cathode	Separator / Electrolyte	Printing technique	Capacity/voltage	Ref
Zn/MnO_2	Zn	MnO_2	separator soaked in a solution of NH_4Cl and $ZnCl_2$ electrolytes	Printing process	15 mAh-25mAh/ 1.45 V	[86]
Zn/MnO_2	Zn	MnO_2	(4.6 M NH_4Cl (aq.)/13.7 wt% polyethyleneimine (PEI)/3.7 wt% Carbopol 940	Screen printing	25mAh	[87]
Zn/MnO_2	Zn	MnO_2	fibrous substrate	Stencil-printing technique	---- / 14V	[6]
Zn/MnO_2	Zn	MnO_2	Poly acrylic acid (PAA) based KOH gel electrolyte	Stencil printed	4 mAh/cm^2	[88]
Zn/MnO_2	Zn	MnO_2	polyvinyl alcohol/cellulose wet-laid nonwoven material soaked in a solution of KOH (5.6m) and ZnO (0.37m)	Embedding the membrane with electrochemically active ink	1.5V and 3 mAh/cm^2	[89]
Zn/MnO_2	Zn wire	MnO_2/carbon fiber	------	-----	158 mAh/g	[90]
Zn/MnO_2	Zn	MnO_2	paper separator soaked in saturated zinc acetate electrolyte	-----	-----	[91]
Zn/MnO_2	Zn	MnO_2	1:1 mixture of P(VdF-HFP) and 0.5 M solution of zinc trifluoromethane-sulfonate (Zn + Tf) salt dissolved in BMIM + TF- ionic liquid	Flexography	0.13 mAh/cm^2 / 1.8V	[92]

Printed thin-film batteries are particularly compelling as power sources for printed electronics as they can be manufactured on the same printing line. A challenge in this integration has been the typically low cell potential of a battery (maximum of 4.2 V), which alone does not meet the typically higher potential requirements of printed thin-film transistors (TFTs) (10 to 30 V) [6]. Addressing this issue, in [6], Zn/MnO_2 batteries were fabricated with MnO_2 ink based on a mixture (by weight) of 45.3% MnO_2 particles (Tronox), 10.6% graphite (KS6, Timcal), 12.1% KOH (9M), 1.8% styrene-butadiene binder (LICO Technology Corp.), and 30.2% deionized water as a solvent. The zinc ink was fabricated by a mixture (by weight) of 69.3% Zn, 7.3% ZnO nanopowder (Inframat), 10.9% Bi_2O_3 (Alfa Aesar), 1.6% styrene-butadiene binder and 10.9% ethylene glycol as solvent.

Batteries using a random network of CNTs serve both as charge collector and as interface with the active components [86]. Devices fabricated by layer-by-layer in an all solution-phase approach are presented suitable for large-scale production such as roll-to-roll printing. The proof-of-concept device is based in anode (Zn foil), which also acts as a charge collector, separator soaked in a solution of NH_4Cl and $ZnCl_2$ electrolytes and cathode fabricated from a paste of MnO_2, CNTs and the same electrolyte mixture. A random CNTs network on top serves as the charge collector, although any conducting nanowire could serve for the same purpose. In addition, the devices can be fabricated using a roll-to-roll or inkjet printing process [86].

On a different approach, a 1.5 V-class film-type Leclanché battery was designed by adopting a multi-layered packaging film and NH_4Cl based adhesive aqueous electrolytes fabricated by screen printing technique in order to improve the barrier and selective permeation property, ionic conductivity and shelf life, respectively [87].

Further, in [88], a flexible printed battery was presented with a mesh support as illustrated in Figure 1.14.

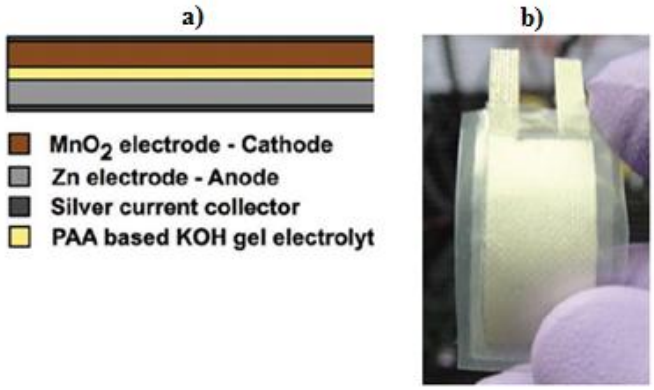

Figure 1.14. a) Schematic diagram of the cross-section of an assembled Zn/MnO_2 alkaline battery with sandwich-type architecture and b) optical image of a flexible Zn/MnO_2 battery laminated inside a polyethylene pouch [88].

The mesh support enables these flexible batteries to exhibit a high capacity, due to increased thickness of the electrode. This battery design can be customized to power devices with various power and energy requirements, and the process can be readily integrated with the current large scale manufacturing techniques. The mesh architecture is not limited to alkaline battery systems and could be used with other battery chemistries. Readily customized flexible batteries, such as those described in [88], will help to realize the potential of flexible mobile electronic devices.

A technique to reinforce arbitrary battery electrodes was developed by supporting them with mechanically tough, low-cost fibrous membranes, which also serve as the separator [89]. This technique was used to fabricate a high energy density, nontoxic Zn/MnO_2 battery with printed current collectors. The Zn and MnO_2 electrodes were prepared by a solution-based embedding process, as represented in Figure 1.15.

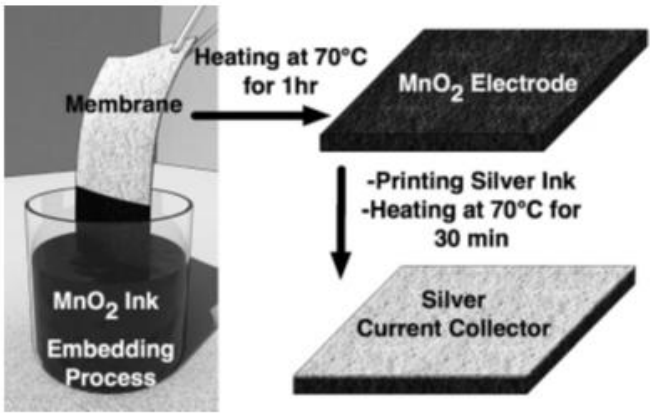

Figure 1.15. Schematic of the process used to reinforce flexible battery electrodes [89].

The cell had a nominal potential of 1.5 V and an effective capacity of ~3 $mA.h.cm^{-2}$. The effect of bending and fatigue on the electrochemical performance and mechanical integrity of the battery were investigated. The battery was able to maintain its capacity, even after 1000 flex cycles to a bend radius of 2.54 cm. The battery showed an improvement in discharge capacity (ca. 10%) if the MnO_2 electrode was flexed to tension as a result of the improvement of particle-to-particle contact. The flexible battery was used to power a light-emitting diode display integrated with a strain sensor and microcontroller.

A novel fiber-type zinc-carbon battery based on carbon fiber was proposed in [90]. The fiber battery comprises two carbon fiber based electrodes, one insulated wire as the separator and electrolyte, which is sealed in a flexible plastic tube. The fiber battery does not exhibit any loss in the capacity during the bending tests, illustrating good flexibility.

The development for all other composite slurry components of the zinc-based battery system for flexographic printing in shown in [92], including water-based zinc anode, nickel

current collector, as well as the inert particle based ionic liquid slurry electrolyte. It is also suggested that further optimization of the ink formulations is possible to achieve better printing quality on a variety of nonconductive and conductive substrates. Specifically, the effects of the polymer binder contents as well as the type and amount of surfactant additives on the printability must be addressed.

1.6.1.3. Other battery types

Previously, we saw the development of printed Li-ion and Zn/MnO_2 batteries taking into account the printing technique and capacity value. However, there are other developed battery types, from which the main characteristics are summarized in Table 1.6.

Table 1.6. Main properties and components of different printed batteries.

Battery Type	Anode	Cathode	Separator / Electrolyte	Printing technique	Capacity / voltage	Ref
Ni/H_2	Ni	Ni	Celgard separator (3501) soaked with 26 wt.% KOH	Microfabrication	1.7mAh at C/12 /1.48V	[93]
Zn/air	Zn/carbon /polymer	PEDOT|Au| Gore-TexTM	LiCl/LiOH electrolyte solution	Screen printing	1.4 mAh/cm^2	[94]
Silver/zinc	Zinc	Silver	10M KOH + ZnO	Inkjet printing	------	[95]
Silver/zinc	Zinc	Silver	57:29:14 H_2O:KOH:PEO (Mv = 600,000)	Printing technique	1.8 mA/cm^2	[96]
Silver/zinc	Zinc	Silver	PAA containing 6MKOH + 1MLiOH	Screen printing	1.3-2.1 mAh/cm^2 / 1.5V	[97]
Silver/zinc	Zinc	Ag_2O	PAA electrolyte	Stencil printing	5.4 mAh/cm^2	[98]
Organic Radical Batteries	------	------	0.1 M solution of tetrabutylammonium hexafluorophosphate in propylene carbonate	Inkjet printing	-------	[99]
Organic Radical Batteries	------	------	0.01 M $AgNO_3$ and 0.1 M solution of tetrabutylammonium perchlorate (TBAP) in CH_3CN	Screen printing	-------	[100]

A conventional Ni-H_2 battery relies on high-pressure hydrogen (55–70 atm) to provide the necessary hydrogen capacity to match the positive electrode capacity. In light of this demand, evaluating the possibility of microfabricating a Ni-H_2 batteries using thick film printing is attractive as it is shown in [93]. Nickel hydroxide powder (Kansai Catalyst Co., Ltd.) was used as the positive active material. The 12 μm powder is 2.5 wt.% cobalt surface-coated and has a 4.5 wt.% zinc and 0.7 wt.% cobalt mixed in a solid solution within the nickel hydroxide. An ink based on platinum black in PVdF/DMF slurry was developed and printed.

A platinum black-based ink was shown to be an acceptable negative electrode ink with reasonable reactivity towards hydrogen oxidation and reduction and negligible mass transfer resistance. A full cell was assembled using the printed positive assembly and the printed negative assembly with a conventional electrolyte-soaked separator.

Sudden upward shifts in charging curves and a corresponding rapid increase in the total cell impedance were observed during cycling. The increase in the cell impedance is related to

poor oxygen recombination/water redistribution within the cell. However, an improvement in the cycle percent utilization was also observed, showing the possibility of acceptable cycling behaviour if better control of the total cell impedance can be achieved [93].

A two-step printing technique to deposit an alkaline electrolyte for a high-energy density silver/zinc printed battery is shown in [96]. An analysis of electrolytes with polyethylene oxide and methyl cellulose was performed, and it was found that a dried 57:29:14 H_2O:KOH:PEO (Mv = 600,000) electrolyte showed the highest areal energy density of 4.1 ± 0.3 mW.h.cm^{-2} and a 94 ± 3% Ag_2O at a C/2 discharge rate of 1.8 mA.cm^{-2}. Through the synthesized PAA separator, it was demonstrated a stencil printed silver oxide battery with areal capacities of 5.4 mA.h.cm^{-2} and volumetric capacities of 7.1 mA.h.cm^{-3} [98].

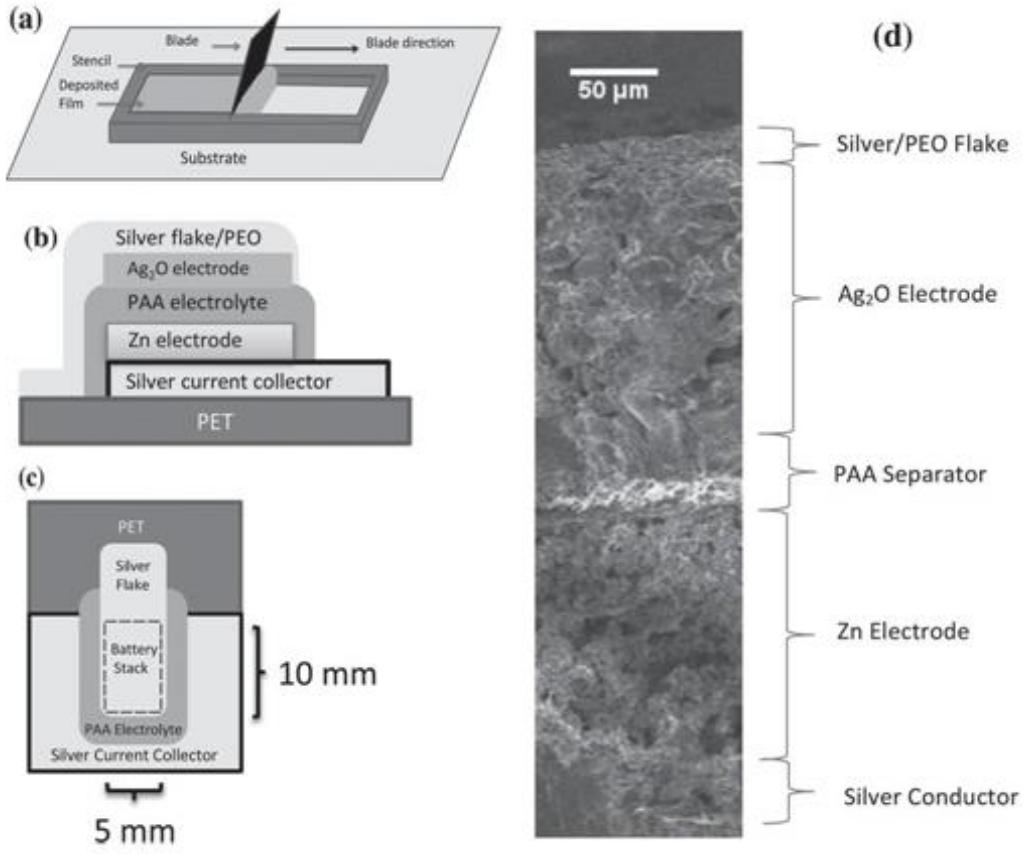

Figure 1.16. a) Stencil printing of slurry to form printed electrodes, b) cross section of a printed battery stack, c) top-down view of battery stack and d) SEM image of a fully printed battery stack [98].

The batteries of Figure 1.16 show no difference in discharge upon flexing at a bend radius of 1.0 cm, indicating their potential in flexible applications. The processes developed are scalable to large scale manufacturing and allow for customization to the application. An organic radical battery with carbon fibers in composite electrodes was fabricated by screen printing technique as is shown in [100]. The authors show that the charge/discharge performance of this

battery was dominated by the interfacial electron transfer processes at the current collector/carbon fiber interface.

1.7. Commercial printed batteries

Batteries manufactured by means of printing techniques are already on the market. Such products offered by the companies presented in Table 1.7 actually serve niche markets.

Table 1.7. Commercial printed batteries.

Company	Voltage (V)	Chemical System	Anode	Cathode	Electrolyte	Capacity	Technique production
PowerPaper	1.5	Zn/MnO_2	Zn	MnO_2	ZnCl	15-30 mAh	Screen Printing /silk-screen printing
Solicore	3	Li/MnO_2	Lithium Metal (Li)	Manganese Dioxide (MnO_2)	Lithium bis-trifluoromethanesulfonimide (LiTFSI)	10- 25 mAh	
Blue Spark	1.5	Zn/MnO_2	Zn	MnO_2	Zinc Chloride	30- 54 mAh	
Enfucell	1.5-3	Metal - MnO_2	Zn	MnO_2	Zinc Chloride	10- 90 mAh	All Printed by Roll to roll
Cymbet Corp	3.6-3.8	Li-ion	Li	$LiCoO_2$	LiPON	1-30 mAh	
Front Edge Technology	3	Lithium-$LiCoO_2$	Li	$LiCoO_2$	LiPON	1-5 mAh	
Infinite Power Solutions	4	X-$LiCoO_2$	Li	$LiCoO_2$	LiPON	0.7 mAh	
Oxis Energy Ltd		Li-Sulphide	Li	Li_2S+S	Aprotic electrolyte; comprising lithium salt		
Ion Technology	3.5	Graphite-aluminum	Al	Graphite	Solid Polymer	30 mAh/ $4cm^2$	
Leeds Lithium		Carbon - lithiated metal oxide (gel electrolyte)	C	$LiMn_2O_4$	Polymer electrolyte		
Varta Microbattery	3	Li/MnO_2	Li metal, alloy, or Li/graphite	MnO_2, $LiCoO_2$, or $LixMnO_2$	Organic electrolyte	25 mAh (@0.03mA)	
Thin Battery Technology	1.5	Zn/ C/MnO_2	Zn	c/MnO_2	$ZnCl_2$, $Zn(OAc)_2$		
Imprint Energy			Zn	Metal Oxide	Solid polymer (zinc ions in Imprint's case)		Screen Printing
Power ID	1.5	Zn/MnO_2	Zn	MnO_2			Electrodes layers are fabricated from proprietary ink that can be printed onto any substrate
Prelonic	1.5	Zn/MnO_2	Zn	MnO_2			Screen Printing

The Advanced Materials Innovation Center (AMIC) developed a lithium polymer battery that can be manufactured by printing technology [101]. The printed lithium-polymer battery

developed is flexible and designed for flexible displays or as attachment to curved surfaces. It is manufactured using screen-printing technology, with dimensions around 500 μm but having an increased surface area than other conventional batteries. Beyond this fact, it shows low cost production and it is rechargeable [101].

A flexible manganese and zinc type battery was also developed by the Fraunhofer Research Institution for Electronic Nano Systems [101] with size (20×20 mm^2), 20 mA.h capacity and 1 mA current.

Enfucell Inc. has created a thin, flexible and eco-friendly soft battery. During the majority of the 20^{th} century, batteries have been cylinders or rectangles in shape and containing heavy metals. Enfucell is taking a different approach. The company is focusing on the environmental impact of its batteries in industry. Enfucell's batteries are made of low-cost, environmentally friendly materials based on zinc and manganese dioxide with zinc chloride as an electrolyte [102]. Enfucell Inc. and Blue Spark Inc. have developed flexible and soft not rechargeable batteries by using a printing method on plastic substrates [5, 102].

On the other hand, Solicore Company produces ultra-thin, flexible, safe, high energy density lithium polymer batteries to meet product's power and design needs [14]. They use the screen printing technology to manufacture this battery replacing liquid, gel and paste electrolytes commonly found in most rechargeable batteries by a polymer electrolyte [14].

The delivered capacity value also depends on the size of the battery. For example, the Softbattery of Enfucell Inc. with dimension of 60 mm x 72 mm presents 90 mA.h at 0.6 mA in comparison with the same battery but from different dimensions (36 mm x 46 mm) which has only 18 mA.h at 0.2 mA [102].

Table 1.7 shows that there are different commercial printed batteries with capacity varying from 0.7 to 90 mA.h. The main difference of the printed batteries is being the electrolyte. The formulation of this material is extremely important as it determines ionic conductivity and diffusion. It is relevant to notice the lack of precise information from the manufacturers in this issue and also about the price.

The price of the battery depends on manufacturer company and size but taking account its applications is predicted to be from $2 to $5 for each battery.

1.8. Batteries based on poly(vinylidene fluoride) materials

Battery separators are often based on porous polymer membranes, including fluorinated polymers, such as poly(vinylidene fluoride) (PVdF) and its copolymers. When compared to

commercial separators, PVdF and its copolymers are more advantageous [111 – 114], due to their high polarity and dielectric constant, which provides larger affinity with polar liquid electrolytes [115 – 118], which can assist ionization of the lithium salts [119 – 127]. Further, these polymers can be tailored in different geometries through binary and ternary polymer/solvent systems, are wetted by organic solvents, chemically inert, show good contact between electrode and electrolyte and are stable in cathodic environment [119 – 127].

Due to selective interactions with the anion, PVdF as battery separator is effective in enhancing the lithium transport number. The ionic conductivity of PVdF is associated to the total solution uptake, which depends on porosity and pore size [128]. Polymer electrolytes based on PVdF for battery applications should present high porosity (50 -80 %) and small pore diameters (<1μm) [129]. Porous battery separators from fluorinated polymers are most commonly obtained by phase inversion processes such as thermal induced phase separation (TIPS), using solvent and non-solvent systems and electrospinning [115, 118]. The achieved porosity of battery separators ranges between 0% to 90% and the pore size from 0.5 μm to 16 μm [116, 130 – 135]. The cells with polymer electrolytes showed good electrochemical and rate performance during cycling [129, 136].

Recently, the copolymer poly(vinylidene fluoride-co-hexafluoropropene) (P(VdF-HFP)) has drawn increasing attention as it seems to be more promising than PVdF for battery separator applications [1, 21], as the addition of the hexafluoropropylene (HFP) group into the main VdF blocks increases the fluorine content, leading to a more hydrophobic material [1], soluble in more solvents and with lower degree of crystallinity [22]. Meanwhile, strong research efforts are being developed on the copolymer poly(vinylidene fluoride-co-chloro-trifluoroethylene) (P(VdF-CTFE)) for electrical energy storage [106 – 109] due to its high ionic conductivity and good compatibility with lithium metal electrodes [110]. This copolymer is relatively recent and should be further studied, being necessary to understand and tailor its microstructure for different applications.

On the other hand, PVdF binder is the most used for electrode slurry preparation for C-$LiFePO_4$ based cathodes, once it is essential for binding active material and conductive additive, for obtaining high adhesion of the electrode to the current collector and mechanical stability and flexibility of the electrode [82]. It also shows high temperature thermal stability, chemical resistance, low permeation, excellent electrical and mechanical properties [83], electrochemical stability from 0 V to 5 V, good and durable adhesion to the current collector and chemical resistance in the electrolyte solution [148]. Other main characteristic of the binder is its molecular weight, which should be high for improving the adhesion between electrode and collector and the cohesion between active material and conductive additive [84].

1.9. Thesis objectives

Taking into account the previous state of the art, there is a scientific and technological need on the development of novel separator membranes as well as to develop novel inks for the different components of the battery.

In order to address some of these challenges, this work has, as main objectives, the development of novel materials for separator membranes based on PVdF co-polymers and to develop novel screen-printable cathode and anode inks. Specifically, it is proposed to:

- understand and to tailor copolymers membranes separators, establishing a correlation among processing conditions, microstructure of the P(VdF-HFP) and PVdF-CTFE membranes, and their properties, in order to evaluate their application range;
- understand and establish a correlation among the microstructure of the P(VdF-HFP) and PVdF-CTFE membranes and their properties for battery applications such as electrolyte solution uptake and ionic conductivity;
- develop new cathode and anode inks for lithium-ion printed batteries.

1.10. Thesis structure

The present thesis is divided into six chapters, showing the evolution of the work during the investigation. Five of the chapters are based on published scientific articles.

In Chapter 1 it is described the general state of the art and future needs on printed batteries. It is to notice that more specific states of the art on each topic are presented in each chapter.

The main characteristics of P(VdF-HFP) membranes, as a result of different solvent/solute ratios and solvent evaporation temperatures, are shown in Chapter 2. Separator membranes with different microstructures have been obtained and their degree of crystallinity, porosity, dielectric and piezoelectric properties have been evaluated.

In Chapter 3 it is presented and discussed the performance as battery separators of the P(VdF-HFP) membranes presented in Chapter 2. Ionic conductivity, voltammetry and charge/discharge cycles were evaluated for the different membranes.

The main characteristics of P(VdF-CTFE) separator membranes as a result of different preparation conditions, including variations of solvent/solute ratio and solvent evaporation temperatures, are shown in Chapter 4. Separator membranes with different microstructures have

been obtained and their degree of crystallinity, porosity, dielectric and piezoelectric properties have been evaluated.

In Chapter 5 the performance as battery separators of the membranes presented in Chapter 4 is presented and discussed. Ionic conductivity, voltammetry and charge/discharge cycles were evaluated for the different membranes.

In Chapter 6 it is shown the production of cathode screen-printable inks, their physico-chemical properties and cycling tests on Li/$LiFePO_4$ half-cells with commercial electrolyte membranes (Whatman brand). Further, results related to the development of anode inks are also presented.

Finally, Chapter 7 provides the general conclusions, as well as suggestions for future work.

1.11. References

[1] A. Kamyshny, S. Magdassi, *Conductive Nanomaterials for Printed Electronics*, Small, 2014. 10 (17): p. 3515–3535.

[2] V. Subramanian, J. B. Chang, A. d. l. F. Vornbrock, D. C. Huang, L. Jagannathan, F. Liao, B. Mattis, S. Molesa, D. R. Redinger, D. Soltman, S. K. Volkman, Z. Qintao, *Solid-State Device Research Conference*, 2008. ESSDERC 2008. 38th European, p. 17-24.

[3] G. Cummins, M. P. Y. Desmulliez, *Inkjet printing of conductive materials,* Circuit World, 2012, 38(4): p. 193-213.

[4] H. Kipphan, *Handbook of Print Media: Technologies and Production Methods*, Springer, 2001;

[5] Blue Spark, *Official webpage: http://www.bluesparktechnologies.com*. May 2014.

[6] A. M. Gaikwad, D. A. Steingart, T. Nga Ng, D. E. Schwartz, G. L. Whiting, *A flexible high potential printed battery for powering printed electronics,* Applied Physics Letters, 2013. 102(23): p. 233302/1-233302/5.

[7] J. Conca, *Are Electric Cars Really That Polluting?*, Forbes, Available from: http://www.forbes.com/sites/jamesconca/2013/07/21/are-electric-cars-really-that-polluting/#4195490c5012, July 2014.

[8] A. Willert, Ulrike Geyer, André Kreutzer, Reinhard R. Baumann, *Thin Film battery manufactured in lab environment using printing technologies*, Fraunhofer ENAS, annual report 2009: p. 26-29.

[9] A. M. Gaikwad, A. C. Arias, D. A. Steingart, *Recent progress on printed flexible batteries: mechanical challenges, printing technologies, and future prospects*, Energy Technology, 2015, *3*: p. 305-328.

[10] G. Zhou, F. Li, H.-M. Cheng, *Progress in flexible lithium batteries and future prospects*, Energy & Environmental Science, 2014, 7(4): p. 1307-1338.

[11] S. Ferrari, M. Loveridge, S. D. Beattie, M. Jahn, R. J. Dashwood, R. Bhagat, *Latest advances in the manufacturing of 3D rechargeable lithium microbatteries.* Journal of Power Sources, 2015, 286: p. 25-46.

[12] G. S. C. V. Bill Moore, *The Roll-to-Roll Battery Revolutionin,* EV World, Available from: http://evworld.com/article.cfm?storyid=933, July 2014.

[13] V. L. Pushparaj, M. M. Shaijumon, A. Kumar, S. Murugesan, L. Ci, R. Vajtai, R. J. Linhardt, O. Nalamasu, P. M. Ajayan, *Flexible energy storage devices based on nanocomposite paper. Proceedings of the National Academy of Sciences,* 2007, 104: p. 13574-13577.

[14] Solicore, *Official webpage: http://www.solicore.com*, May 2014.

[15] Y. Yang, S. Jeong, L. Hu, H. Wu, S. W. Lee, Y. Cui, *Transparent lithium-ion batteries*, Proceedings of the National Academy of Sciences, 2011. 108 (32): p. 13013-13018.

[16] P. Harrop, H. Zervos, *Batteries, Supercapacitors, Alternative Storage for Portable Devices 2009-2019*, IDTechEx, 2014, 1208A.

[17] N. Markets, *Thin-Film and Printed Batteries Markets 2009-2016*, NanoMarkets, 2009, May, p. 1-9.

[18] A. Henry, *Development and Testing of Cathode-type Flexographic Inks*, Rochester Institute of Technology, 2010. 22: p. 20.

[19] N. Markets, *Thin-Film and Printed Batteries Markets*, NanoMarkets, 2007, October, p. 2-9.

[20] N. Markets, *Thin-Film and Printed Batteries Markets 2014-2021*, NanoMarkets, 2014, December, p. 4-9.

[21] N. Markets, *Thin-Film and Printed Batteries:On-Board Solutions for Low-Power Electronics*, NanoMarkets, 2008, March, p. 2-6.

[22] C. T. Rodenbeck, *Planar miniature RFID antennas suitable for integration with batteries*, IEEE Transactions on Antennas and Propagation, 2006. 54(12), 3700-3706.

[23] P. D. Mitcheson, *Energy harvesting for human wearable and implantable bio-sensors*, Engineering in Medicine and Biology Society (EMBC), 2010 Annual International Conference of the IEEE, 2010, p. 3432-3436.

[24] A. Ferrer-Vidal, A. Rida, S. Basat, Y. Li, M. M. Tentzeris, in *Wireless Mesh Networks, 2006. WiMesh 2006. 2nd IEEE Workshop*, 2006, p. 126-128.

[25] S. E. Molesa, B. University of California, *Ultra-low-cost Printed Electronics*, University of California, Berkeley, 2006.

[26] J. Chang, G. Tong, E. Sanchez-Sinencio, *Challenges of printed electronics on flexible substrates*, in Circuits and Systems (MWSCAS), 2012 IEEE 55th International Midwest Symposium, 2012, p. 582-585.

[27] K. Suganuma, *Introduction to Printed Electronics*, Springer, New York, 2014.

[28] V. Di Noto, S. Lavina, G. A. Giffin, E. Negro, B. Scrosati, *Polymer electrolytes: Present, past and future*, Electrochimica Acta, 2011. *57*, p. 4-13.

[29] X. Yuan, H. Liu, J. Zhang, *Lithium-Ion Batteries: Advanced Materials and Technologies*, CRC Press/Taylor & Francis, New York, 2011.

[30] K. Marquardt, R. Hahn, T. Luger, H. Reichl, *Thin Film Encapsulation for Secondary Batteries on Wafer Level*, in Electronics Systemintegration Technology Conference, 2006. 2, p. 1410-1416.

[31] J. Yan, Q. Wang, T. Wei, Z. Fan, *Recent advances in design and fabrication of electrochemical supercapacitors with high energy densities*, Advanced Energy Materials, 2014. 4(4), p. 1300816/1-1300816/43.

[32] S. A. Ahson, M. Ilyas, *RFID Handbook: Applications, Technology, Security, and Privacy*, CRC Press/Taylor & Francis, New York, 2008.

[33] J. Han, K. Zhao, Z. Jiang, *Device-Free Object Tracking Using Passive Tags*, Springer International Publishing, New York, 2014.

[34] S. C. Tung, U. o. Pittsburgh, *An Architectural Approach for Reducing Power and Increasing Security of RFID Tags*, University of Pittsburgh, 2008.

[35] Peter Harrop, Harry Zervos, *Batteries, Supercapacitors, Alternative Storage for Portable Devices 2009-2019*, IDTechEx, 2014, 1208A.

[36] T. M. Jurgensen, S. B. Guthery, *Smart Cards: The Developer's Toolkit*, Prentice Hall PTR, Boston, 2002.

[37] L. Margetts, R. Sawyer, *Transdermal drug* delivery: *Principles* and opioid therapy, Critical Care & Pain, 2007, 7(5): p. 171-176;

[38] G. D. Baura, *Medical Device Technologies: A Systems Based Overview Using Engineering Standards*, Elsevier/Academic Press, Oxford (UK), 2012.

[39] J. Fraden, *Handbook of Modern Sensors: Physics, Designs, and Applications*, Springer, San Diego (USA), 2010.

[40] C. Namjun, S. Seong-Jun, K. Sunyoung, K. Shiho, Y. Hoi-Jun, *A 5.1-μW UHF RFID* tag chip integrated *with sensors for wireless environmental monitoring*, in Solid-State Circuits Conference, 2005. ESSCIRC 2005. Proceedings of the 31st European, 2005, p. 279-282.

[41] R. Tessier, D. Jasinski, A. Maheshwari, A. Natarajan, X. Weifeng, W. Burleson, *An energy-aware active smart card*, Very Large Scale Integration (VLSI) Systems, IEEE Transactions, 2005, 13. p. 1190-1199.

[42] J. Wu, K. S. Paudel, C. Strasinger, D. Hammell, A. L. Stinchcomb, B. J. Hinds, *Programmable transdermal drug delivery of nicotine using carbon nanotube membranes*, Proceedings of the National Academy of Sciences of the United States of America, 2010, 107(26), p. 11698-11702.

[43] T. B. Ashok Sridhar, Reinhard R. Baumann, *Material Matters - Methods for Nanopatterning and Lithography,* Aldrich Material Science, 2011, 6: p. 12-15.

[44] N. Board, *Hand Book on Printing Technology (Offset, Gravure, Flexo, Screen)*, National Institute of Industrial Research, Delhi, 2002.

[45] A. Teichler, J. Perelaer, U. S. Schubert, *Inkjet printing of organic electronics - comparison of deposition techniques and state-of-the-art developments*, Journal of Materials Chemistry C, 2013, 1: p. 1910-1925.

[46] R. H. Leach, *The Printing Ink Manual*, Springer, Netherlands, 1993.

[47] C. Yang, C. P. Wong, M. M. F. Yuen, *Printed electrically conductive composites: conductive filler designs and surface engineering, Journal of Materials Chemistry C* 2013. 1: p. 4052-4069.

[48] H. W. Choi, T. Zhou, M. Singh, G. E. Jabbour, *Recent developments and directions in printed nanomaterials*, Nanoscale, 2015. 7(8): p. 3338-3355.

[49] D. Gamota, *Printed Organic and Molecular Electronics*, Springer, New York, 2004.

[50] P. J. Smith, A. Morrin, *Reactive inkjet printing*, Journal of Materials Chemistry, 2012. 22(22): p. 10965-10970.

[51] G. A. o. America, G. E. Foundation, *Gravure: Process and Technology*, Gravure Association of America, Rochester, New York, 1991.

[52] S. Khan, R. Dahiya, L. Lorenzelli, *Flexible Tactile Sensors using Screen Printed P(VDF-TrFE) and MWCNT/PDMS Composites*, Sensors Journal, IEEE 2014: p. 1-1.

[53] D. S. Kim, J. S. Kim, M. C. Lee, *Japanese Journal of Applied Physics*, 2014, 53, 05HC08.

[54] C. R. Tuck, M. C. B. Ellis, P. C. H. Miller, Techniques for measurement *of droplet size and velocity distributions in agricultural sprays*, Crop Protection, 1997. 16(7): p. 619-628.

[55] R. R. Søndergaard, M. Hösel, F. C. Krebs, Roll-to-Roll fabrication of large area functional organic materials, Journal of Polymer Science Part B: Polymer Physics, 2013. 51(1): p. 16-34.

[56] N. Board, *Screen Printing Technology Hand Book*, NIIR Project Consultancy Services, Asia Pacific Business Press Inc., 2003.

[57] M. Singh, H. M. Haverinen, P. Dhagat, G. E. Jabbour, *Inkjet Printing - Process and Its Applications,* Advanced Materials, 2010, 22(6): p. 673-685.

[58] B. Scrosati, K. M. Abraham, W. A. van Schalkwijk, J. Hassoun, *Lithium Batteries: Advanced Technologies and Applications*, Wiley, New Jersey, 2013.

[59] M. Wakihara, O. Yamamoto, *Lithium Ion Batteries: Fundamentals and Performance*, Wiley, New York, 2008.

[60] R. Dell, D. A. J. Rand, R. S. o. Chemistry, *Understanding Batteries*, Royal Society of Chemistry, Cambridge, 2001.

[61] J. K. Park, *Principles and Applications of Lithium Secondary Batteries*, Wiley, New York, 2012.

[62] C. de las Casas, W. Li, *A review of application of carbon nanotubes for lithium ion battery anode material*, Journal of Power Sources, 2012. 208: p. 74-85.

[63] M. Minakshi, M. Ionescu, *Anodic behavior of zinc in Zn-MnO2 battery using ERDA technique*, International Journal of Hydrogen Energy, 2010. 35(14): p.7618-7622.

[64] S. Logothetidis, *Handbook of Flexible Organic Electronics: Materials, Manufacturing and Applications*, Elsevier Science, Cambridge, 2014.

[65] P. P. Prosini, R. Mancini, L. Petrucci, V. Contini, P. Villano, *$Li_4Ti_5O_{1/2}$ as anode in all-solid-state, plastic, lithium-ion batteries for low-power applications,* Solid State Ionics 2001, 144(1-2): p. 185-192.

[66] M.-S. Park, S.-H. Hyun, S.C. Nam, *Mechanical and electrical properties of a $LiCoO_2$ cathode prepared by screen-printing for a lithium-ion micro-battery,* Electrochimica Acta, 2007. 52(28): p. 7895-7902.

[67] S. Ohta, S. Komagata, J. Seki, T. Saeki, S. Morishita, T. Asaoka, *All-solid-state lithium ion battery using garnet-type oxide and Li_3BO_3 solid electrolytes fabricated by screen-printing,* Journal of Power Sources, 2013, *238*: p. 53-56.

[68] K.-Y. Kang, Y.-G. Lee, D. O. Shin, J.-C. Kim, K. M. Kim, *Performance improvements of pouch-type flexible thin-film lithium-ion batteries by modifying sequential screen-printing* process, Electrochimica Acta, 2014, 138: p. 294-301.

[69] D. Golodnitsky, V. Yufit, M. Nathan, I. Shechtman, T. Ripenbein, E. Strauss, S. Menkin, E. Peled, *Advanced materials for the 3D microbattery*, Journal of Power Sources, 2006, 153: p. 281-287.

[70] Y. Zhao, Q. Zhou, L. Liu, J. Xu, M. Yan, Z. Jiang, *A novel and facile route of ink-jet printing to thin film SnO_2 anode for rechargeable lithium ion batteries*, Electrochimica Acta, 2006, 51(13): p. 2639-2645.

[71] S.-T. Lee, S.-W. Jeon, B.-J. Yoo, S.-D. Choi, H.-J. Kim, S.-M. Lee, *Electrochemical properties of $LiCoO_2$ thick-film cathodes prepared by screen-printing technique*, Journal of Power Sources, 2006, 155(2): p. 375-380.

[72] M. S. Park, S. H. Hyun, S. C. Nam, *Characterization of a LiCoO 2thick film by screen-printing for a lithium ion micro-battery*, Journal of Power Sources, 2006, 159(2): p. 1416-1421.

[73] G. Dennler, S. Bereznev, D. Fichou, K. Holl, D. Ilic, R. Koeppe, M. Krebs, A. Labouret, C. Lungenschmied, A. Marchenko, D. Meissner, E. Mellikov, J. Méot, A. Meyer, T. Meyer, H. Neugebauer, A. Öpik, N. S. Sariciftci, S. Taillemite, T. Wöhrle, *A self-rechargeable and flexible polymer solar battery*, Solar Energy, 2007, 81: p. 947-957.

[74] J. Huang, J. Yang, W. Li, W. Cai, Z. Jiang, *Electrochemical properties of LiCoO2 thin film electrode prepared by ink-jet printing technique*, Thin Solid Films, 2008, 516(10): p. 3314-3319.

[75] L. Hu, H. Wu, F. La Mantia, Y. Yang, Y. Cui, Thin, *Flexible Secondary Li-Ion Paper Batteries*, ACS Nano, 2010, 4(10): p. 5843-5848.

[76] D. Wei, P. Andrew, H. Yang, Y. Jiang, F. Li, C. Shan, W. Ruan, D. Han, L. Niu, C. Bower, T. Ryhanen, M. Rouvala, G. A. J. Amaratunga, A. Ivaska, *Flexible solid state lithium batteries based on graphene inks*, Journal of Materials Chemistry, 2011, 21: p. 9762-9767.

[77] A. Izumi, M. Sanada, K. Furuichi, K. Teraki, T. Matsuda, K. Hiramatsu, H. Munakata, K. Kanamura, *Development of high capacity lithium-ion battery applying three-dimensionally patterned electrode*, Electrochimica Acta, 2012, 79: p. 218-222.

[78] E.-H. Kil, K.-H. Choi, H.-J. Ha, S. Xu, J. A. Rogers, M. R. Kim, Y.-G. Lee, K. M. Kim, K. Y. Cho, S.-Y. Lee, *Imprintable, Bendable, and Shape-Conformable Polymer Electrolytes for Versatile-Shaped Lithium-Ion Batteries*, Advanced Materials, 2013, 25(10): p. 1395-1400.

[79] N. Singh, C. Galande, A. Miranda, A. Mathkar, W. Gao, A. L. M. Reddy, A. Vlad, P. M. Ajayan, *Paintable Battery*, 2012, Scientific Reports 2, Article number: 481.

[80] K. Sun, T.-S. Wei, B. Y. Ahn, J. Y. Seo, S. J. Dillon, J. A. Lewis, *3D Printing of Interdigitated Li-Ion Microbattery Architectures*, Advanced Materials, 2013, 25(33): p. 4539-4543.

[81] D. Beneventi, D. Chaussy, D. Curtil, L. Zolin, E. Bruno, R. Bongiovanni, M. Destro, C. Gerbaldi, N. Penazzi, S. Tapin-Lingua, *Pilot-scale elaboration of graphite/microfibrillated cellulose anodes for Li-ion batteries by spray deposition on a forming paper sheet*, Chemical Engineering Journal, 2014, 243: p.372-379.

[82] J. Pröll, H. Kim, A. Piqué, H. J. Seifert, W. Pfleging, *Laser-printing and femtosecond-laser structuring of LiMn2O4 composite cathodes for Li-ion microbatteries*, Journal of Power Sources, 2014, 255: p.116-124.

[83] A. Izumi, M. Sanada, K. Furuichi, K. Teraki, T. Matsuda, K. Hiramatsu, H. Munakata, K. Kanamura, *Rapid charge and discharge property of high capacity lithium ion battery applying three-dimensionally patterned electrode*, Journal of Power Sources, 2014, 256: p. 244-249.

[84] P. E. Delannoy, B. Riou, B. Lestriez, D. Guyomard, T. Brousse, J. Le Bideau, *Toward fast and cost-effective ink-jet printing of solid electrolyte for lithium microbatteries*, Journal of Power Sources, 2015, 274: p. 1085-1090.

[85] P. Kumar, F.-Y. Wu, L.-H. Hu, S. Ali Abbas, J. Ming, C.-N. Lin, J. Fang, C.-W. Chu, L.-J. Li, *High-performance graphene/sulphur electrodes for flexible Li-ion batteries using the low-temperature spraying method*, Nanoscale, 2015, *7*: p. 8093-8100.

[86] A. Kiebele, G. Gruner, *Carbon nanotube based battery architecture*, Applied Physics Letters, 2007, 91: p.144104.

[87] M. G. Choi, K. M. Kim, Y.-G. Lee, *Design of 1.5 V thin and flexible primary batteries for battery-assisted passive (BAP) radio frequency identification (RFID) tag*, Current Applied Physics, 2010, 10(4): p. e92-e96.

[88] A. M. Gaikwad, G. L. Whiting, D. A. Steingart, A. C. Arias, *Highly Flexible, Printed Alkaline Batteries Based on Mesh-Embedded Electrodes*, Advanced Materials**,** 2011, 23(29): p. 3251-3255.

[89] A. M. Gaikwad, H. N. Chu, R. Qeraj, A. M. Zamarayeva, D. A. Steingart, *Reinforced Electrode Architecture for a Flexible Battery with Paperlike Characteristics*, Energy Technology, 2013, 1(2-3): p. 177-185.

[90] X. Yu, Y. Fu, X. Cai, H. Kafafy, H. Wu, M. Peng, S. Hou, Z. Lv, S. Ye, D. Zou, *Flexible fiber-type zinc–carbon battery based on carbon fiber electrodes*, Nano Energy, 2013, 2(6): p. 1242-1248.

[91] Z. Wang, N. Bramnik, S. Roy, G. Di Benedetto, J. L. Zunino Iii, S. Mitra, *Flexible zinc–carbon batteries with multiwalled carbon nanotube/conductive polymer cathode matrix*, Journal of Power Sources, 2013, 237: p. 210-214.

[92] Z. Wang, R. Winslow, D. Madan, P. K. Wright, J. W. Evans, M. Keif, X. Rong, *Development of MnO 2 cathode inks for flexographically printed rechargeable zinc-based battery*, Journal of Power Sources, 2014, 268, 246-254.

[93] W. G. Tam, J. S. Wainright, *A microfabricated nickel–hydrogen battery using thick film printing techniques*, Journal of Power Sources, 2007, 165: p.481-488.

[94] M. Hilder, B. Winther-Jensen, N. B. Clark, *Paper-based, printed zinc–air battery*, Journal of Power Sources, 2009, 194(2): p. 1135-1141.

[95] C. C. Ho, K. Murata, D. A. Steingart, J. W. Evans, P. K. Wright, *A super ink jet printed zinc–silver 3D microbattery*, Journal of Micromechanics and Microengineering, 2009, 19(9): 094013.

[96] K. T. Braam, S. K. Volkman, V. Subramanian, *Characterization and optimization of a printed, primary silver–zinc battery*, Journal of Power Sources, 2012, 199(1): p. 367-372.

[97] S. Berchmans, A. J. Bandodkar, W. Jia, J. Ramirez, Y. S. Meng, J. Wang, *An epidermal alkaline rechargeable Ag–Zn printable tattoo battery for wearable electronics*, Journal of Materials Chemistry A, 2014, 2(38): p. 15788-15795.

[98] K. Braam, V. Subramanian, *A Stencil Printed, High Energy Density Silver Oxide Battery Using a Novel Photopolymerizable Poly(acrylic acid) Separator*, Advanced Materials, 2015, 27(4): p. 689-694.

[99] T. Janoschka, A. Teichler, B. Häupler, T. Jähnert, M. D. Hager, U. S. Schubert, *Reactive Inkjet Printing of Cathodes for Organic Radical Batteries*, Advanced Energy Materials 2013, 3: p.1025-1028.

[100] S. Yoshihara, H. Isozumi, M. Kasai, H. Yonehara, Y. Ando, K. Oyaizu, H. Nishide, *Improving Charge/Discharge Properties of Radical Polymer Electrodes Influenced Strongly by Current Collector/Carbon Fiber Interface*, The Journal of Physical Chemistry B, 2010, 114(25): p. 8335-8340.

[101] Lin Edwards, *Japanese scientists invent printable lithium battery*, *PhysOrg*, Available from: http://phys.org/news/2010-01-japanese-scientists-printable-lithium-battery.html, July 2014.

[102] Enfucell, *Official webpage: http://www.enfucell.com*. May 2014.

[103] F. Liu, N.A. Hashim, Y. Liu, M.R.M. Abed, K. Li, *Progress in the production and modification of PVdF membranes*, Journal of Membrane Science, 2011, 375: p. 1-27.

[104] Y. Ding, P. Zhang, Z. Long, Y. Jiang, F. Xu, W. Di, *The ionic conductivity and mechanical property of electrospun P(VdF-HFP)/PMMA membranes for lithium ion batteries*, Journal of Membrane Science, 2009, 329: p. 56-59.

[105] J.-H. Cao, B.-K. Zhu, Y.-Y. Xu, *Structure and ionic conductivity of porous polymer electrolytes based on P(VdF-HFP) copolymer membranes*, Journal of Membrane Science, 2006, 281: p. 446-453.

[106] D. Li, W.B. Krantz, A.R. Greenberg, R.L. Sani, *Membrane formation via thermally induced phase separation (TIPS): Model development and validation*, Journal of Membrane Science, 2006, 279: p. 50-60.

[107] N. Ghasem, M. Al-Marzouqi, N. Abdul Rahim, *Modeling of CO_2 absorption in a membrane contactor considering solvent evaporation*, Separation and Purification Technology, 2013, 110: p. 1-10.

[108] A. Venault, Y. Chang, D.-M. Wang, D. Bouyer, A. Higuchi, J.-Y. Lai, *PEGylation of anti-biofouling polysulfone membranes via liquid- and vapor-induced phase separation processing*, Journal of Membrane Science, 2012, 403 - 404: p. 47-57.

[109] S.K. Yong, J.K. Hyo, Y.K. Un, *Asymmetric membrane formation via immersion precipitation method. I. Kinetic effect*, Journal of Membrane Science, 1987, 60: p. 219-232.

[110] C. Feng, K.C. Khulbe, T. Matsuura, S. Tabe, A.F. Ismail, *Preparation and characterization of electro-spun nanofiber membranes and their possible applications in water treatment*, Separation and Purification Technology, 2013, 102: p. 118-135.

[111] C. M. Costa, M. M. Silva, S. Lanceros-Mendez, *Battery separators based on vinylidene fluoride (VDF) polymers and copolymers for lithium ion battery applications*, RSC Advances, 2013, 3(29): p. 11404-11417.

[112] E. Quartarone, P. Mustarelli, A. Magistris, *PEO-based composite polymer electrolytes*, Solid State Ionics, 1998, 110: p. 1-14.

[113] X. Huang, *Separator technologies for lithium-ion batteries*, J Solid State Electrochem, 2011, 15: p. 649-662.

[114] Sarada, T., L.C. Sawyer, and M.I. Ostler, *Three dimensional structure of celgard microporous membranes*. Journal of Membrane Science, 1983. 15(1): p. 97-113.

[115] Kataoka, H., et al., *Conduction Mechanisms of PVDF-Type Gel Polymer Electrolytes of Lithium Prepared by a Phase Inversion Process*. The Journal of Physical Chemistry B, 2000, 104(48): p. 11460-11464

[116] Boudin, F., et al., *Microporous PVdF gel for lithium-ion batteries*. Journal of Power Sources, 1999, 81–82(0): p. 804-807.

[117] Choi, S.-S., et al., *Electrospun PVDF nanofiber web as polymer electrolyte or separator*. Electrochimica Acta, 2004. 50(2–3): p. 339-343.

[118] Cheruvally, G., et al., *Electrospun polymer membrane activated with room temperature ionic liquid: Novel polymer electrolytes for lithium batteries*. Journal of Power Sources, 2007, 172(2): p. 863-869.

[119] Yoshio, M.B., Ralph J; Kozawa, Akiya, Lithium-Ion Batteries: Science and Technologies, New Yorkm, Springer, 2009.

[120] Tian, L.-y., X.-b. Huang, and X.-z. Tang, *Study on morphology behavior of PVDF-based electrolytes*, Journal of Applied Polymer Science, 2004, 92(6): p. 3839-3842.

[121] Ji, G.-L., et al., *PVDF porous matrix with controlled microstructure prepared by TIPS process as polymer electrolyte for lithium ion battery*. Polymer, 2007, 48(21): p. 6415-6425.

[122] Su, Y., et al., *PVDF Membrane Formation via Thermally Induced Phase Separation*, Journal of Macromolecular Science, Part A, 2007, 44(1): p. 99-104.

[123] Cheng, L.-P., et al., *PVDF membrane formation by diffusion-induced phase separation-morphology prediction based on phase behavior and mass transfer modeling*. Journal of Polymer Science Part B: Polymer Physics, 1999, 37(16): p. 2079-2092.

[124] Karabelli, D., et al., *Poly(vinylidene fluoride)-based macroporous separators for supercapacitors*, Electrochimica Acta, 2011, 57(0): p. 98-103.

[125] Kim, K.M., J.-C. Kim, and K.S. Ryu, *Physical and Electrochemical Properties of PVdF-HFP/SiO2-Based Polymer Electrolytes Prepared Using Dimethyl Acetamide Solvent and Water Non-Solvent*, Macromolecular Chemistry and Physics, 2007, 208(8): p. 887-895.

[126] Li, Z., et al., *High ionic conductive PVDF-based fibrous electrolytes*, Journal of Solid State Electrochemistry, 2008, 12(12): p. 1629-1635.

[127] Djian, D., et al., *Macroporous poly(vinylidene fluoride) membrane as a separator for lithium-ion batteries with high charge rate capacity*, Journal of Power Sources, 2009, 187(2): p. 575-580.

[128] Saito, Y., et al., *Carrier Migration Mechanism of Physically Cross-Linked Polymer Gel Electrolytes Based on PVDF Membranes*, The Journal of Physical Chemistry B, 2002, 106(29): p. 7200-7204.

[129] Shi, Q., et al., *Structure and performance of porous polymer electrolytes based on P(VDF-HFP) for lithium ion batteries*, Journal of Power Sources, 2002, 103(2): p. 286-292.

[130] Kim, S.S. and D.R. Lloyd, *Microporous membrane formation via thermally-induced phase separation. III. Effect of thermodynamic interactions on the structure of isotactic polypropylene membranes*, Journal of Membrane Science, 1991, 64(1–2): p. 13-29.

[131] Raghavan, P., et al., *Preparation and electrochemical characterization of gel polymer electrolyte based on electrospun polyacrylonitrile nonwoven membranes for lithium batteries*, Journal of Power Sources, 2011, 196(16): p. 6742-6749.

[132] Jacob, M.M.E., S.R.S. Prabaharan, and S. Radhakrishna, *Effect of PEO addition on the electrolytic and thermal properties of PVDF-LiClO4 polymer electrolytes*, Solid State Ionics, 1997, 104(3–4): p. 267-276.

[133] Chandra, A., R.C. Agrawal, and Y.K. Mahipal, *Ion transport property studies on PEO–PVP blended solid polymer electrolyte membranes*, Journal of Physics D: Applied Physics, 2009, 42(13): p. 135107.

[134] Rao, M., et al., *Preparation and performance of gel polymer electrolyte based on electrospun polymer membrane and ionic liquid for lithium ion battery*, Journal of Membrane Science, 2012, 399–400(0): p. 37-42.

[135] Kumar, A. and M. Deka, *PEO/P(VdF-HFP) blend based Li+ ion-conducting composite polymer electrolytes dispersed with dedoped (insulating) polyaniline nanofibers*, Journal of Solid State Electrochemistry, 2012, 16(1): p. 35-44.

[136] C. M. Costa, M. M. Silva, S. Lanceros-Méndez, *Battery separators based on vinylidene fluoride (VDF) polymers and copolymers for lithium ion battery applications*, RSC Advances, 2013, 3(29): p. 11404-11417-

[137] F. Liu, N.A. Hashim, Y. Liu, M.R.M. Abed, K. Li, *Progress in the production and modification of PVDF membranes*, Journal of Membrane Science, 2011, 375: p. 1-27.

[138] Y. Ding, P. Zhang, Z. Long, Y. Jiang, F. Xu, W. Di, *The ionic conductivity and mechanical property of electrospun P(VdF-HFP)/PMMA membranes for lithium-ion batteries*, Journal of Membrane Science, 2009, 329: p. 56-59.

[139] J.-H. Cao, B.-K. Zhu, Y.-Y. Xu, *Structure and ionic conductivity of porous polymer electrolytes based on P(VdF-HFP) copolymer membranes*, Journal of Membrane Science, 2006, 281: p. 446-453.

[140] D. Li, W.B. Krantz, A.R. Greenberg, R.L. Sani, *Membrane formation via thermally induced phase separation (TIPS): Model development and validation*, Journal of Membrane Science, 2006, 279: p. 50-60.

[141] N. Ghasem, M. Al-Marzouqi, N. Abdul Rahim, *Modeling of CO_2 absorption in a membrane contactor considering solvent evaporation*, Separation and Purification Technology, 2013, 110: p. 1-10.

[142] A. Venault, Y. Chang, D.-M. Wang, D. Bouyer, A. Higuchi, J.-Y. Lai, *PEGylation of anti-biofouling polysulfone membranes via liquid- and vapor-induced phase separation processing*, Journal of Membrane Science, 2012, 403–404: p. 47-57.

[143] S.K. Yong, J.K. Hyo, Y.K. Un, *Asymmetric membrane formation via immersion precipitation method. I. Kinetic effect*, Journal of Membrane Science, 1987, 60: p. 219-232.

[144] C. Feng, K.C. Khulbe, T. Matsuura, S. Tabe, A.F. Ismail, *Preparation and characterization of electro-spun nanofiber membranes and their possible applications in water treatment*, Separation and Purification Technology, 2013, 102: p. 118-135.

[145] Z. Zhang, T. Zeng, C. Qu, H. Lu, M. Jia, Y. Lai, J. Li, *Cycle performance improvement of LiFePO4 cathode with polyacrylic acid as binder*, Electrochimica Acta, 2012, 80: p. 440-444.

[146] S. Ebnesajjad, *Introduction to Fluoropolymers*, William Andrew Publishing, Oxford, 2013.

[147] S.-L. Chou, Y. Pan, J.-Z. Wang, H.-K. Liu, S.-X. Dou, *Small things make a big difference: binder effects on the performance of Li and Na batteries*, Physical Chemistry Chemical Physics, 2014, 16: p. 20347-20359.

[148] A. Gören, C.M. Costa, M.M. Silva, S. Lanceros-Méndeza, *State of the art and open questions on cathode preparation based on carbon coated lithium iron phosphate*, Composites Part B: Engineering, 2015, 83: p. 333–345

2. Microstructural variations of poly(vinylidene fluoride co-hexafluoropropylene) and their influence on the thermal, dielectric and piezoelectric properties

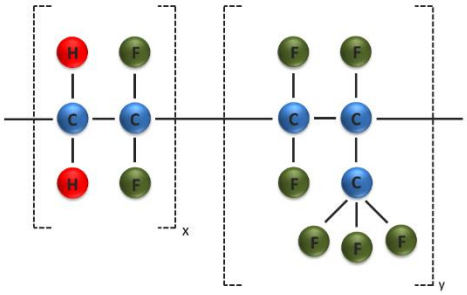

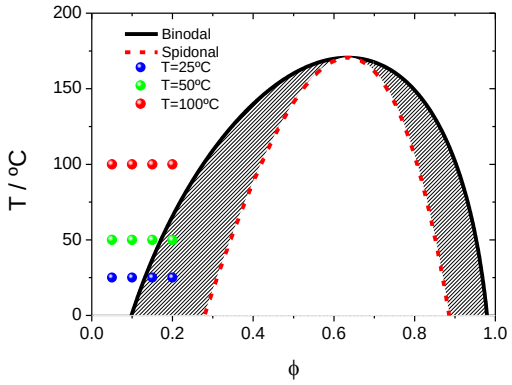

This chapter reports and discusses poly(vinylidene fluoride-co-hexafluoropropylene), P(VdF-HFP), membranes, that have been prepared by thermally induced phase separation (TIPS), allowing to tune microstructure and morphology. The obtained microstructure is explained by the Flory-Huggins theory, depending on polymer concentration and solvent evaporation temperature. The formation of a porous membrane is attributed to a spinodal decomposition of the liquid-liquid phase separation. The effect of the processing conditions on the morphology, degree of porosity, degree of crystallinity and crystalline polymorph, thermal, dielectric and piezoelectric properties of the P(VdF-HFP) polymer were evaluated.

This chapter is based on the following publication: “Microstructural variations of poly(vinylidene fluoride co-hexafluoropropylene) and their influence on the thermal, dielectric and piezoelectric properties”, R. E. Sousa, J. Nunes-Pereira, J. C. C. Ferreira, C. M. Costa, A. V. Machado, M. M. Silva and S. Lanceros-Méndez, Polymer Testing, 40, 2014, 245 – 255.

2.1. Introduction

Significant advances are being performed in scientific and commercial areas for the development of membrane separation technologies [1]. Polymeric membranes are being used for a variety of industrial areas, including microfiltration (MF) [2], ultrafiltration (UF) [1, 2], reverse osmosis (RO) [1, 2], nanofiltration (NF) [3], hyperfiltration [3] and gas separation [2]. The applications of membrane technologies cover almost every industrial sector including environmental, electronic, energy, chemical and biotechnology [1]. For example, the membrane is a critical component of fuel cells [4] and lithium-ion batteries [1, 5] and the control of surface hydrophobicity allows the development of membrane distillation (MD) [6] applications. Each application imposes specific requirements to the membrane material and structure. For micro and ultrafiltration membranes, porosity and pore size of the membranes determine the efficiency of filtration [2].

Much effort is being devoted to improve membrane anti-fouling properties, mechanical strength and chemical resistance [1]. In a general way, the final properties of the polymer membrane depend on processing parameters, including polymer concentration, solvent evaporation temperature, solvent type, non-solvent content in the solution and coagulation bath [7, 8]. The most commonly used technique to produce membranes is the phase separation of polymer solutions by phase inversion, which can be achieved by different methods [2], including TIPS [9], controlled evaporation of solvent from three component systems [10], precipitation from the vapour phase [11], immersion precipitation (IP) [12] and air-casting [13]. Currently, most of the commercial membranes for microfiltration and ultra-filtration [14] are produced by phase inversion methods [14], mainly due to its simplicity and flexible production scales, allowing maintaining low production costs.

Among the aforementioned methods, TIPS has received considerable attention and has become one of the main methods of polymer membrane preparation [15]. In comparison to traditional phase separation processes, TIPS shows some advantages: it can be applied to a wide range of polymers, including those that cannot otherwise be formed into membranes due to its poor solubility [9]; it can be used to generate dense and porous films, the latter with isotropic, anisotropic or asymmetric microstructures with an overall porosity as high as 90 %; and it is more flexible than wet or dry-casting, since it depends primarily on heat transfer rather than the more complex multi-component mass transfer [9].

Poly(vinylidene fluoride) (PVdF) has received large attention as a membrane material due to its outstanding properties such as high mechanical strength, thermal stability, chemical resistance and high hydrophobicity, when compared to other polymer materials, such as polysulfone (PSU), polyethersulfone (PES) and polyimide (PI) [16]. PVdF membranes have been extensively applied in ultrafiltration and microfiltration [17], and are currently being explored as potential candidates in membrane contactor [18] and membrane distillation applications [19]. PVdF dissolves in common organic solvents, in which, porous PVdF membranes can be produced by phase inversion [20].

Besides PVdF, there are some other fluoropolymers which can be used as membrane materials, such as P(VdF-HFP) and poly(vinylidenefluoride-trifluoroethylene) P(VdF-TrFE) [20]. P(VdF-HFP) has drawn much attention [1, 21] and seems to be more promising than PVdF for membrane applications as the addition of the amorphous phase related to the hexafluoropropylene (HFP) group into the main VdF blocks, increases the fluorine content leading to a more hydrophobic material [1], soluble in more solvents and with lower degree of crystallinity [22]. Thus, for lithium-ion battery separator applications, the amorphous phase of HFP helps to capture larger amounts of liquid electrolytes [23], whereas the crystalline VdF phase provides mechanical integrity for the development of free-standing films [21].

Microporous membranes of P(VdF-HFP) have been prepared by phase inversion from acetone/water/P(VdF-HFP) solutions with degrees of porosity between 70 and 90 % [23]. The effect of P(VdF-HFP) concentration for the development of hollow fiber membranes has been studied in the system *N,N*-dimethylacetamide (DMA_C)/ poly(ethylene glycol)/ (PEG)/P(VdF-HFP) and it was verified that internal and external pore sizes decreased with increasing copolymer content [24]. P(VdF-HFP) membranes were also produced on ternary system from PVdF and propylene carbonate (PC) or dimethyl sulfoxide (DMSO) solutions, the gelation occurring at relatively low concentrations and the miscibility area of the ternary diagram being larger for DMSO than for PC [25].

Taking into account the reported literature for production of membranes based on P(VdF-HFP), a systematic approach to the modification of P(VdF-HFP) microstructure is still needed. Thus, the present work is devoted to the preparation of membranes from the P(VdF-HFP)/N,N dimethylformamide (DMF) solution. Membranes were prepared by TIPS varying P(VdF-HFP)/DMF relative concentration and solvent evaporation temperature. Membranes with different microstructures have been obtained and their degree of crystallinity, porosity, dielectric and piezoelectric properties has been evaluated.

2.2. Experimental

2.2.1. Materials

Poly(vinylidene fluoride-co-hexafluoropropylene) P(VdF-HFP) (Solef 21216; M_w = 600,000 g.mol^{-1}; 12 wt.% HFP) was supplied by Solvay. N,N-dimethylformamide (DMF, 99.5 %) was supplied by Merck.

2.2.2. Membrane preparation

The P(VdF-HFP) polymer concentration in solution ranged from 5 wt.% to 20 wt.%. The polymer was dissolved in DMF at room temperature under constant magnetic stirring until a homogeneous solution was obtained. After total polymer dissolution, the solution was placed on clean a glass substrate and spread by blade coating with the thickness of 100 μm followed by isothermal evaporation within an air oven at temperatures from room temperature to 100 ℃.

2.2.3. Sample characterization

The morphology of the P(VdF-HFP) membranes (prepared by fracturing the corresponding film in liquid nitrogen) was obtained by scanning electron microscopy (SEM) (Cambridge, Leica) with an accelerating voltage of 15 kV. Previously, the samples were coated with a thin gold layer using a sputter coating (Polaron, model SC502 sputter coater).

The porosity of the membranes was determined using a pycnometer according to the following expression:

$$\rho_m = \frac{\rho_w m_3}{m_1+m_3-m_2} \quad (2.1)$$

where ρ_m represents the density of the membrane sample (the density of the pristine polymer, ρ_{pol}, is equal to 1.77 g cm^{-3}), ρ_w is the water density, m_1 is the mass of pycnometer with water, m_2 is the mass of pycnometer with water and the membrane and m_3 is the mass of the dry membrane [26].

The degree of porosity was then calculated using the following relation [26]:

$$\phi = 1 - \frac{\rho_m}{\rho_{pol}} \quad (2.2)$$

Contact angle measurements (sessile drop in dynamic mode) were performed at room temperature in a Data Physics OCA20 device using ultrapure water (3 ml droplets) as the test liquid. At least 3 measurements on each sample were performed in different sample locations and the average contact angle was calculated.

The polymer crystalline was identified by Fourier Transformed Infrared spectroscopy (FTIR) at room temperature with a Jasco FT/IR-4100. FTIR spectra were collected in attenuated total reflectance mode (ATR) from 4000 to 600 cm^{-1} after 32 scans with a resolution of 4 cm^{-1}.

Melting temperature and degree of crystallinity were determined by differential scanning calorimetry (DSC) with a Mettler Toledo 821e apparatus. The samples were cut from the central region of the membranes, placed in 50 µl crucibles and heated from 50 to 200 °C at a rate of 10 °C.min^{-1}, under an argon atmosphere. The degree of crystallinity (χ_c) was calculated from the enthalpy of the melting peak (ΔH_f) based on the enthalpy of a 100% crystalline sample, through:

$$\chi_c = \frac{\Delta H_f}{xH_\alpha + y\Delta H_\beta} \qquad (2.3)$$

where x is the weight fraction of the α-phase, y is the weight fraction of the β-phase determined from the FTIR measurements, ΔH_α is the melting enthalpy of pure crystalline α-PVdF and ΔH_β is the melting enthalpy of pure crystalline β-PVdF which are reported to be 93.04 $J.g^{-1}$ and 103.4 $J.g^{-1}$ respectively [27, 28].

Dielectric measurements were performed using a Quadtech 1920 LCR precision meter. The real part of the dielectric function (ε') and the dielectric losses ($tan\ \delta$) were obtained at room temperature in the frequency range of 200 Hz to 1 MHz with an applied voltage of 0.5 V. Circular aluminum electrodes of 5 mm diameter were vacuum evaporated onto both sides of each sample. The error associated to the dielectric measurements is ~2 %, mainly due to the geometrical factors.

The piezoelectric d_{33} coefficients were then measured using a d_{33} meter APC YE2730A. For determination of the piezoelectric coefficient, the P(VdF-HFP) was first poled by corona discharge at a controlled temperature inside a home-made corona chamber with the following parameters: applied voltage of 10 kV at a constant current of 20 µA; constant distance of 2 cm between the sample and the tip; poling time 30 min. The poling conditions were further optimized by varying poling temperature from 80 to 120 °C and then cooled to room temperature under the applied electric field [29].

2.3. Results

The membrane thickness varies between 9 – 76 μm depending on polymer concentration (Figure 2.1) and is independent of the evaporation temperature.

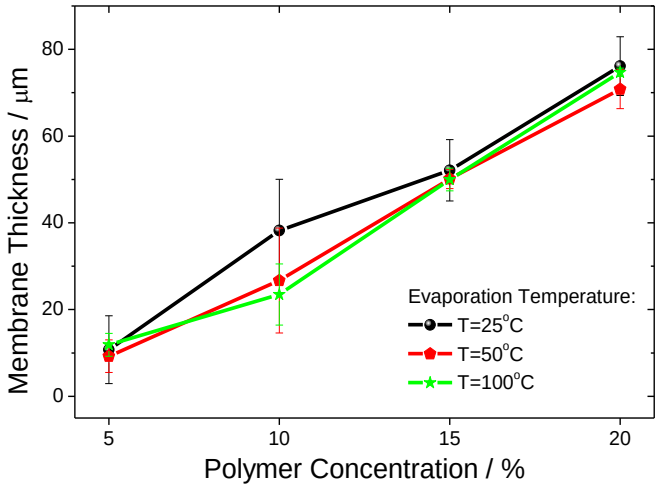

Figure 2.1. Membrane thickness as a function of polymer concentration for the different evaporation temperatures.

SEM images showing the microstructural evolution of the P(VdF-HFP) samples prepared by solvent evaporation at room temperature and varying initial polymer concentration in the P(VdF-HFP)/DMF binary system from 5 to 20 wt.% are presented in Figure 2.2 a) – Figure 2.2 d). The effect of the solvent evaporation temperature on membrane morphology is shown in Figure 2.2 e) – Figure 2.2 f).

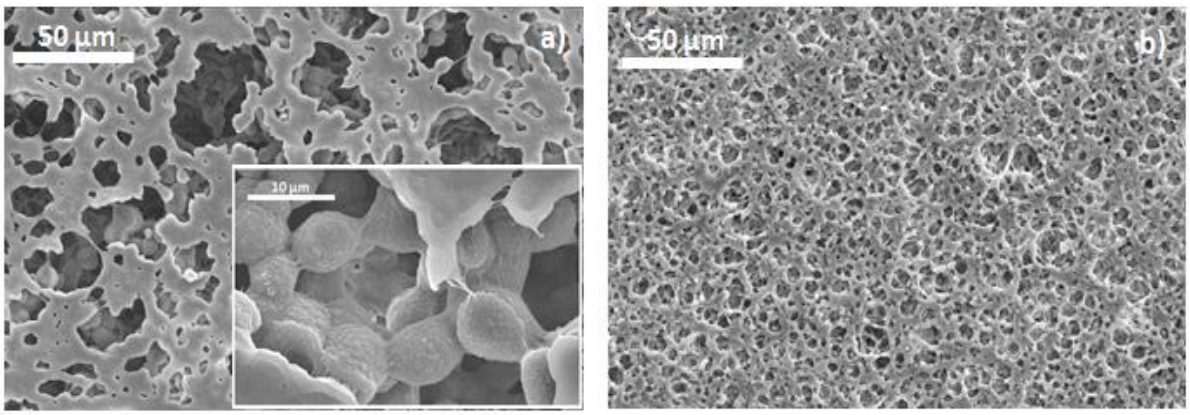

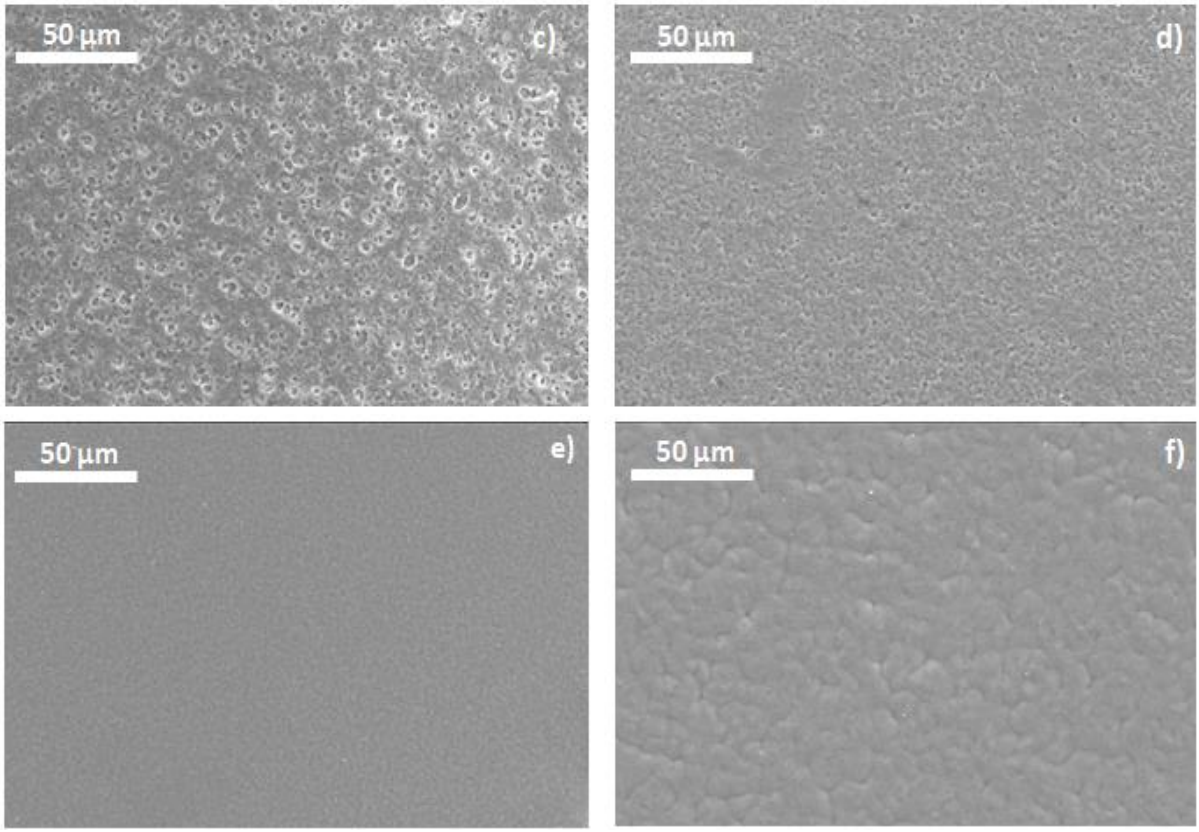

Figure 2.2. Surface images of the P(VdF-HFP) membranes prepared from the P(VdF-HFP)/DMF solution: solvent evaporation at room temperature with a) 5 wt.% P(VdF-HFP), b) 10 wt.% P(VdF-HFP), c) 15 wt.% P(VdF-HFP) and d) 20 wt.% of P(VdF-HFP). Microstructures of the sample with 20 wt.% P(VdF-HFP) with solvent evaporation at e) 50 ºC and f) 100 ºC.

The membranes show a porous morphology evolving from large pore sizes of ~7.5µm (Figure 2.2 a)) to lower pore sizes of ~2µm (Figure 2.2 d)), the pore size decreasing with increasing initial polymer concentration in the P(VdF-HFP)/DMF solution.

In particular, Figure 2.2 a) shows a three dimensional particulate morphology with macro voids or finger-like pores suggesting a precipitation situation dominated by liquid-liquid demixing in the phase diagram [30]. The inset of Figure 2.2 a), shows that the particulate morphology is the spherulitic structure characteristic of PVdF [31].

The degree of porosity of the P(VdF-HFP) membranes is plotted in Figure 2.3 as a function of initial polymer concentration.

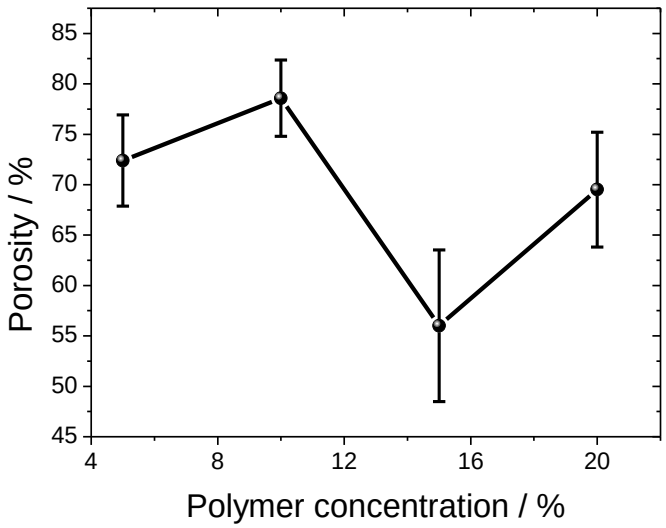

Figure 2.3. Degree of porosity as a function of P(VdF-HFP) initial concentration in the P(VdF-HFP)/DMF system prepared by solvent evaporation at room temperature.

Regardless initial polymer concentration, the membranes show high degrees of porosity between 56 % and 78 % for 15 and 10 wt.% of P(VdF-HFP), respectively, which is in line with the degree of porosity obtained in similar systems (P(VdF-HFP)/DMF/clay) [32]. The high degree of porosity is due to the low evaporation temperature, the polymer chains have reduce mobility and prevent the polymer to occupy the free space left by the evaporated solvent [33]. These effects will be later discussed in relation to the phase diagram of P(VdF-HFP)/DMF system.

The presence of pores is not observed for membranes with 20 wt.% of initial polymer concentration with solvent evaporation temperatures of 50 ℃ and 100 ℃, Figure 2.2 e) and Figure 2.2 f), respectively. The morphology of these membranes is characterized by a dense and compact microstructure. Increasing solvent evaporation temperature above 40 ℃, increased polymer chains mobility, making them able to occupy the free space left by the solvent during evaporation, which results in a compact microstructure. Further, increasing temperature leads to increased solvent evaporation rate and favors polymer diffusion and spherulite growth [34]. The spherulite size increases with increasing evaporation temperature for a given polymer concentration (Figure 2.2 a), Figure 2.2 e) and Figure 2.2 f)).

Further, at solvent evaporation temperatures above 40 ℃ the morphology of the membranes is independent of the polymer concentration.

For samples obtained after high temperature solvent evaporation, no porosity is detected.

One important parameter for the development of membrane applications is the hydrophobicity of the membranes that can be assessed through the measurement of the contact

angle. The contact angle as a function of initial polymer concentration and for the different evaporation temperatures is illustrated in Figure 2.4.

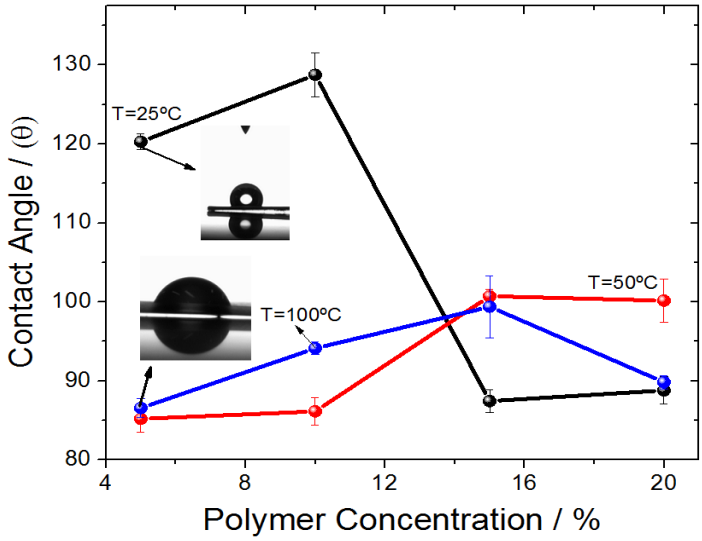

Figure 2.4. Contact angle as a function of P(VdF-HFP) concentration for the different evaporation temperatures.

For membranes up to 10 wt.% initial polymer concentration with solvent evaporation at room temperature, a water contact angle above 125° is measured, which is related to the large pore size and irregular surface [35]. Increasing initial polymer concentration leads thus to a strong decrease of the contact angle to ~85° due to the smoother and more compact morphology (Figure 2.1) [36].

Increasing solvent evaporation temperature leads to a strong decrease of the water contact angle to values around 85°, which increases up to ~95° for increasing initial polymer concentration, associated to increased roughness in this compact morphology, related to the larger spherulite sizes (Figure 2.2), as discussed in [37].

The crystalline phase of the polymer after polymer crystallization is relevant for the different applications of this electroactive polymer [20] and can be determined by FTIR. Table 2.1 shows the most relevant vibration modes of P(VdF-HFP) and Figure 2.5 shows the FTIR-ATR spectra of the membranes.

Table 2.1. Vibration modes characteristics of the P(VdF-HFP) polymer, where ν_s is symmetric stretching, ν_a is antisymmetric stretching, δ is scissoring, w is wagging, t is twisting, r is rocking, CCC δ is skeletal bending of C(F)–C(H)–C(F) and CCC δ' is skeletal bending of C(H)–C(F)–C(H).

Wavenumber (cm^{-1})	Vibration modes	Ref
611	–C–F–wagging modes	[38]
613	CF_2 (δ) and CCC δ'	[39]
615	α-phase	[27]
760	α-phase	[40]
762	CF_2 (δ) and CCC δ	[39]
765	α-phase	[41]
766	α-phase	[42]
794	CF_3 stretching	[40]
795	α-phase	[40]
796	CF_3 stretching	[38]
798	CH_2 (r)	[39]
834	CH_2 (r)	[39]
836	Amorphous region	[40]
838	β-phase	[43]
839	Amorphous phase	[42]
841	γ-phase	[42]
853	α-phase	[40]
871	amorphous phase	[43]
877	CC (ν_s) and CCC δ	[39]
879	Amorphous phase	[42]
974-976	α-phase	[40, 42, 43]
977	α-phase (due to TGTG−(T: trans and G: gauche) conformation)	[38]
978	CH_2 (t)	[39]
1062	C–C skeletal vibration	[40]
1063	symmetrical stretching mode of CF_2	[43]
1069	CF_2 (ν_s) and CH_2 (w)	[39]
1148	symmetrical stretching mode of CF_2	[43]
1151	CC (ν_a) and CF_2 (ν_s)	[39]
1173	Symmetrical stretching mode of CF_2	[44]
1179	Symmetrical stretching mode of CF_2	[43]
1185	CF_2 (ν_s)+CH_2 (t)	[39]
1197	asymmetric stretching vibrations of the –CF_2 group	[42]
1200	—CF_2 groups	[44]
1202	Asymmetrical stretching of –CF_2–	[40]
1203	asymmetrical stretching vibrations of the CF_2 group	[43]
1212	α-phase	[40]
1214	CF_2 (ν_a)+CH_2 (w)	[39]
1276	symmetric stretching vibrations of the –CF_2 group	[42]
1295	CF_2 (ν_a) and CF_2 (r)	[39]
1382	symmetrical stretching mode of CH_2 wagging	[43]
1384	α-phase	[40]

1386	CH_2 (δ)+CH_2 (w)	[39]
1390	CH_2 groups	[44]
1400	–C–F– stretching	[40]
1401	CH_2 (δ), CH_2 (w), and CC (ν_a)	[39]
1402	—CF groups	[44]
2924	CH_2 (ν_s)	[39]
2982	CH_2 (ν_s)	[39]
3025	CH_2 (ν_a)	[39]

In particular, Figure 2.5 a) shows the FTIR-ATR spectra for the sample prepared from 20 wt.% P(VdF-HFP) in the P(VdF-HFP)/DMF system for the different solvent evaporation temperatures and Figure 2.5 b) shows the spectra for the samples obtained at 100 ℃ solvent evaporation temperature for different initial polymer contents.

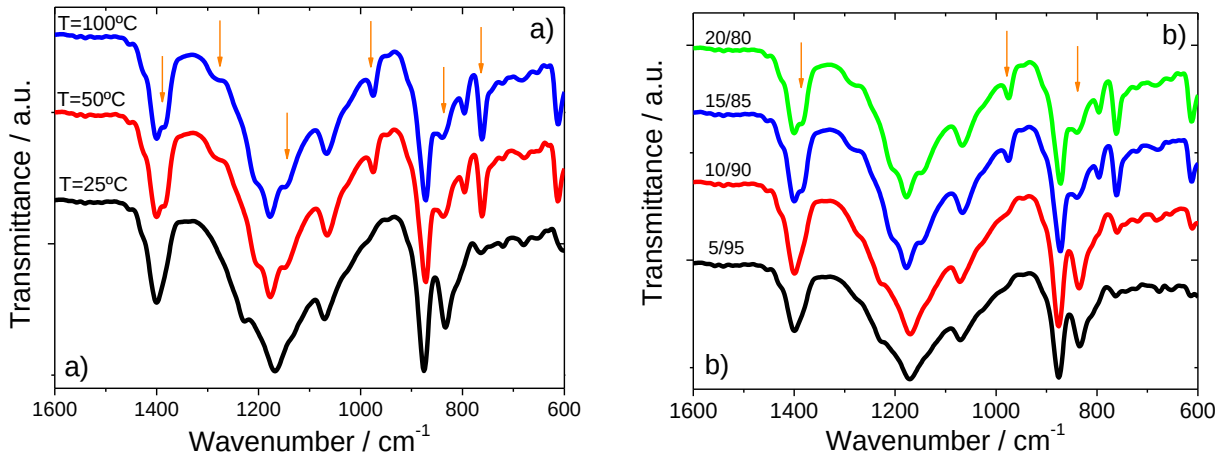

Figure 2.5. FTIR-ATR spectra for a) samples prepared from 20 wt.% P(VdF-HFP) initial polymer concentration with solvent evaporated at different temperatures and b) samples prepared after solvent evaporation at T =100 ℃ for different initial polymer concentration in the P(VdF-HFP)/DMF system.

Most relevant bands (Table 2.1) are clearly identified in all the spectra, indicating with no significant variations in the polymer structure. The arrows in Figure 2.5 represent the vibrational bands at 760, 974, 1148, 1295 and 1384 cm^{-1} which show higher variation depending on samples preparation procedure. The peaks at 760, 974 and 1384 cm^{-1} correspond to α-phase crystals, which increase with increasing solvent evaporation temperature [20]. The vibrations bands at 1148 and 1295 cm^{-1} are assigned to symmetrical stretching mode of CF_2, $CF_2(\nu_a)$ and $CF_2(r)$, respectively. Further, the vibration band at 838 cm^{-1} is characteristic of the β-phase. At a given polymer concentration (Figure 2.5 a)), the vibration bands at 1148 and 1295 cm^{-1} increase with increasing solvent evaporation temperature and polymer/solvent ratio (Figure 2.5 b)).

The specific bands at bands at 760 cm^{-1} and 838 cm^{-1} allow the quantification of the α and

β-phase content following the procedure presented in [20]. The phase content was calculated from the FTIR spectra by applying the following equation:

$$F(\beta) = \frac{X_\beta}{X_\alpha + X_\beta} = \frac{A_\beta}{(K_\beta/K_\alpha)A_\alpha + A_\beta} \qquad (2.4)$$

where $F(\beta)$ represents the β-phase content, A_α and A_β the absorbencies at 760 and 838 cm^{-1}, corresponding to the α and β-phase material, K_α and K_β are the absorption coefficient at the respective wave number and X_α and X_β the degree of crystallinity of each phase. The value of K_α is 6.1×10^4 and K_β is 7.7×10^4 $cm^2.mol^{-1}$ [20].

Table 2.2. β-phase content of the P(VdF-HFP) membranes as a function of the preparation conditions.

Samples	**β-phase / % ± 2 %**
5/95, T =100 ℃	75
10/90, T =100 ℃	66
15/85, T =100 ℃	22
20/80, T =100 ℃	16
20/80, T =50 ℃	24
20/80, T =25 ℃	79

It is observed that the electroactive β-phase content decreases with increasing solvent evaporation temperature for a given initial polymer concentration and also decreases with increasing polymer fraction in the initial P(VdF-HFP)/DMF solution The evaporation rate is essential and affects the crystalline phase of PVdF and copolymers [20]. For low evaporation temperatures, crystallization rate is slow due to lower polymer chain mobility, which leads to nucleation of the electroactive β-phase [20] due to strong polar interactions. For higher evaporation temperature, above 50 ℃, the evaporation rate is high, leading to crystallization of the material in the α-phase (Table 2.2). Regarding membranes evaporated at 100 ℃ with different polymer concentration, it is observed a decrease in the β-phase content with increasing polymer content in the initial solution (Table 2.2). This depends on the sample thickness (Figure 2.1) and is explained by the solvent diffusion. Chinaglia et al. [45] concluded that the polymer concentration affects the diffusivity of the solvent in the dispersed phase at high temperatures, and the evaporation rate grows faster than the solvent diffusivity through the polymeric solution, as observed in our work.

Figure 2.6 shows the DSC heating scans behaviour for the samples prepared from 20 wt.% P(VdF-HFP) initial concentration for the different solvent evaporation as well as for the samples prepared after solvent evaporation at 100 ℃ with different initial polymer concentrations.

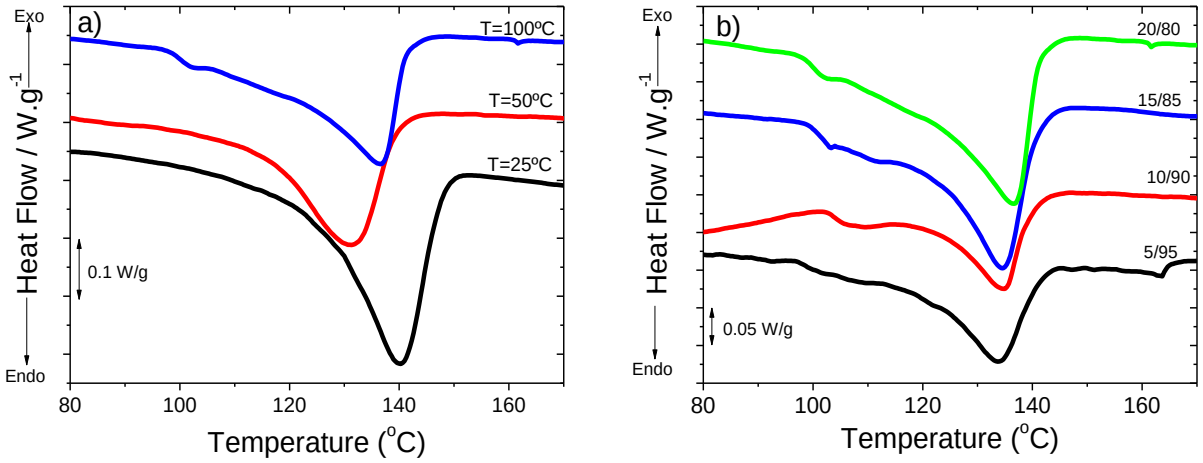

Figure 2.6. DSC scans a) for samples prepared with 20 wt.% initial polymer concentration evaporated at different temperatures and b) for samples prepared after solvent evaporation at T =100 ℃ for different initial polymer concentration content in the P(VdF-HFP)/DMF system.

Independently on solvent evaporation temperature and initial polymer concentration, the melting behaviour is similar and characterized by a broad melting peak in the range 120 to 145 ℃. The large melting peaks observed in Figure 2.6 are due to the melting of the crystalline phase of the polymer. The differences observed in the shape of the peaks are attributed to the existence of more defective crystals and/or the different crystalline phase present in the P(VdF-HFP) polymer. The characteristic features of the materials obtained from the DSC scans of Figure 2.6, melting temperature (T_m) and degree of crystallinity (χ) calculated after (2.3), are summarized in Table 2.3. The melting temperature is similar, within experimental error, for all samples except for the sample evaporated at room temperature (Figure 2.6 a)), and also in line with the values reported in the literature for samples prepared with 12 wt.% of HFP [46]. Thus, it is concluded that solvent evaporation temperature and initial polymer content in the solutions does not influence the melting temperature of the samples, leading to similar crystalline characteristics [45].

Table 2.3. Melting temperature and degree of crystallinity of the membranes as a function of the preparation conditions.

Samples	T_f / ℃ ± 1℃	χ / % ± 2%
5/95, T =100 ℃	134	18
10/90, T =100 ℃	135	14
15/85, T =100 ℃	135	30
20/80, T =100 ℃	138	35
20/80, T =50 ℃	131	27
20/80, T =25 ℃	140	33

The degree of crystallinity, on the other hand, shows a stronger dependence on the processing conditions (Table 2.3): whereas the degree of crystallinity is nearly independent on the solvent evaporation temperature, it shows a strong dependence on the initial polymer content, with the degree of crystallinity increasing for increasing initial polymer concentration within the solution. Decreasing initial polymer concentration leads to weaker polymer interaction during polymer crystallization, due to the larger relative solvent content. This fact leads to an amorphization of a larger polymer concentration, therefore lower degree of crystallinity [47].

Non-porous membranes are used in applications such as sensors and actuators and therefore it is important the characterization of the dielectric and piezoelectric properties. The dielectric behaviour (complex permittivity) of the samples is shown in Figure 2.7.

For PVdF homopolymer and its copolymers, it was reported that dielectric properties were anisotropic with respect to different crystal orientations [48]. The dielectric behaviour (ε', $\tan\delta$ and σ') for the samples obtained after solvent evaporation at 50 ℃ is the same as for the samples obtained after evaporation at 100 ℃ thus, just the dielectric results for the P(VdF-HFP) membranes evaporated at 100 ℃ are shown.

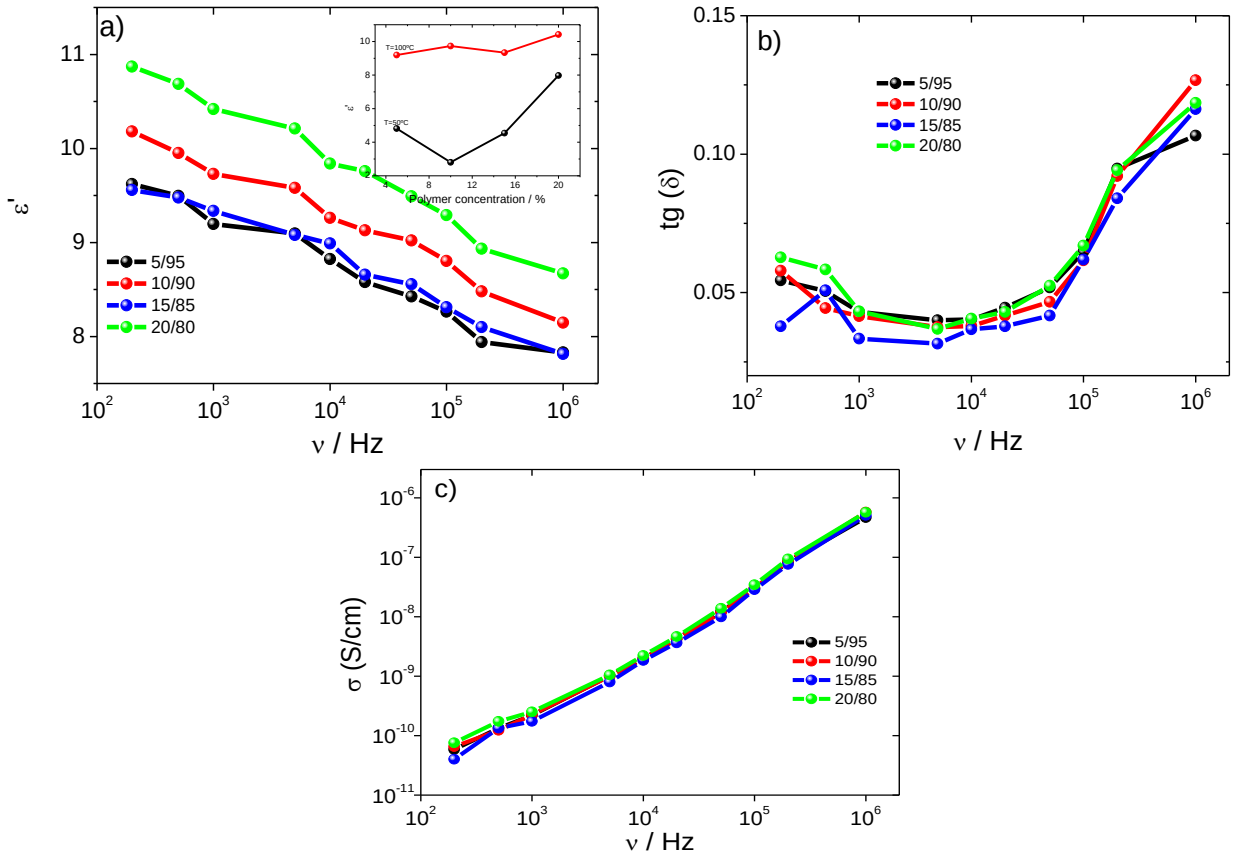

Figure 2.7. Electrical response for the samples obtained after solvent evaporation at T =100 ℃ with different polymer concentrations in the P(VdF-HFP)/DMF system: a) dielectric constant, b) tan δ and c) conductivity. Inset of a) variation of the dielectric constant as a function of polymer concentration at 1 kHz.

Figure 2.7 a) shows the variation of ε' for the samples with different polymer concentration evaporated at 100 ℃, as a function of frequency. All P(VdF-HFP) membranes show a similar behaviour of ε' as a function of frequency. The ε' decreases with increasing frequency due to slower dipole mobility. The differences observed in Figure 2.7 a) between membranes are correlated with the degree of crystallinity (Table 2.3) and thus with the initial polymer concentrations in the P(VdF-HFP)/DMF system. The values of the dielectric constant, shown in Figure 2.7 a) and Figure 2.7 d), are similar to the values of dielectric constant for PVdF homopolymer (α-phase, ε' = 7 and β-phase, ε'= 12) [49]. The value of ε' for P(VdF-HFP) polymer found in the literature varies between 9.9 and 15, depending on the experimental conditions [46]. Regarding tan δ (Figure 2.7 b)), it is observed that it increases with increasing frequency for all P(VdF-HFP) membranes, which can be attributed to the α_a relaxation process, i.e., micro-brownian movement of the amorphous phase chain segments or movement of crystalline-amorphous interphase chain segments [50]. The real part of the dielectric material conductivity can be calculated from the dielectric measurements presented in Figure 2.7 a) by:

$$\sigma'(\omega) = \varepsilon_0 \omega \varepsilon''(\omega) \qquad (2.5)$$

where ε_0 is the permittivity of free space, $\omega = 2\pi f$ is the angular frequency and $\varepsilon'(\omega) = \varepsilon' \tan \delta$ is the frequency dependent imaginary part of the dielectric permittivity [51]. The values for the P(VdF-HFP) membranes at different polymer concentrations as a function of frequency are presented in Figure 2.7 c). For all P(VdF-HFP) membranes, the conductivity increases with increasing of frequency in a similar way.

Figure 2.6 a) shows that the dielectric constant depends on the evaporation temperature, i.e., increases with the increasing temperature and depends on the crystalline phase present in the polymer (α and β-phase). At the same polymer concentration, 20 wt.%, dielectric constant increases with increasing of α-phase (T =50 ℃, α-phase= 76 % and T =100 ℃, α-phase= 84 %).

Poling of the material is a critical step in the optimization of the piezoelectric response of the samples in the electroactive phase [20, 52, 53], the final material response strongly depends on processing conditions and resulting crystal microstructure structures. In this way, the piezoelectric response, as evaluated by the d_{33} piezoelectric coefficient, was optimized as a function of poling temperature and concentration, as shown in Figure 2.8.

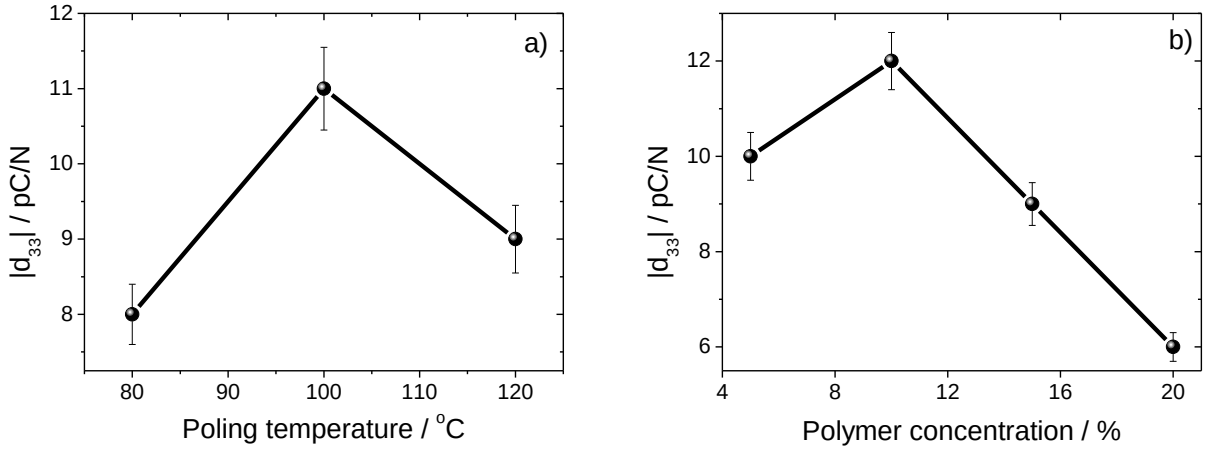

Figure 2.8. a) Modulus of the piezoelectric d_{33} coefficient for the membrane with 20 wt.% of P(VdF-HFP) initial concentration and solvent evaporation temperature of 50 ℃ as a function of poling temperature and b) modulus of the d_{33} piezoelectric coefficient for the solvent evaporation temperature of 100 ℃ and poling temperature of 100 ℃ as a function of polymer concentrations in the P(VdF-HFP)/DMF system.

In a general way, the piezoelectric coefficient increases with increasing poling temperature, as temperature increases the mobility of the molecular chains allowing a more effective orientation of the molecular dipoles though the interaction with the applied electric field [54]. The maximum poling temperature used in the work is below the melting temperature,

T_m ~131-140 ℃, in order to prevent sample degradation. Figure 2.8 a) shows the $|d_{33}|$ behaviour as a function of poling temperature for the membrane with 20 wt.% P(VdF-HFP) initial concentration and solvent evaporation temperature of 50 ℃. The observed behaviour is representative of the remaining samples studied in this work.

The piezoelectric coefficient is negative, and its modulus, $|d_{33}|$, increases with increasing poling temperature from ~8 up to ~11 pC/N ± 2pC/N, by poling at 80 ℃ and 100 ℃, respectively. For increasing poling temperature up to 120 ℃ the $|d_{33}|$ decreases to ~9 pC/N.

In this way, as temperature increases for a given poling field, the molecular chains mobility increases inducing a better alignment of the dipolar moments with the applied electric field and, therefore, an increase of the piezoelectric response [55]. Close to the melting temperature, this behaviour is hindered due to irreversible effects on the crystalline microstructure [56].

Figure 2.8 b) shows the behaviour of the $|d_{33}|$ coefficient as a function of polymer concentration in the P(VdF-HFP)/DMF system for solvent evaporation temperature of 100 ℃. The modulus of the piezoelectric d_{33} coefficient decreases with increasing polymer concentration in the P(VdF-HFP)/DMF system. This behaviour is mainly attributed to the different electroactive β-phase content within the P(VdF-HFP) polymer samples that affects the piezoelectric properties of the polymer: the larger the β-phase content the larger the piezoelectric response of the material [52]. The β-phase of the samples is responsible for the piezoelectric properties. According to Figure 2.8 b), the $|d_{33}|$ behaviour follows the same trend as the β-phase content in the P(VdF-HFP), that depends on the polymer concentration in the P(VdF-HFP)/DMF system.

The values of the d_{33} determined in this work are in accordance with the values observed in the literature, i.e., He et al. [57], $|d_{33}|$ / pC/N=5.4-12.6 for maximum field of 250 MV.m^{-1} at room temperature and Huan et al. [58], $|d_{33}|$ / pC/N=20-24 [58] at poling fields from 20 to 160 MV.m^{-1}.

2.4. Discussion

The isothermal evaporation process can be described by the Flory-Huggins theory [59]. The Gibbs free energy fluctuations for binary systems (polymer/solvent) are described by [60]:

$$\frac{\Delta G}{RT} = \frac{\phi'}{n}\ln\phi' + (1-\phi')\ln(1-\phi') + \chi_{12}\phi'(1-\phi') \qquad (2.6)$$

where n is the degree of polymerization, ϕ' is the polymer volume fraction and χ_{12} is the Flory-

Huggins parameter for a binary mixture. The Flory-Huggins parameter χ_{12} in order to temperature is determined by:

$$\chi_{12} = \frac{v_0}{RT}\delta^2 \qquad (2.7)$$

where R is the gas constant, v_0 is the molar volume of the solvent, T is the temperature, and δ is the Hansen solubility parameter. Through the Flory-Huggins theory (2.6), the phase diagram for the P(VdF-HFP)/DMF system was constructed using $v_0 = 77.4$ cm^3.mol^{-1} (DMF volume molar), N=3.5 (Solvay datasheet) and the solubility parameters ($\delta_{PVDF-HFP} = 17.2$ MPa$^{1/2}$, $\delta_{DMF} = 24.7$ MPa$^{1/2}$) [61, 62].

In Figure 2.9, it is represented the phase diagram for the P(VdF-HFP)/DMF system.

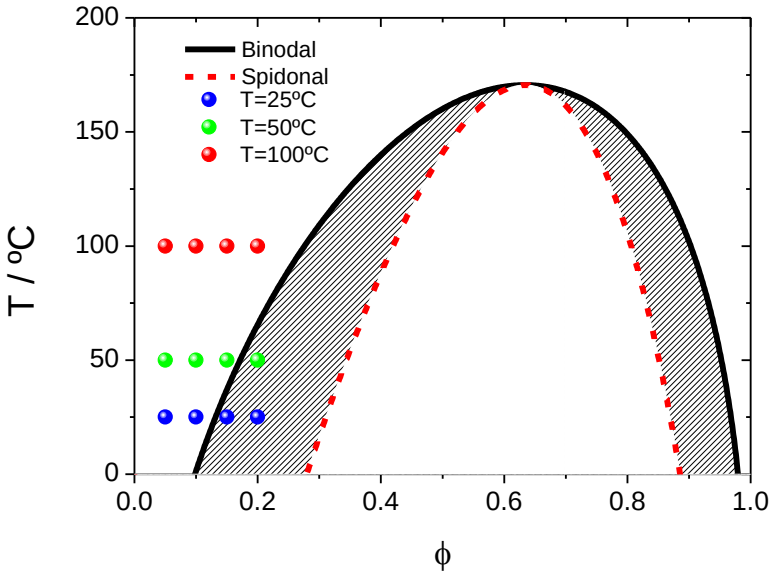

Figure 2.9. Phase diagram for the P(VdF-HFP)/DMF system.

Figure 2.9 shows the regions of stability, metastability and instability of the polymer solution. These regions are separated by the binodal and the spinodal lines, and the phase separation of the P(VdF-HFP)/DMF system can be controlled through the initial polymer concentration and the solvent evaporation temperature. The metastable region between the spinodal and binodal lines is referred as the nucleation and growth region. The phase separation occurs either by spinodal decomposition or by nucleation and growth region (metastable region). The initial position of the P(VdF-HFP)/DMF solution in the phase diagram for the preparation of the membranes is represented by the circles.

The morphology, β-phase content and thermal properties of P(VdF-HFP) samples depend on the initial polymer concentration and solvent evaporation temperature, as shown in Figure 2.2, Figure 2.5 and Figure 2.6. The microstructural variations of the P(VdF-HFP) membranes shown in Figure 2.2 are due to the phase separation during the crystallization process, as demonstrated in

the phase diagram (Figure 2.9).

By solvent evaporation at room temperature, the membranes exhibit a degree of porosity that depends on the polymer concentration, as illustrated in Figure 2.3. Regardless the experimental conditions (P(VdF-HFP) concentration, 5 – 20 wt.% and evaporation solvent temperature, $T = 25$ ℃, $T = 50$ ℃ and $T = 100$ ℃), the membranes show β-phase contents above 79 % (Figure 2.5 and Table 2.2). The degree of crystallinity determined by DSC scans (Figure 2.6) ranges between 11% and 35%, depending on the polymer concentration and solvent evaporation temperature, which may be due to the deferral of liquid-liquid demixing process. The dielectric and piezoelectric properties are correlated with the degree of crystallinity and β-phase content. The variations of the aforementioned properties as explained by the initial position of the solution the P(VdF-HFP)/DMF phase diagram (Figure 2.9).

At room temperature, for the different polymer/solvent ratios, the microstructure formation is governed by a competition between the phase separation dynamics and the evaporation of the solvent. However, when polymer concentration is increased in the P(VdF-HFP)/DMF systems, the system transits from the unstable (5 wt.% of P(VdF-HFP)) to metastable region (20 wt.% of P(VdF-HFP)) in which the process is dominated by nucleation and growth. For this fact, the P(VdF-HFP) membranes present microstructure with different degree of porosity (Figure 2.2 and Figure 2.3).

For a given polymer/solvent ratio (20/80), at different solvent temperatures (20 ℃ and 100 ℃), the system passes from the metastable region to the one-phase region (homogeneous microstructure) and no porous microstructure is observed (Figure 2.2). This fact is also observed for other polymer/solvent ratios, when the solvent evaporation temperature increases. At a given evaporation temperature ($T = 100$ ℃), the piezoelectric coefficient depends on the polymer concentration and is related to β-phase content and degree of crystallinity [52]. The $|d_{33}|$ coefficient decreases with the decreasing of the β-phase content and shows lower variation with the degree of crystallinity of the samples.

2.5. Conclusions

P(VdF-HFP) membranes were prepared by TIPS from DMF solutions varying initial polymer concentration and solvent evaporation temperature and were obtained with a wide range of different morphologies and degree of porosity. Experimental results are correlated with the initial position of the solution in the phase diagram for the binary system described by the Flory-Huggins theory. After solvent evaporation at room temperature the samples show a porous

microstructure with varying degree of porosity, attributed to the spinodal decomposition of the liquid-liquid phase separation. These P(VdF-HFP) membranes present different β-phase content and degree of crystallinity that can be controlled through the polymer concentration and evaporation solvent temperature. These variations depend on the positions of the membranes in the phase diagram determined by P(VdF-HFP)/DMF system. Both degree of crystallinity and β-phase content also determine the piezoelectric response of the P(VdF-HFP) membranes, leading to suitable samples for applications in battery separator, membranes, sensors and actuators.

The membrane solutions prepared with different P(VdF-HFP) contents show different viscosities. Once the range of the viscosities of the printing technologies is large, the solutions are suitable for inks and can be used in printing technology. The rheology requirements and properties of these solutions are simpler than for electrode slurries (with polymer, carbon black and active material particles). The choice of the viscosity will depend on the printing technique and this must be adjusted and optimized depending on the printing technique.

2.6. References

[1] F. Liu, N.A. Hashim, Y. Liu, M.R.M. Abed, K. Li, *Progress in the production and modification of PVdF membranes*, Journal of Membrane Science, 2011, 375: p. 1-27.

[2] P. Van De Witte, P.J. Dijkstra, J.W.A. Van Den Berg, J. Feijen, *Phase separation processes in polymer solutions in relation to membrane formation*, Journal of Membrane Science, 1996, 117: p. 1-31.

[3] A.P. Echavarría, C. Torras, J. Pagán, A. Ibarz, *Fruit Juice Processing and Membrane Technology Application*, Food Engineering Reviews, 2011, 3: p.136-158.

[4] H.S. Thiam, W.R.W. Daud, S.K. Kamarudin, A.B. Mohammad, A.A.H. Kadhum, K.S. Loh, E.H. Majlan, *Overview on nanostructured membrane in fuel cell applications*, International Journal of Hydrogen Energy, 2011, 36: p. 3187-3205.

[5] R. Miao, B. Liu, Z. Zhu, Y. Liu, J. Li, X. Wang, Q. Li, *P(VdF-HFP)-based porous polymer electrolyte membranes for lithium-ion batteries*, Journal of Power Sources, 2008, 184: p. 420-426.

[6] C. Feng, K.C. Khulbe, T. Matsuura, S. Tabe, A.F. Ismail, *Preparation and characterization of electro-spun nanofiber membranes and their possible applications in water treatment*, Separation and Purification Technology, 2013, 102: p. 118-135.

[7] G.R. Guillen, Y. Pan, M. Li, E.M.V. Hoek, *Preparation and Characterization of Membranes Formed by Nonsolvent Induced Phase Separation*: *A Review*, Industrial & Engineering Chemistry Research, 2011, 50: p. 3798-3817.

[8] M. Mulder, *Basic Principles of Membrane Technology*, Springer, 1996.

[9] D. Li, W.B. Krantz, A.R. Greenberg, R.L. Sani, *Membrane formation via thermally induced phase separation (TIPS): Model development and validation*, Journal of Membrane Science, 2006, 279: p. 50-60.

[10] N. Ghasem, M. Al-Marzouqi, N. Abdul Rahim, *Modeling of CO_2 absorption in a membrane contactor considering solvent evaporation*, Separation and Purification Technology, 2013, 110: p. 1-10.

[11] A. Venault, Y. Chang, D.-M. Wang, D. Bouyer, A. Higuchi, J.-Y. Lai, *PEGylation of anti-biofouling polysulfone membranes via liquid- and vapor-induced phase separation processing*, Journal of Membrane Science, 2012, 403–404: p. 47-57.

[12] S.K. Yong, J.K. Hyo, Y.K. Un, *Asymmetric membrane formation via immersion precipitation method. I. Kinetic effect*, Journal of Membrane Science, 1987, 60: p. 219-232.

[13] L. Zeman, T. Fraser, *Formation of air-cast cellulose acetate membranes. Part I. Study of macrovoid formation*, Journal of Membrane Science, 1993, 84: p. 93-106.

[14] M. Liu, Y.M. Wei, Z.L. Xu, R.Q. Guo, L.B. Zhao, *Preparation and characterization of polyethersulfone microporous membrane via thermally induced phase separation with low critical solution temperature system*, Journal of Membrane Science, 2013, 437: p. 169-178.

[15] Y.H. Tang, Y.D. He, X.L. Wang, *Three-dimensional analysis of membrane formation via thermally induced phase separation by dissipative particle dynamics simulation*, Journal of Membrane Science, 2013, 437: p. 40-48.

[16] Y. Zhao, Q. Lu, D. Chen, Y. Wei, *Superhydrophobic modification of polyimide films based on gold-coated porous silver nanostructures and self-assembled monolayers*, Journal of Materials Chemistry, 2006, 16: p. 4504-4509.

[17] Y. Zhou, Z. Wang, Q. Zhang, X. Xi, J. Zhang, W. Yang, *Equilibrium and thermodynamic studies on adsorption of BSA using PVdF microfiltration membrane*, Desalination, 2012, 307: p. 61-67.

[18] A. Gugliuzza, E. Drioli, *PVdF and HYFLON AD membranes: Ideal interfaces for contactor applications*, Journal of Membrane Science, 2007, 300: p. 51-62.

[19] E. Drioli, A. Ali, S. Simone, F. Macedonio, S.A. Al-Jlil, F.S. Al Shabonah, H.S. Al-Romaih, O. Al-Harbi, A. Figoli, A. Criscuoli, *Novel PVdF hollow fiber membranes for vacuum and direct contact membrane distillation applications*, Separation and Purification Technology, 2013, 115: p. 27-38.

[20] P. Martins, A.C. Lopes, S. Lanceros-Mendez, *Electroactive phases of poly(vinylidene fluoride): Determination, processing and applications*, Progress in Polymer Science, 2014, 39: p 683-706.

[21] Y. Ding, P. Zhang, Z. Long, Y. Jiang, F. Xu, W. Di, *The ionic conductivity and mechanical property of electrospun P(VdF-HFP)/PMMA membranes for lithium-ion batteries*, Journal of Membrane Science, 2009, 329: p 56-59.

[22] J.-H. Cao, B.-K. Zhu, Y.-Y. Xu, *Structure and ionic conductivity of porous polymer electrolytes based on P(VdF-HFP) copolymer membranes*, Journal of Membrane Science, 2006, 281: p. 446-453.

[23] W. Pu, X. He, L. Wang, C. Jiang, C. Wan, *Preparation of PVdF–HFP microporous membrane for Li-ion batteries by phase inversion*, Journal of Membrane Science, 2006, 272: p. 11-14.

[24] M.C. García-Payo, M. Essalhi, M. Khayet, *Effects of P(VdF-HFP) concentration on membrane distillation performance and structural morphology of hollow fiber membranes*, Journal of Membrane Science, 2010, 347: p. 209-219.

[25] M. Akkoyun, C. Carrot, B. Blottière, *Ternary Diagrams of Poly(vinylidene fluoride) and Poly[(vinylidene fluoride)-co-hexafluoropropene] in Propylene Carbonate and Dimethyl Sulfoxide*, Macromolecular Chemistry and Physics, 2012, 213: p. 587-593.

[26] K. Smolders, A.C.M. Franken, *Terminology for Membrane Distillation, Desalination*, 1989, 72: p. 249-262.

[27] S. Lanceros-Méndez, J.F. Mano, A.M. Costa, V.H. Schmidt, *FTIR and DSC studies o mechanically deformed β-PVdF films*, Journal of Macromolecular Science, Part B, 2001, 40: p. 517-527.

[28] D.C. Bassett, *Developments in Crystalline Polymers*, Applied Science Publishers, 1982.

[29] T.R. Dargaville, M. Celina, P.M. Chaplya, *Evaluation of piezoelectric poly(vinylidene fluoride) polymers for use in space environments. I. Temperature limitations*, Journal of Polymer Science Part B: Polymer Physics, 2005, 43: p. 1310-1320.

[30] D.-J. Lin, C.-L. Chang, F.-M. Huang, L.-P. Cheng, *Effect of salt additive on the formation of microporous poly(vinylidene fluoride) membranes by phase inversion from LiClO4/Water/DMF/PVdF system*, Polymer, 2003, 44: p. 413-422.

[31] V. Sencadas, C.M. Costa, J.L. Gómez Ribelles, S. Lanceros-Mendez, *Isothermal crystallization kinetics of poly(vinylidene fluoride) in the α-phase in the scope of the Avrami equation*, J Mater Sci, 2010, 45, p. 1328-1335.

[32] M.J. Koh, H.Y. Hwang, D.J. Kim, H.J. Kim, Y.T. Hong, S.Y. Nam, *Preparation and Characterization of Porous P(VdF-HFP)/clay Nanocomposite Membranes*, Journal of Materials Science & Technology, 2010, 26: p. 633-638.

[33] X. Wang, L. Zhang, D. Sun, Q. An, H. Chen, *Formation mechanism and crystallization of poly(vinylidene fluoride) membrane via immersion precipitation method*, Desalination, 2009, 236, p. 170-178.

[34] R. Magalhães, N. Durães, M. Silva, J. Silva, V. Sencadas, G. Botelho, J.L. Gómez Ribelles, S. Lanceros-Méndez, *The Role of Solvent Evaporation in the Microstructure of Electroactive β-Poly(Vinylidene Fluoride) Membranes Obtained by Isothermal Crystallization*, Soft Materials, 2010, 9: p. 1-14.

[35] P. Dietz, P.K. Hansma, O. Inacker, H.-D. Lehmann, K.-H. Herrmann, *Surface pore structures of micro- and ultrafiltration membranes imaged with the atomic force microscope*, Journal of Membrane Science, 1992, 65: p. 101-111.

[36] L.-P. Zhu, J.-Z. Yu, Y.-Y. Xu, Z.-Y. Xi, B.-K. Zhu, *Surface modification of PVdF porous membranes via poly(DOPA) coating and heparin immobilization*, Colloids and Surfaces B: Biointerfaces, 2009, 69: p. 152-155.

[37] P.M. Martins, S. Ribeiro, C. Ribeiro, V. Sencadas, A.C. Gomes, F.M. Gama, S. Lanceros-Mendez, *Effect of poling state and morphology of piezoelectric poly(vinylidene fluoride) membranes for skeletal muscle tissue engineering*, RSC Advances, 2013, 3(39): p. 17938-17944.

[38] D. Kumar, M. Suleman, S.A. Hashmi, *Studies on poly(vinylidene fluoride-co-hexafluoropropylene) based gel electrolyte nanocomposite for sodium–sulfur batteries*, Solid State Ionics, 2011, 202: p. 45-53.

[39] V. Aravindan, P. Vickraman, *Nanoparticulate AlO(OH)[sub n] filled polyvinylidenefluoride-co-hexafluoropropylene based microporous membranes for lithium ion batteries*, Journal of Renewable and Sustainable Energy, 2009, 1: p. 23108.

[40] S. Ramesh, S.-C. Lu, I. Vankelecom, *BMIMTF ionic liquid-assisted ionic dissociation of MgTf in P(VdF-HFP)-based solid polymer electrolytes*, Journal of Physics and Chemistry of Solids, 2013, 74: p 1380-1386.

[41] C.-H. Du, B.-K. Zhu, Y.-Y. Xu, *The effects of quenching on the phase structure of vinylidene fluoride segments in P(VdF-HFP) copolymer and P(VdF-HFP)/PMMA blends*, J Mater Sci, 2006, 41: p. 417-421.

[42] V. Aravindan, P. Vickraman, T.P. Kumar, *Polyvinylidene fluoride–hexafluoropropylene (PVdF–HFP)-based composite polymer electrolyte containing LiPF3(CF3CF2)3*, Journal of Non-Crystalline Solids, 2008, 354: p. 3451-3457.

[43] N. Ataollahi;, A. Ahmad, H. Hamzah;, M.Y.A. Rahman;, N.S. Mohamed, *Preparation and Characterization of P(VdF-HFP)/MG49 Based Polymer Blend Electrolyte*, Int. J. Electrochem. Sci., 2012, 7: p. 6693-6703

[44] M. Ulaganathan, R. Nithya, S. Rajendran, S. Raghu, *Li-ion conduction on nanofiller incorporated PVdF-co-HFP based composite polymer blend electrolytes for flexible battery applications*, Solid State Ionics, 2012, 218: p. 7-12.

[45] D.L. Chinaglia, R. Gregorio, J.C. Stefanello, R.A. Pisani Altafim, W. Wirges, F. Wang, R. Gerhard, *Influence of the solvent evaporation rate on the crystalline phases of solution-cast poly(vinylidene fluoride) films*, Journal of Applied Polymer Science, 2010, 116: p. 785-791.

[46] A.C. Jayasuriya, A. Schirokauer, J.I. Scheinbeim, *Crystal-structure dependence of electroactive properties in differently prepared poly(vinylidene fluoride/hexafluoropropylene) copolymer films*, Journal of Polymer Science Part B: Polymer Physics, 2001, 39: p. 2793-2799.

[47] M.G. Buonomenna, P. Macchi, M. Davoli, E. Drioli, *Poly(vinylidene fluoride) membranes by phase inversion: the role the casting and coagulation conditions play in their morphology, crystalline structure and properties*, European Polymer Journal, 2007, 43, p: 1557-1572.

[48] M.A. Marcus, *Orientation Effects on Dielectric and Piezoelectric Properties of Polyvinylidene Fluoride Films*, *Electrical Insulation*, IEEE Transactions on, 1986, EI-21: p. 519-523.

[49] V. Sencadas, S. Lanceros-Méndez, R. Sabater i Serra, A. Andrio Balado, J.L. Gómez Ribelles, *Relaxation dynamics of poly(vinylidene fluoride) studied by dynamical mechanical measurements and dielectric spectroscopy*, Eur. Phys. J. E, 2012, 35: p. 1-11.

[50] H. Arisawa, O. Yano, Y. Wada, *Dielectric loss of poly(vinylidene fluoride) at low temperatures and effect of poling on the low temperature loss*, Ferroelectrics, 1981, 32: p 39-41.

[51] F. Kremer, A. Schönhals, *Broadband Dielectric Spectroscopy*, Springer, 2003.

[52] J. Gomes, J.S. Nunes, V. Sencadas, S. Lanceros-Mendez, *Influence of the β-phase content and degree of crystallinity on the piezo- and ferroelectric properties of poly(vinylidene fluoride)*, Smart Materials and Structures, 2010, 19: p. 65010.

[53] V.F. Cardoso, G. Minas, C.M. Costa, C.J. Tavares, S. Lanceros-Mendez, *Micro and nanofilms of poly(vinylidene fluoride) with controlled thickness, morphology and electroactive crystalline phase for sensor and actuator applications*, Smart Materials and Structures, 2011, 20: p. 87002.

[54] M. Inoue, Y. Tada, K. Suganuma, H. Ishiguro, *Variations in polymeric structure of ferroelectric poly(vinylidene fluoride) films during annealing at various temperatures*, Journal of Applied Polymer Science, 2009, 111: p .2837-2843.

[55] V.F. Cardoso, C.M. Costa, G. Minas, S. Lanceros-Mendez, *Improving the optical and electroactive response of poly(vinylidene fluoride–trifluoroethylene) spin-coated films for sensor and actuator applications*, Smart Materials and Structures, 2012, 21: p. 85020.

[56] D. Damjanovic, M. Demartin, *Contribution of the irreversible displacement of domain walls to the piezoelectric effect in barium titanate and lead zirconate titanate ceramics*, Journal of Physics: Condensed Matter, 1997, 9: p. 4943.

[57] X. He, K. Yao, B.K. Gan, *Phase transition and properties of a ferroelectric poly(vinylidene fluoride-hexafluoropropylene) copolymer*, Journal of Applied Physics, 2005, 97(8): p. 84101.

[58] Y. Huan, Y. Liu, Y. Yang, *Simultaneous stretching and static electric field poling of poly(vinylidene fluoride-hexafluoropropylene) copolymer films*, Polymer Engineering & Science, 2007, 47: p. 1630-1633.

[59] J.S. Higgins, J.E.G. Lipson, R.P. White, *A simple approach to polymer mixture miscibility*, Philosophical Transactions of the Royal Society A: Mathematical, Physical and Engineering Sciences, 2010, 368: p. 1009-1025.

[60] M. Rubinstein, R.H. Colby, *Polymer Physics*, Oxford, 2003.

[61] A.F.M. Barton, *CRC Handbook of Solubility Parameters and Other Cohesion Parameters*, Second Edition, Taylor & Francis, New York 1991.

[62] X. Tian, X. Jiang, *Poly(vinylidene fluoride-co-hexafluoropropene) (P(VdF-HFP)) membranes for ethyl acetate removal from water*, Journal of Hazardous Materials, 2008, 153: p 128-135.

3. Influence of the degree of porosity of poly(vinylidene fluoride-co-hexafluoropropylene) separators in the performance of Li-ion batteries

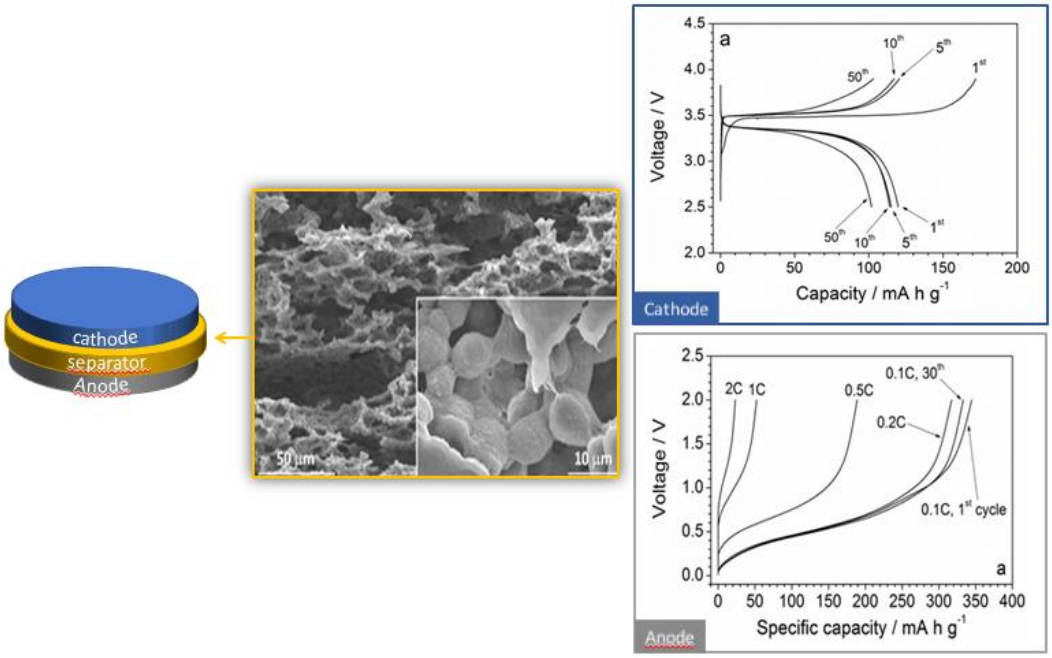

This chapter describes the preparation of poly(vinylidene fluoride-co-hexafluoropropylene), P(VdF-HFP), as separators for lithium batteries, using different polymer/solvent N,N-dimethylformamide (DMF) ratios, as well as their characterization, including physico-chemical and electrochemical characterization, as well as cycling tests, performed on Li/Sn-C and Li/$LiFePO_4$ half-cells with the developed P(VdF-HFP) polymer electrolyte separator membranes.

This chapter is based on the following publication: “Influence of the degree of porosity of poly(vinylidene fluoride-co-hexafluoropropylene) separators in the performance of Li-ion batteries”, R. E. Sousa, J. Nunes-Pereira, C. M. Costa, M. M. Silva, S. Lanceros-Méndez, J. Hassoun, B. Scrosati and G. B. Appetecchi, Journal of Power Sources, 263, 2014, 29 – 36.

3.1. Introduction

In the last decade, rapid developments in electronics miniaturization and novel portable electric devices technologies [1, 2] led to strongly increasing needs of safe and high density energy storage devices, focusing in particular on rechargeable lithium-ion batteries [1, 3]. Recently, lithium-ion battery systems have been expanding for other applications such as aerospace technologies, electric and hybrid vehicles [4].

Liquid electrolytes currently used in commercial lithium-ion batteries are based on organic solvents (mainly alkyl carbonates), which are volatile, flammable and easy to ignite on exposure to high temperatures [5]. Gel polymer electrolytes (GPEs), e.g., formed by a liquid solution trapped through a polymer host, are receiving considerable attention as lithium battery solid separators [6, 7] due to their simple processability, feasibility to suit various cell geometries, cost competitiveness and safety [3] in combination with ionic conduction comparable to the one of the most used liquid electrolytes, low density, mechanical flexibility and stability [6 – 8]. In the last years, various polymer hosts with different chemical structures have been investigated [1 – 8]. Among these, polyvinylidene fluoride (PVdF) and its copolymers have been chosen as potentially interesting hosts by virtue of their appealing properties [9], such as high solubility in dispersed media, low crystallinity degree, low glass transition temperature, high dielectric constant (able to assist ionization of lithium salts), possibility of tuning the separator porosity degree and pore size (through binary and ternary polymer/solvent systems), good contact at electrolyte/electrode interface and stability in cathodic environment [8].

Among PVdF based copolymers, the P(VdF-HFP) material has drawn great attention [1] as polymer host for lithium-ion battery GPEs. The incorporation of hexafluoropropylene (HFP) amorphous phases into vinylidene fluoride (VdF) blocks is able to modify the properties of the homopolymer, e.g., promoting the uptake of larger liquid electrolyte contents [9, 10] and enhancing the flexibility of the polymer chains (and thus enabling the assisted transport of the lithium cations [11]), whereas the crystalline VdF phase provides sufficient mechanical integrity for processing free-standing films [10]. The pore size and shape, the volume fraction and interconnectivity of the pores are key factors for determining the retention ability and, therefore, the ionic conductivity of GPEs [12].

Many techniques have been developed for the preparation of porous polymer electrolyte membranes such as preferential dissolution, immersion precipitation method, template-leaching technique, evaporation phase inversion, melt spinning and cold stretching, thermally induced

phase separation (TIPS) and liquid-liquid extraction process [13]. In order to explore the optimum condition for the pore generation, P(VdF-HFP) based polymer electrolytes were also prepared through different solvent/non-solvents combinations and immersion precipitation [13]. Polymer hosts with large pore size and high porosity can be obtained by adding additives, e.g., polyvinylpyrrolidone (PVP) or polyethyleneglycol (PEG) can be dissolved in the casting solution [12].

The objective of the present work is to establish a correlation among the microstructure (e.g., pore size and porosity degree) of the P(VdF-HFP) membranes, prepared through binary polymer/solvent DMF systems, and their properties for battery applications such as electrolyte solution uptake and ionic conductivity. P(VdF-HFP) films, obtained from polymer/solvent slurries having different weight compositions, were prepared and investigated. The performance of the polymer electrolyte membranes as a function of the porosity degree was evaluated in Li/$LiFePO_4$ and Li/Sn-C half-cells. The results are reported in the present chapter.

3.2. Experimental

3.2.1. Materials

P(VdF-HFP), Solef 21216 (Solvay, M_w = 600.000 Da, VdF/HFP mole ratio equal to 88/12) and lithium bis(trifluoromethanesulfonyl)imide, LiTFSI (Sigma-Aldrich) were dried under vacuum at 25 ℃ for 48 hours and 25 ℃ for 96 hours, respectively. DMF and propylene carbonate (PC) were purchased from Merck and used as received.

3.2.2. Membrane preparation

Appropriate amounts of P(VdF-HFP) were added to DMF to prepare solutions having polymer/solvent weight ratio equal to of 5/95, 10/90, 15/85 and 20/80, respectively. The solutions were prepared at room temperature by stirring the two components until complete polymer dissolution. The solutions were then cast on clean glass substrates and spread by blade coating (once this method produces results similar to the screen printing technique) to obtain membranes ranging from 30 to 75 μm. Finally, the full removal of the DMF solvent was allowed by drying in an oven at 25 ℃ for 24 hours.

3.2.3. Morphological characterization

The morphology of the polymer membranes was analyzed using the method described in section 2.2.3. Membrane porosity was determined through density measurements using a pycnometer according to (2.1), and the porosity (ϕ) was calculated according to (2.2), both defined in section 2.2.3.

The tortuosity (τ) of the electrolyte membrane conduction pathways (pores), e.g., the ratio between the thickness sample and the effective pore length, was determined by the relation:

$$\tau = \sqrt{\frac{\sigma_0 \phi}{\sigma_i}} \qquad (3.1)$$

where σ_0 is the conductivity of the liquid electrolyte and σ_i and ϕ represent the conductivity and the porosity of the membrane, respectively.

3.2.4. Liquid electrolyte uptake

The electrolyte uptake was determined by immersing the membranes in a solution of 1 M LiTFSI in PC, i.e., showing a conductivity (σ_0) equal to 6.5×10^{-3} S.cm^{-1} at 25 ℃, for 24 hours. The electrolyte content ($E_{content}$) was evaluated according to:

$$E_{content} = \frac{m - m_0}{m_0} \times 100 \qquad (3.2)$$

where m_0 is the mass of the dry membrane and m is the mass of the membrane upon loading with electrolyte solution.

3.2.5. Physicochemical characterization

Polymer phase in the membranes was investigated by Fourier Transformed Infrared (FTIR) spectroscopy and the thermal properties of the membranes were determined by differential scanning calorimetry (DSC), as described in section 2.2.3 and the crystallinity degree (χ_c) was calculated according to (2.3).

3.2.6. Transport properties

The ionic conductivity was evaluated by impedance spectroscopy, using an Autolab PGSTAT-12 (Eco Chemie) set-up, in a frequency range from 65 kHz through 500 mHz. The

samples were housed within symmetrical two gold blocking electrode cells located in a Buchi TO50 oven. The measurements were performed within an argon filled glove box in a temperature (controlled by a type K thermocouple) range from 20 ℃ to 120 ℃ by heating scans at 8 ℃.h^{-1}. The ionic conductivity (σ_i) was calculated according to the following equation:

$$\sigma_i = \frac{d}{R_b A} \qquad (3.3)$$

where R_b represents the electrolyte membrane bulk resistance, obtained by impedance spectroscopy, d is the thickness of the electrolyte sample and A is the electrochemical active area, respectively.

3.2.7. Lithium cell manufacturing and testing

The Sn-C anode active material, e.g., formed by tin nanoparticles uniformly dispersed in a micrometric carbon matrix with a Sn:C weight ratio equal to 3:7, was prepared as described in previous papers [15 – 18] with a tin content of about 35% corresponding to a theoretical capacity equal to 400 mA.h.g^{-1}. The $LiFePO_4$ cathode material, displaying a theoretical specific capacity of 170 mA.h.g^{-1}, is a commercial product (Model A1100, LFP-NCO product line) developed and manufactured by Advanced Lithium Electrochemistry (Aleees Taiwan) [17].

Composite electrodes were prepared by blending the active material (Sn-C or $LiFePO_4$), the electronic conductor (Super-P carbon, MMM) and the binder (PVdF, Solvay) in *N*-methyl-pyrrolidone. The so-obtained slurry was cast onto copper (Sn-C) or aluminum ($LiFePO_4$) foil, allowing the solvent removal. Coin electrodes, having a 10 mm diameter and thickness ranging from 40 µm to 50 µm, were punched from the tapes. Finally, the electrodes were dried under vacuum at 110 ℃ overnight and transferred in the glove box. The weight composition of electrodes resulted 80(active material):10(electronic conductor):10(binder) with an active material mass loading of 2.0 mg.cm^{-2} (anodes) and 4.0 mg.cm^{-2} (cathodes), corresponding to 0.8 mA.h.cm^{-2} (Sn-C anodes) and 0.68 mA.h.cm^{-2} ($LiFePO_4$ cathodes), respectively.

The Li/Sn-C and Li/$LiFePO_4$ half-cells were fabricated by housing in 2032 coin-type containers the sequence composed by a lithium disc anode (10 mm diameter), a swollen PVdF/HFP-based electrolyte membrane (14 mm) and a Sn-C (or $LiFePO_4$) electrode (10 mm). The cycling performance of the half-cells was evaluated using a multichannel Maccor 4000 battery tester at room temperature. The (galvanostatic) measurements were performed within the 0.01 – 2.0 V (anode half-cells) and 2.5 – 4.0 V (cathode half-cells) voltage range, respectively, at current rates from 0.1C (40 mA.g^{-1} and 17 mA.g^{-1} for the Sn–C and the $LiFePO_4$ electrode, respectively) through 2C (0.8 A.g^{-1} and 0.34 mA.g^{-1}).

3.3. Results and discussion

The procedure route described above allowed us to obtain homogenous P(VdF-HFP) separator membranes having good mechanical properties and thickness ranging from 80 to 120 μm. Membranes prepared from slurries having a P(VdF-HFP)/DMF weight ratio equal to 5/95 resulted in white coloured samples, whereas an increase of the polymer/solvent ratio up to 20/80 gives translucid appearance.

The membrane morphology strongly affects the performance of the battery as well as the assembly process. Figure 3.1 shows the cross-section SEM image of P(VdF-HFP) separator membranes obtained from slurries having different polymer/solvent weight ratios.

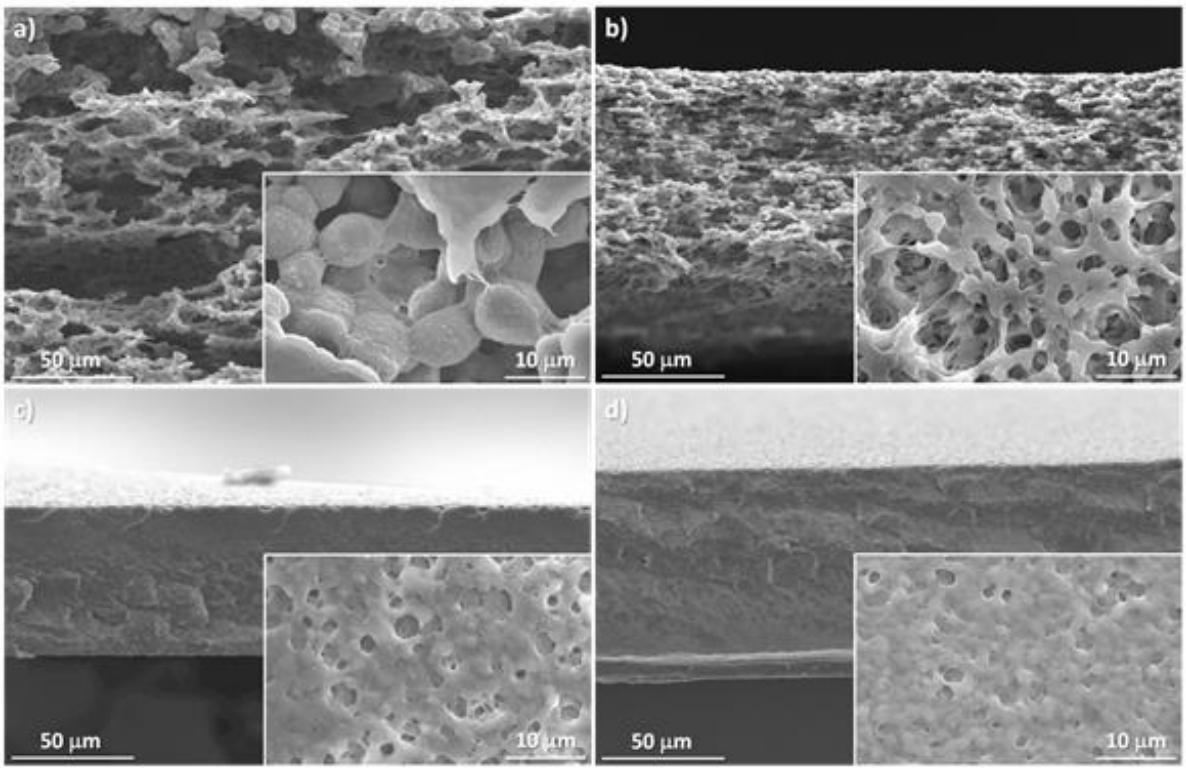

Figure 3.1. Cross-section SEM picture of P(VdF-HFP) separator membranes prepared from slurries having different polymer/solvent weight ratios: a) 5/95; b) 10/90; c) 15/85; d) 20/80.

The porosity of the P(VdF-HFP) membranes is the result of the polymer-solvent (DMF) interaction in the phase diagram of binary systems [19] and might be explained as a liquid-liquid phase separation and consequent crystallization of the copolymer rich phase [20]. The presence of open and homogeneously distributed porosity with interconnected pathways is well evidenced in the membranes, particularly in samples 5/95 (Figure 3.1 a)) and 10/90 (Figure 3.1 b)). A further increase of the polymer fraction within the slurry, prepared for obtaining the separator membranes, leads to a decrease in porosity content and pore size as shown in Figure 3.1 c)

(sample 15/85) and Figure 3.1 d) (sample 20/80). Therefore, optimal P(VdF-HFP) separator membranes can be obtained from polymer/DMF slurries with a solvent content equal or above to 90% in weight.

Figure 3.2 reports the porosity and electrolyte content trend of P(VdF-HFP) separator membranes obtained from slurries having different polymer/solvent weight ratios.

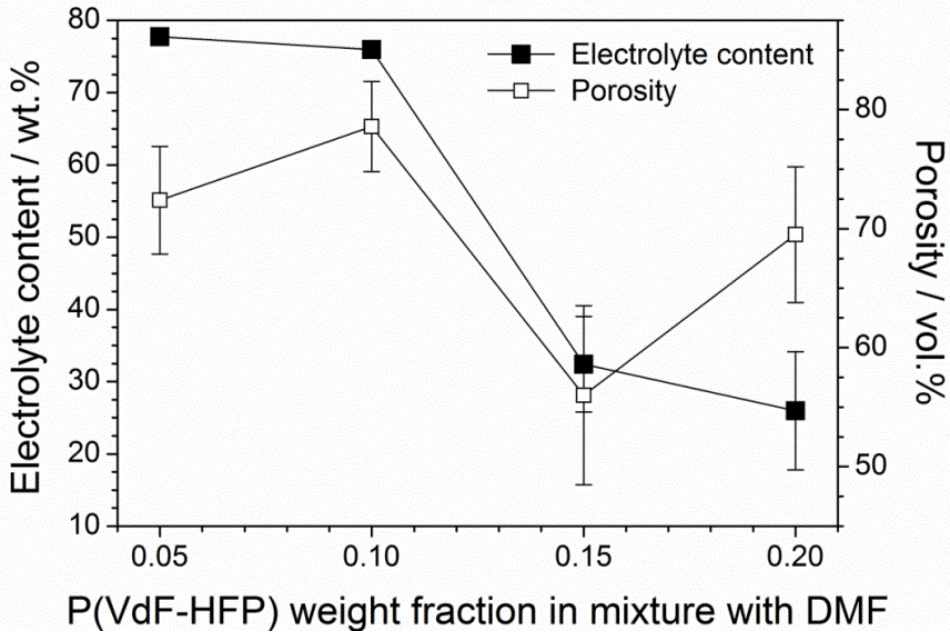

Figure 3.2. Liquid uptake and porosity of P(VdF-HFP) separator membranes prepared from slurries having different polymer/solvent weight ratios.

It is observed a generally decreasing liquid uptake (solid squares) with increasing polymer content in the starting slurry. The solution content (e.g., LiTFSI in PC) ranges from 76% to 77% (in weight) for polymer fractions equal or below 10% in weight, whereas further increase of the P(VdF-HFP) content leads to a sharp decrease of the liquid uptake down to 26% – 32%. However, this does not seem to be in good agreement with the trend exhibited by the porosity (open squares). For instance, a liquid uptake decreasing from 32% to 26% (in volume) is observed, by passing from a polymer weight fraction of 0.15 to 0.20, despite an increase in porosity from 56% to 70% in volume. This apparently contrasting behaviour is likely ascribable to the presence of blind (closed) pores (due to the higher polymer fraction in the P(VdF-HFP)/DMF preparation slurry), which are not filled by the liquid electrolyte and, therefore, do not take part in the uptake process.

The tortuosity (τ) value of these samples is reported in Table 3.1.

Table 3.1. Physico-chemical properties of P(VdF-HFP) electrolyte membranes obtained through polymer/solvent slurries having different weight compositions.

Electrolyte sample	Porosity / vol.%	Liquid uptake / wt.%	Tortuosity	Crystallinity degree / %	Conductivity (20 °C) / S.cm^{-1}
5/95	72 ± 5	77 ± 1	2	31	$(1.3 \pm 0.1) \times 10^{-3}$
10/90	79 ± 4	76 ± 1	6	29	$(1.4 \pm 0.1) \times 10^{-4}$
15/20	56 ± 7	32 ± 1	16	35	$(1.4 \pm 0.1) \times 10^{-5}$
20/80	70 ± 6	26 ± 1	11	32	$(3.8 \pm 0.1) \times 10^{-5}$

The tortuosity gives information about pore connectivity relating the mean actual path with sample thickness and is correlated with the conduction process through ionic conductivity [21]. High tortuosity values indicate longer ionically conductive pathways, resulting in lower ionic conductivity and enhancing diffusive phenomena through the polymer electrolyte. Otherwise, low tortuosity values highlight short conduction pathways, leading to faster ion transport properties and, consequently, to higher battery cycling performance and rate capability. The ideal τ value is equal to 1, corresponding to a perpendicular conduction pathway across the polymer electrolyte, which represents the optimal condition for assuring high conduction values. The results of Table 3.1 indicate a marked tortuosity increase with the polymer fraction in the starting slurry for obtaining the P(VdF-HFP) membrane, this resulting correlated with the porosity degree and pore connectivity. The sample 5/95 shows a τ value equal to 2, which raises up to 16 for the membrane 15/85.

The results obtained from FTIR analysis and thermal measurements performed on P(VdF-HFP) membranes are shown in Figure 3.3.

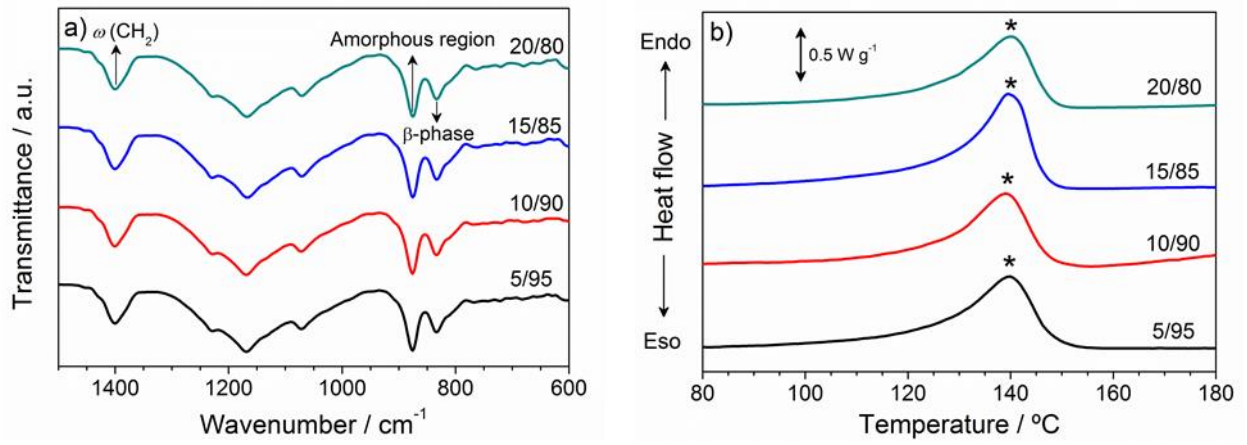

Figure 3.3. a) FTIR spectrum and b) DSC trace of P(VdF-HFP) separator membranes prepared from slurries having different polymer/solvent weight ratios.

The characteristic vibration modes (833 cm^{-1} and 1402 cm^{-1}) of the β-phase crystalline of the P(VdF-HFP) polymer do not change independently on the preparation conditions and porosity degree, indicating that the polymer crystallizes in the same phase [9, 22]. The amorphous phase of this copolymer is confirmed by the presence of a vibrational band at 874 cm^{-1} [23].

The DSC traces (Figure 3.3 b)) highlight an endothermic peak centered at about 140 ℃ corresponding to the melting of the P(VdF-HFP) copolymer. No relevant difference on the thermal properties was observed with the polymer fraction increase within the starting slurry. The degree of crystallinity (χ_c) for all samples is presented in

Table 3.1. This parameter ranges from 29% to 35%, being therefore independent on the polymer/solvent weight ratio within experimental error.

The transport properties were investigated in terms of ionic conductivity as a function of the temperature, determined by impedance spectroscopy measurements taken on symmetric two gold electrode cells (Au°/electrolyte membrane sample/Au°) at temperature intervals ranging from 20 ℃ to 120 ℃. The room temperature AC responses, represented in Figure 3.4 a) as Nyquist plots, show an inclined straight-line (typical of the blocking electrode capacitive behaviour) which intercepts with the real axes, Z', gives the PVdF based electrolyte membrane ionic resistance [24, 25].

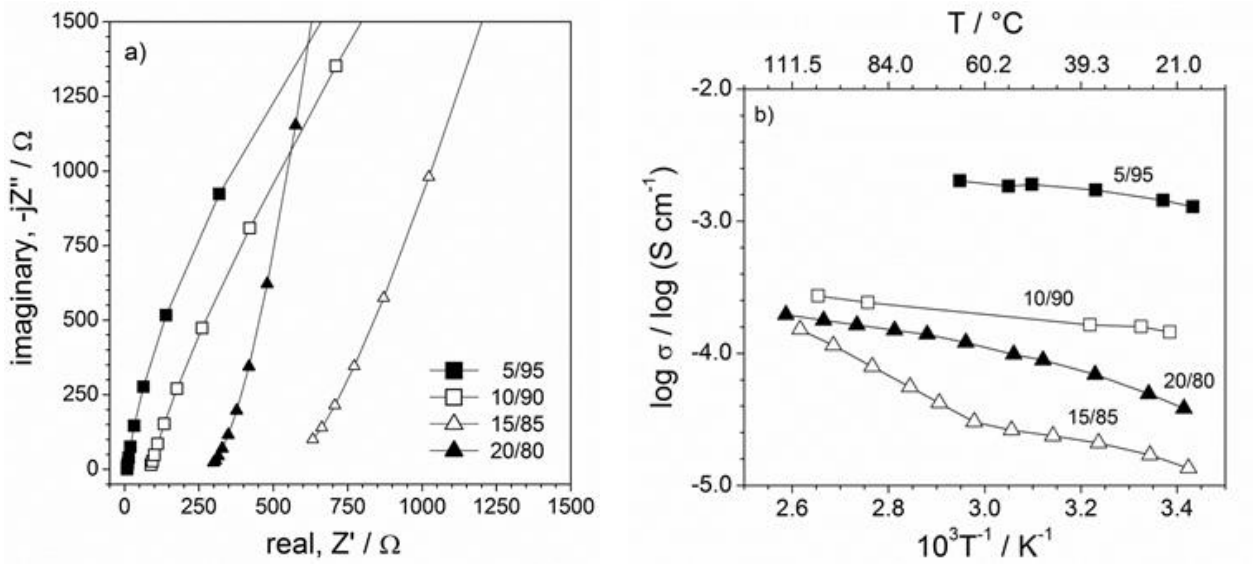

Figure 3.4. a) Room temperature AC response and b) conductivity Arrhenius plot of polymer electrolytes based on P(VdF-HFP) separator membranes prepared from slurries having different polymer/solvent weight ratios.

This value was obtained through analysis of the impedance responses, performed using a common approach, i.e., by defining an equivalent circuit taking into account all possible contributions to the impedance of the tested electrolyte membranes [24, 25]. The validity of the chosen circuit

was confirmed by fitting the impedance responses using a Non-Linear Least-Square (NLLSQ) fit software developed by Boukamp [26, 27]. Only fits characterized by a χ^2 factor [26, 27] lower than 10^{-4} were considered acceptable to assure the validity of the proposed model. The equivalent circuit, proposed to represent the electrochemical cell under study, is constituted by two elements connected in series, e.g., the electrolyte bulk resistance (R) and the double layer capacitance at electrolyte/electrode interface (Q_{dl}). A constant-phase element, CPE (Q), was used instead of pure capacitance (C).

The ionic conductivity vs. temperature dependence of the P(VdF-HFP) based electrolyte membranes is plotted in Figure 3.4 b), which denotes how conduction values above 10^{-3} S.cm^{-1} are exhibited at room temperature (below 20 °C) by the 5/95 sample (solid square). An increase of the P(VdF-HFP) fraction above 0.05 (5 wt.%) in the polymer/solvent slurry, prepared for obtaining the separator membranes, leads to a progressive decrease in ionic conduction. Above a polymer fraction equal to 0.10, the conduction values do not exceed 10^{-4} S.cm^{-1} even at medium-high temperatures. This issue is in good agreement with the results reported in Figure 3.2 and

Table **3.1**, which evidence a decay in porosity and liquid uptake and an increase in tortuosity of the ion conduction pathways with the increasing of the polymer/solvent weight ratio. For instance, the 5/95 polymer electrolyte sample displays the highest conductivity values. Surprisingly, the 20/80 sample exhibits higher conduction values with respect to the 15/85 electrolyte membrane. This behaviour may be ascribed to an optimal pore size and interconnection, thus allowing a better distribution of the liquid content. A moderate raise in conductivity is observed with increasing temperature, suggesting that the ion movement is activated by modest energy amounts, as generally expected in gel electrolytes [28 – 30].

Table 3.2 compares the physico-chemical properties of the polymer electrolyte developed in the frame of this work with those of similar P(VdF-HFP) electrolyte membranes containing different Li^+ conducting, organic solutions as reported in literature [31 – 34].

Table 3.2. Physico-chemical properties of P(VdF-HFP) membranes swollen in different lithium-ion conducting organic solutions. References are reported in the table.

Electrolyte solution	Porosity %	Ionic conductivity S.cm^{-1}	Reference
LiTFSI (1 M) e PC	72	1.3×10^{-3}	This work
$LiClO_4$ (1 M) - EC/PC (1/1 w/w)	83	1.5×10^{-3}	[31]
$LiPF_6$ (1 M) - EC/DMC (1/1 w/w)	78	3.4×10^{-4}	[8]
$LiBF_4$ (1 M) - EC/γBL (1/3 w/w)	n.a	3.4×10^{-3}	[32]
$LiPF_6$ (1 M) - EC/DEC (1/1 w/w)	70-90	1.2×10^{-3}	[33]

The different values of the porosity degree depend on the processing techniques, whereas the ionic conductivity value is affected by the liquid solution used in the polymer electrolytes. It is to note that the P(VdF-HFP) electrolyte system developed in the present work exhibits comparable ion conduction value despite a lower porosity degree. This suggests a better pore distribution through the P(VdF-HFP) host ascribable to a good optimization of the solvent/polymer ratio.

The electrochemical performance of the P(VdF-HFP) based polymer electrolyte membranes was evaluated in Li/Sn-C and Li/$LiFePO_4$ half-cells. The sample 5/95, showing the best liquid uptake (Figure 3.2) and ion-transport properties (Figure 3.4), was selected as the preferred ionically conducting separator.

Figure 3.5 shows selected voltage vs. capacity profiles obtained upon prolonged cycling tests run on a Li/Sn-C half-cell.

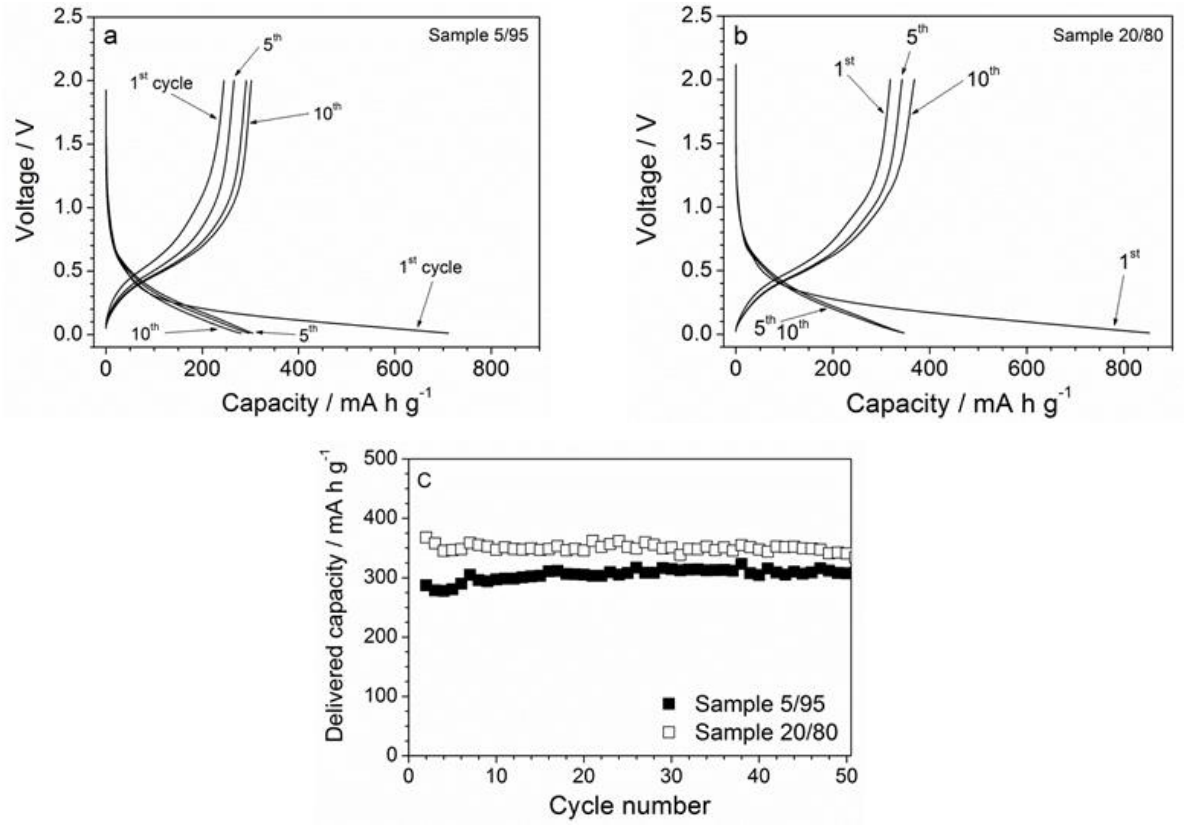

Figure 3.5. a) and b) Selected voltage vs. capacity profiles and c) cycling performance of a Li/Sn-C anode half-cell using the polymer electrolyte separator membrane 5/95. Current rate: 0.2C. Room temperature.

The typical voltage signature of the Sn–C material was displayed, characterized by an initial irreversible capacity, e.g., associated with the electrode structural reorganization, solid electrolyte interface (SEI) film formation [35] and eventual impurities decomposition (reduction),

followed by reversible cycles (i.e., lithium-Sn alloying-dealloying [15, 17, 36]), with average voltage value about 0.6 V vs. Li/Li^+. A capacity of about 300 $mA.h.g^{-1}$ was delivered, corresponding to 75% of the theoretical value and approaching the performance observed in liquid electrolytes [15]. Apart the first cycle, the discharge/charge efficiency quickly levels around 100%, highlighting a highly reversible alloying-dealloying process. Prolonged cycling tests (Figure 3.5 c)), performed at medium charge/discharge current rate (C/5) and deep of discharge (DoD) equal to 100%, indicate a good capacity retention.

The applicability of the P(VdF-HFP) polymer electrolytes was further studied in lithium cells using $LiFePO_4$ as the working electrode. Figure 3.6 shows selected voltage vs. capacity profiles obtained upon prolonged cycling tests, run at C/5 and 100% of DoD, on a $Li/LiFePO_4$ cathode half-cell.

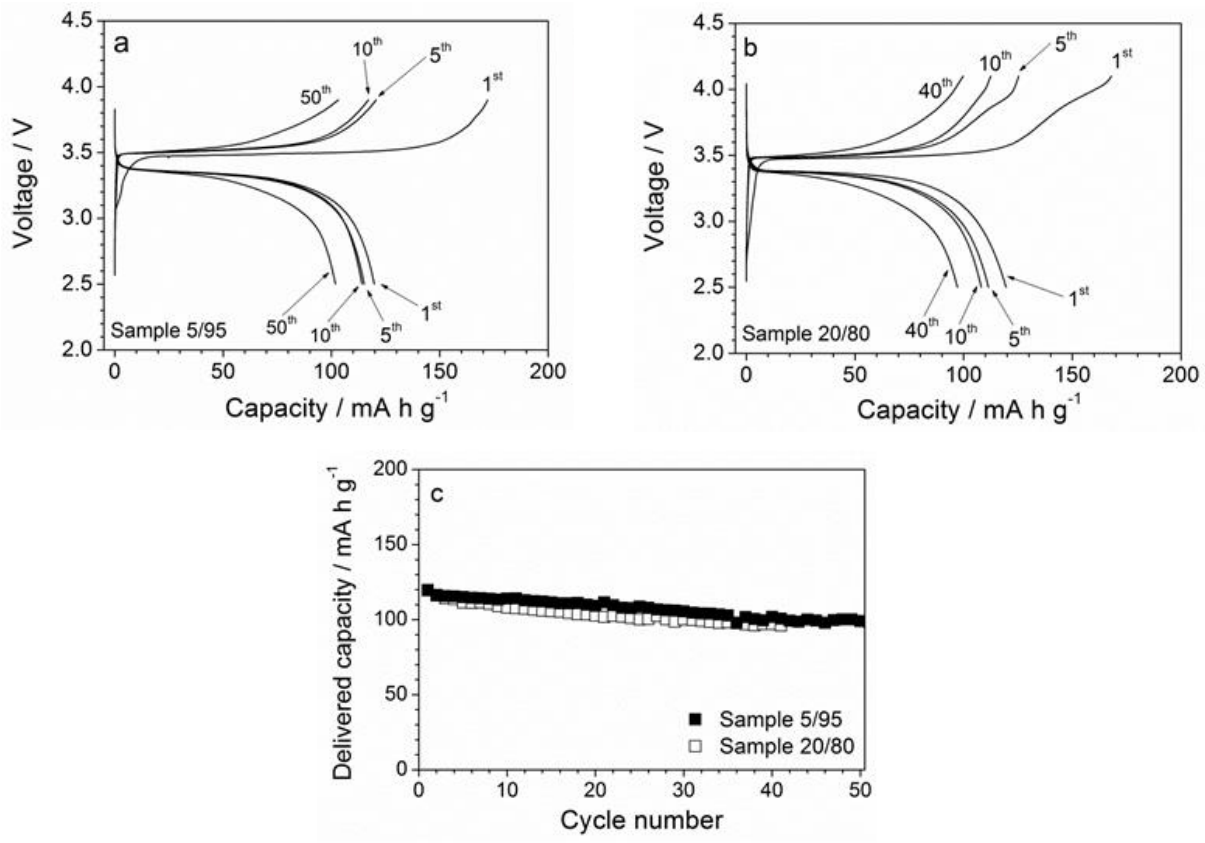

Figure 3.6. a) and b) Selected voltage vs. capacity profiles and c) cycling performance of a $Li/LiFePO_4$ cathode half-cell using the polymer electrolyte separator membrane 5/95. Current rate: 0.2C. Room temperature.

The voltage profile feature reflects the reversible charge (lithium removal)-discharge (lithium uptake) cycling behaviour of $LiFePO_4$, characterized by a flat plateau evolving at around 3.5 V vs. Li/Li^+, with first charge capacity extending up to 180 $mA.h.g^{-1}$ and reversible capacity during the following cycles in the order of 120 $mA.h.g^{-1}$ (e.g., 71% of the theoretical

value). The irreversible capacity observed during the first charge half-cycle is most likely due to SEI film formation [35] and oxidation of eventual impurities in the electrolyte membrane. The discharge/charge efficiency, apart the initial irreversible capacity, levels at 100% starting from the second cycle for both cathode half-cells. Figure 3.6 b) plots the cycling performance obtained at a current rate of C/5. The results show a modest capacity fading during cycling tests. For cathodic half-cells, the delivery capacity at 0.1C is 122.1 mA.h.g^{-1} (71% of the theoretical value), approaching the one observed in $LiPF_6$-EC-DMC liquid electrolyte supported by glass fiber separators (155 mA.h.g^{-1} at 0.1C) [17, 18, 37].

The half-cells (anodic and cathodic) based on the P(VdF-HFP) 5/95 separator membrane have been selected for further investigation in terms of the rate capability. Figure 3.7 reports the voltage vs. capacity profiles (a) and c)) and the capacity evolution (b) and d)), obtained at different current rates (from 0.1C through 2C), for Li/Sn–C (a) and b)) and Li/$LiFePO_4$ (c) and d)) half-cells.

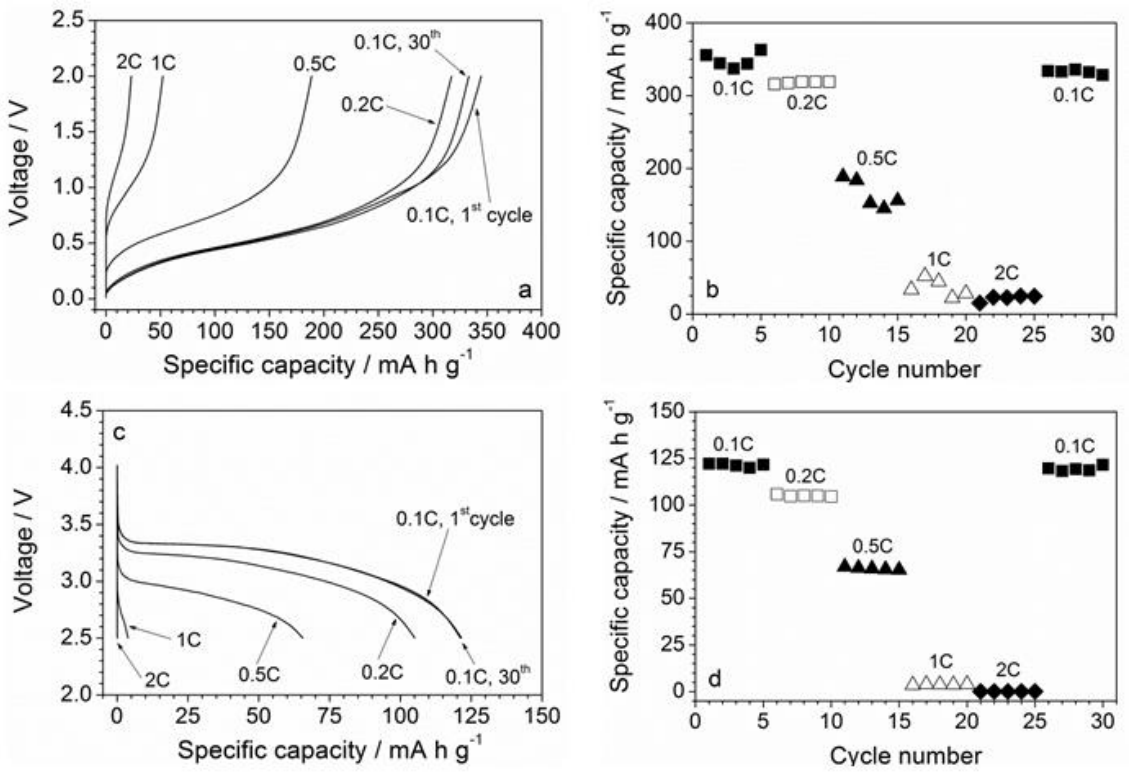

Figure 3.7. a) and c) Voltage vs. capacity profiles and b) and d) capacity evolution, obtained at different current rates (from 0.1C through 2C), for Li/Sn-C (a) and b)) and Li/$LiFePO_4$ (c) and d)) half-cells using the polymer electrolyte separator membrane 5/95. Room temperature.

As expected, a progressive increase of the discharge plateau slope, as well as the ohmic drop, is observed with the increasing of the current density (Figure 3.7 a) and Figure 3.7 c)). The results depicted in Figure 3.7 b) and Figure 3.7 d), and also summarized in Table 3.3, indicates

that the half-cells are able to deliver appreciable capacity values up to a current rate of 0.5C, e.g., more than 85% and 50% of the initial capacity are discharged at 0.2C and 0.5C, respectively (Table 3.3), this representing a remarkable value considering the gel configuration of the membrane.

Table 3.3. Room temperature specific capacity values delivered, at different current rates, by Li/Sn-C and Li/$LiFePO_4$ half-cells based on the P(VdF-HFP) 5/95 polymer electrolyte separator membrane.

	Delivered capacity / mA.h.g^{-1}				
Half-cell	0.1C	0.2C	0.5C	1C	2C
Li/Sn-C	362.8	319.1	188.9	52.2	24.7
Li/$LiFePO_4$	122.1	105.8	66.9	3.9	0.05

Higher current rates, i.e., 1C and 2C, result in modest delivered capacity values (Table 3.3), most likely limited by the polarization associated by the electrolyte diffusion kinetics. However, following cycling tests run again at 0.1C have evidenced capacities close to the initial value (Figure 3.7 b) and Figure 3.7 d)), this clearly indicating good capacity uptake for both anode and the cathode cells. This behaviour is also evidenced in Figure 3.8, which displays the delivered capacity, normalized with respect to the nominal one, vs. current rate dependence.

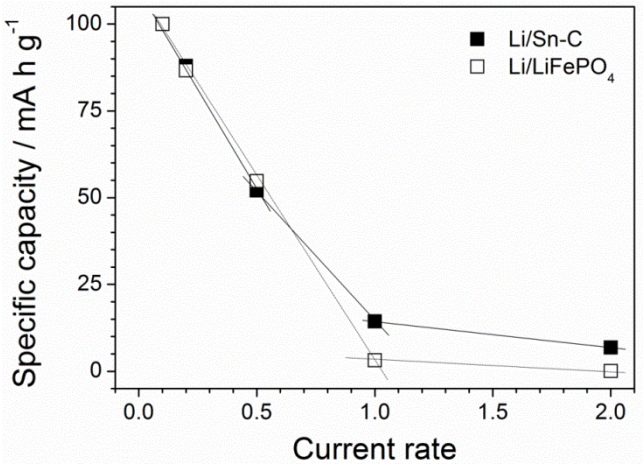

Figure 3.8. Delivered capacity, normalized with respect to the nominal one, vs. current rate dependence for Li/Sn-C and Li/$LiFePO_4$ half-cells using the polymer electrolyte separator membrane 5/95 at room temperature.

3.4. Conclusions

A progressive, almost linear, decrease in capacity is observed with the increasing of the current density up to 1C, associated to diffusion phenomena taking place within the electrode active material phase and polymer electrolyte separator membrane. Further raises in current rate above 1C result just in modest capacity decay. This behaviour can be ascribable to the intercalation of the Li^+ ion present in the electrode pores only. Nominally, no contribution from the Li^+ ion diffusion in the bulk electrolyte exists in this current regime.

The physico-chemical properties of polymer electrolyte membranes, based on the P(VdF-HFP) copolymer and prepared through different polymer/solvent (DMF) ratios, as separators for lithium battery systems, were investigated.

SEM results have shown that optimally distributed porosity membranes with moderately tortuous pathways can be obtained from polymer/DMF slurries with a solvent content equal or above to 90% in weight. The P(VdF-HFP) samples were found able to retain liquid solution up to a fraction equal to 77% in weight. Impedance measurements revealed conduction values above 10^{-3} $S.cm^{-1}$ at room temperature.

Cycling tests, performed on Li/Sn-C and Li/$LiFePO_4$ half-cells based on P(VdF-HFP) polymer electrolyte membranes, have evidenced nominal capacities ranging from 70% to 90% of the theoretical value with very good capacity retention and charge/discharge efficiency close to 100% even at high current rates and 100% of DoD. A capacity decay is observed at current regime above 1C, associated to the diffusion phenomena taking place within the electrode active material phase and polymer electrolyte membrane. Further work is in progress for enhancing the rate capability especially at high rates, e.g., improving the pore distribution and interconnection within the separator membranes.

To summarize, the good cycling behaviour exhibited by the half-cell indicates that the P(VdF-HFP) polymer electrolyte membranes developed in this work may be used as separators in lithium cell both in the anodic and in the cathodic region.

3.5. References

[1] Y. Ding, P. Zhang, Z. Long, Y. Jiang, F. Xu, W. Di, *The ionic conductivity and mechanical property of electrospun P(VdF-HFP)/PMMA membranes for lithium ion batteries*, Journal of Membrane Science. 2009, 329(1–2): p. 56-59.

[2] P.G. Bruce, B. Scrosati, J.-M. Tarascon, Angew. *Nanomaterials for rechargeable lithium batteries*, Chem. Intern, 2008, 47(16): p. 2930-2946.

[3] V. Aravindan, P. Vickraman, A. Sivashanmugam, R. Thirunakaran, S. Gopukumar, *Comparison among the performance of LiBOB, LiDFOB and LiFAP impregnated polyvinylidenefluoride-hexafluoropropylene nanocomposite membranes by phase inversion for lithium batteries*, Appl. Phys, 2013, 13(1): p. 293-297.

[4] X. Huang, *Separator technologies for lithium ion batteries*, J. Solid State Electrochem. 2011, 15: p. 649-662.

[5] H.-S. Kim, P. Periasamy, S.-I. Moon, *Electrochemical properties of the Li-ion polymer batteries with P(VdF-co-HFP)-based gel polymer electrolyte*, J. Power Sources, 2005, 141(2): p. 293-297.

[6] L.N. Sim, S.R. Majid, A.K. Arof, *FTIR studies of PEMA/PVdF-HFP blend polymer electrolyte system incorporated with $LiCF_3SO_3$ salt*, Vibrational Spectroscopy, 2012, 58: p. 57-66.

[7] D.-W. Kim, K.A. Noh, J.-H. Chun, S.-H. Kim, J.-M. Ko, *Highly conductive polymer electrolytes supported by microporous membrane*, Solid State Ionics, 2001, 144(3-4): p. 329-337.

[8] R. Miao, B. Liu, Z. Zhu, Y. Liu, J. Li, X. Wang, Q. Li, *PVDF-HFP-based porous polymer electrolyte membranes for lithium-ion batteries*, J. Power Sources, 2008, 184(2): p. 420-426.

[9] P. Martins, A. C. Lopes, S. Lanceros-Mendez, *Electroactive phases of poly(vinylidene fluoride): Determination, processing and applications*, 2014, 29(4): p. 683-706

[10] L. Shi, R. Wang, Y. Cao, C. Feng, D.T. Liang, J.H. Tay, *Fabrication of Poly (Vinylidene Fluoride-co-hexafluropropylene) (PVDF-HFP) asymmetric microporous hollow fiber mem-brane*, J. Membr. Sci, 2007, 305(1-2): p. 215-225.

[11] M.J. Koh, H.Y. Hwang, D.J. Kim, H.J. Kim, Y.T. Hong, S.Y. Nam, *Preparation and Characterization of Porous PVdF-HFP/clay Nanocomposites Membranes*, J. Mater. Sci. Tech. 2010, 26(7): p. 633-638.

[12] J.-H. Cao, B.-K. Zhu, Y.-Y. Xu, *Structure and ionic conductivity of porous polymer electrolytes based on PVDF-HFP copolymer membranes*, J. Membr. Sci., 2006, 281(1-2): p. 446-453.

[13] G.G. Kumar, K.S. Nahm, R.N. Elizabeth, *Electro chemical properties of porous PVdF-HFP membranes prepared with different nonsolvents*, J. Membr. Sci., 2008, 325(1): p. 117-124.

[14] K. Smolders, A.C.M. Franken, *Terminology for Membrane Distillation*, Desalination, 1989, 72(3): p. 249-262.

[15] J. Hassoun, G. Derrien, S. Panero, B. Scrosati, *A Nanostructured Sn–C Composite Lithium Battery Electrode with Unique Stability and High Electrochemical Performance*, Adv. Mater., 2008, 20: p. 3169-3175.

[16] J. Hassoun, D.-J. Lee, Y.-K. Sun and B. Scrosati, *A lithium ion battery using nanostructured Sn-C anode, LiFePO4 cathode and polyethylene oxide-based electrolyte*, Solid State Ionics, 2011, 202(1): p. 36-39.

[17] S. Brutti, J. Hassoun, B. Scrosati, C.-Y. Lin, H. Wu, H.-W. Hsieh, *A high power Sn–C/C–$LiFePO_4$ lithium ion battery*, J. Power Sources, 2012, 217: p.72-76.

[18] G.A. Elia, S. Panero, A. Savoini, B. Scrosati and J. Hassoun, *Mechanically milled, nanostructured Sn C composite anode for lithium ion battery*, Electrochim. Acta, 2013, 90: p. 690-694.

[19] A. California, V.F. Cardoso, C.M. Costa, V. Sencadas, G. Botelho, J.L. Gómez-Ribelles and S. Lanceros-Mendez, *Tailoring porous structure of ferroelectric poly(vinylidene fluoride-trifluoroethylene) by controlling solvent/polymer ratio and solvent evaporation rate*, European Polymer Journal, 2011, 47(12): p. 2442-2450.

[20] A. Ferreira, J. Silva, V. Sencadas, J.L.G. Ribelles and S. Lanceros-Méndez, *Poly [(vinylidene fluoride)-co-trifluoroethylene] Membranes Obtained by Isothermal Crystallization from Solution*, Macromolecular Materials and Engineering, 2010, 295(6): p. 523-528.

[21] C.M. Costa, M.M. Silva, S. Lanceros-Mendez, *Battery separators based on vinylidene fluoride (VDF) polymers and copolymers for lithium ion battery applications*, RSC Advances, 2013, 3(29): p. 11404.

[22] N. Ataollahi, A. Ahmad, H. Hamzah, M.Y.A. Rahman, N.S. Mohamed, *Preparation and characterization of PVDF-HFP/MG49 based polymer blend electrolyte*, Int. J. Electrochem. Sci., 2012, 7: p. 6693.

[23] D. Kumar, M. Suleman, S.A. Hashmi, *Studies on poly(vinylidene fluoride-co-hexafluoropropylene) based gel electrolyte nanocomposite for sodium–sulfur batteries*, Solid State Ionics, 2011, 202: p. 45-53.

[24] J.R. MacDonald, *Impedance Spectroscopy*, John Wiley & Sons Editor, New York, 1987.

[25] B.-Y. Chang, and S.-M. Park, *Electrochemical Impedance Spectroscopy*, Annual Review of Analytical Chemistry, 2010, 3(1): p. 207-229.

[26] B.A. Boukamp, *A package for impedance/admittance data analysis*, Solid State Ionics, 1986, 18: p. 136-140.

[27] B.A. Boukamp, *A Nonlinear Least Squares Fit procedure for analysis of immittance data of electrochemical systems*, Solid State Ionics, 1986, 20: p. 31-44.

[28] G.B. Appetecchi, P. Romagnoli and B. Scrosati, *Composite gel membranes: a new class of improved polymer electrolytes for lithium batteries*, Electrochem. Comm., 2001, 3: p. 281-284.

[29] Y. Aihara, G.B. Appetecchi and B. Scrosati, *A New Concept for the Formation of Homogeneous, Poly(ethylene oxide) based, Gel-Type Polymer Electrolyte*, J. Electrochem. Soc., 2002, 149: p. A849-A854.

[30] C.M. Costa, J.L. Gomez Ribelles, S. Lanceros-Méndez, G.B. Appetecchi, B. Scrosati, *Poly(vinylidene fluoride)-based, co-polymer separator electrolyte membranes for lithium-ion battery systems*, J. Power Sources, 2014, 245: p. 779-786.

[31] Q. Shi, M. Yu, X. Zhou, Y. Yan and C. Wan, *C. R. Structure and performance of porous polymer electrolytes based on P(VDF-HFP) for lithium ion batteries*, J. Power Sources, 2002, 103: p.286-292

[32] R. Miao, B. Liu, Z. Zhu, Y. Liu, J. Li, X. Wang and Q. Li, *PVDF-HFP-based porous polymer electrolyte membranes for lithium-ion batteries*, J. Power Sources, 2008, 184(2), p. 420-426

[33] S. S. Zhang, K. Xu, D. L. Foster, M. H. Ervin and T. R. Jow, *Microporous gel electrolyte Li-ion battery*, J. Power Sources, 2004, 125: p. 114-118.

[34] W. Pu, X. He, L. Wang, C. Jiang and C. Wan, *Preparation of PVDF–HFP microporous membrane for Li-ion batteries by phase inversion*, J. Membr. Sci., 2006, 272(1): p. 11-14.

[35] D. Aurbach, *Review of selected electrode-solution interactions which determine the performance of Li and Li-ion batteries*, J. Power Sources, 2000, 89(2): p. 206.

[36] J. Hassoun, K-S. Lee, Y-K. Sun, B. Scrosati, *An advanced lithium ion battery based on high performance electrode materials*, J. Am. Chem. Soc., 2011, 133(9): p. 3139-3143.

[37] B. Scrosati, *Recent advances in lithium ion battery materials*, Electrochimica Acta, 2000. 45(15–16): p. 2461-2466.

4. Tailoring poly(vinylidene fluoride-co-chlorotrifluoroethylene) microstructure and physico-chemical properties by exploring its binary phase diagram with dimethylformamide

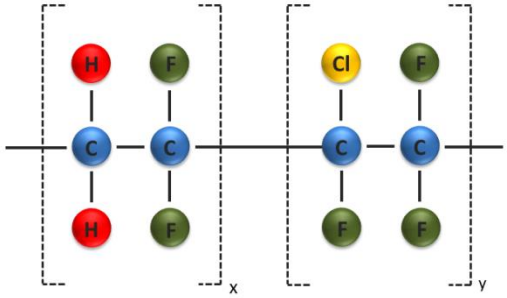

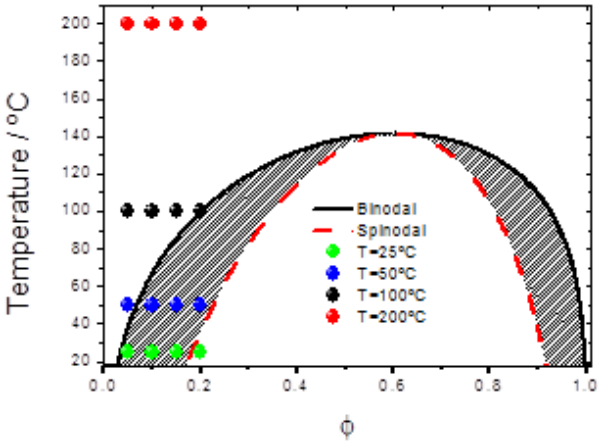

This chapter reports and discusses poly(vinylidene fluoride-co-chlorotrifluoroethylene), P(VdF-CTFE), membranes, which were prepared by solvent casting from N,N dimethylformamide (DMF). The preparation conditions involved a systematic variation of polymer/solvent ratio and solvent evaporation temperature. The microstructural variations of the P(VdF-CTFE) membranes depend on the different regions of the P(VdF-CTFE)/DMF phase diagram, explained by the Flory-Huggins theory. The effect of the polymer/solvent ratio and solvent evaporation temperature on the morphology, degree of porosity, β-phase content, degree of crystallinity, mechanical, dielectric and piezoelectric properties of the P(VdF-CTFE) polymer were evaluated.

This chapter is based on the following publication: "Tailoring poly(vinylidene fluoride-co-chlorotrifluoroethylene) microstructure and physico-chemical properties by exploring its binary phase diagram with dimethylformamide", R. E. Sousa, J. C. C. Ferreira, C. M. Costa, A. V. Machado, M. M. Silva and S. Lanceros-Méndez, Journal of Polymer Science B: Polymer Physics, 53 (11), 2015, 761 – 773.

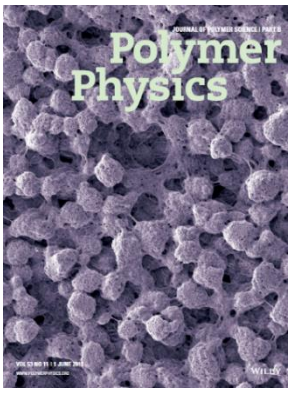

4.1. Introduction

Fluoropolymers are a class of polymers with increasing interest due to their wide range of actual and potential applications [1]. In particular, they are being used for aerospace applications [2, 3], gaskets, seals, petrochemical, automotive, medical and electrical industries [3], lubricants, thermal insulators, chemically resistant materials, filter membranes and as electrical insulators [2]. Potential applications include energy storage and advanced electronic devices begin explored due to the electroactive properties of some fluoropolymers [4]. Among their most interesting properties are chemical, thermal [2, 3, 5] and electrical stabilities, inertness to acids, high resistance to aging and oxidation [2, 3], low refractive index, low or no flammability [3] and mechanical strength. On the other hand, some characteristics such as their highly hydrophobic and solvophobic nature leading to poor solubility, wettability and miscibility with other materials, limit their applications in fields such as filtration membranes and medical devices [2].

In this way, strong research efforts have been developed to tune materials properties by varying the chemical compositions and therefore to extend their application range. Fluoropolymers that contain certain functional groups such as tetrafluoroethylene (TFE) and hexafluoropropene (HFP) have been developed by direct copolymerization with functional fluoro-monomers or by modification of fluoropolymers without any functional groups [1, 2, 4, 6]. One of these fluoropolymers is the P(VdF-CTFE) copolymer.

P(VdF-CTFE) copolymers with small VdF content are semicrystalline copolymer with a hexagonal structure [4, 7]. The copolymers with high VdF content (containing 25 – 70 mol% VdF) are semicrystalline with a monoclinic crystalline structure [4] and can be also obtained in the amorphous state. P(VdF-CTFE) copolymer shows the $[(CH_2CF_2)_x(CF_2CFCl)_y]_n$ [4, 7] chemical structure, the relative Chlorotrifluoroethylene (CTFE) content being critical in determining the copolymer physico-chemical properties [7]. In particular, there is a strong influence on the thermal properties, the glass transition temperature, T_g, ranging from ~ – 40 ℃ for pure PVdF to 45 ℃ for P(VdF-CTFE) [7].

Ferroelectric PVdF and its copolymers (P(VdF-CTFE)) show strong dipolar moments originating from the C-F bonds, the orientation of dipoles in the crystalline phase being responsible for the piezoelectric properties [8]. A high electromechanical response is reported for P(VdF-CTFE) [4, 7] containing 9 and 12 mol.% CTFE and its dielectric permittivity is 13 and dependent on CTFE content. The first applications of P(VdF-CTFE) were wire and cable covers

due to its high flexibility, high elongation and cold impact resistance. Nowadays, this polymer also begins to find applications in membranes for water and organic liquid treatment [1] and non-volatile polymer memories [9]. The pseudo-block structure of P(VdF-CTFE) offers feasibility for possible grafting modification via atom transfer radical polymerization (ATRP) preserving the high mechanical, thermal and chemical stabilities [5]. Nowadays, strong research efforts are being develop on the use of the materials for electrical energy storage [9 – 12], as high energy material [3] and the development of gel electrolyte membranes containing. In particular, its key features for energy storage application are its high ionic conductivity and good compatibility with lithium metal electrodes [6].

CTFE is also used in ternary polymers with VdF and trifluoroethylene (TrFE) or HFP to further tune electromechanical transduction and dielectric permittivity, etc. [6, 7, 13]. In the terpolymers, the CTFE units disrupts the sequence length of the crystal, which lowers both the melting and Curie transitions, leading to good electromechanical response through the more mobile polar domains [13]. The presence of the chlorine atom in the terpolymers of VdF and TrFE imposes a larger steric hindrance, which favors the (ferroelectric) trans conformation of the polymer backbone [13]. The addition of CTFE to the VdF–HFP copolymer has the effect of increasing the melting point and increasing the amorphous content [6].

Several techniques have been used for the processing of P(VdF-CTFE) membranes, including solution casting [2, 4, 13], electrospinning [12, 14] and non-solvent induced phase inversion [5]. Terpolymer films have been produced from solvent/non-solvent systems [6] and spin-coating [9], but there is still a need to stablish clear processing-morphology-physical properties relationships for this important copolymer, in particular for the development of polymer membranes.

Taking into account the state of art for P(VdF-CTFE) membranes and the need of understanding and tailoring its microstructure for different of applications, the novelty of this chapter is the fabrication of P(VdF-CTFE) membranes by solvent casting from DMF, by varying systematically polymer concentration and evaporation temperature along the phase diagram of the polymer/solvent system. Thus, membranes with different microstructures have been obtained with distinct thermal, mechanical, dielectric and piezoelectric properties, suitable for a wide range of applications.

4.2. Experimental

4.2.1. Materials

P(VdF-CTFE) (Solef 31508 with Mw = 270-290 kg.mol^{-1}; 18.66wt.% of CTFE content [15]) was supplied by Solvay. The solvent DMF (99.5%) was purchased from Merck.

4.2.2. Membrane preparation

P(VdF-CTFE) polymer concentration in solution ranged from 5 wt.% to 20 wt.%, concentration at which the polymer showed already a large viscosity. The polymer was dissolved in DMF at room temperature under constant magnetic stirring until a homogeneous solution was obtained. After polymer dissolution, the solution was placed on a clean glass substrate, spread by blade coating with the thickness of 100 μm and submitted to isothermal evaporation in a temperature range between 25 ℃ and 200 ℃ within an air oven from Binder, ED23 oven.

The samples produced were identified as (*x* CTFE *y*), where *x* represent the polymer concentration and *y* represents the solvent evaporation temperature.

4.2.3. Sample characterization

The morphology of the P(VdF-CTFE) membranes was obtained by the method described in section 2.2.3.

The porosity of the samples (ϕ) was measured by the pycnometer method:

$$\phi = \frac{W_2 - W_3 - W_S}{W_1 - W_3} \qquad (4.1)$$

where W_1 is the weight of the pycnometer filled with ethanol, W_S is the weight of the sample, W_2 is the weight after the sample was soaked in ethanol and additional ethanol was added to complete the volume of the pycnometer and W_3 is obtained when the sample was removed from the pycnometer and the residual weight of the pycnometer with ethanol was measured [16]. The mean porosity of each membrane was obtained as the average of the values determined in three samples.

Contact angle measurements were performed, polymer phase in the membranes was investigated by Fourier Transformed Infrared (FTIR) spectroscopy and the thermal properties of the membranes were determined by differential scanning calorimetry (DSC), as described in section 2.2.3.

Mechanical tests were carried out at room temperature through stress-strain measurements in the tensile mode of a Shimadzu-AG-IS testing instrument at a strain rate of 1mm/min.

The real part of the dielectric permittivity (ε') and the dielectric losses ($\tan\delta$) were obtained as described in section 2.2.3.

The piezoelectric d_{33} coefficients were measured using a d_{33} meter APC YE2730A. For determination of the piezoelectric coefficient, the P(VdF-CTFE) samples were first poled by corona discharge at a controlled temperature inside a home-made corona chamber with the following parameters obtained after process optimization: applied voltage of 8 kV at a constant current of 10 μA; constant distance of 1.5 cm between the sample and the tip; poling time 1 hour, poling temperature at 120 ℃ and then cooled to room temperature under the applied electric field [17].

4.2.4. Mesoscale simulation

Mesoscopic models based on dynamic density functional were used for describing the phase separation phenomena in the polymer/solvent mixture.

The dynamic density functional (DDF) model (mesoscale model based on the Gibbs free energy) consists on representing the total functional free energy as a function of time. This model is represented by the diffusion equation of the time-dependent Ginzburg-Landau model:

$$\frac{\partial\phi(r,t)}{\partial t} = M.\nabla^2\frac{\delta F}{\delta\phi(r,t)} + \eta(r,t) \qquad (4.2)$$

where $F = F^{id} + F^{mf}$ (F^{id} is the ideal free energy function and F^{mf} is the mean field free energy that correspond to Gibbs free energy), ϕ is the volume fraction of the polymer, M is the kinetic coefficient and $\eta(r,t)$ is a Gaussian random force, corresponding to a force correction factor [18].

The simulation was executed through the MesoDyn Model of Materials Studio software v6.0.0. The MesoDyn software solves the DDF problem applied to polymer mixtures by varying volume fraction and temperature, in order to assess the conditions for crystallization nucleation to occur. Within this process, it was necessary to build a polymer chain of P(VdF-CTFE) and a DMF molecule. Further, it was required to build an amorphous cell of polymer mixture based on the polymer-solvent volume fractions corresponding to the ones established in the experimental work. Finally, the polymer phase separation was studied as a function of the polymer concentration within the solution and the solvent evaporation temperature independently of the size of the box [19]. The size of the box was 502×502×32 nm with a number of simulation steps of 2000.

4.3. Results

The microstructural variations observed through the SEM images obtained from the P(VdF-CTFE)/DMF binary system, by varying initial polymer concentration (5 to 20 wt.%) and solvent evaporation temperature (from 25 ℃ to 200 ℃) are shown in Figure 4.1.

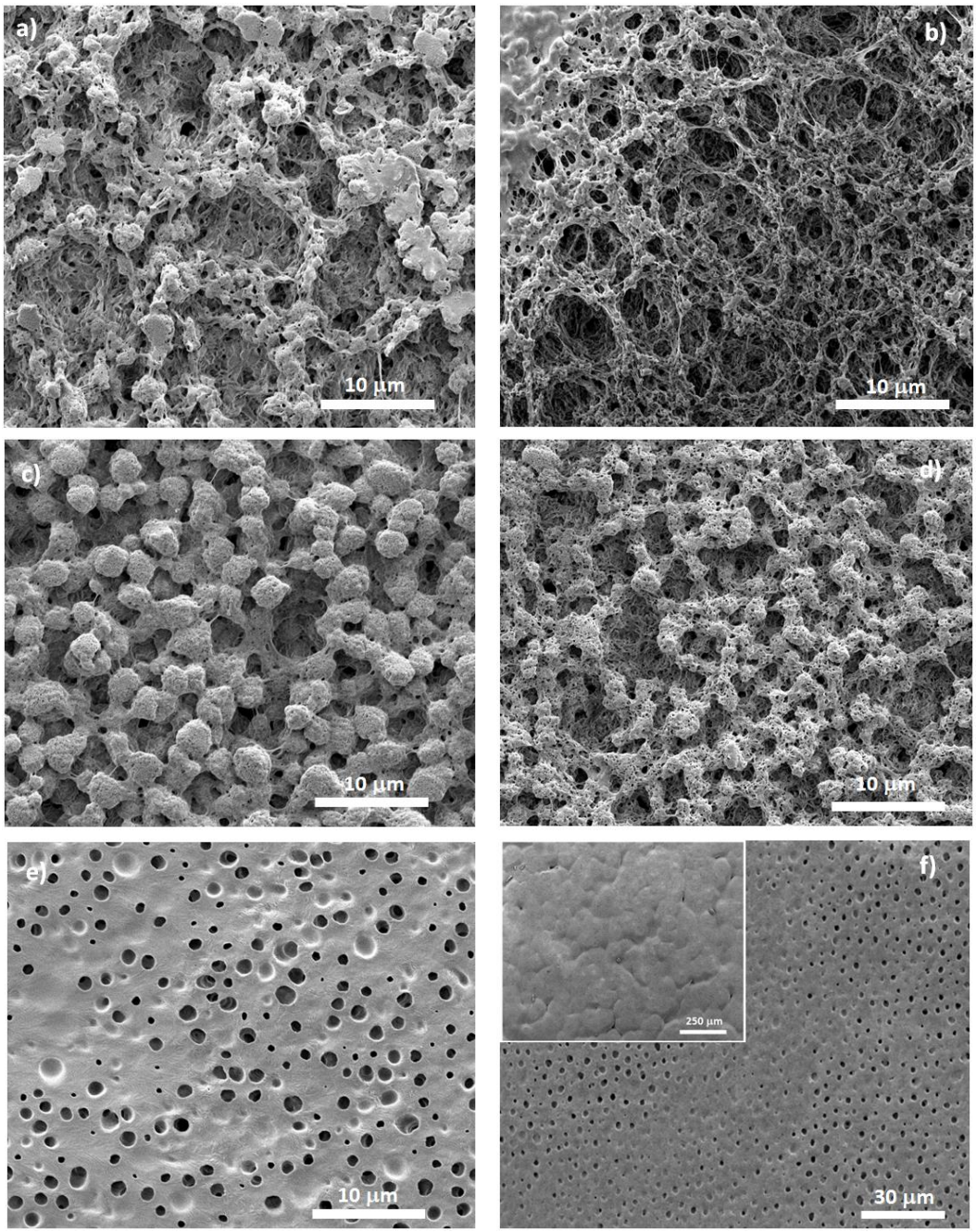

Figure 4.1. Surface images of the P(VdF-CTFE) membranes prepared from the P(VdF-CTFE)/DMF solution: solvent evaporation at 25 ℃ for a) 5 wt.% and b) 20 wt.% P(VdF-CTFE) samples. Solvent evaporation at 50 ℃ for c) 5 wt.% and d) 20 wt.% P(VdF-CTFE) samples. Morphologies of the samples with 20 wt.% P(VdF-CTFE) with solvent evaporation at e) 100 ℃ and f) 200 ℃.

As a function of initial polymer concentration (Figure 4.1 a), 5wt.% and Figure 4.1 b), 20wt.%) at 25 ℃, it is observed a porous morphology formed by sponge-like macrovoids as a result from a precipitation situation dominated by liquid-liquid demixing in the phase diagram [20]. A porous morphology is also observed in the samples prepared after solvent evaporation at 50 ℃ (Figure 4.1 c), 5wt.% and Figure 4.1 d), 20 wt.%). For low solvent evaporation temperatures (25 ℃ and 50 ℃) at a given polymer concentration (5 wt.%) – Figure 4.1 a) and Figure 4.1 c) – the membranes are characterized by a uniformly distributed spherulitic particulate morphology. Figure 4.1 a) and Figure 4.1 c) also show that the size of the spherulites increases with increasing solvent evaporation temperature. This behaviour is the same independently of the polymer concentration in the solution, as shown by Figure 4.1 b) and Figure 4.1 d) for the 20 wt.% samples concentration. Moreover, for a given polymer concentration, the size of the spherulites increases with increasing of solvent evaporation temperature (Figure 4.1 b) and Figure 4.1 d)). The particular morphology observed in Figure 4.1 a) – Figure 4.1 d) is ascribed to the relevance of the amorphous fraction in the formation of the membrane at lower crystallization temperatures (25 ℃ and 50 ℃). At these temperatures, the amorphous phase supplies sufficient chain mobility through the reorganization of the membrane structure, which is interrupted at the time of polymer vitrification [21], leading to low values of degree of crystallinity. A different microstructure is observed at high solvent evaporation temperatures for the 20 wt.% sample. As observed in Figure 4.1 e) and Figure 4.1 f) for solvent evaporation at 100 ℃ and 200 ℃, the membranes exhibit a dense morphology as temperature improves the polymer diffusion and the spherulite growth due to increased mobility of the polymer chains, that occupy the free space left by the solvent, giving rise therefore to a dense morphology [22]. The pores observed in Figure 4.1 e) for the samples evaporated at 100 ℃ are the result of the high evaporation rate of the DMF solvent that limits the mobility of polymer chains. The morphology observed for the samples evaporated at 200 ℃ (Figure 4.1 f)) consists on thick films with just surface pores within spherulites of diameters around 100 μm (insert of Figure 4.1 f)).

The different morphologies shown in Figure 4.1 are attributed to the initial position of the solution in the phase diagram of the P(VdF-CTFE)/DMF system, as it will be later discussed. The evaporation temperature of the solvent and the P(VdF-CTFE) concentration strongly affects the membrane morphology and the degree of porosity (Figure 4.2).

Figure 4.2 represents the degree of porosity of the P(VdF-CTFE) membranes evaporated at 25 ℃ as a function of the initial polymer concentration.

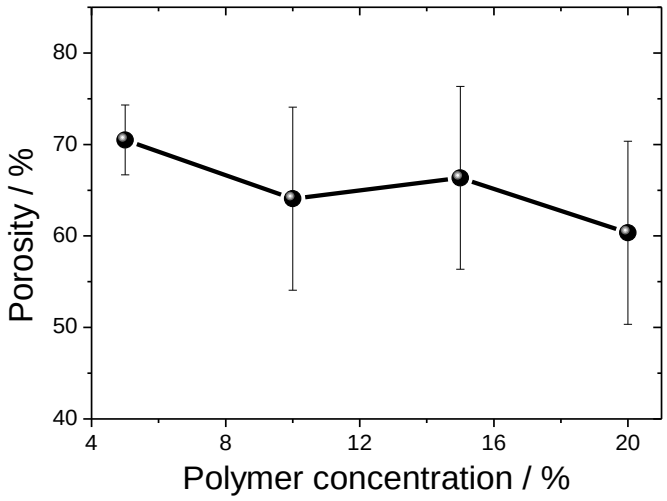

Figure 4.2. Degree of porosity as a function of P(VdF-CTFE) initial concentration in the P(VdF-CTFE)/DMF system prepared by solvent evaporation at room temperature.

The degrees of porosity ranges between 70% and 60% for all initial polymer concentrations in the solution between 5 and 20 wt.%. The explanation of this morphology is that, at low evaporation temperature, the polymer chains have a reduced mobility hindering the polymer to occupy the free space left by the evaporated solvent [23]. This behaviour at 25 ℃ is also detected for P(VdF-CTFE) membranes evaporated at 50 ℃, ranging the degree of porosity, in this case, between 56 % and 40 % for 5 and 20 wt.% of P(VdF-CTFE) in the initial solution, respectively. The decrease in the degree of porosity for P(VdF-CTFE) membrane evaporated at 50 ℃ and 100 ℃ in comparison with the samples at 25 ℃ for a given polymer concentration (e.g. 5 wt.%) is due to the increase of solvent evaporation rate and increased polymer chain mobility [24]. For higher solvent evaporation temperature at 200 ℃, a thick film is observed with no porosity. It is to notice that the evaporation temperature is above the melting temperature of the copolymer and under this temperature conditions, and different from the other situations, melt crystallizations occurs.

The analysis of the hydrophobicity of the membranes is essential to determine their range of applicability. Figure 4.3 shows the contact angle as a function of initial polymer concentration for the different solvent evaporation temperatures.

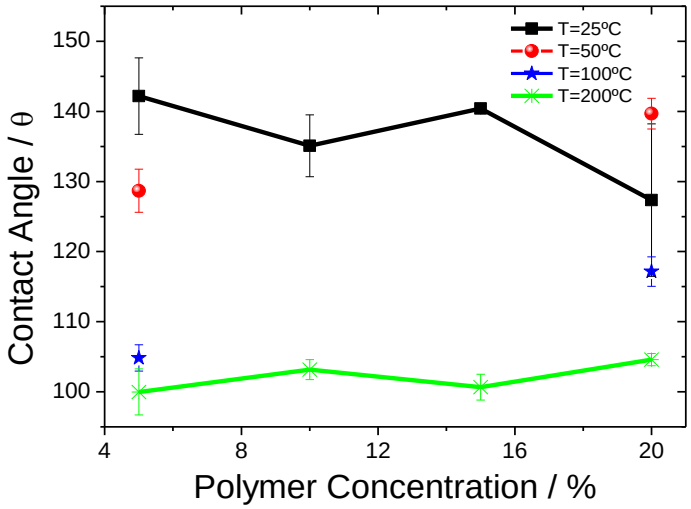

Figure 4.3. Contact angle as a function of P(VdF-CTFE) polymer concentration at different evaporation temperatures.

For P(VdF-CTFE) membranes evaporated at 25 ℃ the water contact angle is approximately between 130° and 140°, independently of the initial polymer concentration. The hydrophobic character observed for these membranes is mainly related to the large pore size and irregular surface [25]. In a general way, the water contact angle decreases with increasing solvent evaporation temperature, as shown in Figure 4.3 for the 5 wt.% initial polymer concentration, suffering minor variations with the initial polymer concentration. Thus, for the initial polymer concentration of 5 wt.% there is a strong decrease of the contact angle from ~140° to ~100° from the samples evaporated at 25 ℃ and 200 ℃, respectively (Figure 4.1 f)). This fact is mainly attributed to the variations in the morphology of the samples [26], but can also attributed to the polymer phase and therefore the polarity of the polymer chains.

Typically P(VdF-CTFE) polymer with less than 17 mol.% CTFE content crystallizes in the non-polar α-phase [27]. The identification and quantification of the crystalline phase of P(VdF-CTFE) as a function of the initial polymer concentration and solvent evaporation temperature was performed by FTIR (Figure 4.4).

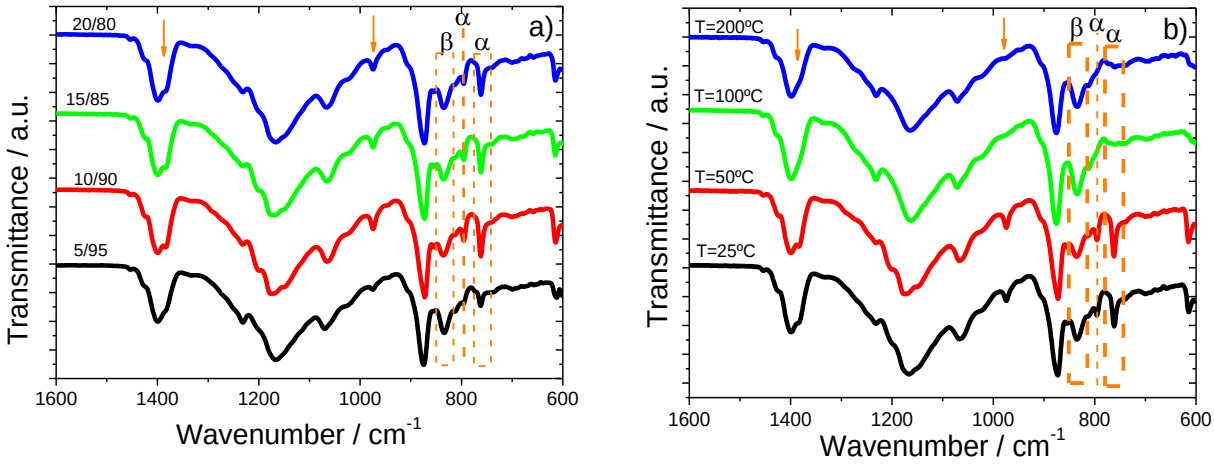

Figure 4.4. FTIR-ATR spectra for a) samples prepared after solvent evaporation at T =25 ℃ for different initial polymer concentrations in the P(VdF-CTFE)/DMF system and b) samples prepared from 20 wt.% P(VdF-CTFE) initial polymer concentration with solvent evaporated at different temperatures.

The specific bands characteristics of the α and β-phases of the pure PVdF polymer are 765, 796, 855 and 976 cm^{-1} and 840 and 1232 cm^{-1}, respectively [28]. The more representative vibration bands of P(VdF-CTFE) copolymer are: C-C stretch at 649, 666 and 698 cm^{-1}, C-Cl stretch at 902, 937 and 970 cm^{-1}, F-C-F asymmetrical stretch at 1202 cm^{-1}, F-C-F symmetrical stretch at 1130 cm^{-1} and C-F stretch at 1285 cm^{-1} [29]. FTIR-ATR spectra for the P(VdF-CTFE) membranes prepared after solvent evaporation at 25 ℃ for different initial polymer concentration are shown in the Figure 4.4 a). Figure 4.4 b) shows the FTIR-ATR spectra for the membranes prepared with the same initial polymer concentration (20 wt.%) but with solvent evaporation temperature between 25 ℃ to 200 ℃.

It can be observed that the polymer concentration (Figure 4.4 a)) and solvent evaporation temperature (Figure 4.4 b)) have a significant effect on vibrations bands of the P(VdF-CTFE) polymer and, therefore, different polymer phase contents are presented in the different samples. Independently of the experimental conditions, it is detected the presence of the vibrations bands at 760, 795, 974 and 1384 cm^{-1} that correspond to the α crystalline phase, but also the specific band at 838 cm^{-1} , identifying the β-phase [28]. This fact confirms the coexistence of multiple phases of P(VdF-CTFE) polymer, as detected through of XRD and DSC, as a function of crystallization condition [30].

The quantification of the crystalline phases present in the samples was performed using the specific bands at 766 cm^{-1} and 840 cm^{-1}, identified with the presence of the α and β-phases, respectively, and following the method explained in [28]. Assuming that the samples are composed just by the α and β-phases, the β-phase content is calculated by (2.4), as described in section 2.3,

with A_α and A_β the absorbencies at 766 and 840 cm^{-1}, corresponding to the α and β-phase material, K_α and K_β are the absorption coefficient at the respective wave number and X_α and X_β the degree of crystallinity of each phase. The value of K_α is 6.1×10^4 and K_β is 7.7×10^4 $cm^2.mol^{-1}$ [28].

The β-phase fraction obtained for the different P(VdF-CTFE) membranes is summarized in Table 4.1.

Table 4.1. β-phase content of the P(VdF-CTFE) membranes prepared from different initial polymer concentrations and solvent evaporation temperatures.

Samples	β-phase / % ± 2%
5CTFE25	56
10CTFE25	25
15CTFE25	32
20CTFE25	33
20CTFE50	26
20CTFE100	87
20CTFE200	82

Table 4.1 shows that the β-phase content decreases with increasing of polymer concentration in the P(VdF-CTFE)/DMF system for a given solvent evaporation temperature (25 ℃) and increases with increasing solvent evaporation temperature for a given initial polymer concentration (20 wt.%). The observed behaviour is determined by the solvent evaporation rate influencing the PVdF crystalline [31, 32] and also by the inclusion of the CTFE fraction in the PVdF polymer.

Concerning of the P(VdF-CTFE) membranes with different initial polymer concentration evaporated at 25 ℃, it was observed a decrease of the β-phase content with increasing initial polymer content up to 10 wt.%, remaining then practically constant until the initial polymer concentration of 20 wt.% in which the inclusion of the CTFE fraction is the factor determining the β-phase content. This behaviour can also be explained by the solvent diffusion, as initial polymer concentration affects the diffusivity of the solvent and the evaporation rate is dominated by the solvent diffusion coefficient [32]. For higher polymer concentration of 20 wt.%, the increase of the β-phase fraction by increasing solvent evaporation temperature is related to the inclusion of CTFE in the PVdF which leads to an oriented packing of the CH_2-CF_2 dipoles favoring the formation of the β-phase, as reported in [33].

The melting behaviour and degree of crystallinity of the P(VdF-CTFE) membranes were determined by differential scanning calorimetry (DSC).

The DSC thermographs of the P(VdF-CTFE) membranes as a function of the initial polymer concentration and solvent evaporation temperature are shown in Figure 4.5 a) and Figure 4.5 b), respectively.

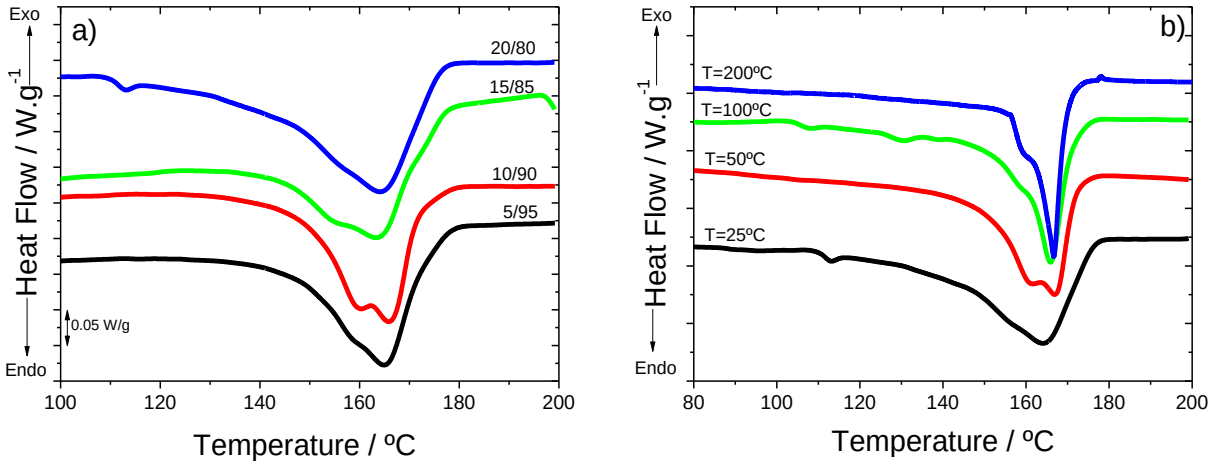

Figure 4.5. DSC scans for a) samples prepared after solvent evaporation at $T = 25$ ℃ for different initial polymer concentration in the P(VdF-CTFE)/DMF system and b) samples prepared from 20 wt.% P(VdF-CTFE) initial polymer concentration with solvent evaporation at different temperatures.

Figure 4.5 shows, in all cases, a bimodal peak that represents the melting temperature of the polymer. The bimodal peak, with maximum around 166 ℃, represents the melting temperature of the P(VdF-CTFE) polymer [5]. Figure 4.5 and Table 4.2 shows that the maximum melting temperature (164 ℃ – 167 ℃) of the P(VdF-CTFE) membranes is not affected by the solvent evaporation temperature and polymer concentration, within experimental error. The differences observed in the bimodal peak for all P(VdF-CTFE) are attributed to the increase of lamellae thickness, i.e. the interlamella diffusion of the polymer chains [34] and the coexistence of the two crystalline phases with different crystal types.

The degree of crystallinity of the P(VdF-CTFE) membranes, represented in Table 4.2, was obtained by (2.3) as described in section 2.2.3 [28].

Table 4.2. Maximum melting temperature and degree of crystallinity of the membranes as a function of polymer concentration and solvent evaporation temperature.

Samples	T_f / ℃ ± 1 ℃	χ / % ± 2%
5CTFE25	165	21
10CTFE25	165	21
15CTFE25	164	22
20CTFE25	164	27
20CTFE50	167	25
20CTFE100	166	15
20CTFE200	167	18

The degree of crystallinity shown in Table 4.2, slightly depends on solvent evaporation temperature and initial polymer concentration. For a given solvent evaporation temperature (25 ℃), the degree of crystallinity increases slightly with increasing polymer concentration, due to increased polymer-polymer interaction during polymer crystallization [35]. On the other hand, for a given initial polymer concentration (20 wt.%), the degree of crystallinity decreases with increasing solvent evaporation temperature, due to the increasing of crystallization kinetics leading to more defective structures [36]. It has been reported that the degree of crystallinity for P(VdF-CTFE) with 9 wt.% CTFE content is around 25%, the degree of crystallinity decreasing with increasing CTFE content in the P(VdF-CTFE) polymer [4].

The determination of the mechanical properties of the P(VdF-CTFE) films and membranes is a relevant factor associated to the integrity and safety of the membranes, which is critical in certain applications such as filtration, microelectronics applications and battery separators, among others.

Stress/strain curves for the different P(VdF-CTFE) membranes as a function of initial polymer concentration and solvent evaporation temperature are shown in Figure 4.6.

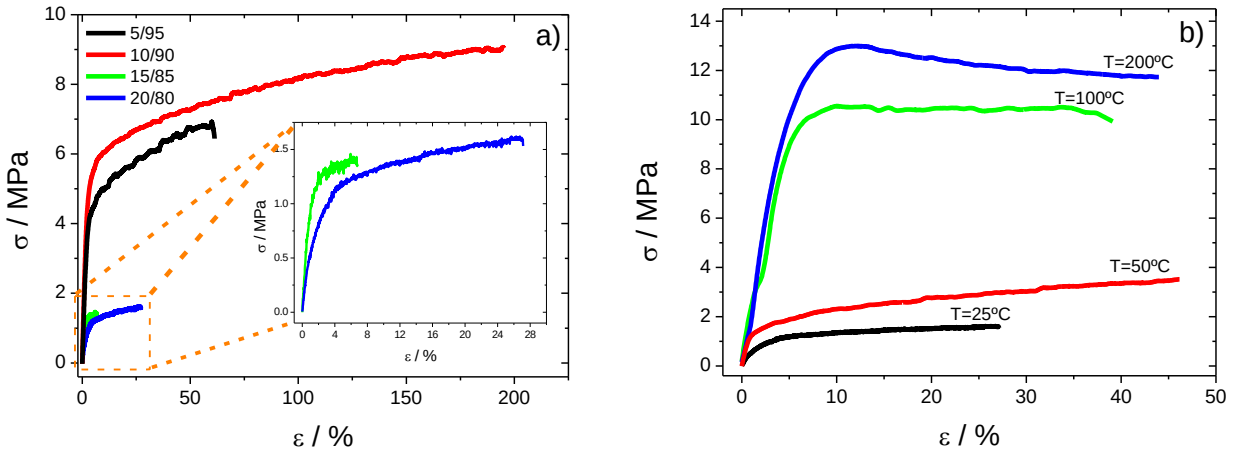

Figure 4.6. Stress-strain curves for a) samples prepared after solvent evaporation at T =25 ℃ for different initial polymer concentration in the P(VdF-CTFE)/DMF system and b) samples prepared from 20 wt.% P(VdF-CTFE) initial polymer concentration with solvent evaporation at different temperatures.

The behaviour in the stress/strain curve for all P(VdF-CTFE) membranes is typical for a thermoplastic polymer in which an elastic linear region characterized by the Young's modulus (slope of stress-strain in the elastic region at a deformation of 5%) is detected, followed by the yielding strain/stress, separating the elastic from the plastic region [37].

The mechanical parameters (Young's modulus, yielding stress/strain) calculated from the data in Figure 4.6 are represented in Table 4.3.

Table 4.3. Young´s modulus (E'), yielding stress (σ_y) and yielding strain (ε_y) of the membranes as a function of polymer concentration and solvent evaporation temperature.

Samples	E' **/ MPa ± 2%**	ε_y **/ % ± 1%**	σ_y **/ MPa ± 2%**
5CTFE25	155	3	5.0
10CTFE25	155	5	6.0
15CTFE25	100	3	1.3
20CTFE25	38	4	1.2
20CTFE50	110	2	1.8
20CTFE100	180	6	10.4
20CTFE200	230	11	13

Figure 4.6 and Table 4.3 show that that the Young's modulus and yielding stress decrease with increasing polymer concentration at 25 ℃. This behaviour is fully ascribed to the different porous morphologies of the P(VdF-CTFE) membranes, as the degree of crystallinity is practically constant for those samples (Table 4.2). In relation to the effect of the solvent evaporation temperature,

both Young's modulus, yielding stress and yielding strain are enhanced with increasing solvent evaporation solvent temperature for a given initial polymer concentration: as the solvent temperature increases, the degree of porosity present in the P(VdF-CTFE) membranes decreases, increasing the mechanical properties.

Technological developments based on the use of electroactive polymers such as P(VdF-CTFE) are mainly based on its dielectric and piezoelectric properties, in particular for applications as sensors, actuators, electromechanical and acoustic transducers.

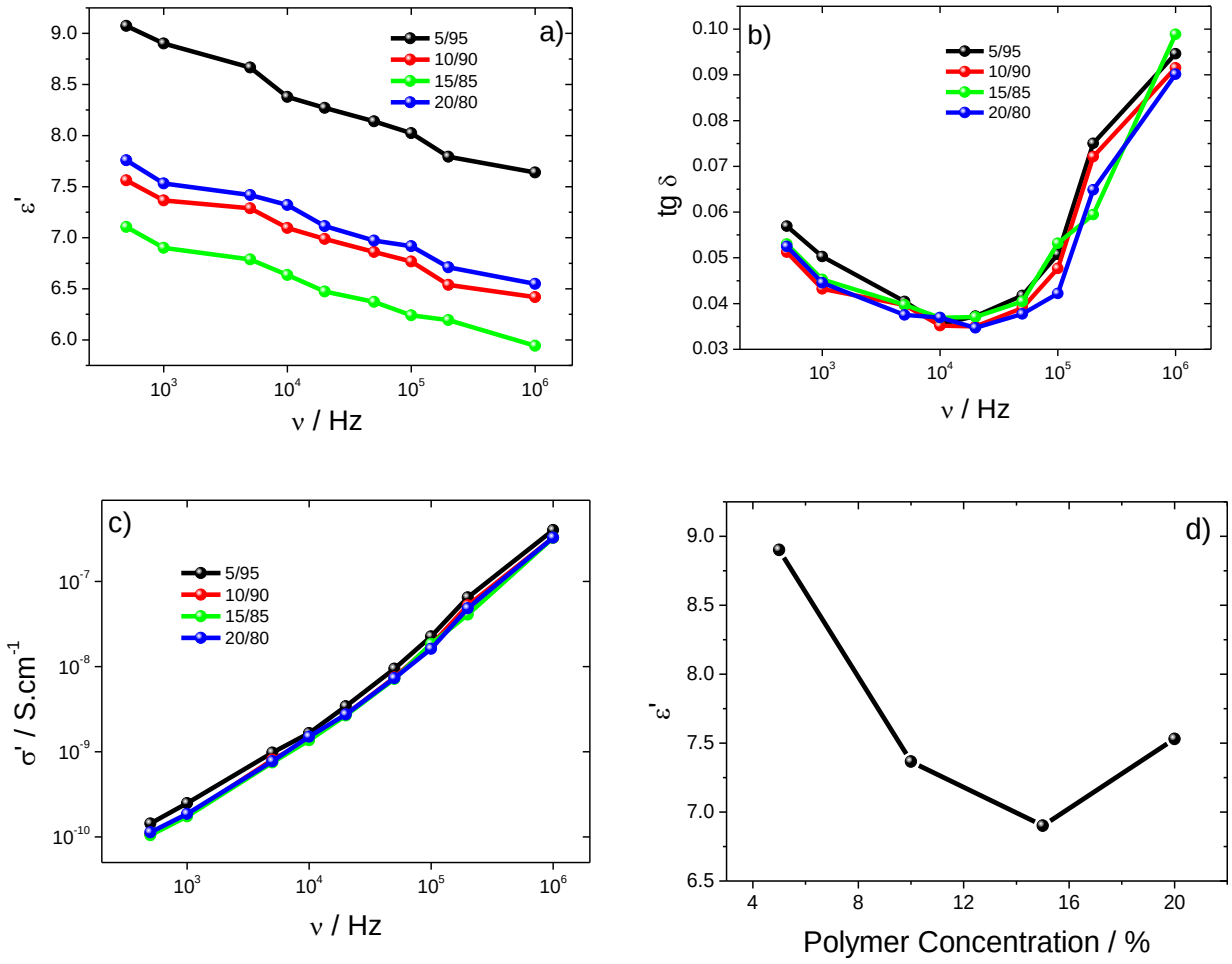

Figure 4.7. Electrical results for the samples prepared by solvent evaporation at T =200 ℃ from different initial polymer concentrations in the P(VdF-CTFE)/DMF system: a) dielectric constant, b) tan δ and c) conductivity. d) Variation of the dielectric constant in function of polymer concentration at 1 kHz.

Figure 4.7 a) shows the variation of ε' for the P(VdF-CTFE) membranes evaporated at 200 ℃ as a function of polymer concentration. These measurements are presented just for the samples prepared under these conditions, as they are processed in the form of thin films and not porous microstructures, which hinder precise electrical characterization. ε' decreases with increasing

frequency such as for pure PVdF [38], and the behaviour is practically the same between all the samples. The dielectric constant ε' present in Figure 4.7 a) is correlated and depends on the degree of crystallinity and the crystalline phase of the polymer (Table 4.1 and Table 4.2). The dielectric constant ε' at 1 kHz as a function of polymer concentration represented in Figure 4.7 d) shows the effect of the crystalline phase and degree of crystallinity in the dielectric behaviour. The values of ε' for the P(VdF-CTFE) films shown in Figure 4.7 a) and Figure 4.7 d) are between the values of the dielectric constant obtained for the PVdF homopolymer in the α-phase, $\varepsilon' = 7$, and β-phase, $\varepsilon' = 12$ [38]. The values of ε' for P(VdF-CTFE) polymer depend on the CTFE content and processing conditions, being reported values up to $\varepsilon' = 15$ [39].

Figure 4.7 b) shows the behaviour of the $\tan\delta$ as a function of frequency. Regarding $\tan\delta$ for frequencies above 104 Hz, the increase in the $\tan\delta$ is attributed to the α_a relaxation process, i,e., micro-brownian movement of the amorphous phase chain segments or movement of crystalline-amorphous interphase chain segments [40].

From (2.5), the real part of the conductivity of the dielectric material can be calculated from the dielectric measurements presented in Figure 4.7 a).

Figure 4.7 c) shows the $\sigma'(\omega)$ values for the P(VdF-CTFE) films as a function of frequency. The behaviour of all P(VdF-CTFE) films is the same, the conductivity increasing with increasing frequency (Figure 4.7 c)). Normally in the fluorinated polymers (PVdF polymer and its copolymers), the conductivity behaviour as a function of frequency shows two regimes, i.e., one regime for lower frequencies up to 104 Hz dominated by the DC conductivity and the second for higher frequencies, assigned to the AC conductivity [42]. In Figure 4.7 c), for all P(VdF-CTFE) films, the conductivity increases with increasing of frequency in a similar way.

Finally, Figure 4.8 shows the d_{33} piezoelectric coefficient as a function of polymer concentration after poling conditions optimization.

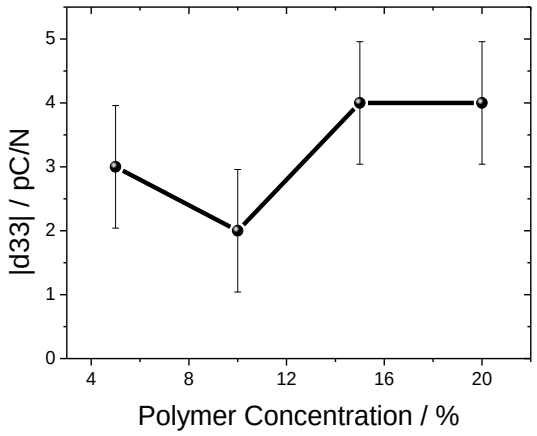

Figure 4.8. Modulus of the piezoelectric d_{33} coefficient for the films evaporated at 200 ℃ as a function of the P(VdF-CTFE) initial concentration.

The piezoelectric coefficient d_{33} is negative and its modulus is practically independent, within experimental error, of the polymer concentration in the P(VdF-CTFE)/DMF system, as demonstrated in Figure 4.8.

In [43] it is demonstrated the dependence of the piezoelectric response with the β-phase content and it was shown that for β-phase contents above 82% the piezoelectric response practically remains constant. The piezoelectric d_{33} coefficient is around 4pC/N for the sample with the highest β-phase content (20 wt.%, 82%). The β-phase of the samples is responsible for the piezoelectric properties (-CH_2CF_2-) [43] and the degree of crystallinity. In the present case, though large values of electroactive phase are obtained, the low value of the degree of crystallinity in comparison with PVdF (25% to 18% for P(VdF-CTFE) vs. 40% to 55% for PVdF) leads to lower values of the d_{33} response [44].

4.4. Discussion

Figure 4.9 shows the variation of the free energy of mixing (ΔG) as a function of polymer concentration in the P(VdF-CTFE)/DMF system for different evaporation temperatures and the phase diagram for the P(VdF-CTFE)/DMF system.

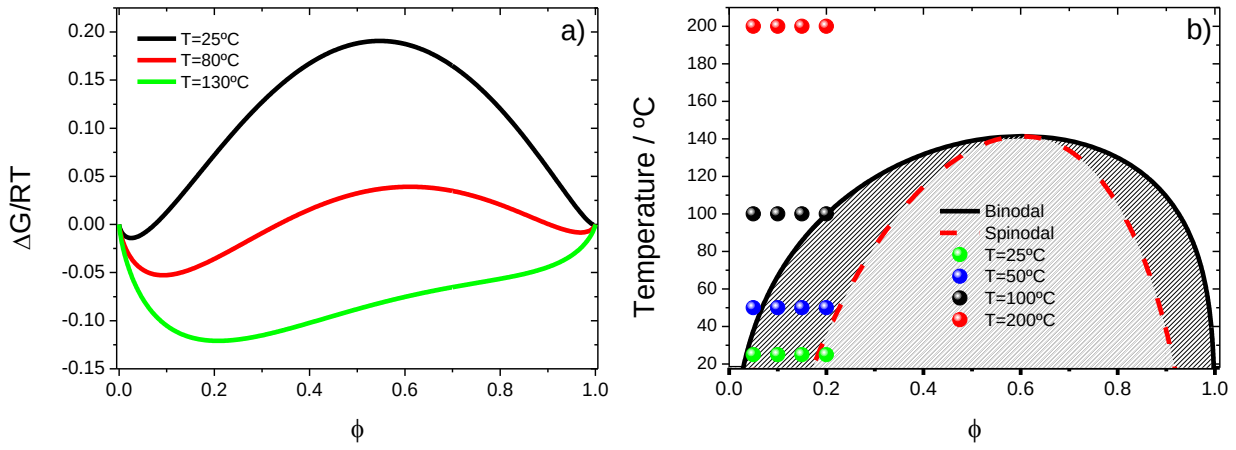

Figure 4.9. a) Variation of the Gibbs free energy and b) phase diagram for the P(VdF-CTFE)/DMF system.

The influence of polymer concentration and solvent evaporation temperature in the sample microstructure of the P(VdF-CTFE) polymer (Figure 4.1) is due to a phase separation process between polymer and solvent illustrated in the phase diagram of the P(VdF-CTFE)/DMF system (Figure 4.9 b)).

Through the Flory-Huggins theory based on a lattice model that ignores “free volume”, the

Gibbs free energy fluctuations in the isothermal evaporation process for binary systems (polymer/solvent) are described by (2.6) [45] as defined in section 2.4.

For the P(VdF-CTFE)/DMF system, the Gibbs free energy density (ΔG) (Figure 4.9 a)) and the phase diagram (Figure 4.9 b)) have been constructed using ν_0 =77.4 $cm^3.mol^{-1}$ (DMF volume molar), n =23 and the Hansen solubility parameters, δ = 3.31, determined with the Blends software including in Material Studio Modeling software. This solubility parameter indicates the strong interaction between the DMF molecule and the P(VdF-CTFE) chain.

The Flory-Huggins theory adopted here was the extended theory that is found on Materials Studio software. The extended Flory-Huggins theory introduces two new topics and combines the Flory-Huggins model and molecular simulation to calculate the miscibility of polymer solutions. The first one, consists on the interaction parameter, in that the previous model don't take in consideration the variation with temperature, but this is taken in this calculation. The second one, is an off-lattice calculation, this means that molecules are not distributed as a regular lattice, as write by Flory-Huggins theory. The simulation generates a multiple possible molecular pairs and calculates, for each one, the number of coordination number. These computer simulations are carried out in isolated molecules and there are normalized by the other interactions. This is present on the results.

These two topics were previous discussed by [46, 47]. This extension of Flory-Huggins model it is necessary to approximate the simulation to the experimental data.

The miscibility ($\Delta G < 0$) of the system increases with increasing temperature [48] and is affected by specific interactions between polymer and solvent and the polymer molecular weight. This behaviour of miscibility is dependent on the polymer concentration for low temperatures and becomes independent of the initial polymer concentration for temperatures above 80 ℃.

Figure 4.9 b) shows the phase diagram of the P(VdF-CTFE)/DMF system in which the three main regions – stability, metastability and instability – of the polymer solution are observed. These regions are separated by the binodal and the spinodal lines illustrated. In this way, the phase separation process of the P(VdF-CTFE)/DMF system and therefore the resulting sample microstructure, can be controlled through the initial polymer concentration and the solvent evaporation temperature.

The initial sample preparation conditions (polymer concentration and solvent evaporation temperature) are represented in the phase diagram of Figure 4.9 b) by the circles.

As represented in Figure 4.9 a) at 25 ℃ for the different polymer/solvent ratios, the microstructure formation of the P(VdF-CTFE) membranes is dominated by nucleation and growth, as samples are located in the metastable region (region between the spinodal and binodal

lines). This phase separation process, leading later to morphology formation, is simulated for the P(VdF-CTFE)/DMF phase diagram at 25 ℃ in Figure 4.10 a) and Figure 4.10 b). The simulated phase separation is represented by the color-codes, representing the variation of the density on the system (polymer/solvent) in which red represents a higher density and blue a lower density.

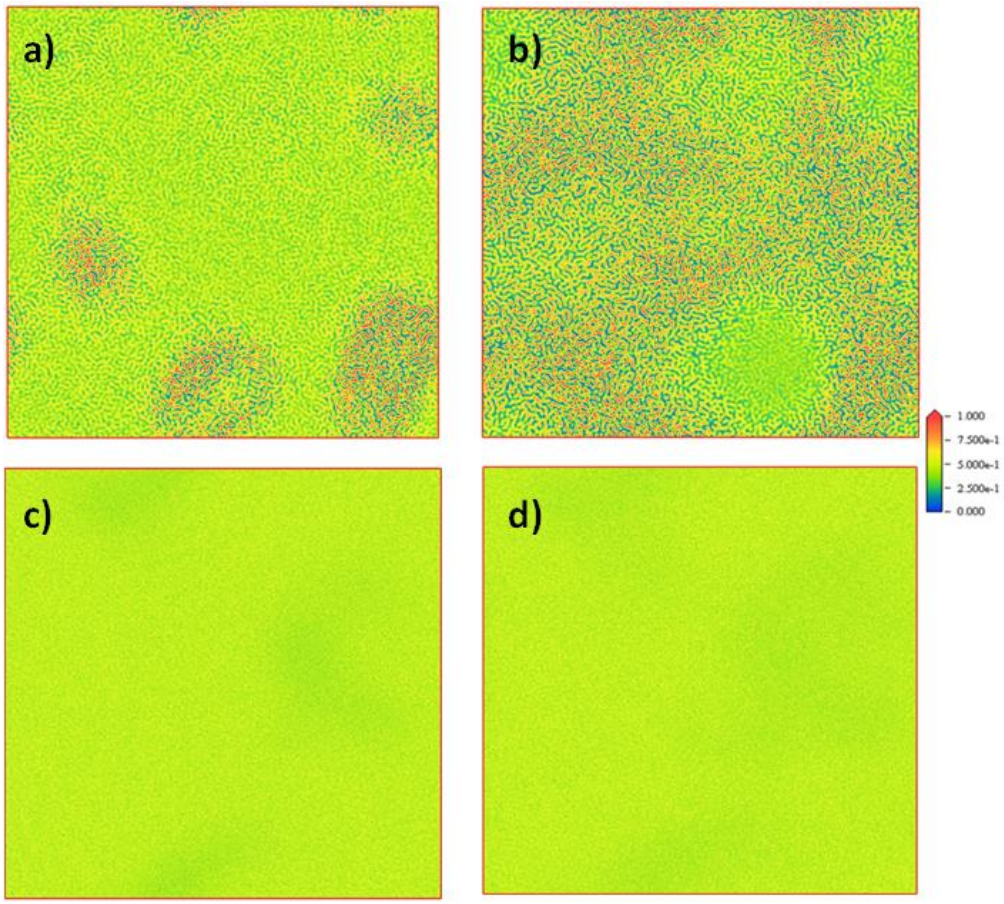

Figure 4.10. Representation of the P(VdF-CTFE) structure in the P(VdF-CTFE)/DMF system at 25 ℃ for a) 5% of P(VdF-CTFE) and b) 20% of P(VdF-CTFE) and at 200 ℃ for c) 5% of P(VdF-CTFE) and d) 20% of P(VdF-CTFE) in the initial solution. The colour-code represents the variation of the density on the system (polymer/solvent) in which red represents a higher density and blue a lower density.

Thus, simulations at 25 ℃ show a microphase separation where the phase separation occurs. The microphase separation (Figure 4.10 a)) is lower in the more diluted solution and increases with increasing polymer concentration in the P(VdF-CTFE)/DMF system (Figure 4.10 b)). Taking this fact into account, the P(VdF-CTFE) membranes result in final microstructures with different degree of porosity (Figure 4.2). For a given polymer/solvent ratio (20/80) at different solvent temperatures (25 ℃, 50 ℃, 100 ℃ and 200 ℃) the system passes from the metastable region to the one-phase region (homogeneous microstructure) above 100 ℃ and no porous microstructure is observed (Figure 4.2). This fact is also observed in the simulated initial

morphology (Figure 4.10 c) and Figure 4.10 d)).

For high evaporation temperature (200 ℃), independently of the polymer concentration, the sample preparation conditions are located outside the binodal line and no liquid-liquid phase separation is observed (Figure 4.10 c) and Figure 4.10 d)).

Finally, the factor that affects more the phase separation, observed in Figure 4.10, is the solvent evaporation temperature in comparison with polymer concentration, within the ranges used in the present investigation.

The β-phase content, thermal, mechanical, dielectric and piezoelectric properties of P(VdF-CTFE) samples depend on the initial polymer concentration and solvent evaporation temperature, as shown in Figure 4.4, Figure 4.5, Figure 4.6, Figure 4.7 and Figure 4.8, respectively.

At room temperature, the degree of porosity of P(VdF-CTFE) membranes depends on the polymer concentration as illustrated in Figure 4.2. The β-phase content of P(VdF-CTFE) membranes depends more on solvent evaporation temperature than on polymer concentration (Figure 4.4). The maximum β-phase fraction (87%) was determined for 20 wt.% initial polymer concentration at a solvent evaporation temperature of 100 ℃.

The differences observed in the degree of crystallinity (values between 15% and 27%) (Figure 4.4 and Table 4.3) for all P(VdF-CTFE) membranes, are ascribed to the deferral of liquid-liquid demixing process and correlated to the phase separation and solvent evaporation rate influenced by thermodynamic parameters (affinity) and kinetics factors (molar volumes). The Young's modulus and yielding stress depend on the evaporation solvent temperature and polymer concentration as they are mainly affected by the degree of crystallinity.

Finally, the dielectric and piezoelectric properties of P(VdF-CTFE) membranes are correlated mainly with the β-phase content (Figure 4.7 and Figure 4.8, respectively).

4.5. Conclusions

P(VdF-CTFE) membranes have been prepared by solvent casting and the influence of polymer/solvent ratio and solvent evaporation temperature in the microstructure and physico-chemical properties of P(VdF-CTFE) membranes prepared was evaluated. We obtained membranes with a wide-range of different morphologies, and their porous microstructure is attributed to spinodal decomposition of the liquid-liquid phase separation. These microstructures are correlated through the phase diagrams for the binary system (P(VdF-CTFE)/DMF) obtained by the Flory-Huggins theory, assuming random mixing of chains in the calculation of the entropy

and segments in the calculation of the enthalpy. For P(VdF-CTFE) membranes, the β-phase content, thermal, mechanical, dielectric and piezoelectric properties depends on the initial polymer concentration and solvent evaporation temperature. We argue that P(VdF-CTFE) membranes with different morphologies, thermal, dielectric and piezoelectric properties are suitable for their use in different applications from sensor and actuator to different membrane technologies.

The membrane solutions prepared with different P(VdF-CTFE) contents can be prepared with a large range of viscosities, making them suitable for inks to be used in printing technology. As previously mentioned, the choice of the viscosity will depend on the selected printing technique.

4.6. References

[1] Cui, Z.; Drioli, E.; Lee, Y. M., *Recent progress in fluoropolymers for membranes*, Progress in Polymer Science, 2014, 39(1): p. 164-198.

[2] Tan, S.; Li, J.; Gao, G.; Li, H.; Zhang, Z., *Synthesis of fluoropolymer containing tunable unsaturation by a controlled dehydrochlorination of P(VDF-co-CTFE) and its curing for high performance rubber applications*, Journal of Materials Chemistry, 2012, 22: p. 18496-18504.

[3] Singh, A.; Soni, P. K.; Shekharam, T.; Srivastava, A., *A study on thermal behavior of a poly(VDF-CTFE) copolymers binder for high energy materials*, Journal of Applied Polymer Science, 2013, 127(3): p. 1751-1757.

[4] Li, Z.; Wang, Y.; Cheng, Z.-Y., *Electromechanical properties of poly(vinylidene-fluoride-chlorotrifluoroethylene) copolymer*, Applied Physics Letters, 2006, 88(6): p. 062904-062904-3.

[5] Liu, F.; Abed, M. R. M.; Li, K. *Hydrophilic modification of P (VDF-co-CTFE) porous membranes*, Chemical Engineering Science, 2011, 66(1): p. 27-35.

[6] Jarvis, C. R.; Macklin, A. J.; Teagle, D. A.; Cullen, J.; Macklin, W., *The use of novel VDF–HFP–CTFE terpolymers in lithium-ion polymer cells*, J. Journal of Power Sources, 2003, 119–121: p. 465-468.

[7] Ameduri, B., *From Vinylidene Fluoride (VDF) to the Applications of VDF-Containing Polymers and Copolymers: Recent Developments and Future Trends*, Chemical Reviews, 2009, 109: p. 6632-6686.

[8] Lovinger, *Ferroelectric polymers*, A. J. Science, 1983, 220: p. 1115-1121.

[9] Kim, R. H.; Kang, S. J.; Bae, I.; Choi, Y. S.; Park, Y. J.; Park, C., *Thin ferroelectric poly (vinylidene fluoride-chlorotrifluoro ethylene) films for thermal history independent non-*

volatile polymer memory, Organic Electronics, 2012, 13(3): p.491-497.

[10] Amirinejad, M.; Madaeni, S. S.; Navarra, M. A.; Rafiee, E.; Scrosati, B., *Solvent-free nanocomposite proton-conducting membranes composed of cesium salt of phosphotungstic acid doped PVDF–CTFE/PEO blend*, Ionics, 2010, 16(8): p. 681-687.

[11] Lee, H.; Alcoutlabi, M.; Watson, J. V.; Zhang, X., *Polyvinylidene fluoride-co-chlorotrifluoroethylene and polyvinylidene fluoride-co-hexafluoropropylene nanofiber-coated polypropylene microporous battery separator membranes*, Journal of Polymer Science Part B: Polymer Physics, 2013, 51(5): p. 349-357.

[12] Lee, H.; Alcoutlabi, M.; Watson, J. V.; Zhang, X., *Electrospun nanofiber-coated separator membranes for lithium-ion rechargeable batteries*, Journal of Applied Polymer Science, 2013, 129(4): p. 1939-1951.

[13] Buckley, G. S.; Roland, C. M.; Casalini, R.; Petchsuk, A.; Chung, T. C., *Electrostrictive Properties of Poly(vinylidenefluoride−trifluoroethylene−chlorotrifluoroethylene)*, Chemistry of Materials, 2002, 14(6): p. 2590-2593.

[14] Lee, H.; Alcoutlabi, M.; Toprakci, O.; Xu, G.; Watson, J.; Zhang, X., *Preparation and characterization of electrospun nanofiber-coated membrane separators for lithium-ion batteries*, Journal of Solid State Electrochemistry, 2014, 1-8.

[15] Zhang, M.; Russell, T. P., *Graft Copolymers from Poly(vinylidene fluoride-co-chlorotrifluoroethylene) via Atom Transfer Radical Polymerization*, Macromolecules 2006, 39: p. 3531-3539.

[16] California, A.; Cardoso, V. F.; Costa, C. M.; Sencadas, V.; Botelho, G.; Gómez-Ribelles, J. L.; Lanceros-Mendez, S., *Tailoring porous structure of ferroelectric poly(vinylidene fluoride-trifluoroethylene) by controlling solvent/polymer ratio and solvent evaporation rate*, European Polymer Journal, 2011, 47(12): p. 2442-2450.

[17] Dargaville, T. R.; Celina, M.; Chaplya, P. M., *Evaluation of piezoelectric poly (vinylidene fluoride) polymers for use in space environments. I. Temperature limitations*, Journal of Polymer Science Part B: Polymer Physics 2005, 43(11): p. 1310-1320.

[18] Petschek, R. G.; Metiu, H., *A computer simulation of the time-dependent Ginzburg-Landau model for spinodal decomposition*, The Journal of Chemical Physics, 1983, 79(7): p. 3443-3456.

[19] Altevogt, P.; Evers, O. A.; Fraaije, J. G. E. M.; Maurits, N. M.; van Vlimmeren, B. A. C, *The MesoDyn project: software for mesoscale chemical engineering*, Journal of Molecular Structure: THEOCHEM, 1999, 463(1-2): p. 139-143.

[20] Lin, D.-J.; Chang, C.-L.; Huang, F.-M.; Cheng, L.-P., *Effect of salt additive on the formation of microporous poly(vinylidene fluoride) membranes by phase inversion from LiClO4/Water/DMF/PVDF system*, Polymer, 2003, 44: p. 413-422.

[21] Pinnau, I.; Koros, W. J., *A Qualitative Skin Layer Formation Mechanism for Membranes Made by Dry/Wet Phase Inversion*, Journal of Polymer Science Part B: Polymer Physics, 1993, 31(4): p. 419-427.

[22] Magalhães, R.; Durães, N.; Silva, M.; Silva, J.; Sencadas, V.; Botelho, G.; Gómez Ribelles, J. L.; Lanceros-Méndez, *The role of solvent evaporation in the microstructure of electroactive β-poly(vinylidene fluoride) membranes obtained by isothermal crystallization*, S. Soft Materials, 2010, 9(1): p. 1-14.

[23] Wang, X.; Zhang, L.; Sun, D.; An, Q.; Chen, H., *Formation mechanism and crystallization of poly(vinylidene fluoride) membrane via immersion precipitation method*, Desalination, 2009, 236: p. 170-178.

[24] Ma, W.; Yuan, H.; Wang, X., *The Effect of Chain Structures on the Crystallization Behavior and Membrane Formation of Poly(Vinylidene Fluoride) Copolymers*, Membranes, 2014, 4: p. 243-256.

[25] Dietz, P.; Hansma, P. K.; Inacker, O.; Lehmann, H.-D.; Herrmann, K.-H., *Surface pore structures of micro- and ultrafiltration membranes imaged with the atomic force microscope*, Journal of Membrane Science, 1992, 65: p. 101-111.

[26] Martins, P. M.; Ribeiro, S.; Ribeiro, C.; Sencadas, V.; Gomes, A. C.; Gama, F. M.; Lanceros-Mendez, S., *Effect of poling state and morphology of piezoelectric poly(vinylidene fluoride) membranes for skeletal muscle tissue engineering*, RSC Advances, 2013, 3(39): p. 17938-17944.

[27] Han, R.; Jin, J.; Khanchaitit, P.; Wang, J.; Wang, Q., *Effect of crystal structure on polarization reversal and energy storage of ferroelectric poly(vinylidene fluoride- co-chlorotrifluoroethylene) thin films*, Polymer, 2012, 53(6): p. 1277-1281.

[28] Martins, P.; Lopes, A. C., Lanceros-Mendez, S., *Electroactive phases of poly(vinylidene fluoride): Determination, processing and applications*, Progress in Polymer Science, 2014, 39: p. 683-706.

[29] Boschet, F.; Ameduri, B., *(Co)polymers of Chlorotrifluoroethylene: Synthesis, Properties, and Applications*, Chemical Reviews, 2013, 114(2): p. 927-980.

[30] Yang, X.; Li, Z.; Odum, L.; Cheng, Z.-Y., *Influence of Crystallization Condition on Structure of P(VDF-CTFE) Copolymers*, MRS Online Proceedings Library, 2005, 889, p. 0889-W07-03.1-03.6.

[31] Gregorio, J. R.; Cestari, M., *Effect of crystallization temperature on the crystalline phase content and morphology of poly (vinylidene fluoride)*, Journal of Polymer Science Part B: Polymer Physics, 1994, 32(5): p. 859-870.

[32] Chinaglia, D. L.; Gregorio, R.; Stefanello, J. C.; Pisani Altafim, R. A.; Wirges, W.; Wang, F.; Gerhard, R., *Influence of the solvent evaporation rate on the crystalline phases of solution-cast poly(vinylidene fluoride) films*, Journal of Applied Polymer Science, 2010, 116(2): p. 785-791.

[33] Gee, R. H.; Fried, L. E.; Cook, R. C., *Structure of chlorotrifluoroethylene/Vinylidene fluoride random copolymers and homopolymers by molecular dynamics simulations*, Macromolecules, 2001, 34: p. 3050-3059.

[34] Marega, C.; Marigo, A., *Influence of annealing and chain defects on the melting behaviour of poly(vinylidene fluoride)*, European Polymer Journal, 2003, 39(8): p.1713-1720.

[35] Olabis, O., *Polymer-Polymer Miscibility*, Elsevier Science, Burlington, 2012.

[36] Zhang, M.; Zhang, A.-Q.; Zhu, B.-K.; Du, C.-H.; Xu, Y.-Y., *Air gap membrane distillation of aqueous alcohol solutions*, Journal of Membrane Science, 2008, 319: p. 169-175.

[37] Ward, I. M.; Sweeney, J. *An Introduction to the Mechanical Properties of Solid Polymers*, Wiley, West Sussex (UK), 2004.

[38] Sencadas, V.; Lanceros-Méndez, S.; Sabater i Serra, R.; Andrio Balado, A.; Gómez Ribelles, J. L., *Relaxation dynamics of poly(vinylidene fluoride) studied by dynamical mechanical measurements and dielectric spectroscopy*, The European Physical Journal E, 2012, 35(5): p. 1-11.

[39] Xiao, J.; Zhou, X.; Zhang, Q. M.; Dowben, P., *The effect of defects on the electronicstructure of long chain ferroelectric polymers*, A. Journal of Applied Physics, 2009, 106: p. 44105.

[40] Arisawa, H.; Yano, O.; Wada, Y., *Dielectric loss of poly (vinylidene fluoride) at low temperatures and effect of poling on the low temperature loss*, Ferroelectrics 1981, 32(1): p. 39-41.

[41] Kremer, F.; Schönhals, A., *Broadband Dielectric Spectroscopy*, Springer, Berlin Heidelberg, 2003.

[42] Dyre, J. C., The random free-energy barrier model for ac conduction in disordered solids, *Journal of Applied Physics*, 1988, 64(5): p. 2456-2468.

[43] Gomes, J.; Nunes, J. S.; Sencadas, V.; Lanceros-Mendez, S., *Influence of the β-phase content and degree of crystallinity on the piezo-and ferroelectric properties of poly (vinylidene fluoride)*, Smart Materials and Structures, 2010, 19(6): p.65010.

[44] Wise, D. L., *Electrical and Optical Polymer Systems: Fundamentals: Methods, and Applications*; Taylor & Francis, New York, 1998.

[45] Rubinstein, M.; Colby, R. H., *Polymer Physics*, OUP Oxford, 2003.

[46] Fan, C.F.; Olafson, B.D.; Blanco, M.; Hsu, S. L., *Application of molecular simulation to derive phase diagrams of binary mixtures*, Macromolecules, 1992, 25(15): p. 3667-3676.

[47] Blanco, M. J. J., *Molecular silverware.1. General solutions to excluded volume constrained problems*, Comput. Chem., 1991, 12: p. 237-247.

[48] Robeson, L. M., *Polymer Blends: A Comprehensive Review*, Hanser, 2007.

5. Poly(vinylidene fluoride-co-chlorotrifluoro-ethylene) lithium-ion battery separator membranes

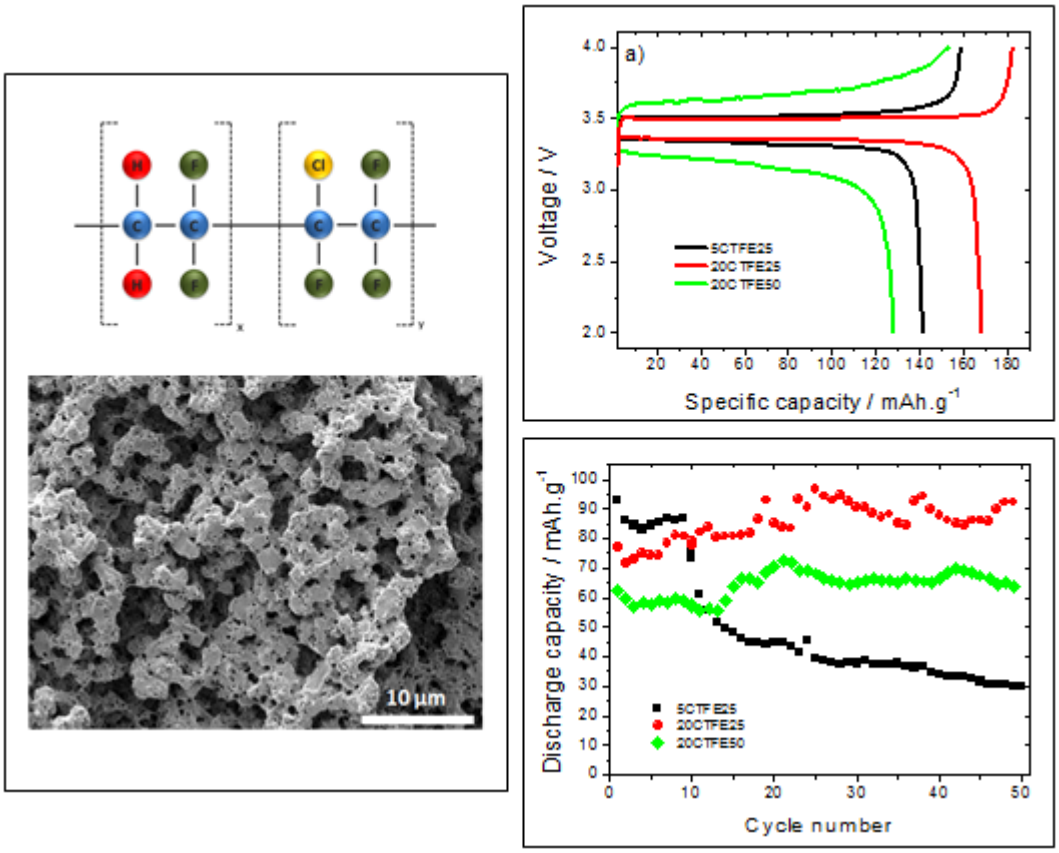

This chapter describes the preparation of poly(vinylidene fluoride-co-chlorotrifluoro-ethylene), P(VdF-CTFE), as separators for lithium batteries, using different polymer/solvent N,N-dimethylformamide (DMF) ratios, as well as their characterization, including physico-chemical and electrochemical characterization, as well as cycling tests, performed on Li/$LiFePO_4$ half-cells with P(VdF-CTFE) as electrolyte separator membrane.

This chapter is based on the following publication: “Poly(vinylidene fluoride-co-chloro-trifluoroethylene) lithium-ion battery separator membranes prepared by phase inversion”, R. E. Sousa, Manab Kundu, A. Gören, M. M. Silva, Lifeng Liu, C. M. Costa and S. Lanceros-Méndez, RSC Advances, 5 (110), 2015, 90428 – 90436.

5.1. Introduction

Rechargeable lithium-ion batteries with higher energy density and safety are necessary taking into account the rapid technological development in applications such as mobile phones, computers, e-labels, e-packaging, disposable medical testers, hybrid electric vehicles (PHEVs) and electric vehicles (EVs) [1, 2].

Rechargeable lithium-ion batteries are one of the most efficient technologies for energy storage [3 – 5], due to their excellent characteristics: they are light, cheap, show high energy density (210 $Wh.kg^{-1}$), low self-discharge rate (2 – 8% per month), no memory effect, prolonged service-life and high number of charge/discharge cycles (> 1000 cycles), high-operation voltage (2.5 – 4.2 V) and capability to store 2 – 3 times the energy per unit weight and volume when compared to Ni-Cd rechargeable batteries [3, 6 – 8].

The basic constituents present in a lithium-ion battery are the anode, cathode and the electrolyte separator. The electrolyte separator separates anode and cathode and serves as the medium for the transfer of charges, preventing internal short circuit and providing a pathway for ionic conduction in the liquid electrolyte [9 – 12]. The electrolyte separator can be constituted by a porous polymer matrix in which the membrane is soaked by the electrolyte solution, i.e., a liquid electrolyte where lithium salts are dissolved in solvents, water or organic molecules. Other possibility for the fabrication the polymer electrolyte separators is the incorporation of the lithium salts directly in the polymer matrix [13]. An ideal separator should have an low ionic resistance and dimensional stability at elevated temperature [8].

Different polymer matrices have been used as separators [12, 14 – 16] such as poly(ethylene oxide) (PEO) [17], poly(acrylonitrile) (PAN) [18], poly(methyl methacrylate) (PMMA) [19], poly(vinyl chloride) (PVC) [20], poly(vinylidene fluoride) (PVdF) [21] and its copolymers, poly(vinylidene fluoride-hexafluoropropylene), P(VdF-HFP) (as studied in chapter 3), poly(vinylidene-fluoride-co-trifluoroethylene), P(VdF-TrFE) [22], and P(VdF-CTFE) [23].

PVdF and its copolymers have excellent properties for being used as separator membrane in comparison with other polymer matrixes [12]. These properties include high polarity, high dielectric constant, low degree of crystallinity, morphology control through binary and ternary polymer/solvent phase diagram, good wettability and electrochemically stability due to the presence of a strong electron-withdrawing group (C-F).

P(VdF-CTFE) is the less studied co-polymer of PVdF for battery separators [12], despite its interesting characteristics: high electromechanical response, high flexibility, high elongation and cold impact resistance (as referred in section 1.1).

P(VdF-CTFE) has been prepared by electrospinning with [24] and without fillers [23] but the battery performance has just been evaluated by Sn–C/PVdF-CTFE/$LiNi_{0.5}Mn_{1.5}O_4$ cells for the material without fillers. It is claimed that this polymer guarantees environmental sustainability, high energy content, low safety hazard and that shows stable behaviour with a capacity decay, for cycles run at rates lower than 1 C, of just 0.06 $mA.h.g^{-1}$ per cycle [23].

Other works with P(VdF-CTFE) polymer for battery separator membranes involve nanofiber-coated polypropylene (PP) separator membranes [25, 26]. It is shown that electrolyte uptake and separator-electrode adhesion are improved by the nanofiber coatings. The improvement in electrolyte uptake is not just related to the gelation capability of the P(VdF-CTFE) nanofibers, but also attributed to the porosity and capillary effect on nanofibrous structure [25]. Thus, in these works it is not presented the electrochemical properties and battery performance of P(VdF-CTFE) polymer.

Taking into account the poor state of the art for this interesting co-polymer, the main goal of this work is to prepare P(VdF-CTFE) membranes with different microstructures and correlate them with battery performance. The different microstructures (i.e., pore size and degree of porosity) are obtained by solvent casting of the binary polymer/solvent (DMF) systems varying systematically polymer concentration and solvent evaporation temperature (as referred in chapter 4).

Morphology, thermal, mechanical and electrical properties were investigated for the different P(VdF-CTFE) membranes, together with battery performance in high-rate capability and cycle life in Li/C-$LiFePO_4$ half-cells.

5.2. Experimental

5.2.1. Materials

P(VdF-CTFE) (Solef 31508; Mw = 270–290 kg/mol; 18.66 wt.% CTFE content) was supplied by Solvay. The solvents DMF (99.5%), propylene carbonate (PC) and lithium bis(trifluoromethanesulfonyl)imide, LiTFSI were purchased from Merck and Sigma-Aldrich, respectively.

5.2.2. Separator membrane preparation

The different experimental steps involved in the P(VdF-CTFE) membrane preparation are shown in Figure 5.1, indicating also relevant parameters such as processing time and temperature.

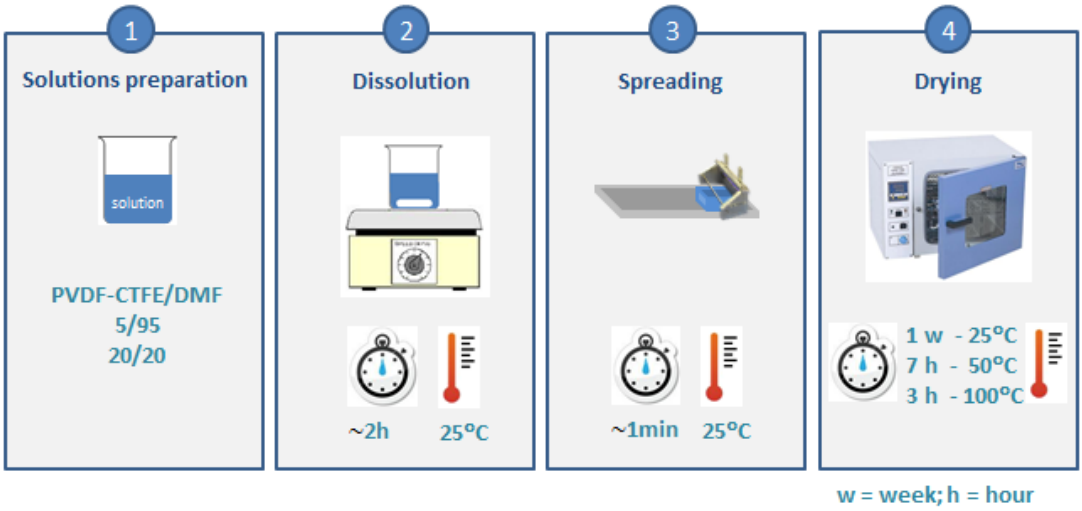

Figure 5.1. Experimental procedure for the P(VdF-CTFE) membrane preparation.

In the solution preparation step, P(VdF-CTFE) polymer concentration in solution of 5 wt.% and 20 wt.% were used. For polymer concentration above 20 wt.%, the polymer showed a large viscosity, being impossible to reach films with good quality. The polymer was dissolved in DMF for 2 hours at 25 ℃, under constant magnetic stirring until a homogeneous solution was obtained (step 2 of Figure 5.1).

Then, the solution was placed on a clean glass substrate, spread by blade coating (once this method produces results similar to the screen printing technique) with the thickness of 100 µm and placed within an air oven (Binder, ED23) for isothermal solvent evaporation at 25 ℃, 50 ℃ and 100 ℃. The samples prepared were identified as (*x* CTFE *y*) where *x* represents the polymer concentration and *y* represents the solvent evaporation temperature.

The initial position of the P(VdF-CTFE) membranes in the phase diagram studied in this work is represented by the blue stars in the phase diagram of the P(VdF-CTFE)/DMF system shown in Figure 5.2.

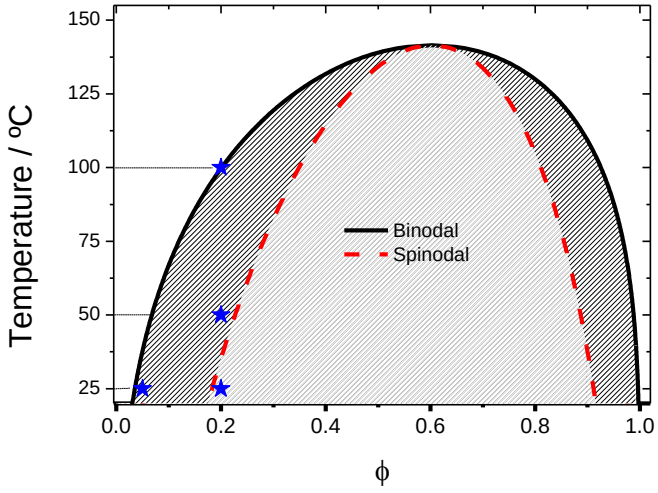

Figure 5.2. Phase diagram of the binary PVdF-CTFE/DMF system.

The samples studied in this work are representative of the possible phase separation dynamics of the P(VdF-CTFE)/DMF system as a function of polymer concentration and evaporation temperature, as shown in chapter 4. This phase diagram presents three main regions: stable, metastable and instable regions where are separated by the binodal and spinodal lines. The phase separation process (pore size and porosity) occur in the metastable region, i.e., region between the spinodal and binodal lines). At room temperature, the phase separation process is dominated by nucleation and growth where the samples are located in the metastable region. For P(VdF-CTFE) concentration below 5 wt.%, the mechanical stability of the membranes is very low whereas for polymer concentration above 20 wt.% P(VdF-CTFE), the viscosity of the system is high, leading to a poor control over the final membrane microstructure.

For a given polymer concentration (e.g., 20 wt.% of P(VdF-CTFE)), but different solvent evaporation temperatures (25 ℃, 50 ℃ and 100 ℃), the system goes through the metastable region to the one phase region (homogeneous microstructure), i.e., no liquid-liquid phase separation is observed.

5.2.3. Electrolyte solution uptake and porosity

The electrolyte solution uptake was performed by immersing the membranes for 24 h in a 1 M LiTFSI in PC electrolyte solution, with an ionic conductivity (σ_0) of 6.5×10^{-3} S.cm^{-1} at 25 ℃.

The uptake value was evaluated according to (3.2), as defined in section 3.2.4.

The porosity of the samples (ϕ) was measured by the pycnometer method [27], using (4.1), as defined in section 4.2.3.

The mean porosity of each membrane was obtained as the average of the values determined in three samples.

5.2.4. Characterization techniques

The morphology of the polymer membranes was analyzed using the method described in section 2.2.3.

Mechanical properties were determined as described in section 3.2.3.

Polymer phase was investigated by Fourier Transformed Infrared (FTIR) spectroscopy and the thermal properties were determined by differential scanning calorimetry (DSC), as described in section 2.2.3.

5.2.5. Electrochemical properties

The ionic conductivity was evaluated by impedance spectroscopy, as described in section 3.2.6, and calculated according to (3.3), defined in section 3.2.6.

The tortuosity (τ) was determined by (3.1), defined in section 3.2.3, with the porosity of the membrane, ϕ obtained according to (4.1), defined in section 4.2.3.

The MacMullin number, N_M, describes the relative contribution of a separator to cell resistance and is therefore related to the effective conduction process. The MacMullin number, N_M, is defined by:

$$N_M = \frac{\sigma_0}{\sigma_{eff}} \tag{5.1}$$

where σ_{eff} is the conductivity of the membrane and liquid electrolyte pair and σ_0 is the conductivity of pure liquid electrolyte [28].

The ionic conductivity temperature dependence follows the Arrhenius equation, as defined by:

$$\sigma_i = \sigma_0 \exp\left(\frac{-E_a}{RT}\right) \tag{5.2}$$

where σ_0, is the pre-exponential factor, E_a is the apparent activation energy for ion transport, R is the gas constant (8.314 J/mol.K) and T is the temperature.

5.2.6. Lithium cell manufacturing and testing

The cathode material was prepared containing C-$LiFePO_4$ (Phostech Lithium, Lda), carbon black (Super P, Timcal Graphite & Carbon, Switzerland) and PVdF (Binder, Solef 5130, Solvay) in a weight of 8:1:1 in the slurry with N-methyl-1-pyrrolidone (NMP) solvent. After stirring, the slurry was casted on an aluminum foil through doctor-blade technique and dried at 100 ℃ for 4 h in a conventional oven, Binder (ED23 oven). The active mass loading of the cathode material was ~ 2.5 $mg.cm^{-2}$.

All separator membranes studied in this work were immersed in the electrolyte solution (1M LiTFSI in PC) for 10 minutes within an argon filled glove box (JACOMEX, Germany, the moisture and oxygen levels of the glove box being ~ 1.0 ppm.

2032 coin-type Li/C-$LiFePO_4$ half-cells were prepared using the swollen membranes as separators (14 mm diameter), metallic lithium (10 mm diameter) as anode and C-$LiFePO_4$ electrode as cathode (10 mm diameter).

Charge-discharge and cycling tests were carried out at room temperature in the voltage

range of 2.0 V and 4.0 V at a current density between 0.1C and 2C using a Biologic VMP3 station. The activation cycle was carried out at 0.1C (17 $mA.g^{-1}$) in all cases.

5.3. Results and discussion

Morphology and microstructure of the samples were investigated by SEM images, as the microstructure strongly affects the performance of the battery [22].

Representative SEM images of the cross-section of the separator membranes are shown in Figure 5.3.

For all samples except for the 20CTFE100 a porous morphology is observed with uniform pore features and porosity distribution along the thickness of the samples.

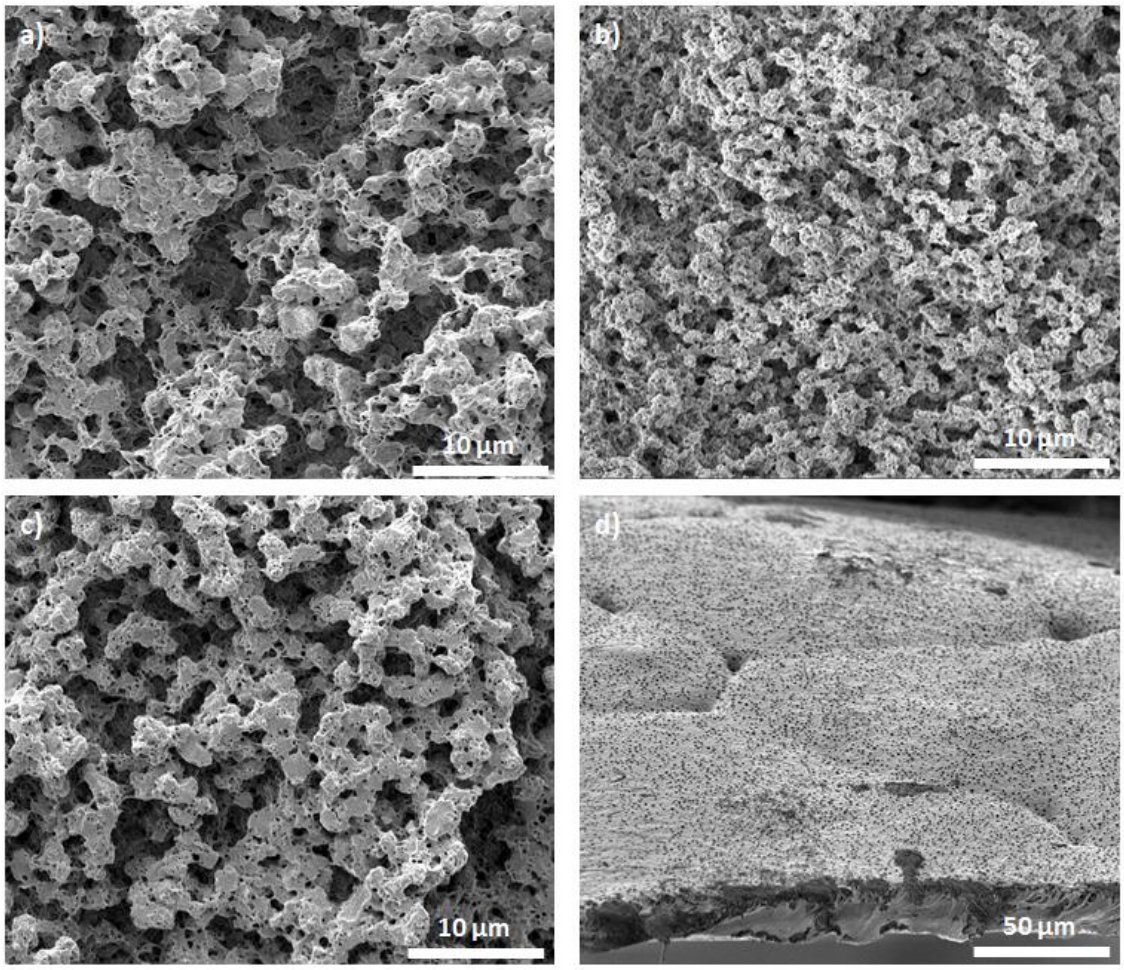

Figure 5.3. Cross section images of the membranes prepared from the P(VdF-CTFE)/DMF solution: solvent evaporation at 25 ℃ for 5 wt % (a) and 20 wt % (b) of P(VdF-CTFE) samples. Samples with 20 wt % of P(VdF-CTFE) with solvent evaporation at 50 ℃ (c) and 100 ℃ (d).

This fact is explained by the position of each sample in the phase diagram of the P(VdF-CTFE)/DMF system (Figure 5.2), as explained in chapter 4.

The samples show a particulate microstructure in that the spherulitic size depends on the polymer concentration and solvent evaporation temperature.

The porous morphology of the 5CTFE25, 20CTFE25 and 20CTFE50 is due to the lower polymer chains mobility when the solvent is evaporated a low temperature so that the polymer do not occupy the free space left by the solvent where the phase separation occurs.

In relation to the 20CTFE100 sample, (Figure 5.3 d)), cross section plus surface morphology of the membrane), the top of the sample shows a slightly different pore structure with pore sizes around 2 μm resulting from the rapid evaporation of the solvent. On the other hand, the cross-section image of this sample shows a compact structure without the presence of the pores.

The degree of crystallinity, as obtained by differential scanning calorimetry, and β-phase content, as obtained by infrared spectroscopy, of the samples, calculated after the procedures indicated in detail in chapter 4, together with the degree of porosity are summarized in Table 5.1.

The degree of crystallinity and β -phase content slightly depends on polymer concentration and solvent evaporation temperature, the variations being therefor not relevant for the influence in battery performance [12, 29].

Table 5.1. Degree of porosity, β-phase content and degree of crystallinity for the prepared membranes.

Samples	**Porosity / % ± 5%**	**β-phase / % ± 2%**	**χ/ % ± 2%**
5CTFE25	71	56	21
20CTFE25	60	33	27
20CTFE50	40	26	25
20CTFE100	35	87	15

Table 5.1 shows that with solvent evaporation at 25 ℃, the degree of porosity is between 70% and 60% for polymer concentration between 5 to 20 wt.% in the solution. It is also shown that the degree of porosity decreases with increasing solvent evaporation temperature due the increase of the solvent evaporation rate, polymer chain mobility and no phase separation process. For 20CTFE100 sample, the degree of porosity value present in Table 5.1 refers only to porosity value in the top layer of the sample.

One of the most relevant parameters in separator membranes is the uptake value once an elevated electrolyte solution content, facilitates ion transport between the two electrodes during the charge and discharge process [30]. The uptake value of the electrolyte solution for the separator membranes as a function of dipping time is shown in Figure 5.4. For all samples, the saturation is achieved after approximately 10 min, with an electrolyte solution content indicating that the void volume of the porous membranes was fully filled.

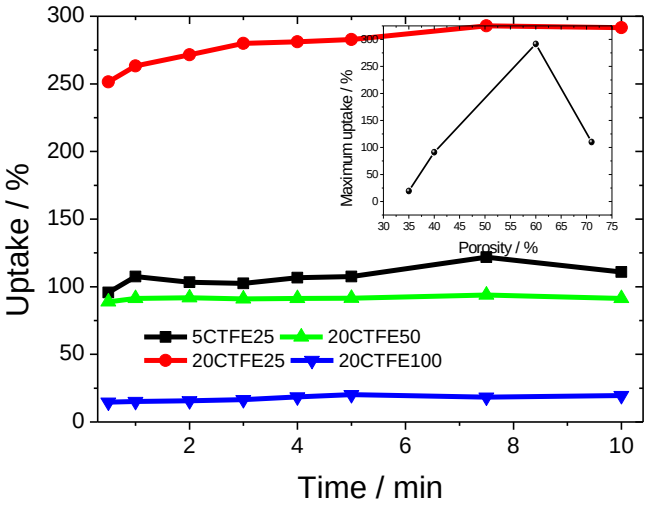

Figure 5.4. Electrolyte uptake value as a function of time for the P(VdF-CTFE) separators samples.

The correlation between uptake value and degree of porosity is revealed in Figure 5.4, i.e., the uptake value increases with increasing the degree of porosity for the PVdF-CTFE membranes with 20 wt.% polymer concentration. This fact is also observed in the insert of Figure 5.4, showing the correlation between maximum uptake and degree of porosity.

In particular, for solvent evaporation temperature at 25 ℃, the highest uptake value (~ 290%) is observed for the P(VdF-CTFE) membranes with 20 wt.% polymer concentration. The enhanced interaction between this sample and electrolyte solution is attributed to the initial polymer concentration which is beneficial for cycling performance [31].

To ensure safe operation of the battery, the mechanical properties of the separator are essential for dimensional stability and to avoid short-circuit and therefore electrical contact between electrodes [32]. The mechanical properties of the P(VdF-CTFE) membranes were determined by the stress-strain curves, as represented in Figure 5.5.

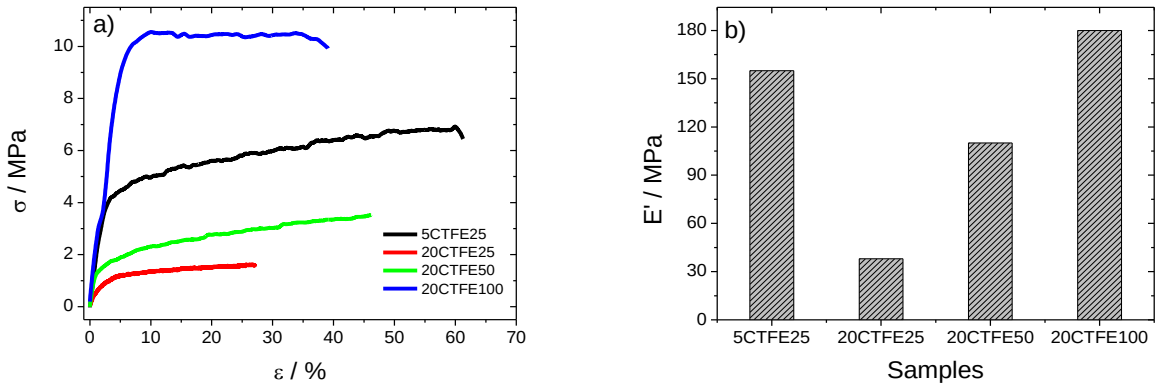

Figure 5.5. a) Stress-strain curves and b) Young's modulus (*E´*) for the P(VdF-CTFE) separators samples.

Figure 5.5 shows the stress–strain curves (left) and the Young's modulus (right) of the samples. All stress-strain curves (Figure 5.5 a)) show the typical characteristics of thermoplastic PVdF polymers, characterized by the elastic and inelastic regions separated by the yielding stress and strain [33].

As the degree of crystallinity of the samples in similar (Table 5.1), the differences observed in the mechanical measurements presented in Figure 5.5 a) are fully ascribed to the different microstructures and degree of porosity of the samples (Figure 5.3 and Table 5.1).

Figure 5.5 b) shows the Young's modulus calculated from the strain-stress curves shown in Figure 5.5 a) through the slope in the elastic region at a deformation of 5%. It is observed that for a given initial polymer concentration in the solutions, 20 wt.%, the Young's modulus increases with increasing the solvent evaporation temperature due to a decrease of the degree of porosity.

In relation a given solvent evaporation temperature, 25 ℃, the difference of the Young's modulus within the different two samples is also in agreement with the different porous morphology of the samples (Figure 5.3). Finally, the mechanical properties of the samples are suitable for lithium-ion battery applications.

Impedance spectroscopy measurements were used for the determination of the ionic conductivity of the P(VdF-CTFE) membranes soaked with the electrolyte solution at different temperatures.

Figure 5.6 shows the Nyquist plot at 25 ℃ for the different P(VdF-CTFE) separator membranes.

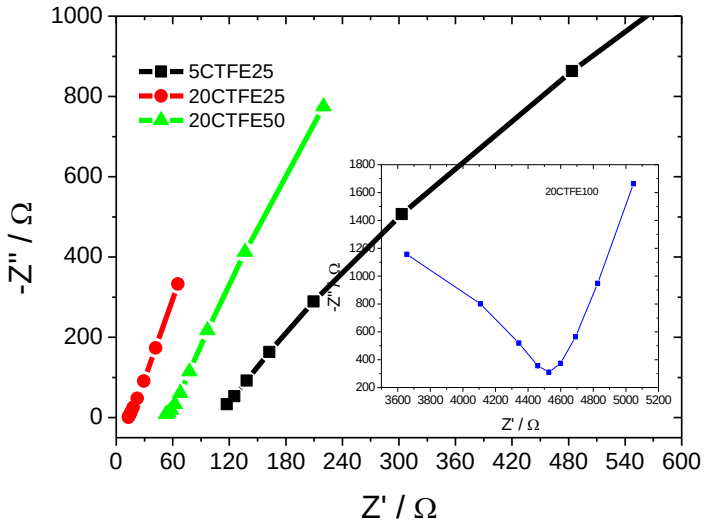

Figure 5.6. Nyquist plots for the P(VdF-CTFE) separators samples.

Figure 5.6 shows for the 5CTFE25, 20CTFE25 and 20CTFE50 samples the inclined straight line inclined that represents the electrode/electrolyte double layer capacitance behaviour [34]. For the 20CTFE100 sample, the Nyquist plot consists in a high frequency semicircle followed by a lower frequency straight line, which correspond to the bulk resistance contribution and the diffusion of lithium ions, respectively [35]. The disappear of the high frequency semi-circle for 5CTFE25, 20CTFE25 and 20CTFE50 samples indicates an increase of the total conductivity due to its microstructure and uptake value [36]. The resistance of the P(VdF-CTFE) membranes

soaked with electrolyte solution has been determined by the intersection of the straight line on the real axis [22].

The ionic conductivity value for the P(VdF-CTFE) separator membranes is presented in Table 5.2, showing ionic conductivity values above 10^{-4} S.cm^{-1} at room temperature, value that is suitable for lithium battery applications, except for the 20CTFE100 sample [37].

Table 5.2. Room temperature ionic conductivity value, tortuosity, MacMullin number (N_m) and activation energy (E_a) for the P(VdF-CTFE) separator membranes soaked in 1 M LiTFSI-PC.

Samples	σ_i / mS.cm^{-1}	T	N_m	E_a / kJ.mol^{-1}
5CTFE25	0.06	9.0	108.3	8.0
20CTFE25	1.5	1.6	4.3	4.7
20CTFE50	0.21	5.1	30.9	3.1
20CTFE100	2.8×10^{-3}	28.5	2321.4	9.1

Table 5.2 shows that the highest ionic conductivity value is obtained for the P(VdF-CTFE) separator membrane with the highest electrolyte uptake, i.e., ionic conductivity value is, as expected, mainly determined by the liquid electrolyte uptake, which in turn depends on the degree of porosity of the samples (Table 5.1).

Table 5.2 also shows the tortuosity value and the MacMullin number (N_m) calculated by (3.1) (defined in section 3.2.3) and (5.1), respectively.

The tortuosity value gives information about the conduction process, i.e., the pore connectivity describes a conductivity pathway for the faster ion transport [12]. The value of tortuosity of the P(VdF-CTFE) separator membranes are between 1.6 and 28.5 depending on the degree of porosity and electrolyte uptake value. The lower tortuosity value is observed for the 20CTFE25 sample, and is close to the ideal value, which supports better pore connectivity, leading to faster ion transport properties and, consequently, to high battery cycling performance and rate capability [38].

It is also is observed that the MacMullin number (N_m) is comprehended between 4.3 to 2321.4 which in turn is correlated with the tortuosity value, degree of porosity and electrolyte uptake value of the samples. The lowest value of the MacMullin number is obtained for the 20CTFE25 sample, with a high degree of porosity, electrolyte uptake and ionic conductivity values and low tortuosity.

Table 5.3 compares the physico-chemical properties of the P(VdF-CTFE) separator membranes developed in this work with related ones reported in the literature.

Table 5.3. Ionic conductivity value and degree of porosity for the best P(VdF-CTFE) sample produced in this work and comparison with other various PVdF separator membranes reported in the literature. The electrolyte solution is also indicated.

Samples	σ_i/ mS/cm	Porosity %	Electrolyte solution	Ref
P(VdF-CTFE)	1.5	60	1M LiTFSI in PC	This work
P(VdF-CTFE)	2	-----	1M $LiPF_6$ in EC:DMC	[23]
P(VdF-HFP)	1.5-2	-----	1M $LiPF_6$ in EC/DEC	[39]
P(VdF-HFP)	0.8	-----	1M $LiPF_6$ in EC/PC	[40]
PVdF	0.13	75	1M LiTFSI in EC/DEC	[41]
PVdF	1.4	70	1M $LiPF_6$ in EC/DMC/EMC	[42]
PVdF-TrFE	2.6	72	1M $LiPF_6$ in EC:DMC	[22]

The ionic conductivity value determined for the P(VdF-CTFE) sample is analogous or superior to the values observed for other PVdF separator membranes reported in the literature (Table 5.3). The differences can be related to the microstructure but also to the degree of porosity and electrolyte uptake value once that the ionic conductivity value of the various electrolyte solutions is similar [43]. The difference between the ionic conductivity value for the P(VdF-CTFE) sample obtained in this work and the other one reported in the literature [23] is related to the processing technique: in the present work, the P(VdF-CTFE) membrane was produced by solvent casting technique, whereas the one reported in the literature was produced by electrospinning technique. Also the P(VdF-CTFE) sample produced by electrospinning technique has high porosity and uptake value and low mechanical properties in comparison of P(VdF-CTFE) membrane produced in this work.

The ionic conductivity as a function of temperature is illustrated in Figure 5.7, and a linear correlation is observed in the temperature range between 25 ℃ and 100 ℃. This behaviour indicates that the ionic conductivity as a function of temperature obeys the Arrhenius model [44].

The activation energy for ion transportation calculated through the fitting with (5.2) to the data presented in Figure 5.7 is shown in Table 5.2. The activation energy E_a value is proportional to the ionic conductivity and electrolyte uptake values. For the 20CTFE25 sample with higher ionic conductivity and electrolyte uptake values, the E_a value is 4.7 $kJ.mol^{-1}$. This low E_a shows the weak dependence of the conductivity with temperature, fact which is an advantage for battery applications.

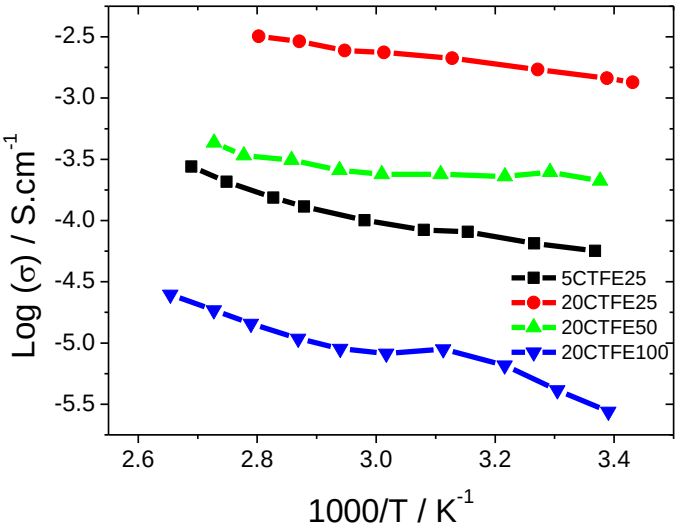

Figure 5.7. Log σ as a function of 1000/T for the P(VdF-CTFE) separator membranes.

For the different P(VdF-CTFE) separator membranes, the ionic conductivity value increases with increasing temperature as observed in Figure 5.7. This behaviour is due to the increase of the free volume and segmental mobility of the polymer with increasing temperature leading to higher ion mobility of the ionic charge carriers [45].

Further, the heating scan shown in Figure 5.7 shows the good stability of the ionic conductivity value for the P(VdF-CTFE) separator membranes in the temperature range between 25 ℃ to 100 ℃.

The battery performance of the P(VdF-CTFE) membranes was evaluated in Li/C-$LiFePO_4$ cathodic half-cells at room temperature. The 5CTFE25, 20CTFE25 and 20CTFE samples were selected for charge-discharge evaluation taking into account its ionic conductivity value (Figure 5.6 and Table 5.3). Charge-discharge curves of the 5CTFE25 samples in the first cycle at different scan rates from 0.1C to 2C are shown in Figure 5.8.

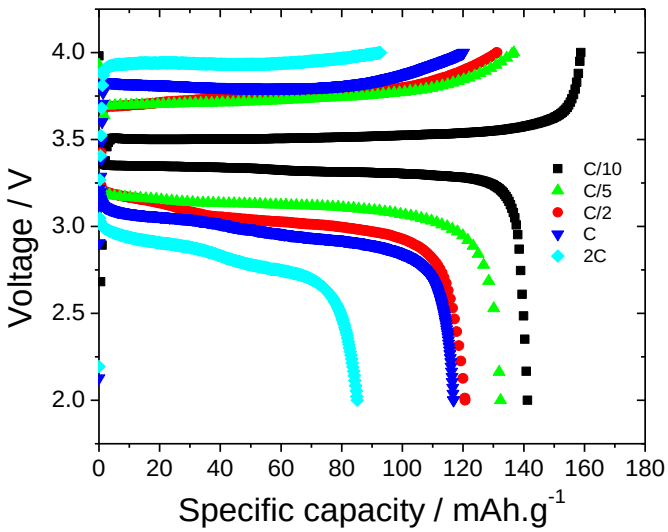

Figure 5.8. Charge-discharge profiles for 5CTFE25 at different scan rates.

The profiles shown in Figure 5.8 are characterized by two pseudoplateaus varying between 3.2 and 3.8V that depend of the scan rate and reflects the typical electrochemical behaviour of the C-$LiFePO_4$ spinel for the reversible charge (lithium removal)-discharge (lithium insertion) cycling process. Through Figure 5.8, we see that the discharge capacity is 142 $mA.h.g^{-1}$, 132 $mA.h.g^{-1}$, 121 $mA.h.g^{-1}$, 117 $mA.h.g^{-1}$, and 85 $mA.h.g^{-1}$ at rates of C/10, C/5, C/2, C and 2C, respectively. Figure 5.8 also shows that the voltage and discharge capacity value decreases progressively as the scan rates increase, which is a result the significant influence of ionic transport on ohmic polarization [34].

The charge-discharge behaviour as a function of different scan rates for the 5CTFE25 sample is representative to the one observed for the other two samples.

Figure 5.9 depicts a comparison of the room temperature charge-discharge curves at C/10 (Figure 5.9 a)) and 2C (Figure 5.9 b)) for the half-cell containing the different P(VdF-CTFE) separator membranes. At C/10 (Figure 5.9 a)), half-cells using 20CTFE25, 5CTFE25 and 20CTFE50 showed stable charge-discharge profiles with discharge capacity about 168 $mA.h.g^{-1}$, 141 $mA.h.g^{-1}$ and 127 $mA.h.g^{-1}$, respectively. Also for 2C (Figure 5.9 b)), it is observed a cycling behaviour similar to C/10 but with lower discharge capacity value. For 2C, the discharge capacity value is 102 $mA.h.g^{-1}$, 85 $mA.h.g^{-1}$ and 69 $mA.h.g^{-1}$ for 20CTFE25, 5CTFE25 and 20CTFE50 samples, respectively.

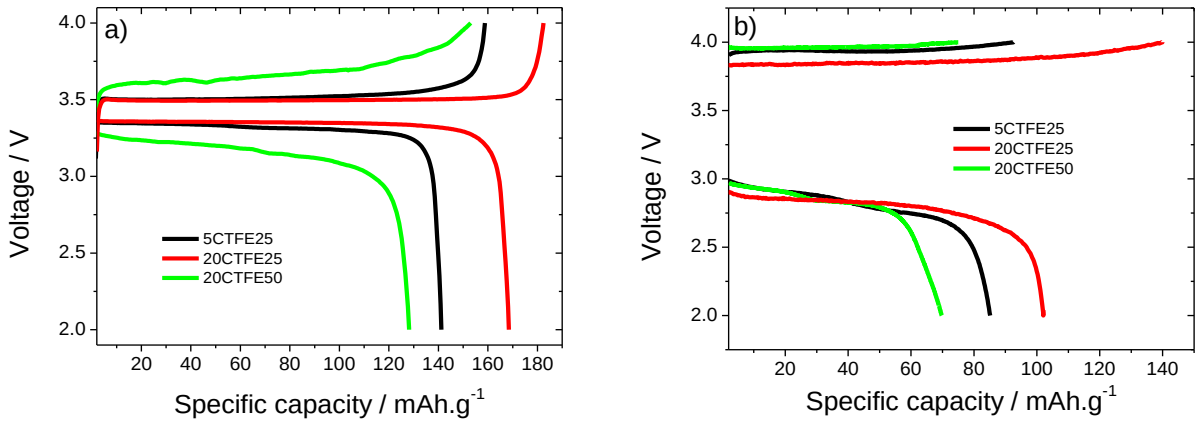

Figure 5.9. Charge-discharge profiles for the P(VdF-CTFE) separator membranes at a) C/10 and b) 2C.

The discharge capacity value of the 20CTFE25 sample is higher in comparison to the other P(VdF-CTFE) separator membranes (5CTFE25 and 20CTFE50 samples) for low (C/10) and high (2C) scan rates. This fact is due to the higher conduction of Li^+ ions (ionic conductivity value) resulting from the higher electrolyte uptake value of the 20CTFE25 samples

The cycling performance of the C-$LiFePO_4$ half-cells is shown in Figure 5.10. For half cells containing 20CTFE25, 20CTFE50 and 5CTFE25 samples, the discharge capacity values after 50 cycles are 92 $mA.h.g^{-1}$, 64 $mA.h.g^{-1}$ and 30 $mA.h.g^{-1}$, respectively.

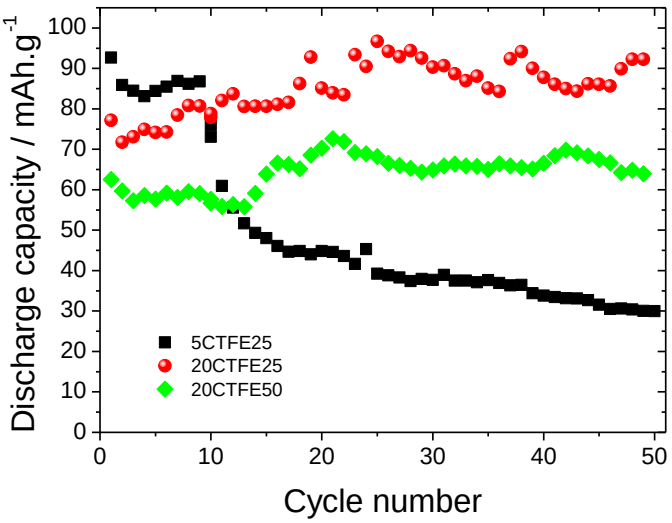

Figure 5.10. Cycling performance of C-$LiFePO_4$ cathodic half cells containing the different P(VdF-CTFE) separator membranes at 2C.

The corresponding capacity retentions after 50 cycles is 54%, 38% and 18%, respectively. The capacity retentions were calculated based on the theoretical capacity, 170 $mA.h.g^{-1}$, of C-$LiFePO_4$.

The higher discharge value and capacity retention after 50 cycles of the half-cell with 20CTFE25 sample is attributed to the higher ionic conductivity and electrolyte uptake value that facilitates the repeated lithium-ion insertion/de-insertion in/from the C-$LiFePO_4$ electrodes even at high scan rate, as demonstrated in Figure 5.10.

In conclusion, the 20CTFE25 sample shows high discharge capacity value with high rate capability. However, it is observed in Figure 5.10 at 2C (charge and/or discharge process in half an hour), that the battery with the 20CTFE25 membrane shows a discharge value of 92 $mA.h.g^{-1}$, which is still 54% of the theoretical value.

This fact is very good and means that in half an hour the battery has 54% of its capacity value for release all stored charge or being completely recharged.

5.4. Conclusions

Regarding to P(VdF-CTFE) separator membranes, they have been prepared by solvent casting through its phase diagram with DMF solvent. Different morphologies have been obtained varying initial polymer concentration in the solution and solvent evaporation temperature. A porous microstructure is achieved for P(VdF-CTFE) membranes with solvent evaporation temperature up to 50 ℃.

The mechanical properties of the P(VdF-CTFE) separator membranes are suitable for lithium-ion batteries and are correlated with the degree of porosity and microstructure of the membranes. Also the ionic conductivity value depends on the degree of porosity and electrolyte uptake value. The best ionic conductivity value at room temperature is 1.5 $mS.cm^{-1}$ for the membrane prepared with 20 wt.% initial polymer concentration and solvent evaporation temperature at 50 ℃, leading to a degree of porosity of 60% and an electrolyte uptake value of 292% .

The prepared P(VdF-CTFE) separator membranes show good cyclability and rate capability. At C/10 and 2C presents the discharge values are 168 and 92 $mA.h.g^{-1}$, respectively. P(VdF-CTFE) separators are thus excellent candidate for their use in high-power and safety lithium-ion batteries applications.

5.5. References

[1] R. Huggins, Advanced Batteries: Materials Science Aspects, Springer, New York, 2008.

[2] P.G. Bruce, B. Scrosati, J.-M. Tarascon, *Nanomaterials for rechargeable lithium batteries*, Angewandte Chemie - International Edition, 2008, 47(16): p. 2930–2946.

[3] J.-M. Tarascon, *Key challenges in future Li-battery research*, Philosophical Transactions of the Royal Society A: Mathematical, Physical and Engineering Sciences, 2010, 368: p. 3227-3241.

[4] J.M. Tarascon, M. Armand, *Issues and challenges facing rechargeable lithium batteries*, Nature, 2001, 414: p. 359-367.

[5] W.A. Van Schalkwijk, B. Scrosati, *Advances in Lithium-Ion Batteries*, Kluwer Academic/Plenum Publishers, Boston, 2002.

[6] M. Wakihara, O. Yamamoto, *Lithium Ion Batteries: Fundamentals and Performance*, John Wiley & Sons, New York, 2008.

[7] K.E. Aifantis, S.A. Hackney, R.V. Kumar, *High Energy Density Lithium Batteries: Materials, Engineering, Applications*, John Wiley & Sons, New York, 2010.

[8] X. Huang, *Separator technologies for lithium-ion batteries*, J Solid State Electrochem, 2011, 15: p. 649-662.

[9] P.B. Balbuena, Y. Wang, *Lithium-Ion Batteries: Solid-Electrolyte Interphase*, Imperial College Press, London, 2004.

[10] K.H.J. Buschow, *Encyclopedia of materials: science and technology*, Elsevier, Cambridge, 2001.

[11] L.-L. Zhang, Z.-L. Wang, D. Xu, X.-B. Zhang, L.-M. Wang, *The development and challenges of rechargeable non-aqueous lithium–air batteries*, International Journal of Smart and Nano Materials, 2012, 4(1): p. 27-46.

[12] C.M. Costa, M.M. Silva, S. Lanceros-Mendez, *Battery separators based on vinylidene fluoride (VDF) polymers and copolymers for lithium ion battery applications*, RSC Advances, 2013, 3(29): p. 11404-11417

[13] P. Arora, Z. Zhang, *Battery Separators*, Chemical Reviews, 2004, 104(10): p. 4419-4462.

[14] H. Lee, M. Yanilmaz, O. Toprakci, K. Fu, X. Zhang, *A review of recent developments in membrane separators for rechargeable lithium-ion batteries*, Energy & Environmental Science, 2014, 7(12): p. 3857-3886.

[15] V. Deimede, C. Elmasides, *Separators for Lithium-Ion Batteries: A Review on the Production Processes and Recent Developments*, Energy Technology, 2015, 3(5): p. 453-468.

[16] A. Manuel Stephan, K.S. Nahm, *Review on composite polymer electrolytes for lithium batteries*, Polymer, 2006, 47(16), p. 5952-5964.

[17] F.S. Fiory, F. Croce, A. D'Epifanio, S. Licoccia, B. Scrosati, E. Traversa, *PEO based polymer electrolyte lithium-ion battery*, Journal of the European Ceramic Society, 2004, 24(6): p. 1385-1387.

[18] A.I. Gopalan, P. Santhosh, K.M. Manesh, J.H. Nho, S.H. Kim, C.-G. Hwang, K.-P. Lee, *Development of electrospun PVdF–PAN membrane-based polymer electrolytes for lithium batteries*, Journal of Membrane Science, 2008, 325(2): p. 683-690.

[19] O. Bohnke, G. Frand, M. Rezrazi, C. Rousselot, C. Truche, *Fast ion transport in new lithium electrolytes gelled with PMMA. 1. Influence of polymer concentration*, Solid State Ionics, 1993, 66(1-2): p. 97-104.

[20] Z. Zhong, Q. Cao, B. Jing, X. Wang, X. Li, H. Deng, *Electrospun PVdF-PVC nanofibrous polymer electrolytes for polymer lithium-ion batteries*, Materials Science and Engineering: B, 2012, 177(1): p. 86-91.

[21] A. Magistris, E. Quartarone, P. Mustarelli, Y. Saito, H. Kataoka, *PVDF-based porous polymer electrolytes for lithium batteries*, Solid State Ionics, 2002, 152–153: p. 347-354.

[22] C.M. Costa, J.L. Gomez Ribelles, S. Lanceros-Méndez, G.B. Appetecchi, B. Scrosati, *Poly(vinylidene fluoride)-based, co-polymer separator electrolyte membranes for lithium-ion battery systems*, Journal of Power Sources, 2014, 245: p. 779-786.

[23] F. Croce, M.L. Focarete, J. Hassoun, I. Meschini, B. Scrosati, *A safe, high-rate and high-energy polymer lithium-ion battery based on gelled membranes prepared by electrospinning*, Energy & Environmental Science, 2011, 4(3): p. 921-927.

[24] M. Zaccaria, C. Gualandi, D. Fabiani, M.L. Focarete, F. Croce, *Effect of oxide nanoparticles on thermal and mechanical properties of electrospun separators for lithium-ion batteries*, Journal of Nanomaterials, 2012, 2012: p. 8.

[25] H. Lee, M. Alcoutlabi, J.V. Watson, X. Zhang, *Polyvinylidene Fluoride-co-Chlorotrifluoroethylene and Polyvinylidene Fluoride-co-Hexafluoropropylene Nanofiber-Coated Polypropylene Microporous Battery Separator Membranes*, Journal of Polymer Science Part B: Polymer Physics, 2013, 51: p. 349-357.

[26] M. Alcoutlabi, H. Lee, J. Watson, X. Zhang, *Preparation and properties of nanofiber-coated composite membranes as battery separators via electrospinning*, J Mater Sci, 2013, 48(6): p. 2690-2700.

[27] A. California, V.F. Cardoso, C.M. Costa, V. Sencadas, G. Botelho, J.L. Gómez-Ribelles, S. Lanceros-Mendez, *Tailoring porous structure of ferroelectric poly(vinylidene fluoride-trifluoroethylene) by controlling solvent/polymer ratio and solvent evaporation rateEuropean Polymer Journal*, 2011, 47(12): p. 2442-2450.

[28] K.K. Patel, J.M. Paulsen, J. Desilvestro, *Numerical simulation of porous networks in relation to battery electrodes and separators*, Journal of Power Sources, 2003, 122(2): p. 144-152.

[29] J. Nunes-Pereira, C.M. Costa, S. Lanceros-Méndez, *Polymer composites and blends for battery separators: State of the art, challenges and future trends*, Journal of Power Sources, 2015, 281: p. 378-398.

[30] W.-K. Shin, J.-H. Yoo, D.-W. Kim, *Surface-modified separators prepared with conductive polymer and aluminum fluoride for lithium-ion batteries*, Journal of Power Sources, 2015, 279: p. 737-744.

[31] J. Shi, H. Hu, Y. Xia, Y. Liu, Z. Liu, *Polyimide matrix-enhanced cross-linked gel separator with three-dimensional heat-resistance skeleton for high-safety and high-power lithium ion batteries*, Journal of Materials Chemistry A, 2014, 2: p. 9134-9141.

[32] J. Cannarella, X. Liu, C.Z. Leng, P.D. Sinko, G.Y. Gor, C.B. Arnold, *Mechanical properties of a battery separator under compression and tension*, Journal of The Electrochemical Society, 2014, 161(11): p. F3117-F3122.

[33] C.M. Costa, V. Sencadas, I. Pelicano, F. Martins, J.G. Rocha, S. Lanceros-Mendez, *Microscopic origin of the high-strain mechanical response of poled and non-poled poly(vinylidene fluoride) in the β-phase*, Journal of Non-Crystalline Solids, 2008, 354: p. 3871-3876.

[34] W. Xiao, L. Zhao, Y. Gong, S. Wang, J. Liu, C. Yan, *Preparation of high performance lithium-ion batteries with a separator–cathode assembly*, RSC Advances, 2015, 5: p. 34184-34190.

[35] B.-Y. Chang, S.-M. Park, *Electrochemical Impedance Spectroscopy*, Annual Review of Analytical Chemistry, 2010, 3: p. 207-229.

[36] J. Malathi, M. Kumaravadivel, G.M. Brahmanandhan, M. Hema, R. Baskaran, S. Selvasekarapandian, *Structural, thermal and electrical properties of PVA–LiCF 3 SO 3 polymer electrolyte*, Journal of Non-Crystalline Solids, 2010, 356(43): p. 2277-2281.

[37] J. Hassoun, D.-J. Lee, Y.-K. Sun, B. Scrosati, *A lithium ion battery using nanostructured Sn-C anode, LiFePO"4 cathode and polyethylene oxide-based electrolyte*, Solid State Ionics, 2011, 202(1): p. 36-39.

[38] G. Venugopal, J. Moore, J. Howard, S. Pendalwar, *Characterization of microporous separators for lithium-ion batteries*, Journal of Power Sources, 1999, 77(1): p. 34-41.

[39] Y. Wang, J. Travas-Sejdic, R. Steiner, *Polymer gel electrolyte supported with microporous polyolefin membranes for lithium ion polymer battery*, Solid State Ionics, 2002, 148(3-4): p. 443-449.

[40] J.M. Tarascon, A.S. Gozdz, C. Schmutz, F. Shokoohi, P.C. Warren, *Performance of Bellcore's plastic rechargeable Li-ion batteries*, Solid State Ionics, 1996, 86–88, Part 1: p. 49-54.

[41] Y. Saito, H. Kataoka, E. Quartarone, P. Mustarelli, *Carrier migration mechanism of physically cross-linked polymer gel electrolytes based on PVDF membranes*, The Journal of Physical Chemistry B, 2002, 106: p. 7200-7204.

[42] G.-L. Ji, B.-K. Zhu, Z.-Y. Cui, C.-F. Zhang, Y.-Y. Xu, *PVDF porous matrix with controlled microstructure prepared by TIPS process as polymer electrolyte for lithium ion battery*, Polymer, 2007, 48: p. 6415-6425.

[43] A. Gören, C.M. Costa, M.M. Silva, S. Lanceros-Méndez, *State of the art and open questions on cathode preparation based on carbon coated lithium iron phosphate*, Composites Part B: Engineering, 2015, 83: p. 333-345.

[44] C.M. Costa, L.C. Rodrigues, V. Sencadas, M.M. Silva, S. Lanceros-Méndez, *Effect of the microsctructure and lithium-ion content in poly[(vinylidene fluoride)-co-trifluorethylene)]/lithium perchlorate trihydrate composite membranes for battery applications*, Solid State Ionics, 2012, 217: p. 19-26.

[45] F.M. Gray, R.S.O. Chemistry, *Polymer Electrolytes*, Royal Materials Monographs (Royal Society of Chemistry), London, 1997.

6. High performance screen printable lithium-ion battery cathode ink based on C-$LiFePO_4$ and anode ink based on graphite

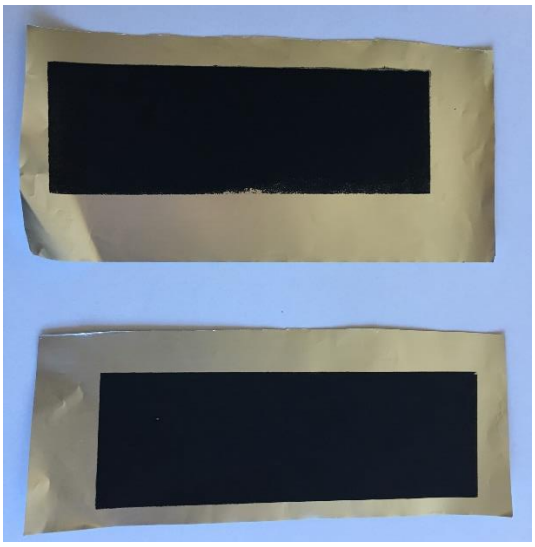

Screen printing is among the most interesting technologies for lithium-ion battery fabrication by printing technologies. Taking into account that $LiFePO_4$ is among the most promising active materials, the main objective of this chapter is the development of a new ink formulation based on carbon coated $LiFePO_4$, suitable for screen printing.

The rheological properties of the ink and the polymer solution, as well as the cathode film electrochemical properties, including impedance spectroscopy, cycling voltammetry and charge-discharge performance, were determined. Finally, an anode ink based on graphite is also presented.

This chapter is based on the following publication: "High performance screen printable lithium-ion battery cathode ink based on C-$LiFePO_4$", R. E. Sousa, J. Oliveira, A. Gören, D. Miranda, M. M. Silva, Loic Hilliou, C. M. Costa, S. Lanceros-Mendez, Electrochimica Acta, 196, 2016, 92-100.

6.1. Cathode

6.1.1. Introduction

The growing demand of energy produced by renewable sources such as solar, wind or biomass, together with the constant development and use of portable electronic devices, such as mobile-phones and computers [1, 2], leads to an increasing need of efficient energy storage systems for increasing autonomy and life time of the products [3].

Nowadays, the most important energy storage systems are rechargeable batteries [4, 5] and, among them, lithium-ion batteries represent 75% of the global rechargeable battery market as they show high energy density, flexible and lightweight design, and longer lifespan than other competing battery technologies [6 – 9].

Lithium-ion battery main constituents are cathode, anode and a separator membrane [10] and thus, a wide range of materials are being developed for those components in order to improve specific energy, power, safety and reliability [7].

Cathodes are typically composed by a polymer binder, conductive additive and active material, and is responsible for the cell capacity and cycle life [11].

Among the different active materials used for lithium-ion batteries, such as lithium iron phosphate ($LiFePO_4$), lithium nickel manganese cobalt oxide ($LiNiMnCoO_2$), lithium nickel cobalt aluminum ($LiNiCoAlO_2$), lithium titanate oxide ($LiTiO_2$) and lithium manganese spinel oxide ($LiMn_2O_4$), among others, $LiFePO_4$ stands out due to its moderately low cost, high rate performance, slow reaction with electrolyte and increased safety (no oxygen release) [12, 13]. It also shows low density (3.6 $g.cm^{-3}$) and a high theoretical capacity of 170 $mA.h.g^{-1}$ (2.0 – 4.0V) [14, 15].

The increasing trend towards miniaturization, integration and flexibility of lithium-ion batteries for the development of smart cards, RFID tags and remote sensors, leads to the consideration of printing technologies (as referred in Chapter 1) for the fabrication of batteries.

Printing technologies allow to obtain batteries which are thinner and lighter in comparison to conventional batteries, the printing process also allowing cost reduction and efficient large scale production, as referred in Chapter 1.

Independently of the printing technique, one of the most important parameters affecting the final performance of the printed device is the ink rheology, which mainly depends on particle size, solid loading concentration and solvent type [16].

The most popular printing technique for battery production is screen printing, which is among the fastest and more versatile printing technologies [17].

Thus, screen printing has been used for printing cathodes based on lithium cobalt oxide ($LiCoO_2$) with a discharge curve close to the theoretical value [18, 19]. This technique was also used for printing all solid state lithium-ion batteries using garnet-type oxide and Li_3BO_3 solid electrolytes [20], electrode layers and gel polymer electrolyte layers [21]. Li-O_2 battery cathodes have also been produced by screen printing [22].

Ink-jet printing has also been used for the fabrication of micro-batteries based on $LiFePO_4$ [23, 24] and $LiCoO_2$ [25] as cathode based material and tin oxide (SnO_2) for anode [26]. Finally, spray coating has been used for pilot-scale lithium-ion battery production [27].

Thus, taking into account both that screen printing is among the most interesting technologies for lithium-ion battery fabrication and that $LiFePO_4$ is among the most promising active materials, this work reports on the development of an ink formulation based on carbon coated $LiFePO_4$, suitable for screen-printing.

6.1.2. Experimental

6.1.2.1. Materials

C-$LiFePO_4$ (LFP, Particle size: D10＝0.2μm, D50＝0.5μm and D90＝1.9μm), carbon black (Super P-C45), poly(vinylidene fluoride) (PVdF, Solef 5130) and N-methyl-2-pyrrolidone (NMP) were acquired from Phostech Lithium, Timcal Graphite & Carbon, Solvay and Fluka, respectively.

6.1.2.2. Preparation of the ink and fabrication of the printed cathode

A screen printable ink for battery cathode fabrication was prepared by mixing LFP, Super P, and the polymer binder in NMP solvent with a weight ratio of 80:10:10 (wt.%), selected based on [11]. The ink is composed by 1 g of solid material for 2.25 ml of NMP solvent and, in order to obtain good dispersion, it was maintained under stirring on a magnetic stirrer plate (Agimatic-N) at 1000 rpm, in a beaker (size 25 ml) for 3 hours. The magnetic stir bar has dimensions 25.0 × 7.5 mm and the weight of ~ 4g.

For cathode fabrication, the ink was pressed using a squeegee over the screen (polyester mesh with 62 monofilament by cm) placed at a 100 µm distance of the aluminium substrate, as illustrated in Figure 6.1.

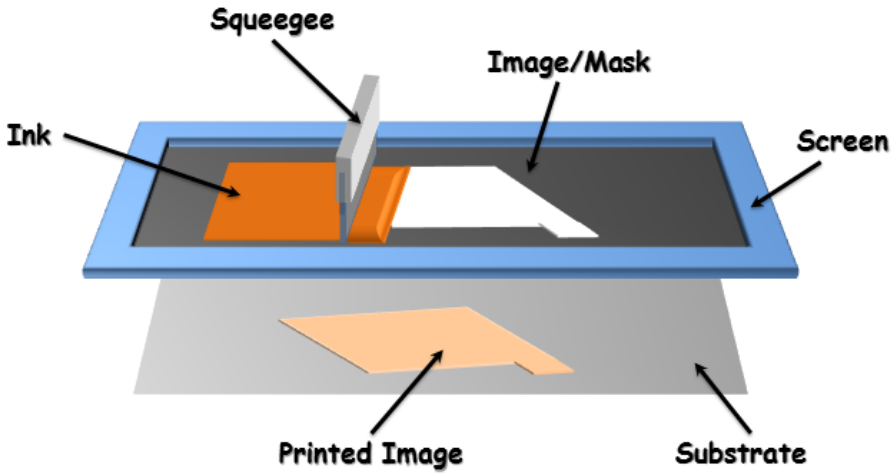

Figure 6.1. Schematic representation of the screen-printing process.

Finally, the electrode film was dried in air atmosphere at 80 ºC in a conventional oven, ED 23 Binder, during 90 minutes. The active mass loading, thickness and porosity of the cathode film are ~ 1.1 mg/cm^2, ~ 26 µm and ~ 80%, respectively.

6.1.2.3. Characterization techniques

Ink characterization: The rheological behaviour of the polymer solutions (polymer binder + solvent) before particle addition was characterized at 25 ºC using a stress-controlled rotational rheometer Physica MCR-300 (Anton Paar, Austria) equipped with a Couette geometry. After loading the solutions into the shearing geometry, steady shear rates were ramped from 1500 s^{-1} down to 10 s^{-1} within 5 minutes. This test was immediately followed by another ramp with steady shear rates from 10 s^{-1} up to 1500 s^{-1} also within 5 minutes. The viscosity data obtained from the two ramps nicely overlapped indicating that flow curves were obtained under steady state conditions and that the polymer solutions showed no thixotropy. After particle addition, the inks were studied at 30 ºC with the same rheometer but equipped with parallel plates (25 mm diameter) to facilitate the loading of samples. The latter were first pre-sheared at a steady shear rate of 0.5 s^{-1} during 60 s to erase the mechanical history associated with the sample loading in the shearing geometry. Then, samples were left to equilibrate for 120 s whereas both shear storage (G') and loss (G'') moduli were monitored using small amplitude oscillatory shear at 1 Hz and a strain of 0.1%. Finally, steady shear rates were ramped (logarithmic distribution of shear rates

in the ramp) between 0.1 s^{-1} and 100 s^{-1} within 400 s and the acquisition times for viscosity reading varied from 100 s at the smaller shear rates to 1 s for the larger shear rates.

Printed electrode characterization: the cohesion and flexibility of the electrode film as well as its adhesion to the current collector were evaluated using a homemade "bend tester" [28]. The morphology of the electrode film was obtained by scanning electron microscopy (SEM) (NanoSEM – FEI Nova 200 and EDAX – Pegasus X4M) with an accelerating voltage of 10 kV. The electrical conductivity measurements were performed by the four point probe method with a current source DC 9818 from Time Electronics and a nano-voltmeter 2182 from Keithley. For the measurements, the electrode material was deposited in an insulator substrate and the electrical conductivity (σ_e, $S.cm^{-1}$) of the cathode was calculated by:

$$\sigma_e = \frac{I}{3.3625tV} \quad (6.1)$$

where t is the thickness of the sample in cm, I is the current in Amperes and V is the voltage in Volts [29].

6.1.2.4. Cell manufacturing and testing

Swagelok type (two or three electrodes) Li/C-$LiFePO_4$ half-cells were assembled in a home-made argon-filled glove box where metallic lithium (8 mm diameter) was used as anode material; Whatman glass microfiber filters (grade GF/A) (10 mm diameter) was used as separator; 1M $LiPF_6$ in ethylene carbonate-diethyl carbonate (EC-DEC, 1:1 vol) mixture from Solvionic namely LP 40 was used as electrolyte and the prepared LFP printed electrode film as cathode (8 mm diameter).

Electrochemical impedance spectroscopy (EIS) was measured with an Autolab PGSTAT12 instrument in a frequency range from 1 MHz to 10 mHz with an amplitude of 10 mV. The cyclic voltamogram (CV) was performed also with an Autolab PGSTAT12 in the range from 2.5 V to 4.2 V at the scan rate 0.1$mV.sec^{-1}$.

Charge-discharge and cycling testes were carried out at room temperature in the voltage range from 2.5 to 4.2 V at different current densities (C/6, C/5, C/2, C, 2C and 5C) using a Landt CT2001A Instrument. The activation cycle was carried out at C/6 in all cases.

6.1.2.5. Theoretical simulation model

The simulation of the experimental discharge curves was carried out with a theoretical model of the Li/C-$LiFePO_4$ half-cells. The simulation is based on the Doyle/Fuller/Newman model

and it was carried out by the finite elements method. Table 6.1 shows the main equations governing the operation of the half-cell battery components (cathode and separator) [30 – 34].

Table 6.1. Summary of the main equations governing the different processes involved in Li/C-$LiFePO_4$ half-cells. The nomenclature is indicated in Table 6.3.

Electrochemical Reactions	**Governing Equation (*i=c(cathode), s(separator)*)**	**Region**
Solid phase conduction	$-\frac{\sigma_{ef,i}}{\delta^2}\frac{\partial^2\phi_E}{\partial X^2} = -FaJ_{Li^+}$	Electrode
Electrolyte phase conduction	$-\frac{K_{ef,i}}{\delta^2}\frac{\partial^2\phi_L}{\partial X^2} = -Faj_{Li^+} + \frac{2kRT}{F}(1-t_+^0)\frac{\partial^2 \ln C_L}{\partial X^2}$	Electrode, Separator
Electrolyte phase diffusion	$\varepsilon\frac{\partial C_L}{\partial t} = \frac{D_{ef,i}}{\delta^2}\frac{\partial^2 C_L}{\partial X^2} + a(1-t_+^0)$	Electrode, Separator
Solid phase diffusion	$\frac{\partial C_E}{\partial t} = D_{Li}\left[\frac{\partial^2 C_E}{\partial r^2} + \frac{2}{r}\frac{\partial C_E}{\partial r}\right]$	Electrode
Activation reaction (Butler-Volmer Kinetics)	$j_{Li^+} = 2k_i\left(C_{E,max,i} - C_{E,i}\vert_{r=R_i}\right)^{0.5}\left(C_{E,i}\vert_{r=R_i}\right)^{0.5}C^{0.5}\sinh\left[\frac{0.5F}{RT}(\varphi_E - \varphi_L - U_i)\right]$	Electrode
Diffusion/ionic and electronic conductivity	$k_{ef,i} = k_l\varepsilon_i^{brugg}, brugg = 1.5$	Electrode, Separator
	$D_{ef,i} = D_l\varepsilon_i^{brugg}, brugg = 1.5$	Electrode, Separator
	$\sigma_{ef,c} = \sigma_c\left(1-\varepsilon_c-\varepsilon_{f,c}\right)$	Electrode
Specific interfacial area	$a_c = \frac{3}{R_i}\left(1-\varepsilon_c-\varepsilon_{f,c}\right)$	Electrode

The values of the parameters used for the different components of the Li/C-$LiFePO_4$ half-cell are listed in Table 6.2. The corresponding nomenclature is indicated in Table 6.3.

Table 6.2. Parameters used for the simulation of the Li/C-$LiFePO_4$ half-cells. The corresponding nomenclature is indicated in Table 6.3.

Parameter	**Unit**	**Separator/Electrolyte**	**Cathode (C-$LiFePO_4$)**
$C_{E,i,0}$	mol/m^3		800
$C_{E,i,max}$	mol/m^3		22806
C_L	mol/m^3	1000	

r	m		1.45×10^{-6}
L_i	m		26×10^{-6}
e_sep	m	430×10^{-6}	
$k_{ef,i}$	S/m	(value [a])$\times0.30^{1.5}$	(value [a])$\times0.81^{1.5}$
D_i	m^2/s	$(3.0\times10^{-10}$ [c])$\times0.30^{1.5}$	$(3.0\times10^{-10}$ [c])$\times0.81^{1.5}$
D_{Li}	m^2/s		8×10^{-18} [b], [e]
k_i	$mol/s.m^2$		3×10^{-13} [b]
$brugg$ or p		1.5	1.5
ε_i		0.30	0.81
σ_i	S/m		5×10^{-3} [b],[d], [e]
i_{1C}	A/m^2	1.75	
General parameters			
Cut-off voltage	V	2.4	
F	C/mol	96487	
T	K	298.15	
R	J/mol K	8.314	
t_+^0		0.363 [c]	
A_{bat}	m^2	5.02×10^{-5}	
Electrolyte material	$LiPF_6$ in EC:DEC		
Inert filler material	PVdF		

a) Model Fits: Ionic conductivity as a function of salt of concentration of mixture of $LiPF_6$ in EC: DEC [35]: $k(c,T) = e^{\left(\frac{15840}{R}\right)\left(\frac{1}{298}-\frac{1}{T}\right)}(1.147c^3 - 22.38c^{1.5} + 29.15c)$

b) Based on [36].

c) Based on [37].

d) Based on [30].

e) Based on [34].

Table 6.3. Nomenclature.

List of symbols	
a	specific interfacial area, m^2/m^3
C_L	concentration of Li ions in the electrolyte, mol/m^3
C_E	concentration of Li ions in the electrode, mol/m^3
D	diffusion coefficient of the salt in the electrolyte, m^2/s
D_{Li^+}	diffusion coefficient of Li ions in the electrode, m^2/s
k_i	Reaction rate constant, $mol/s.m^2$
F	Faraday's constant, 96487 C/mol

$f_{\pm}$	activity of the salt in the electrolyte, mol/m^3
i_E	current density in the electrode, A/m^2
i_L	current density in the electrolyte phase, A/m^2
I_{TOTAL}	total current density, A/m^2
j_{Li^+}	pore wall flux of Li ions, mol/cm^2 s
L	Width, m
e_sep	Separator thickness, m
R	gas constant, 8,314 J/mol K
R_f	film resistance, Ω m^2
r	radius of electrode spherical particle, m
T	Temperature, K
t	time, s
t_+^0	transport number of the positive ion
u^0	open circuit voltage, V
A_{bat}	Cell cross section area, m^2
P	Parameter porosity in separator
brugg	Parameter de brugg in electrodes

Greek symbols	
ε_i	porosity of region *i*(*i* = a,s,c)
$\varepsilon_{f,i}$	volume fraction of fillers in electrode *i* (*i* = a,s,c)
η	over-potential, V
φ_E	potential of the electrodes, V
φ_L	potential of electrolyte, V
κ_l	ionic conductivity of the electrolyte, S/m
$\kappa_{ef,i}$	effective ionic conductivity of the electrolyte *i* (*i* = a,c), S/m
κ_f	effective ionic conductivity of the polymer film in separator, S/m
σ	electronic conductivity of the solid phase of the electrode *i* (*i* = a,s,c), S/m
$\sigma_{ef,i}$	effective electronic conductivity of the solid phase of the electrode *i* (*i* = a,s,c), S/m

Subscripts referring specific components of the battery and initial condition	
A	anode
C	cathode
S	separator
0	initial condition

6.1.3. Results and discussion

6.1.3.1. Rheology properties of the ink

Figure 6.2 shows the shear rate dependence of the steady shear viscosity of the polymer solutions prepared with various polymer concentrations in the NMP solvent.

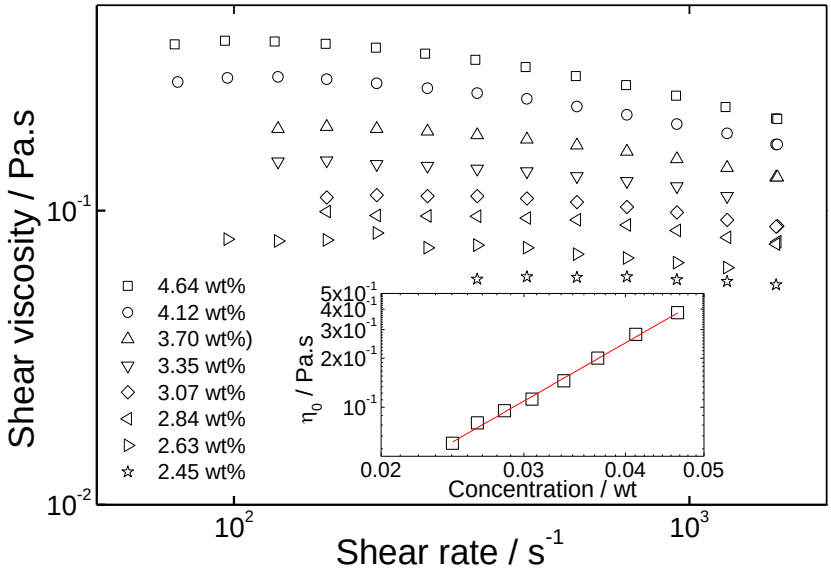

Figure 6.2. Flow curves of the ink solutions prepared with different polymer concentrations. Inset: concentration dependence of the zero shear viscosity η_0.

Figure 6.2 shows that when increasing amounts of polymer are added to the solvent, the solutions evolve from a nearly Newtonian behaviour to a shear thinning viscoelastic behaviour. The zero shear viscosity η_0 (extracted from the low shear rate regime where a viscosity plateau is obtained) as a function of the polymer concentration in a double logarithmic plot (see inset in Figure 6.2) indicates that the increase follows a power law behaviour with exponent 2.8 ± 0.1. This exponent is intermediate between those predicted from scaling theories of polymer solutions in good and neutral solvents [38]. As such, slightly entangled polymers in the semi-dilute regime are at the origin of the enhanced solution viscosity and the shear thinning behaviour.

However, a larger range of polymer concentrations should be tested to compare power law exponents with scaling theories and conclude about the solvent quality of NMP with respect to the polymer. Nevertheless, data in Figure 6.2 suggest that polymer solutions showing shear thinning plus zero shear viscosity of the order of 0.4 Pa.s are needed to produce satisfactory pastes. This is because pastes formulated with more diluted binders resulted in bad film forming properties. In particular, films with weak mechanical resistance upon bending (crack formation) were produced with polymer concentrations lower than 4 wt.%.

The rheological properties of the ink pastes are known to be very difficult to assess with minimal experimental artifact. Issues such as slip of material at the shearing walls, non-reproducible structural break-up and recovery upon sample loading, shear localization and yield stress phenomena during flow are responsible for the poor reproducibility of data and the difficulty in interpreting the rheological response [39]. We thus provide here a rheological study of the optimal ink formulation following the strategy described above. Figure 6.3 a) presents the time evolution of the shear stress recorded during the pre-shear at a constant shear rate of 0.5 s^{-1} of two paste samples loaded using two different sample thicknesses.

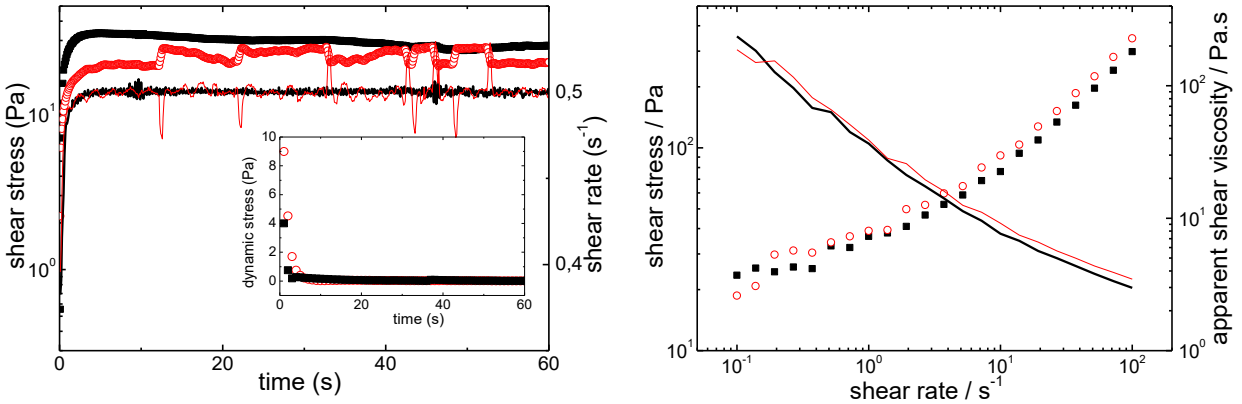

Figure 6.3. a) Pre-shear at constant shear rate of 0.5 s^{-1} of two ink pastes with thickness of 0.8 (thick line and solid symbols) and 0.6 mm (thin line and empty symbols). Inset: recovery after steady flow cessation. b) Shear rate dependence of the shear stress (symbols) and apparent shear viscosity (lines) for two ink samples with different thicknesses: 0.8 mm (solid and thick) and 0.6 mm (thin and empty).

After a first transient which is thickness dependent, the shear stress reaches a steady state value of nearly 25 Pa for both samples. These results indicate that under such flow conditions, the pastes exhibit an apparent fluid-like behaviour with a shear viscosity of the order of 50 Pa.s and that flow instabilities such as wall slip, shear banding or shear localization can be neglected since reproducibility in the shear viscosity value is nearly achieved. The inset in Figure 6.3 a) shows that the structural recovery of the paste takes place within one minute as the elastic behaviour of the

paste is constant after 40 seconds. From the value of the shear modulus G' after 1 minute rest (result not shown), it can be inferred that the paste elasticity is of the order of 500 Pa. As such, this ink shows a certain stability towards sedimentation due to its solid-like behaviour at rest.

The shear rate dependence of the apparent shear viscosity and shear stress measured during an increasing ramp in shear rate is pictured in Figure 6.3 b). Essentially, data obtained with the two sample thicknesses show a satisfactory level of reproducibility. This again indicates that, although slip occurs during shearing, it has a rather small impact on the shear viscosity reading. Indeed, the formulated ink possesses an apparent shear viscosity of 3 Pa.s for shear rates of the order of 100 s^{-1}, which is the range of shear rates typically used during the screen printing (if one takes a 100 microns thick layer of ink sheared at a velocity of 0.01 ms^{-1}). In addition, the shear rate dependence of the stress reported in Figure 6.3 b) is reminiscent from a yield stress phenomenon at smaller shear rates, since the stress shows a finite value at zeroing shear rates, which is in agreement with the elastic behaviour exhibited by the paste under quiescent conditions (see inset in Figure 6.3 a)). However, additional work involving in-situ structural characterization is needed to further probe the yielding of the paste and also assess the effect of confinement by the shearing walls. This will help elucidating whether unstable and/or non homogeneous flows develop under processing conditions where nearly 10 times thinner ink samples are spread on a substrate.

The rheology requirements and properties of electrode slurry for screen printing applications are similar to standard battery slurries, that means the slurry should have high viscosity, low vapor pressure and an adequate volatile solvent concentration (ml/mg) because these factors have an strong impact on the morphology and on the electrochemical performance of the electrode composite [40, 41].

The ink viscosity interval for screen printing technique is very large between 0.1 Pa.s up to 1000 Pa.s. [40] and consequently the electrode slurry must be adjusted and optimized in function of the solvent type, polymer binder, active material, conductive additive and printing technique. The obtained wet thickness of the screen-printed layer depends on the resolution of the mesh, printing speed, as well as by the fraction of ink transferred to the substrate. For solvent concentration below the optimal one yield stress that difficults flow is observed during stirring and printing processes instead for solvent concentration above the optimal one is observed settling of active material and conductive additive.

Based on the previous description, electrode slurries with different solvent concentrations were prepared, screen-printed and the final film was evaluated. An optimized screen-printed cathode film was obtained using proportion of 1 g of solid material for 2.25 ml of NMP solvent

(solvent concentration = 2.25 ml.g^{-1}; polymer solution concentration = 4.12%). Using less solvent (< 2.25 ml) the magnetic stir wasn´t able to rotate with a minimum adequate rotation velocity to obtain a good dispersion. Increasing the quantity of solvent (> 2.25ml), the polymer solution concentration decreases, the obtained screen-printed cathode film isn´t sufficiently thick to coat totally the substrate (aluminum foil) and cracks were observed on the surface of the screen-printed film. The active mass loading decreases with increasing solvent concentration reducing the stored gravimetric and areal energy of the screen-printed film.

6.1.3.2. Morphological features of the cathode

Figure 6.4 a) shows images of the screen-printed cathode film on the aluminum current collector layer. Typically, the dimensions of the printed cathode film are 3.5 cm × 3 cm × 26 µm. The adhesion of the cathode film to the current collector layer was evaluated using an homemade "bend tester", which is constituted by a series of metal rods of decreasing diameters from 10 mm to 1.5 mm [28]. For the printed cathodes, and independently of the rod size of the bend tester, no separation between cathode film and current collector foil is observed. No cracks were detected either on the cathode film.

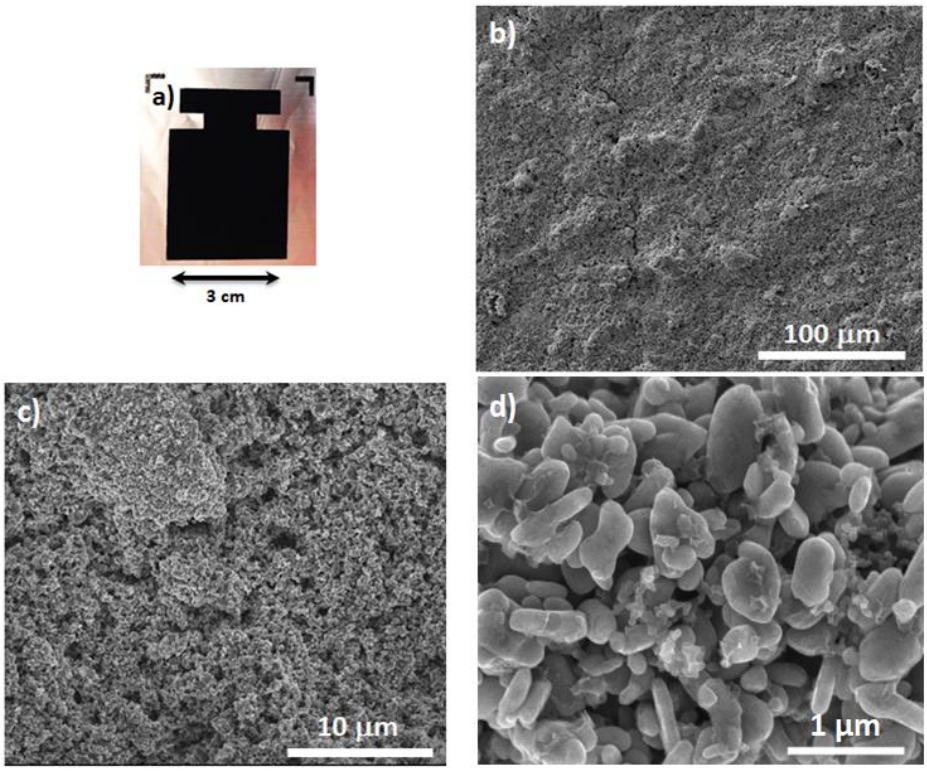

Figure 6.4. a) Picture of the printed cathode and b)-d) SEM images of the surface of the cathode film with different magnifications.

The SEM image of the printed cathode film with lower magnification (Figure 6.4 b)) shows the existence of roughness and voids, related to the heterogeneity of sizes and behaviour of the ink components during solvent evaporation [11]. The cathode shows a three-dimensional (3-D) interconnected structure formed by the active material and conductive additive particles within the polymer binder. Figure 6.4 c) shows a homogeneous distribution of the different components, as no large agglomerates are detected and the distributions of voids are homogeneous. The presence of the voids is particularly relevant as it contributes to larger electrode/electrolyte contact area.

Finally, larger magnifications (Figure 6.4 d)) show rod-like particles with sizes between 0.2 μm to 1.9 μm. The non-spherical size of C-LiFePO$_4$ particles increases the effective contact area between active material and electrolyte, leading to improved battery performance.

Figure 6.4 d) also allows to discriminate the more dense active material, which appears in white colour, and the polymer binder and conductive additive, which appear in dark grey.

In previous research work, was observed [42] for discharge rate C5, discharge capacity values in order of 150 mA.h.g^{-1}. In order to understand the origin of the low discharge capacity for low rate the electrical conductivity was measured. The dc-electrical conductivity value for the screen-printed cathode composite is 0.24 ± 0.05 S.cm^{-1} and is similar to the ones reported in literature [43] . This means that exists a proper electrical network in the whole cathode composite and that the carbon additive is well distributed in the screen printed cathode composite. Also as the obtained electrical value is more than one order of magnitude higher than the ionic conductivity of the electrolyte solution ($\sigma_i = 11.6$ ms/cm) [11, 44] the overall electrical impedance of the cell isn't so much influenced by the electrical conductivity.

6.1.3.3. Electrochemical performance

Figure 6.5 a) shows the electrochemical impedance spectroscopy spectra of the printed cathode after 2 CV cycles in open circuit voltage. The Nyquist plot is characterized by a semicircle at high frequencies (overall resistance) and an approximately 45° inclined line in the low-frequency range, which can be considered as Warburg impedance, associated with the lithium ion diffusion in the bulk of the active material [45].

The total resistance of the semicircle corresponds to the sum of the electrolyte resistance (R_e, intercept at the Z'-axis at high frequency), surface film resistance (R_f, Li-ion migration resistance through the solid electrolyte interface (SEI) film formed on the cathode surface) and charge-transfer reaction resistance ascribed to the lithium-intercalation process (R_{ct}) at the middle

frequency range. The value of the total resistance of the printed cathode film is ~ 450 Ω.

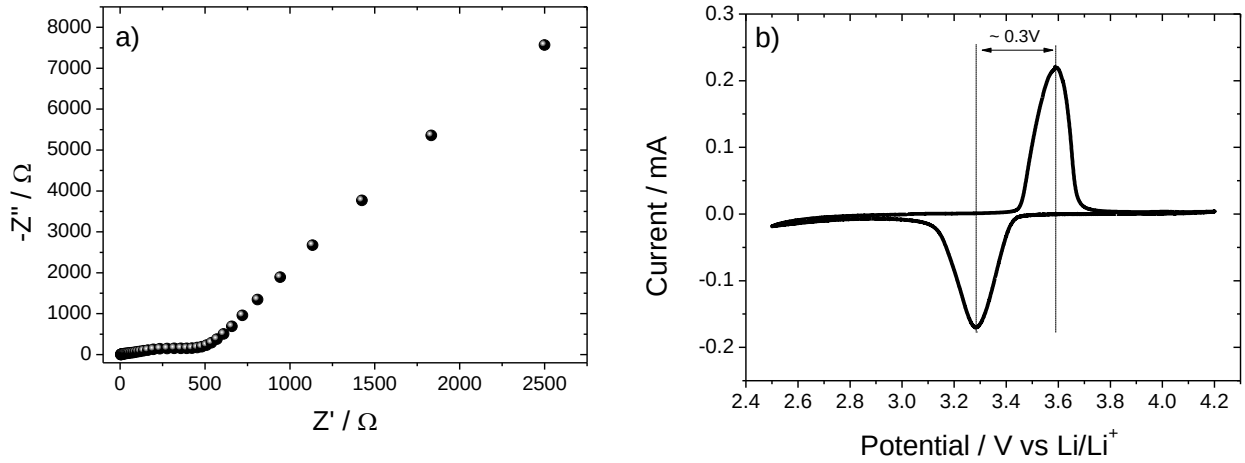

Figure 6.5. a) Electrochemical impedance spectroscopy (EIS) spectra and b) cyclic voltammetry (CV) curve of the printed cathode.

The Li^+ diffusion coefficient (D_{Li^+}) of the printed cathode is calculated according to (6.2) and (6.3):

$$D_{Li^+} = \frac{R^2T^2}{2A^2n^4F^4c^2\sigma_W^2} \quad (6.2)$$

$$Z' = R_e + R_f + R_{ct} + \sigma_W W^{-\frac{1}{2}} \quad (6.3)$$

where R is the gas constant, T is the absolute temperature, A is the surface area of the cathode, n is the number of electrons per molecule during oxidization, F is the Faraday constant, C is the concentration of Li^+, σ_W is the Warburg factor, R_e is the electrolyte resistance, R_f is the resistance of the solid electrolyte interface (SEI) formation, R_{ct} is charge transfer resistance and W is the angular frequency [46].

The Li^+ diffusion coefficient of the printed cathode film, calculated from (6.2) and (6.3) and the EIS spectra (Figure 6.5 a)), is 2.5×10^{-16} $cm^2.s^{-1}$, which is similar to the one obtained for conventional films [47].

Figure 6.5 b) shows the cyclic voltammetry (CV) curve of the printed cathode film at a scanning rate of 0.1 $mV.s^{-1}$, showing a symmetric single pair of oxidation and reduction peaks, which correspond to the Fe^{2+}/Fe^{3+} redox transformation that corresponds to the charge and discharge processes, respectively [48].

These peaks are centered at 3.6/3.3 V and the low electrochemical polarization (0.3 V) demonstrates easy insertion and extraction of lithium ions in the printed cathode.

The cycle performance of the printed cathode was measured in Li/Separator/C-$LiFePO_4$ cathode half-cells at different scan rates.

Typical charge/discharge curves at room temperature of the half-cells prepared with the printed cathode at C/6 and 5C in the voltage range between 2.5 and 4.2 V are shown in Figure 6.6.

Figure 6.6 a) shows that the charge/discharge curves are characterized by a flat voltage plateau at around 3.2 – 3.6 V that depends on the scan rate. For low scan rate (C/6), it is observed a flat discharge curve due to the coexistence of the two-phase redox reaction that occurs via a first-order transition between $FePO_4$ and $LiFePO_4$ [43]. It is also detected a decrease in the plateau potential with increasing current density (C/6 to 5C). Moreover, it is observed an increasing slope in the discharge curves at higher current densities in the plateau region due to electrode polarization at higher rates. In relation to the scans at 5C (Figure 6.6 a)) and independently of the cycle number, the charge/discharge curves show relatively short constant current charge and suffers from a large ohmic drop and activation overpotential.

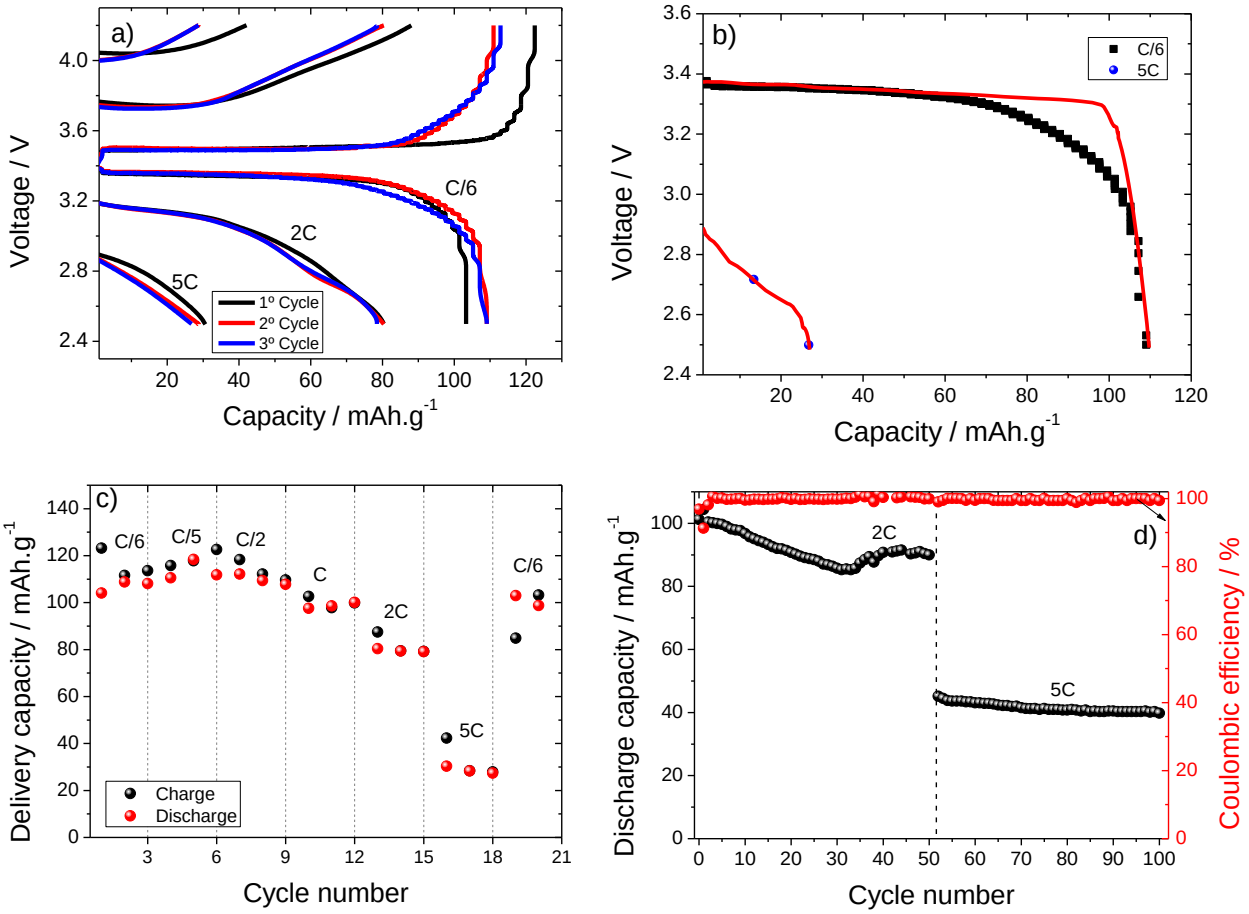

Figure 6.6. a) Experimental charge-discharge curves for various cycles, b) theoretical (red line) and experimental charge-discharge curve at C/6 and 5C, c) rate performance of the printed cathode during the charge-discharge process and d) cycling performance and coulombic efficiency of the printed cathode films at 2C and 5C-rate in the voltage range from 2.5 to 4.2 V.

The discharge capacities values are 108.1, 79.1 and 27.4 $mA.h.g^{-1}$ at C/6, 2C and 5C-rates, respectively, the values being reasonably stable over cycling as it is shown in Figure 6.6 a).

For low scan-rates (C/6), it is also detected an extra capacity during charging, attributed to aluminum current collector oxidation parasitic reactions due to degradation of the $LiPF_6$ salt that occurs during half-cell charging [23, 50, 51].

Also in Figure 6.6 a) and independently the scan rate, it is observed that the discharge voltage plateau increases with increasing the number of cycles due to the low electronic conductivity of the C-$LiFePO_4$ active material [45].

Figure 6.6 b) also shows good agreement between the theoretical curve (red line) and the experimental curve for both scan rates. The small differences between the curves is attributed to the effect of charge-transfer resistance and the electronic /ionic conductivity value assumed in the theoretical model, on the rate performance of the C-$LiFePO_4$ cathode.

Figure 6.6 c) shows the room temperature rate performance of the printed cathode during the charge and discharge processes. The cycling performance is strongly affected by the SEI formation during the first 2 – 3 cycles, in which the discharge capacity steadily increases up to the C/2 rate.

For scan-rates above C/2, the capacity value decreases with increasing current density, independently of the charging process. This fact is attributed to the increase of the electrical resistance as well as to limitations of the diffusion process. The Li^+ ion diffusion is always associated with electron transport phenomena within the battery circuit, and the internal electrical field generated by the electrons strongly enhances its migration [52]. The rate performance exhibits excellent capacity value (108.1 mA.h.g^{-1} at C/6, 111.8 mA.h.g^{-1} at C/5, 107.8 mA.h.g^{-1} at C/2, 100.1 mA.h.g^{-1} at C, 79.1 mA.h.g^{-1} at 2C and 27.4 mA.h.g^{-1} at 5C) as it is shown by the recovering cycle at C/6.

Thus, the printed cathode material displays a good rate performance, showing remarkably improved rate capability at higher rates (C/6 to 5C), related to the low thickness of the printed cathode. Further, it also delivers a discharge capacity as high as 27.4 mA.h.g^{-1} even at 5C.

The limitation at low rates (C/6 to C/2) -could be attributed to solid-state mass transport limitations within the C-$LiFePO_4$ particles, while at higher rates above 5C, the limitation is due to Li^+ transport within the electrolyte trapped in the electrode, as the amount of Li ions in the electrode alone is not enough for discharging all the $FePO_4$ active particles [49].

Another factor that could affect the low discharge capacity value for low rate is a large contact resistance between the active material and conductive additive and also between the electrode and the current collector [11, 43].

After calendering, it has been shown, through the impedance and capacity retention values, that the major contributor for enhancing the electrochemical performance of the electrode

is the variation between electrode and Al interface [11, 53].

In order to reduce the contact resistance the cathodes were pressed during 1 min at 1.4 ton/cm^2 (90 bar). The obtained cathodes have a porosity of ~ 55%.

As it is observed in Figure 6.6 c), the calendered cathode shows an improvement for discharge capacity for all rates. The increase of the average discharge capacity value is ~ 20 mA.h.g^{-1} and ~ 55 mA.h.g^{-1} for low rate (C6 and C5) and high rate (5C), respectively.

Figure 6.6 d) shows the discharge capacity as a function of the cycle number at 2C and 5C. At 2C, the initial discharge capacity of 101.2 mA.h.g^{-1} drops to 90 mA.h.g^{-1} after 50 cycles, the capacity retention being 89%. In relation of 5C, the initial discharge capacity value is 48.2 mA.h.g^{-1} and after 50 cycles, this value is 39.8 mA.h.g^{-1} that represent 83% of capacity retention.

The slight decrease of the discharge value after the initial cycle and 35 cycles may be caused by the loss of electrical contact between active material and conductive additive particles, or event with the current collector. In the later, the electrolyte can penetrate into the detached areas giving rise to capacity loss [26].

Figure 6.6 d) also shows the coulombic efficiency (CE), where a good reversibility is observed (above 99% for all cycles), combined with high capacity and low cumulative irreversible capacity loss.

Cycling life (Figure 6.6 d)) of the printed cathode shows 90 mA.h.g^{-1} at 2C (charge and/or discharge process in half an hour) and 39.8 mA.h.g^{-1} at 5C (charge and/or discharge process in twenty minutes) after 50 cycles which is still 53% and 23% of the theoretical value, respectively, indicating the good performance of the battery.

At low current rates, C/6, the printed cathode delivered a near theoretical capacity with high coulombic efficiency and capacity retention of ~76%. At high current rates, 2C and 5C, the cathode exhibits a satisfactory delivered capacity with excellent cyclability.

In conclusion, and taking into account the experimental results presented in this work, the cathode film produced by screen-printing with very low active mass loading shows an excellent performance, comparable to conventional cathodes based on the same active material [54], being therefore suitable for the development of printed lithium-ion batteries. After calendering, it was observed an improvement for discharge capacity for all rates.

6.2. Anode

The method reported on subsection 6.1.2 was also used to produce the anode inks, using graphite as active material.

The microstructural morphology of the anodes is shown in the SEM image of Figure 6.7, in which a homogeneous distribution of the graphite particles is observed, partially covered by the conductive additive.

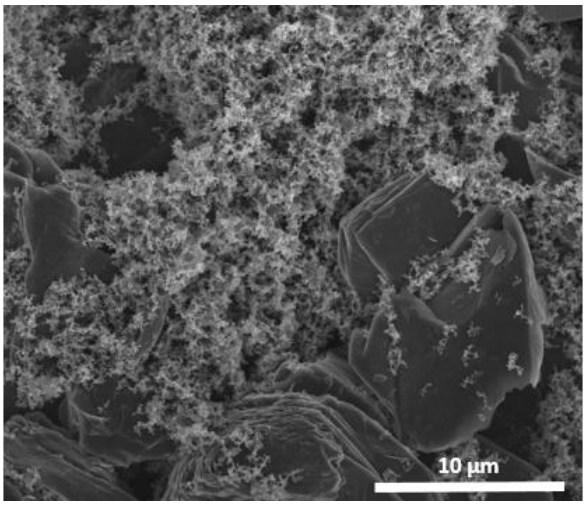

Figure 6.7. Surface SEM image of the anode film.

Figure 6.7 also shows the graphite particles with flake geometry and average particle size ranging from 10 to 15 µm.

The anode films were tested as anodic half-cells at different scan rates between C/6 and 2C for three cycles, the cycling performance being represented in Figure 6.8.

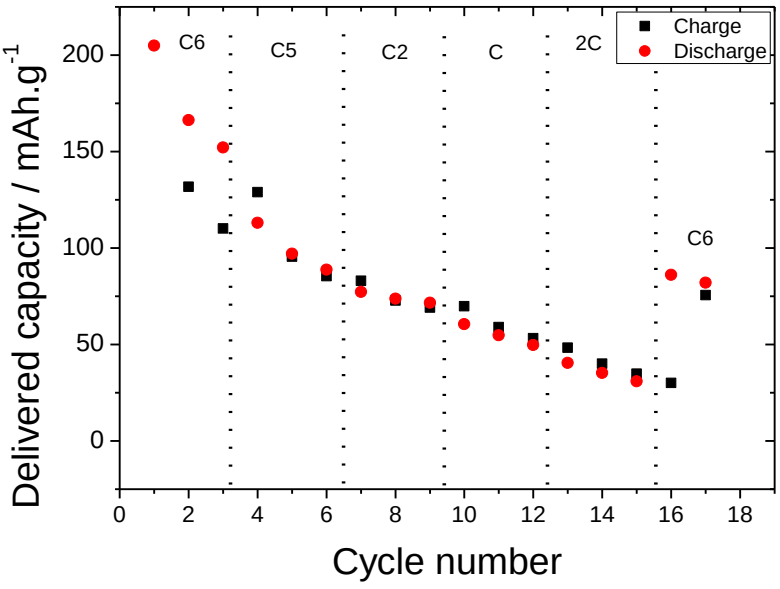

Figure 6.8. Rate performance of the printed anode during the charge-discharge process from C/6 up to 2C.

It is observed that increasing cycle number leads to a decrease of the discharge capacity for all scan rates, with values 152, 88, 72, 48 and 32 $mAh.g^{-1}$ at C/6, C/5, C/2, C and 2C-rates, respectively.

This preliminary work shows that it is possible to obtain suitable anode inks for printed batteries with excellent performance.

6.3. Conclusions

A thin cathode film with a thickness of 26 μm was produced by screen-printing after the development of an ink based on C-$LiFePO_4$. The developed ink paste exhibits a fluid-like behaviour with an apparent viscosity of 3 Pa.s for a shear rate of 100 s^{-1}. The printed cathode presents a homogeneous distribution of all components (active material, conductive additive and polymer binder).

The total resistance and diffusion coefficient (D_{Li}) of the printed cathode are ~ 456 Ω and 2.5×10^{-16} $cm^2.s^{-1}$, respectively. Further, the CV curve shows low electrochemical polarization (0.3 V), demonstrating easy insertion and extraction of lithium ions. With respect to rate performance, the printed cathodes show 108.1 $mA.hg^{-1}$ at C/6, 111.8 $mA.h.g^{-1}$ at C/5, 107.8 $mA.h.g^{-1}$ at C/2, 100.1 $mA.h.g^{-1}$ at C, 79.1 $mA.h.g^{-1}$ at 2C and 27.4 $mA.h.g^{-1}$ at 5C, independently the cycle number, representing high delivered capacity. With respect to the cycling performance at 5C, this cathode shows an initial discharge capacity of 48.2 $mA.h.g^{-1}$ and after 50 cycles the discharge value is 39.8 $mA.h.g^{-1}$ with a capacity retention of 83%, demonstrating the good performance of the battery. After calendering, it was observed an improvement for discharge capacity for all rates.

In this way, an ink formulation has been achieved based on C-$LiFePO_4$ active material, which is suitable for the preparation of screen printed lithium-ion batteries.

With respect to the anodes, inks based on graphite shows a homogeneous distribution of the these particles and the discharge capacity values are 152, 88,72, 48, and 32 $mAh.g^{-1}$ at C/6, C/5, C/2, C and 2C-rates, respectively, showing their suitability for printed anodes.

6.4. References

[1] J. Twidell, T. Weir, *Renewable Energy Resources*, Taylor & Francis, New York, 2015.

[2] M.S. Whittingham, *Lithium Batteries and Cathode Materials*, Chemical Reviews, 2004, 104: p. 4271-4302.

[3] M. Yoshio, R.J. Brodd, A. Kozawa, *Lithium-Ion Batteries: Science and Technologies*, Springer, New York, 2010.

[4] R. Dell, D.A.J. Rand, *Understanding Batteries*, Royal Society of Chemistry, Cambridge, 2001.

[5] R. Huggins, *Advanced Batteries: Materials Science Aspects*, Springer, New York, 2008.

[6] J.M. Tarascon, M. Armand, *Issues and challenges facing rechargeable lithium batteries*, Nature, 2001, 414: p. 359-367.

[7] B. Scrosati, J. Garche, *Lithium batteries: Status, prospects and future*, Journal of Power Sources, 2010, 195: p. 2419-2430.

[8] K. Amine, R. Kanno, Y. Tzeng, *Rechargeable lithium batteries and beyond: Progress, challenges, and future directions*, MRS Bulletin, 2014, 39: p. 395-401.

[9] N. Nitta, F. Wu, J.T. Lee, G. Yushin, *Li-ion battery materials: present and future*, Materials Today, 2015, 18: p. 252-264.

[10] M. Wakihara, O. Yamamoto, *Lithium Ion Batteries: Fundamentals and Performance*, Wiley, New York, 2008.

[11] A. Gören, C.M. Costa, M.M. Silva, S. Lanceros-Méndez, *State of the art and open questions on cathode preparation based on carbon coated lithium iron phosphate*, *Composites Part B: Engineering*, 2015, 83: p. 333-345.

[12] N. Omar, M. Daowd, P.v.d. Bossche, O. Hegazy, J. Smekens, T. Coosemans, J.v. Mierlo, *Rechargeable Energy Storage Systems for Plug-in Hybrid Electric Vehicles - Assessment of Electrical Characteristics*, Energies, 2012, 5: p. 2952.

[13] M. Doeff, *Battery battery Cathodes battery cathode*, Encyclopedia of Sustainability Science and Technology, Springer, New York, 2012, p. 708-739.

[14] L.-X. Yuan, Z.-H. Wang, W.-X. Zhang, X.-L. Hu, J.-T. Chen, Y.-H. Huang, J.B. Goodenough, *Development and challenges of LiFePO4 cathode material for lithium-ion batteries*, *Energy & Environmental Science*, 2011, 4: p. 269-284.

[15] F. Yu, L. Zhang, Y. Li, Y. An, M. Zhu, B. Dai, *Mechanism studies of LiFePO4 cathode material: lithiation/delithiation process, electrochemical modification and synthetic reaction*, RSC Advances , 2014, 4. p. 54576-54602.

[16] S. Lawes, A. Riese, Q. Sun, N. Cheng, X. Sun, *Printing nanostructured carbon for energy storage and conversion applications*, Carbon, 2015, 92: p. 150-176.

[17] R.R. Søndergaard, M. Hösel, F.C. Krebs, *Roll-to-Roll fabrication of large area functional organic materials*, *Journal of Polymer Science Part B: Polymer Physics*, 2013, 51: p. 16-34.

[18] M.-S. Park, S.-H. Hyun, S.-C. Nam, Mechanical and electrical properties of a $LiCoO_2$ cathode prepared by screen-printing for a lithium-ion micro-battery, Electrochimica Acta, 2007, 52: p. 7895-7902.

[19] M.S. Park, S.H. Hyun, S.C. Nam, *Characterization of a LiCoO2 thick film by screen-printing for a lithium ion micro-battery*, Journal of Power Sources, 2006, 159: p 1416-1421.

[20] S. Ohta, S. Komagata, J. Seki, T. Saeki, S. Morishita, T. Asaoka, *All-solid-state lithium ion battery using garnet-type oxide and Li_3BO_3 solid electrolytes fabricated by screen-printing*, Journal of Power Sources, 2013, 238: p. 53-56.

[21] K.-Y. Kang, Y.-G. Lee, D.O. Shin, J.-C. Kim, K.M. Kim, *Performance improvements of pouch-type flexible thin-film lithium-ion batteries by modifying sequential screen-printing process*, Electrochimica Acta, 2014, 138: p. 294-301.

[22] C.Y. Jung, T.S. Zhao, L. An, L. Zeng, Z.H. Wei, *Screen printed cathode for non-aqueous lithium–oxygen batteries*, Journal of Power Sources, 2015, 297: p. 174-180.

[23] P.E. Delannoy, B. Riou, B. Lestriez, D. Guyomard, T. Brousse, J. Le Bideau, *Toward fast and cost-effective ink-jet printing of solid electrolyte for lithium microbatteries*, *Journal of Power Sources*, 2015, 274: p. 1085-1090.

[24] P.E. Delannoy, B. Riou, T. Brousse, J. Le Bideau, D. Guyomard, B. Lestriez, *Ink-jet printed porous composite LiFePO4 electrode from aqueous suspension for microbatteries*, Journal of Power Sources, 2015, 287: p 261-268.

[25] J. Huang, J. Yang, W. Li, W. Cai, Z. Jiang, *Electrochemical properties of LiCoO2 thin film electrode prepared by ink-jet printing technique*, Thin Solid Films, 2008, 516: p. 3314-3319.

[26] Y. Zhao, Q. Zhou, L. Liu, J. Xu, M. Yan, Z. Jiang, *A novel and facile route of ink-jet printing to thin film SnO2 anode for rechargeable lithium ion batteries*, Electrochimica Acta, 2006, 51: p. 2639-2645.

[27] D. Beneventi, D. Chaussy, D. Curtil, L. Zolin, E. Bruno, R. Bongiovanni, M. Destro, C. Gerbaldi, N. Penazzi, S. Tapin-Lingua, *Pilot-scale elaboration of graphite/microfibrillated cellulose anodes for Li-ion batteries by spray deposition on a forming paper sheet*, Chemical Engineering Journal, 2014, 243: p. 372-379.

[28] T. Marks, S. Trussler, A.J. Smith, D. Xiong, J.R. Dahn, *A Guide to Li-Ion Coin-Cell Electrode Making for Academic Researchers*, Journal of The Electrochemical Society , 2011, 158: p. A51-A57.

[29] F.M. Smits, *Measurement of Sheet Resistivities with the Four-Point Probe*, Bell System Technical Journal, 1958, 37: p. 711-718.

[30] M. Wang, J. Li, X. He, H. Wu, C. Wan, *The effect of local current density on electrode design for lithium-ion batteries*, Journal of Power Sources, 2012, 207: p. 127-133.

[31] M. Safari, C. Delacourt, *Modeling of a Commercial Graphite/LiFePO4 Cell*, Journal of The Electrochemical Society, 2011, 158: p. A562-A571.

[32] S. Wang, L. Lu, X. Liu, *A simulation on safety of LiFePO4/C cell using electrochemical–thermal coupling model*, Journal of Power Sources, 2013, 244: p. 101-108.

[33] Y. Ye, Y. Shi, A.A.O. Tay, *Electro-thermal cycle life model for lithium iron phosphate battery*, Journal of Power Sources, 2012, 217: p. 509-518.

[34] V. Srinivasan, J. Newman, *Discharge Model for the Lithium Iron-Phosphate Electrode*, Journal of The Electrochemical Society, 2004, 151: p. A1517-A1529.

[35] H. Lundgren, M. Behm, G. Lindbergh, *Electrochemical Characterization and Temperature Dependency of Mass-Transport Properties of LiPF6 in EC:DEC*, Journal of The Electrochemical Society, 2015, 162: p A413-A420.

[36] V. Srinivasan, J. Newman, *Design and Optimization of a Natural Graphite/Iron Phosphate Lithium-Ion Cell*, Journal of The Electrochemical Society, 2004, 151: p. A1530-A1538.

[37] S. Yu, S. Kim, T.Y. Kim, J.H. Nam, W.I. Cho, *Model Prediction and Experiments for the Electrode Design Optimization of LiFePO4/Graphite Electrodes in High Capacity Lithium-ion Batteries*, Bulletin of the Korean Chemical Society, 2013, 34: p. 9.

[38] R. Colby, *Structure and linear viscoelasticity of flexible polymer solutions: comparison of polyelectrolyte and neutral polymer solutions*, Rheol Acta, 2010, 49: p. 425-442.

[39] R.G. Larson, *The Structure and Rheology of Complex Fluids*, OUP USA, 1999.

[40] A.M. Gaikwad, A.C. Arias, D.A. Steingart, *Recent Progress on Printed Flexible Batteries: Mechanical Challenges, Printing Technologies, and Future Prospects*, Energy Technology, 2015, 3: p. 305-328.

[41] E. Ligneel, B. Lestriez, A. Hudhomme, D. Guyomard, *Effects of the Solvent Concentration (Solid Loading) on the Processing and Properties of the Composite Electrode*, Journal of The Electrochemical Society, 2007, 154: p. A235-A241.

[42] A. Gören, D. Cíntora-Juárez, P. Martins, S. Ferdov, M.M. Silva, J.L. Tirado, C.M. Costa, S. Lanceros-Méndez, *Influence of Solvent Evaporation Rate in the Preparation of Carbon-Coated Lithium Iron Phosphate Cathode Films on Battery Performance*, Energy Technology, (2015) n/a-n/a.

[43] H. Zheng, L. Tan, G. Liu, X. Song, V.S. Battaglia, *Calendering effects on the physical and electrochemical properties of* $Li[Ni_{1/3}Mn_{1/3}Co_{1/3}]O_2$ *cathode*, Journal of Power Sources, 2012, 208: p. 52-57.

[44] H. Zheng, R. Yang, G. Liu, X. Song, V.S. Battaglia, *Cooperation between Active Material, Polymeric Binder and Conductive Carbon Additive in Lithium Ion Battery Cathode*, The Journal of Physical Chemistry C , 2012, 116: p. 4875-4882.

[45] Y. Shi, S.-L. Chou, J.-Z. Wang, D. Wexler, H.-J. Li, H.-K. Liu, Y. Wu, *Graphene wrapped LiFePO4/C composites as cathode materials for Li-ion batteries with enhanced rate capability*, Journal of Materials Chemistry , 2012, 22: p. 16465-16470.

[46] K. Feng, Y. Cheng, M. Wang, H. Zhang, X. Li, H. Zhang, *Synthesis and electrochemical properties of $Li_3V_2(P_{1-x}B_xO_4)3/C$ cathode materials*, Journal of Materials Chemistry A, 2015, 3: p. 19469-19475.

[47] P. Prosini, *Determination of the Diffusion Coefficient of $LiFePO_4$, in: Iron Phosphate Materials as Cathodes for Lithium Batteries*, Springer, London, 2011, pp. 21-27.

[48] C.H. Mi, X.G. Zhang, H.L. Li, *Electrochemical behaviors of solid LiFePO4 and Li0.99Nb0.01FePO4 in Li2SO4 aqueous electrolyte*, Journal of Electroanalytical Chemistry, 2007, 602, p. 245-254.

[49] C. Fongy, A.-C. Gaillot, S. Jouanneau, D. Guyomard, B. Lestriez, *Ionic vs Electronic Power Limitations and Analysis of the Fraction of Wired Grains in LiFePO4 Composite Electrodes*, Journal of The Electrochemical Society, 2010, 157: p. A885-A891.

[50] L.J. Krause, W. Lamanna, J. Summerfield, M. Engle, G. Korba, R. Loch, R. Atanasoski, *Corrosion of aluminum at high voltages in non-aqueous electrolytes containing perfluoroalkylsulfonyl imides; new lithium salts for lithium-ion cells*, Journal of Power Sources, 1997, 68: p. 320-325.

[51] R. Younesi, G.M. Veith, P. Johansson, K. Edstrom, T. Vegge, *Lithium salts for advanced lithium batteries: Li-metal, Li-O2, and Li-S*, Energy & Environmental Science, 2015, 8: p. 1905-1922.

[52] C. Wang, J. Hong, *Ionic/Electronic Conducting Characteristics of LiFePO4 Cathode Materials: The Determining Factors for High Rate Performance*, Electrochemical and Solid-State Letters, 2007, 10: p. A65-A69.

[53] A. van Bommel, R. Divigalpitiya, *Effect of Calendering LiFePO4 Electrodes*, Journal of The Electrochemical Society, 2012, 159: p. A1791-A1795.

[54] L. Yu, D. Cai, H. Wang, M.-M. Titirici, *Synthesis of Microspherical LiFePO4-Carbon Composites for Lithium-Ion Batteries*, Nanomaterials, 2013, 3: p. 443.

7. Conclusions and future work

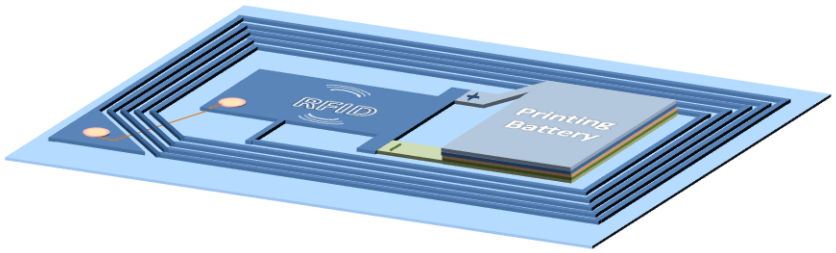

This chapter presents the main conclusions of the present work as well as some guidelines for future work.

7.1. Conclusions

This work started by presenting the most important developments in printed batteries and printing techniques, leading to the conclusion of the need of developing novel separators and electrode inks.

Thus, P(VdF-HFP) and P(VdF-CTFE) were selected to produce membranes by the doctor blade technique (once this method produces results very similar to screen printing technique) and characterize them with respect to their physico-chemical and electrochemical properties.

It was verified that the phase diagram allows tailoring the microstructure of P(VdF-HFP) and P(VdF-CTFE) membranes and that the microstructural features are explained by the Flory-Huggins theory, depending on polymer concentration and solvent evaporation temperature.

It was concluded that the formation of a porous membrane is attributed to a spinodal decomposition of the liquid-liquid phase separation, and that controlling polymer concentration and solvent evaporation temperature allows to obtain different sample microstructures with different β-phase content and thermal, mechanical, dielectric and piezoelectric properties.

In the P(VdF-HFP)/DMF system, it is observed a decrease of the electroactive β- phase content by increasing solvent evaporation temperature for a given initial polymer concentration and also by increasing polymer fraction in the solution. In the P(VdF-CTFE)/DMF system, the electroactive β- phase content decreases with increasing polymer concentration for a given solvent evaporation temperature and increases with increasing solvent evaporation temperature for a given initial polymer concentration. Depending on the solvent evaporation temperature and for a 20/80 polymer/solvent relative concentration, P(VdF-HFP) shows β-phase contents of 16 (T=100 ℃), 24 (T=50 ℃), 79 (T=25 ℃) and P(VdF-CTFE) shows β-phase contents of 87 (T=100℃), 26 (T=50℃), 33 (T=25℃). The degree of crystallinity ranging between 14% and 35%, depending on the polymer concentration and solvent evaporation temperature.

The dielectric constant, ′, of P(VdF-HFP) and P(VdF-CTFE) depends on the degree of crystallinity and the crystalline phase of the polymer as well as on the FHP and CTFE content, respectively.

The 5/95 P(VdF-HFP) polymer electrolyte sample displays the highest electrical conductivity, with values above 10^{-3} S.cm^{-1} at room temperature. This sample shows the best electrolyte liquid uptake and ion-transport properties and is selected for the ionically conducting separator. P(VdF-CTFE) membranes showed the best ionic conductivity value at room temperature, 1.5 mS.cm^{-1}, with a degree of porosity of 60% and an electrolyte uptake value of 292%.

According to these results, separator membranes were prepared in order to stablish a correlat1ion between their microstructure and their performance for battery applications.

P(VdF-HFP) polymer electrolyte membranes showed nominal capacities ranging from 70% to 90% of the theoretical value with very good capacity retention and charge/discharge efficiency close to 100%. The good cycling behaviour exhibited by the half-cells indicate that the P(VdF-HFP) polymer electrolyte membranes developed in this work may be used as separators in lithium cells both in the anodic and in the cathodic region.

The prepared P(VdF-CTFE) separator membranes show two pseudoplateaus varying between 3.2 and 3.8 V and good cyclability and rate capability. The voltage and discharge capacity values decrease progressively as the scan rates increase. At C/10 and 2C the discharge values are 168 and 92 mA.h.g^{-1}, respectively. Further, the discharge capacity is 142 mA.h.g^{-1}, 132 mA.h.g^{-1}, 121 mA.h.g^{-1}, 117 mA.h.g^{-1}, and 85 mA.h.g^{-1} at rates of C/10, C/5, C/2, C and 2C, respectively. For half cells containing 20CTFE25, 20CTFE50 and 5CTFE25 samples, the discharge capacity values after 50 cycles are 92 mA.h.g^{-1}, 64 mA.h.g^{-1} and 30 mA.h.g^{-1}, respectively. The good cycling behaviour exhibited by the half-cell indicates that the P(VdF-CTFE) separators are thus excellent candidate for their use in high-power and safety lithium-ion batteries applications.

The membrane solutions prepared with different P(VdF-HFP) and P(VdF-CTFE) contents can be prepared with a large range of viscosities, making them suitable for the development of inks to be used in printing technology. The choice of the viscosity will depend on the selected printing technique.

In relation to the cathodes, inks based on $LiFePO_4$ were prepared for screen-printing technique, revealing 69% of capacity retention, which represents 48% of the theoretical value, indicating the good performance of the battery and making these cathodes suitable candidates for printed Li-ion batteries. The charge/discharge curves are characterized by a flat voltage plateau at around 3.2 – 3.6 V that depends on the scan rate. The printed cathodes show 108.1 mA.hg^{-1} at C/6, 111.8 mA.h.g^{-1} at C/5, 107.8 mA.h.g^{-1} at C/2, 100.1 mA.h.g^{-1} at C, 79.1 mA.h.g^{-1} at 2C and 27.4 mA.h.g^{-1} at 5C, independently the cycle number, representing high delivered capacity. With respect to the cycling performance at 5C, the cathodes show an initial discharge capacity of 48.2 mA.h.g^{-1} and after 50 cycles the discharge value is 39.8 mA.h.g^{-1} with a capacity retention of 83%, demonstrating the good performance of the battery. In relation to the anodes, inks based on graphite shows a homogeneous distribution of the these particles and the discharge capacity values are 152, 88,72, 48, and 32 mAh.g^{-1} at C/6, C/5, C/2, C and 2C-rates, respectively.

As a final remark, al materials and battery components developed in this work show suitable properties for application in Li-ion printed battery applications.

7.2. Future work

Printed batteries still have large challenges to face. In fact, both at academic and industrial level still there is not a fully printed battery. Thus, the main challenge will be the development of inks that allow the use of layer-by-layer technique in the fabrication of printed batteries.

The use of printed batteries is growing up, thus it is essential to develop inks that allow the fabrication of each component of the battery. Depending on the equipment to use in the printing technique, the inks should show different viscosities, which change their rheological characteristics. It is thus mandatory to find inks with suitable properties for each component of the battery but also that can be formulated for the different printing techniques.

Further, materials with larger capacity, allowing the development of thinner batteries are needed, as well as more ecological materials, in particular the solvents used for the ink formulations.

For some applications (power applications), the conductivity of the battery is limited by the separator, and so it is necessary to find new ways to improve it, for instance by using ionic liquids.

The resolution of these related issues will allow the development of fully printed batteries in the near future.